Otwin Breitenstein
Wilhelm Warta
Martin Langenkamp

SPRINGER SERIES IN ADVANCED MICROELECTRONICS 10

Lock-in Thermography

Basics and Use for Evaluating Electronic Devices and Materials

Second Edition

Springer Series in
ADVANCED MICROELECTRONICS 10

Springer Series in

ADVANCED MICROELECTRONICS

Series Editors: K. Itoh T. Lee T. Sakurai W.M.C. Sansen D. Schmitt-Landsiedel

The Springer Series in Advanced Microelectronics provides systematic information on all the topics relevant for the design, processing, and manufacturing of microelectronic devices. The books, each prepared by leading researchers or engineers in their fields, cover the basic and advanced aspects of topics such as wafer processing, materials, device design, device technologies, circuit design, VLSI implementation, and subsystem technology. The series forms a bridge between physics and engineering and the volumes will appeal to practicing engineers as well as research scientists.

Please view available titles in *Springer Series in Advanced Microelectronics* on series homepage http://www.springer.com/series/4076

O. Breitenstein
W. Warta
M. Langenkamp

Lock-in Thermography

Basics and Use for Evaluating Electronic Devices and Materials

Second Edition

With 89 Figures

Springer

Dr. Otwin Breitenstein
Max-Planck-Institut für Mikrostrukturphysik
Weinberg 2, 06120 Halle, Germany
E-mail: breiten@mpi-halle.de

Dr. Wilhelm Warta
Fraunhofer-Institut für Solare Energiesysteme (ISE), Heidenhofstr. 2, 79110 Freiburg, Germany
E-mail: wilhelm.warta@ise.fraunhofer.de

Dr. Martin Langenkamp
Sandhof 6b, 24768 Rendsburg, Germany
E-mail: martin.langenkamp@web.de

Series Editors:
Dr. Kiyoo Itoh
Hitachi Ltd., Central Research Laboratory, 1-280 Higashi-Koigakubo
Kokubunji-shi, Tokyo 185-8601, Japan

Professor Thomas Lee
Stanford University, Department of Electrical Engineering, 420 Via Palou Mall, CIS-205
Stanford, CA 94305-4070, USA

Professor Takayasu Sakurai
Center for Collaborative Research, University of Tokyo, 7-22-1 Roppongi
Minato-ku, Tokyo 106-8558, Japan

Professor Willy M. C. Sansen
Katholieke Universiteit Leuven, ESAT-MICAS, Kasteelpark Arenberg 10
3001 Leuven, Belgium

Professor Doris Schmitt-Landsiedel
Technische Universität München, Lehrstuhl für Technische Elektronik
Theresienstrasse 90, Gebäude N3, 80290 München, Germany

ISSN 1437-0387
ISBN 978-3-642-02416-0 e-ISBN 978-3-642-02417-7
DOI 10.1007/978-3-642-02417-7
Springer Heidelberg Dordrecht London New York

Library of Congress Control Number: 2010935594

© Springer-Verlag Berlin Heidelberg 2003, 2010

This work is subject to copyright. All rights are reserved, whether the whole or part of the material is concerned, specifically the rights of translation, reprinting, reuse of illustrations, recitation, broadcasting, reproduction on microfilm or in any other way, and storage in data banks. Duplication of this publication or parts thereof is permitted only under the provisions of the German Copyright Law of September 9, 1965, in its current version, and permission for use must always be obtained from Springer. Violations are liable to prosecution under the German Copyright Law.
The use of general descriptive names, registered names, trademarks, etc. in this publication does not imply, even in the absence of a specific statement, that such names are exempt from the relevant protective laws and regulations and therefore free for general use.

Cover design: eStudio Calamar Steinen

Printed on acid-free paper

Springer is part of Springer Science+Business Media (www.springer.com)

Preface

In the last 7 years, the first edition of “Lock-in Thermography” has established as a reference book for all users of this technique for investigating electronic devices, especially solar cells. At this time, a vital further development of lock-in thermography could be observed. Not only the experimental technique was improved by applying new and better infrared cameras, solid immersion lenses, and novel timing strategies, but also completely new application fields of lock-in thermography were established by implying irradiation of light during the measurements. The two groups of new techniques are different kinds of Illuminated Lock-In Thermography (ILIT) and Carrier Density Imaging, resp. Infrared Lifetime Imaging (CDI/ILM). While ILIT is performed on solar cells, CDI/ILM is performed on bare wafers for imaging the local minority carrier lifetime and the local concentration of trapping centers. The new edition of this book implements these new developments.

One new section entitled “Timing strategies” is added. In this, new ways are introduced to overcome previous limitations of the choice of the lock-in frequency in comparison with the frame rate of the camera. The previous diffraction limit of the spatial resolution can be overcome by a factor of up to 4 by applying so-called solid immersion lenses. This technique is introduced and its application for failure analysis of ICs, where highest possible spatial resolution is desired, is shown in another new section. The new section “Heat Dissipation and Transport Mechanisms in Solar Cells” provides the physical background of several newly introduced lock-in thermography techniques. Here and in the section “Influence of the Peltier Effect,” new findings about the relevance of the Peltier effect for the interpretation of lock-in thermography results are presented. The new section “Carrier Density Imaging” introduces the basic concepts of lifetime imaging using CDI/ILM. Different variants of its practical realization and typical applications of this technique are shown in two other new sections. The section on the application of dark lock-in thermography to solar cells was extended by introducing several new techniques for measuring local series resistances, also implying electroluminescence imaging, and for measuring physical parameters of breakdown sites. Finally, the new section “Illuminated Lock-in Thermography (ILIT)” describes different new techniques on solar cells, which differ by their kind of illumination (pulsed or continuous) and their biasing conditions of the cell. These techniques not only allow to investigate shunts without contacting the cell but also to display the inhomogeneity of the series resistance, the

lifetime in the base material, and the avalanche multiplication factor under reverse bias. Altogether, the new edition contains more than 50 new figures, 100 new references, and 50 additional printed pages. Known misprints of the old edition were corrected and sections on Dynamic Precision Contact Thermography, which is not used anymore, and some less prominent application fields such as bonded wafers and gate oxide integrity defects, were skipped for saving space. We hope that this considerably extended new edition will become as useful as the first edition was.

Halle
May 2010

Otwin Breitenstein
Wilhelm Warta
Martin Langenkamp

Preface to the First Edition

Although the first publication on lock-in thermography appeared in 1988 concerning electronic device testing, this technique only became popular in the 1990s in connection with the nondestructive testing of materials (NDT, especially photothermal and thermoelastic investigations). In the early 1990s our group at the Max Planck Institute of Microstructure Physics in Halle had the task to image small leakage currents in silicon solar cells. We soon realized that neither conventional (steady-state) thermography nor the only available lock-in thermography system of that time was sensitive enough to image the tiny temperature differences caused by these leakage currents. Therefore we developed the "Dynamic Precision Contact Thermography" technique (DPCT), which was the first lock-in thermography system having a detection limit below 100 μK. However, this system turned out to be too impracticable for general use, since it worked in a mechanical contacting mode, and its measurement time was necessarily many hours. With the availability of highly sensitive focal plane array thermocameras at the end of the 1990s, the way was opened to construct highly sensitive IR-based lock-in thermography systems. This was done independently by groups working in NDT and by us working in electronic device testing, whereby the different demands in the different fields lead to partly different approaches in the realization. For photothermal investigations a low lock-in frequency is usually used in order to see sub-surface details, and for thermoelastic investigations the thermocamera cannot usually be synchronized to the temperature modulation. In electronic device testing, on the other hand, the main challenge was to achieve a noise level as low as possible and to work at high frequencies in order to detect weak heat sources at the surface with a good spatial resolution. For NDT the heat introduction is usually harmonic and is realized externally, e.g. by light irradiation, ultrasonic incoupling, or mechanical vibration. In electronic device testing the heat introduction has to be rectangular and is realized internally by applying bias pulses, which can easily be synchronized to the thermocamera. It emerged that our highly sensitive lock-in thermography system is very useful not only for investigating solar cells, but also for many other kinds of electronic device testing such as integrated circuit (IC) testing, characterizing bonded semiconductor wafers, and mapping gate oxide integrity (GOI) defects in MOS devices. Our developments led to the construction of the TDL 384 M 'Lock-in' system at Thermosensorik GmbH Erlangen (Germany), which has been available since 2000 and is specialized for the

functional testing of electronic components. For the above-mentioned reasons, this system differs considerably from those constructed for NDT purposes.

This book addresses, in particular, the application of lock-in thermography for the functional testing of electronic devices. Deliberately we have not treated here the issue of theory and practice of infrared technology for NDT, since this topic is thoroughly covered e.g. in the recently re-edited book of X.P.V. Maldague. However, the technique of lock-in thermography is only briefly considered in that book, without even mentioning that it can also be used for electronic device testing. Since we are convinced that lock-in thermography will play a considerable role in electronic device testing in future, and since many of the physical and technical details of this technique are so far only described in the original literature, we believe that this book will be useful to everybody wishing to use lock-in thermography, especially in electronic device testing and failure analysis. There is some original material first published here, such as the technique for correcting temperature drifts and some new aspects for deconvoluting thermograms, which may also become interesting in the field of NDT. We have tried to restrict the mathematical treatment to the extent necessary for understanding the basic principles of the technique. Thus this book will be useful not only for physicists but also for technicians, engineers, and students who wish to become acquainted with the technique of lock-in thermography. Readers are encouraged to inform the authors about any errors found in this book or to propose further topics which could be included in a later edition.

Halle/Saale — *Otwin Breitenstein*
January 2003 — *Martin Langenkamp*

Contents

1 Introduction 1

2 Physical and Technical Basics 7
- 2.1 IR Thermography Basics 7
- 2.2 The Lock-in Principle and its Digital Realization 14
- 2.3 Lock-in Thermography 22
- 2.4 Timing Strategies 26
- 2.5 Influence of Non-harmonic Heating 33
- 2.6 Noise Analysis 38
- 2.7 Calibration 42
- 2.8 Heat Dissipation and Transport Mechanisms in Solar Cells 44
- 2.9 Carrier Density Imaging 51

3 Experimental Technique 61
- 3.1 Different (Lock-in) Thermography Realizations 61
- 3.2 Commercial Lock-in Thermography Systems 72
- 3.3 Illumination Systems 80
- 3.4 Solid Immersion Lenses 85
- 3.5 Realization of CDI/ILM Systems 91
  - 3.5.1 Absorption Mode 91
  - 3.5.2 Emission Mode 94
  - 3.5.3 Lifetime Calibration 94

4 Theory 101
- 4.1 Influence of the Heat Conduction to the Surrounding 101
- 4.2 Temperature Drift Compensation 107
- 4.3 Thermal Waves of Point Sources 114
- 4.4 Thermal Waves of Extended Sources 118
- 4.5 The Quantitative Interpretation of Lock-in Thermograms 125
  - 4.5.1 The Image Integration/Proportionality Method 129
  - 4.5.2 Deconvolution of Lock-in Thermograms 137

5 Measurement Strategies 149
5.1 Which Signal Should be Displayed? 149
5.2 Influence of the Lock-in Frequency 156
5.3 Influence of the IR Emissivity 159
5.4 Influence of the Peltier Effect 168

6 Typical Applications 177
6.1 Integrated Circuits 178
6.2 Solar Cells 186
6.2.1 Dark Lock-in Thermography (DLIT) 188
6.2.2 Illuminated Lock-in Thermography (ILIT) 201
6.2.3 Summary of Solar Cell Applications 212
6.3 Failure Analysis of Solar Modules 213
6.4 CDI/ILM on Solar Materials 219
6.4.1 Analysis of Material Evolution During Processing 219
6.4.2 Temperature-dependent measurements 219
6.4.3 Trap density images from CDI/ILM 224

7 Summary and Outlook 229

References 235

Thermal and IR Properties of Selected Materials 245

List of Symbols 247

Abbreviations 251

Index 253

Chapter 1
Introduction

With the greater availability and effectively falling prices of thermocameras, in the last years thermography has developed from a rarely used technique towards an increasingly popular investigation method. The technical development of thermocameras to a great extent had been triggered by military research, where night vision means are providing tactic advantages. With the end of the cold war, highly sensitive infrared (IR) technology is increasingly less restricted, now also entering the civil market. Apart from night vision applications, the dominant applications of thermography are the imaging of temperature differences in daily life (e.g., heat losses in buildings), in technique (e.g., monitoring of power stations), and in biology/medicine (e.g., skin temperature mapping). In the following we will call these applications "classical" or steady-state thermography, since here steady-state temperature contrasts are imaged. This book, however, will not deal with classical thermography, since there are a number of books on general thermography available (e.g., [1, 2]).

On the other hand, there are a number of techniques evaluating the time dependence of temperature distributions. While steady-state thermography is often called "passive thermography", the techniques evaluating dynamic temperature changes are also called "active thermography", since here the sample temperature is actively influenced by certain means. The most prominent examples of this class of non-steady-state or dynamic thermography are pulse thermography and lock-in thermography (e.g., [3, 4]). Pulse thermography had been developed for the purpose of non-destructive testing (NDT) of materials and components, hence for "looking below the surface" of solid bodies. Note that one of the basic properties of heat is its ability to penetrate all bodies more or less instantly, depending on the heat capacity and the heat resistance of the material. In pulse thermography, a pulsed heat flux is generated at the surface, usually by the pulsed irradiation of light (e.g., by a flash lamp), and the time evaluation of the surface temperature is monitored. Whenever an inhomogeneity like a crack, a hole, or a buried body of different heat parameters is lying below the surface of the test object, this inhomogeneity will influence the dynamic local heat flux through the sample crossing this inhomogeneity. The time evaluation of the surface temperature reflects this inhomogeneity, and an appropriate display of the results allows one to "look below the surface".

Since the temperature wave needs some time to penetrate to the depth of the material, the imaging time after the pulse corresponds to the information depth [5]). The advantage of pulse thermography is that information about different depths is gained from a number of thermograms, which can be taken within seconds after a single excitation pulse. The disadvantage is that the induced temperature modulations have to exceed the noise level of the camera. Hence, pulse thermography is not appropriate to measure very weak temperature signals. Commercial pulse thermography systems for NDT are available (e.g. [6]).

The alternative technique is lock-in thermography, which is also known as thermal wave imaging, since it can be described by the theory of oscillating thermal waves (see Chap. 4). Here, the heat introduction occurs periodically with a certain lock-in frequency, and the local surface temperature modulation is evaluated and averaged over a number of periods. Thereby the lock-in period has a similar physical meaning as the time after the pulse in pulse thermography has. Hence, the lower the lock-in frequency is, the larger is the information depth of lock-in thermography. The advantage of lock-in thermography is that due to its averaging nature its sensitivity may improve considerably compared to the nominal sensitivity of the camera used. Its disadvantage compared to pulse thermography is that it needs a longer measure time, since it usually averages over a number of lock-in periods. Moreover, for gaining information about different depths, one has to make several measurements using different lock-in frequencies in sequence. Hence, lock-in thermography needs considerably more time than pulse thermography.

In spite of the similarities between both techniques, in this book we will focus our attention only to lock-in thermography, since we are primarily interested in detecting weak heat sources in electronic devices caused by inhomogeneous current flows under applied bias. Note that the signal level in pulse thermography and any other kind of non-destructive testing can always be increased by increasing the light excitation intensity, since all processes underlying this technique are linear in nature. Contrary to that, the heat sources in electronic devices often depend highly nonlinearly on the applied bias. Hence, electronic devices have to be operated at a well defined working point, and the amount of generated heat is usually strictly limited. Since the development of electronic components (except power devices) tends towards a lower power consumption, the heat sources in these devices are naturally weak. Therefore, achieving an ultimate detection sensitivity is much more important for investigating electronic components than for non-destructive testing.

Another common field of application of lock-in thermography, which is often regarded to belong to NDT, are thermo-elastic investigations. Here mechanical components are cyclically loaded and unloaded, with the resulting cyclical surface temperature modulation being detected. This technique allows one to measure local mechanical strain fields and to image the regions of plastic deformation [7]. Another type of thermo-mechanical investigations is to expose the sample to amplitude-modulated ultrasonic energy [2]. Here, the acoustic energy causes heat dissipation at cracks, delaminations, or other mechanical damages of the material, which may be detected by lock-in thermography. Both theses thermo-mechanical techniques are sometimes called “vibrothermography” [2]. Also these techniques are beyond the

scope of this book, since they are described elsewhere [2,7]. We only will refer to the lock-in thermography systems which have been developed for thermo-mechanical investigations as well as for NDT, since they also can be used for investigating electronic components.

The main topic of this book will be the imaging of local heat sources within electronic components by lock-in thermography. In this second edition, the second topic is thermocamera-based imaging of the excess minority carrier density and thus the minority carrier lifetime in semiconductor wafers, since for these investigations the same lock-in thermography equipment can be used as for investigating electronic devices. Electronic components are devices made from semiconductors and other materials whose function rely on internal current flows. These current flows inevitably lead to an internal heat generation within these components owing to the path resistances (Joule heating) and owing to other internal electronic energy dissipation mechanisms like carrier recombination, carrier thermalization, or Peltier effect. Moreover, certain types of defects in electronic devices like leakage currents, latch ups, or shorts, give rise to additional heat sources in these positions. Thus, thermography is a natural candidate to test the function of any electronic devices. Indeed, classical (steady-state) thermography has proven to be very useful to test electronic components, provided that the temperature contrast at the surface of these components exceeds the detection limit of the IR camera [8–10]. Note that the nominal sensitivity of even most recent thermocameras is of the order of 10–20 mK [11]. In order to detect a temperature contrast using a single thermographic image, the lateral temperature contrast at the sample surface has to exceed this value in order to be detectable. This condition sets a serious limitation to the application of classical IR thermography for device testing, since the temperature contrasts generated by many electronic components are below this limit. In most cases, it is not possible to increase the dissipated power since most devices under investigation do not behave linearly, they may even be destroyed at higher voltages. If the sensitivity of thermographic investigations could be increased by, say, two orders of magnitude to about 100 μK, this would dramatically enhance the range of application of thermography in electronic device testing. Another limitation of steady-state thermography is due to the large heat conductivity especially of silicon-based devices. The low thermal resistivity of silicon material is one of its advantages for electronic power devices, since it enables an instant dissipation of the generated heat into some heat sinks. On the other hand, this heat conductivity also leads to an instant lateral dissipation of locally generated heat. Hence, even if there are inhomogeneously distributed internal heat sources in silicon devices, their temperature contrasts may widely get "smeared out" under steady-state imaging conditions. Finally, the different IR emissivity of different materials greatly obscures the thermograms of inhomogeneous surfaces like that of integrated circuits.

Using lock-in thermography instead of the steady-state one enables a new quality of investigating local heat sources in electronic devices. Both the detection limit and the effective spatial resolution of thermographic investigations of electronic devices may improve by several orders of magnitude compared to steady-state thermography. Moreover, lock-in thermography is much easier to apply than precision

steady-state thermography, since thermal drifts are no longer disturbing the measurement (or may easily be compensated, see Sect. 4.2), and even stray light from the surrounding does not disturb in most cases. Also the influence of the IR emissivity can easily be compensated without any surface treatment by displaying the phase signal or the "emissivity-corrected 0° signal", as proposed in Sect. 4.5.2 and discussed in more detail in Sects. 5.1 and 5.3. Finally, the quantitative evaluation of lock-in thermography results is much more straightforward than that of steady-state thermography results, since the sample usually can be regarded as adiabatic so that heat conduction to the surrounding does no longer influence the result (see Sect. 4.1).

Therefore, lock-in thermography is already now a very advantageous tool in electronic device testing and failure analysis. This book was written to further facilitate the introduction of lock-in thermography, which is already established in non-destructive testing (NDT), into the field of electronic device testing. In this field, the technical demands on the system are considerably different from that of NDT applications. While for NDT an external sin-modulated heat source is used, lock-in thermography on electronic devices uses the square-wave modulated internal heat generation of the components due to their internal current flow. The aim of NDT is the detection of inhomogeneities of the thermal parameters of the test objects or, in the case of vibrothermography, the detection of load-induced stress or of ultrasonic-induced heat sources. Lock-in thermography of electronic devices, on the other hand, is looking for local internal heat sources within these devices. This internal heat generation can be pulsed most easily by pulsing the supply voltage of the components, but also more sophisticated triggering modes are possible (see Sect. 2.3). This sophisticated triggering allows detailed functional investigations to be carried out, which would be impossible by steady-state thermography. In general, the sensitivity demands are much more striking for investigating electronic components than for NDT.

In 2000 a new application of IR-thermography to solar wafers called Infrared Lifetime Imaging (ILM, [12]) was published by Bail et al. This technique implies homogeneous irradiation of near-infrared light for generating minority carriers in the wafer. The local concentration of excess carriers is detected by the IR camera due to their free carrier absorption/emission and utilized for displaying the local minority carrier lifetime. The sensitivity of this technique was later considerably increased by the implementation of lock-in techniques. The first publication of this implementation was called Carrier Density Imaging (CDI, [13]). Since both versions refer essentially to the same principle, we will in this book refer to this technique as CDI/ILM. In the CDI/ILM technique the measured effect does not rely on temperature changes but rather on the changes of the free carrier concentration, this technique may thus be called a "non-thermal" application of lock-in thermography. Later on lock-in thermography implying near-infrared light irradiation was also applied to solar cells [14, 15]. This technique is now referred to as "Illuminated Lock-In Thermography" (ILIT, [16]). Both ILIT and CDI/ILM may be performed with one and the same experimental setup and are described in this book.

This book is intended to present todays state of the art of highly sensitive lock-in thermography on electronic devices and materials. Meanwhile, a number of commercial lock-in thermography systems are available [17–28]. This book should be useful for beginners and advanced users of these and similar systems, if electronic devices or materials have to be tested. Since many of the topics dealt with in this book are also interesting for NDT, like the technique for temperature drift compensation or approaches to solve the inverse problem of lock-in thermography, also the NDT community should benefit from this book. Especially, however, it is intended for researchers and engineers involved in IC and other electronic component testing and in solar cell development, where lock-in thermography is already now one of the standard test tools. Since the design philosophy of the introduced systems is described in more detail, this book may also be helpful to develop novel lock-in thermography systems.

In the following Chap. 2, the basics of conventional (steady-state) infrared thermography are reviewed, as well as the physical and technical basics for the lock-in technique itself and for its application in lock-in thermography. Different strategies to organize the timing of these measurements are introduced. It is discussed how non-harmonic heating, which is usually applied for the diagnostics of electronic components, affects the accuracy of the obtained results. A noise analysis of lock-in thermography is presented, relating the noise properties of the infrared camera to the noise level of the lock-in thermograms. Then, a simple calibration procedure for lock-in thermography is proposed. Since until now the main application of lock-in thermography is the investigating solar cells, a special section describes the different heat generation and consumption mechanisms, which are underlying the measured temperature modulation in solar cells. In addition, the physical basics of lifetime mapping in wafers by CDI/ILM are introduced. Chapter 3 describes the experimental technique of thermographic methods. It starts with a general overview of the most important steady-state and non-steady-state thermography techniques cited in the literature. Then the presently existing commercial lock-in thermography systems are briefly described and their features are compared. Different realizations of illumination systems, which are necessary for both CDI/ILM and ILIT, are reported, and the application of solid immersion lenses for improving the spatial resolution of lock-in thermography down to 1 μm is described. A special section deals with the realization of CDI/ILM for lifetime mapping in solar wafers. Chapter 4 presents an overview of the theory of lock-in thermography on electronic devices. First, the terms “thermally thin and thick samples” and “quasi-adiabatic measurement conditions” are introduced, which are important for the quantitative interpretation of lock-in thermography results. Then, a simple procedure is described which allows one to compensate any lock-in thermography result for temperature drifts. Finally, the propagation of thermal waves is theoretically evaluated, followed by instructions how to interpret lock-in thermography results quantitatively. Based on these theoretical findings and on general considerations, Chap. 5 gives some practical advice how to find optimum imaging parameters for lock-in thermography and how to regard the local emissivity of the devices. Here, a novel kind of presenting lock-in results is discussed, which is especially advantageous for microscopic IC investigations.

Moreover, the physics of the Peltier effect, which acts both at metal–semiconductor contacts and at the p–n junction, is described and it is described how Joule-type heating can be distinguished from the Peltier effect. Finally, a number of application examples of lock-in thermography investigations of electronic devices and materials is introduced in Chap. 6. These examples demonstrate the great number of different problems that can be addressed by different types of lock-in thermography in failure analysis of ICs, in the characterization of solar cells and modules, and in the evaluation of wafers for producing solar cells. Finally, in Chap. 7 a summary and an outlook for possible future developments of this technique are given.

Chapter 2
Physical and Technical Basics

First, in Sect. 2.1 the general basics of infrared (IR) thermography are briefly reviewed, which are also applicable to IR camera based lock-in thermography. In Sect. 2.2, the principles of the lock-in technique itself and of its digital realization are described. In Sect. 2.3, the two principal variants of lock-in thermography, which are serially measuring systems and camera-based systems, are introduced and compared. Different strategies to organize the timing of the lock-in correlation in relation to the frame rate of the IR camera are described in Sect. 2.4. Section 2.5 discusses the influence of non-harmonic (square wave) heat introduction, which is standard in electronic device testing, in contrast to the harmonic (sin-shaped) heat introduction mostly used in NDT. A detailed noise analysis is presented in Sect. 2.6, which relates the noise properties of the temperature measurement system to the noise level of the lock-in thermography result. Here, the "pixel related system noise density" is introduced as a universal parameter describing the figure of merit of different lock-in thermography systems. Section 2.7 deals with the problem of an easy and reliable calibration of lock-in thermography measurement systems by using a resistively heated test structure. In Sect. 2.8 the elementary processes in a solar cell with their heat generation and transport properties are described, which is the physical base for understanding lock-in thermography on solar cells. The detection of free carriers in semiconductors by IR lock-in thermography, which is a novel application of this technique based on non-thermal effects, is introduced in Sect. 2.9.

2.1 IR Thermography Basics

Section 3.1 will show that infrared (IR) thermography is by far not the only way to measure surface temperature distributions. Nevertheless, it is maybe the most elegant one, since it can be applied even to rough surfaces, and it can image the sample from a certain distance without contacting the surface at all. It even may investigate structures at the backside of a silicon wafer by looking through the wafer material, which is essentially transparent to the IR radiation. Most importantly, with the availability of modern focal plane array IR cameras combining high sensitivity with high frame rates, IR camera-based lock-in thermography systems have proven to provide today's best possible performances with respect to the detection sensitivity

within a limited measure time, which will be shown in Sect. 3.1. Thus, IR camera based lock-in thermography systems have already shown to be very useful to test electronic components. Therefore, in the following section the basic principles of IR thermography will briefly be reviewed, which also hold good for IR lock-in thermography.

If electromagnetic radiation (light) falls onto the surface of a specimen, three and only three things possibly may happen with the irradiated light: It may be reflected from the surface, it may be absorbed by the specimen, or it may be transmitted if the specimen is totally or partly transparent to the light. The probabilities of these three processes to happen are described by the reflection coefficient or reflectance ρ, the absorption coefficient or absorbance α, and the transmission coefficient or transmittance τ. These three coefficients are usually wavelength-dependent and may depend on the directional distribution of the irradiation. They are dimensionless, and their sum is always unity. For an ideally reflecting specimen, ρ is unity, and α and τ are zero, for a non-reflecting totally transparent specimen, τ is unity and α and ρ are zero, and for a black body, α is unity, and ρ and τ are zero. Each body at a finite temperature spontaneously emits electromagnetic radiation, which is called thermal radiation. The magnitude M_λ (in units of $\mathrm{W\,m^{-2}\mu m^{-1}}$) is called the spectral specific irradiation. It describes the electromagnetic power, which is irradiated within a differential wavelength range by a plane unit area into one half-space. The specific irradiation of a black body as a function of the wavelength λ is given by Planck's law:

$$M_\lambda(T) = \frac{2\pi \mathrm{hc}^2}{\lambda^5}\left(\mathrm{e}^{\frac{\mathrm{hc}}{\lambda k T}} - 1\right)^{-1} \tag{2.1}$$

(h = Planck constant, c = velocity of light, k = Boltzmann constant, T = absolute temperature in Kelvin). Figure 2.1 shows the spectral distribution of the specific irradiation of a black body for two temperatures near room temperature. The noticeable room temperature radiation starts at 3 microns, the maximum appears around 10 microns, and the radiation spreads to above 30 microns. For a real (not black) specimen, the thermal emission also depends on optical properties of the specimen. Let us imagine a closed volume with homogeneous optical properties of the walls at a certain temperature in thermal equilibrium. Then the inner surface loses energy by thermal radiation, and it absorbs energy by radiation absorption. Thus at any wavelength, each part of the inner surface has to emit the same amount of radiation as it absorbs, otherwise the system would not be in thermal equilibrium. This means that the probability of a surface to emit radiation (the so-called emissivity ε) has to be equal to the absorption probability α at this wavelength. This identity is known as Kirchhoff's law. For an ideal black body, $\alpha = \varepsilon = 1$ holds, for real bodies ε is more or less smaller than 1. If within a certain wavelength range the emissivity ε is < 1 but wavelength-independent, this specimen is called a "grey emitter". If ε strongly depends on the wavelength, this specimen is called a "selective emitter". In order to obtain the specific irradiation of a real body, (2.1) has to be multiplied by the wavelength-dependent emissivity $\varepsilon(\lambda)$.

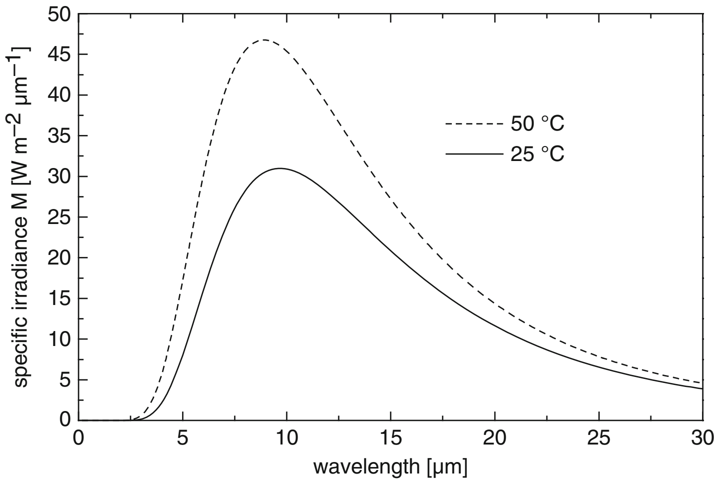

Fig. 2.1 Black body radiation for room temperature (25°C) and for 50°C

The dominant uncertainty in quantitative thermography is due to the fact that the IR emissivity ε of the investigated object is often unknown and may even be position-dependent. In order to determine the temperature of an object from the thermal radiation, the emissivity in the detection range has to be known or measured (see Sect. 5.3). Thus, though thermograms are usually scaled in °C, this scaling is based on the assumption of a certain emissivity, which does not need to be correct. Especially, reflecting objects like metallic surfaces usually show a low emissivity due to their high reflectivity, and the radiation coming from these objects contains a high amount of reflected light from the surrounding. This makes thermography on highly reflecting objects especially difficult. A proven way to overcome this problem is to cover the surface of these objects with a thin layer (e.g. a black paint), which has a high emissivity within the sensitivity range of the camera.

Thermography was invented for imaging temperature distributions from certain distances through the air. If there is any absorption of thermal radiation by the air, this causes errors in thermographic T-measurements. In order to keep these errors small, the wavelength range of a thermocamera has to be chosen so to avoid the dominant absorption regions. Figure 2.2 shows the transmission of a typical wet atmosphere as a function of the wavelength. The absorption is mostly due to water vapor and CO_2. In the interesting IR range between 3 and 30 μm there are two wavelength "windows" where the atmosphere is essentially transparent. The so-called "mid-range" window is between 3 and 5 μm, and the "long-range" window is above 8 μm. Thermocameras are usually supplied to work within one of these windows. The residual absorption within these windows may be regarded in the software-based scaling of modern IR cameras as a function of the distance, the temperature, and the humidity. Note, however, that for Fig. 2.2 a large distance of 6000 ft (1250 m) was chosen. If lock-in thermography has to be performed on single

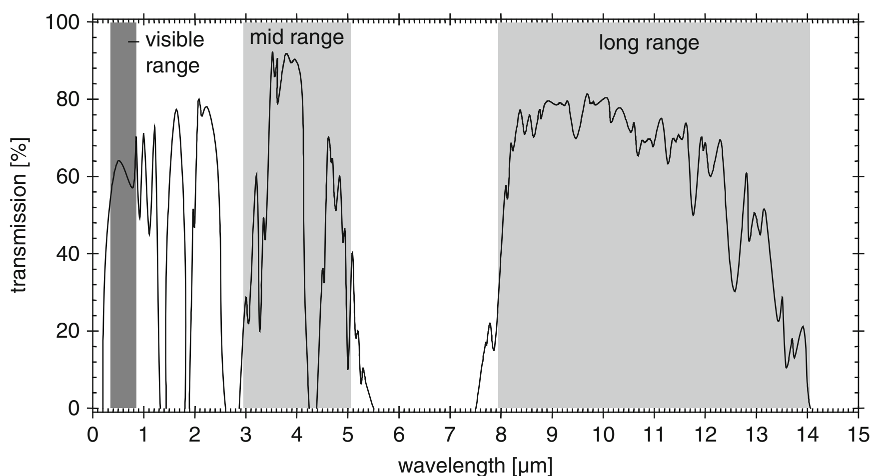

Fig. 2.2 Transmission of the atmosphere in the wavelength range between 0.2 and 14 μm. This measurement was done over a distance of 6000 ft (1250 m) at 20°C and 100% relative humidity [1]

electronic devices, the typical imaging distances are well below 1 m. Even in the range between 5 and 8 μm the transmission of wet air over a distance of 30 cm is still above 80%. Hence, for this special application the sensitivity range of IR cameras might also reach into this range, which could be advantageous in achieving a higher sensitivity. Unfortunately, today's highly sensitive IR cameras generally are still working in only one of these windows and do not use the spectral range between 5 and 8 μm. The spectral range of mid-range and long-range thermocameras is often artificially cut below 3 and 8 μm, respectively, using an optical filter.

The major inaccuracy of radiometric temperature measurements arises from the uncertainty in knowing ε and from the influence of reflected light. Fortunately, reflected light disturbs lock-in thermography only slightly, since this is an a.c. measurement. Though, in principle, also the reflection coefficient may be temperature-dependent, it can be assumed to be constant within the small temperature fluctuations appearing in lock-in thermography. Thus, reflected light contributes a constant additive component to the thermographic images, which is effectively cancelled by the lock-in process if it does not include frequency components near the lock-in frequency (see Sects. 2.2 and 2.3). Therefore lock-in thermography usually does not require any shading of the imaging scene, and persons may move around the measurement set-up, which may be disturbing in standard thermography. Only for low lock-in frequencies around or below 1 Hz, the light reflected from a laboratory surrounding contains frequency components near the lock-in frequency, which may affect also a lock-in thermography measurement.

Some remarks should follow as to the different types of thermocameras. The classical thermocameras, which are no more available, were actually serially working. Hence, they contained only one highly sensitive IR detector and a mechanical mirror scanner system, which successively leads the light pixel by pixel from the imaged

scene to the detector. The actual IR detector was a quantum detector (photodiode type), usually liquid nitrogen cooled and made from InSb (indium-antimonide) or HgCdTe (mercury-cadmium-telluride, MCT). InSb detectors are only sensitive in the mid-range spectrum (3–5 μm), whereas MCT detectors may be designed to work either in the mid-range or in the long-range one (8–10 μm).

All modern thermocameras are so-called "staring" or focal plane array (FPA) cameras [11], usually having quartz-stabilized frame rates. Just like the well-known silicon-based CCD cameras working in the visible range, these FPA cameras employ a 2-dimensional array of IR-detectors, which is positioned in the focal plane of the IR optics. However, this focal plane array has to be made from a material like InSb or MCT, which is sensitive in the infrared range. Each photodiode of this detector array has to be electrically connected with one readout channel of a separate silicon readout-chip attached to the detector chip, which is technologically very demanding. These detectors have to be cooled to about liquid nitrogen temperature (<80 K), which is done today mostly by using Stirling coolers. Also thermocameras based on Quantum Well Infrared Photodetectors (QWIP) on a GaAs wafer are available, which are not quantum detectors but rather photoconductors. Their sensitivity is comparable to that of InSb or MCT detectors, but their frame rate is lower. In the past also, detectors based on platinum-silicide Schottky diodes on a silicon wafer were used, but they also have disappeared from the market.

Today's most popular thermocameras are uncooled cameras, which are based on an array of thin film thermoresistors on free-lying membranes on an Si-chip. These so-called microbolometer cameras are sensitive in the long range. They are about a factor of 2–4 less sensitive than cooled quantum detector cameras and operate at a frame rate between 30 and 60 Hz, but they are much cheaper than any cooled detector camera. In cases where an ultimate detection sensitivity is not needed, they can also be used for lock-in thermography.

Another important aspect is the frame rate of the camera. As the noise analysis in Sect. 2.6 will show, a high frame rate is desirable for attaining a high detection sensitivity. In this respect, the long range MCT FPAs are optimum of all, since they reach their sensitivity of about 20–30 mK at a frame integration time of only about 200 μs. The frame integration time is the time where "the shutter of the camera is opened". Of course, modern FPA cameras do not have a mechanical shutter anymore but an electronic one, which governs the exposure time when photons are captured. Depending on the object temperature and on the properties of the objective, there is an optimum integration time for each measurement. The signal-to-noise ratio of the camera increases with the square root of the integration time. Hence, if the integration time is chosen too low, the camera noise increases. On the other hand, if the integration time is chosen too large, the storage capacitors of the readout circuit get saturated, hence the pixel readout values do not depend on the object temperature anymore. This has to be avoided, of course. In older FPA cameras the moment of exposure was dependent on the image position, hence different pixels were not only read-out sequentially but also exposed to the light sequentially. This operation mode was called "rolling frame mode". Modern FPA cameras are working mostly in the "snapshot mode", hence all pixels are exposed to the light at the same time. In

the past, only one capacitor per image pixel was used in the read-out circuit to store the collected charges of this pixel. Here the readout process started after the exposure period ("integrate-then-read", ITR-mode), hence the minimum frame period was the sum of the frame integration time and the readout time. Newer IR-cameras contain two storage capacitors per pixel and may charge-up one of them while the other is read-out ("integrate-while-read", IWR-mode). In these cameras the maximum possible frame rate may be close to the inverse of the frame integration time. Thus, long range cameras, needing an integration time of only 200 μs for achieving optimum signal-to-noise ratio at room temperature, could reach a frame rate of about 5 kHz. In practice, however, the readout circuit still limits the maximum full frame rate to values between 100 and 800 Hz. The readout speed is given in units of megapixel per second. Hence, the larger the array, the harder is it to reach high frame rates. However, if only some part of the detector is used (sub-frame modus), depending on the size of the sub-frame, the attainable frame rates may reach several kilohertz. It can be hoped that the speed of readout circuits will further increase in future. The InSb and MCT mid range FPAs need a frame integration time of about 1–2 ms to reach their best sensitivity at room temperature of 10–20 mK. Thus, they can be used up to a frame rate of about 500 Hz, which is within the possibilities of modern readout circuits. Uncooled IR cameras show a frame rate of only 30–60 Hz, hence also for this reason they are less appropriate to achieve highest detection sensitivity (see Sect. 2.6). Regarding the spectral distribution of the thermal radiation given in Fig. 2.1, one could assume that the sensitivity of cameras in the long-range should generally exceed that in the mid-range. However, the practically obtained signal-to-noise ratio depends not only on the flow rate of received photons but also on the noise properties, on the quantum yield, and on the sensitive area of one pixel (pitch size) of the detector elements as well as on the noise parameters of the read-out electronics. Also, the relative change of the photon flux with temperature plays a role, which is larger in the mid-range than in the long-range. Altogether, mid-range cameras usually show an even somewhat higher nominal sensitivity at room temperature than long-range ones [11]. If microscopic investigations have to be made, like failure analysis on ICs, mid-range cameras have to be preferred, since they provide a better diffraction-limited spatial resolution, see Sect. 3.4. Thus, the choice of the optimum thermocamera for a certain application depends on many factors, which here could be discussed only briefly.

It should be mentioned that compared to the old scanner cameras the highly sensitive Focal Plane Array cameras may have special problems. Thus, as a rule, not all pixels of an array are operative. Some of them show strongly outrunning properties, some of them are totally insensitive, and some of them are "flickering". Usually, also the scatter of the light conversion parameters (gain and offset) of the nominally operative pixels is so large that the raw image from such a camera looks very poor. Note that monocrystals of the III-V compounds InSb and HgCdTe (MCT), which the most sensitive FPAs are made from, cannot be grown as perfectly as monocrystalline silicon crystals can be made. Fortunately, these problems can be solved using digital technology. All modern FPA cameras are digital ones, hence their originally analog video signal is digitized and further processed as a stream of data within the

camera via digital signal processors (DSPs). In the so-called two-point calibration procedure, both the gain and the offset of each pixel are software corrected on-line to yield the correct temperature values. The user can gain the data necessary for the two-point calibration procedure by imaging a homogeneous black body at two different temperatures in the interesting temperature range. Independently, he can easily make an offset correction procedure by imaging any homogeneous object at any temperature. Instead of using a black body, the simplest way to perform the calibration procedure is the following: First cover the objective with a homogeneous object at room temperature, like the plastic lens cap or a sheet of paper, for creating a homogeneous room temperature image and make the first image, which corresponds to room temperature (typically 25°C). Then cover the objective with the heel of your hand (without touching the lens!) and make the second image, which corresponds to the temperature of your hand (approximately 35°C). If not high accuracy measurements have to be performed, the accuracy of this procedure is sufficient. Note that the IR emissivity of the human skin is close to 1, and objects directly in front of the lens, lying far outside of the lens focus, appear very blurred. Hence, even if your hand shows a somewhat inhomogeneous temperature distribution, this will average out across the whole area. If even after this calibration procedure the image quality is not good enough, this is often an indication that the frame integration time was chosen too large, so that the storage capacitors were already saturated at the higher temperature. Note that the data for the image correction depend on both frame rate and frame integration time of the camera. The DSP of the camera can also replace missing pixels by the content of one or several neighboring pixels on-line, so that the final image looks defect-free. The data necessary for a bad-pixel correction are usually given by the manufacturer of the camera. More sophisticated digital cameras used for standard thermography also allow one to correct the image on-line for different emissivities and atmospheric absorption (depending on distance, humidity, and temperature) as well as to regard the non-linear dependence of the IR irradiation of the temperature according to Planck's law (2.1). They may even be equipped with a thermostatted internal black body to provide automatic temperature calibration. For lock-in thermography on electronic devices, however, only the emissivity correction might be interesting, since the absolute temperature reading does not influence the result, the temperature modulations hardly exceed some K, and the objects are usually imaged from a short distance. Details of the local emissivity correction procedure will be described in Sect. 5.3.

Let us finally mention the so-called "Narcissus effect", which is well known to every experienced thermographer. Narcissus was the man in Greek mythology who fell in love with his own mirror image. In thermography the Narcissus effect describes the black spot which is visible whenever a cooled thermocamera is directed to a flat reflective surface where it "sees itself". Since the interior of the camera is cooled and the objective is transparent to the detected IR radiation, the image of the objective of an IR camera in operation detects a cool object. The farer away the mirror is the smaller becomes the dark spot and vice versa. In a microscope objective where the object is very close, the dark spot usually occupies the whole image field. Then the influence of reflected light from the surrounding is

very small, which simplifies the emissivity correction of microscopic IR images (see Sect. 5.3). Since the Narcissus effect is a steady-state phenomenon, it only affects the topography image but not any lock-in thermography result. It can be avoided by slightly inclining a plane object from the normal orientation. Then the dark spot is lying outside of the image field.

2.2 The Lock-in Principle and its Digital Realization

The lock-in principle is the technique of choice, if signals have to be extracted from statistical noise. Prerequisite to using this technique is that the primary signal (before the detection and the first amplification stage!), can be periodically pulsed or anyhow else amplitude-modulated with a certain frequency called "lock-in frequency" $f_{\text{lock-in}}$. In some cases, this modulation is part of the experiment, e.g. in cyclical mechanical loading experiments. If any kind of light causes the primary signal as, e.g., in light absorption experiments, mechanical chopping of the light beam or simply switching the light on and off are convenient means to produce an amplitude-modulated signal. The most elegant method to produce an amplitude-modulated signal is given if the signal generation itself can be controlled electronically. This usually occurs in the functional diagnostics of electronic components if the generated heat is our primary signal. In the simplest case, the heat generation can be modulated by simply pulsing the supply voltage of the tested component. Other more sophisticated triggering modes will be discussed at the end of Sect. 2.3.

The aim of the lock-in principle is to evaluate only the oscillating "alternating current" (a.c.) part of the detected signal. The classical way of converting an a.c. signal into a "direct current" (d.c.) one is to rectify it via some diodes. In a full-wave rectifier, the negative part of a signal is converted into a positive one and then passed by some diodes. The positive part is directly passed by other diodes. Hence, the momentary sign of the a.c. signal itself controls whether the signal is passed by directly, or inverted. If this procedure is performed with a noisy signal, also the noise is rectified, therefore the noise share contributes to the output signal. In order to suppress the noise, the signal before rectification can be fed through an appropriate small-band amplifier, with its center frequency matched to the signal frequency. This measure already improves the signal-to-noise ratio at the output. Nevertheless, also the small-band noise at the modulation frequency makes a positive contribution after conventional rectification, if its intensity is strong enough.

In the lock-in process, the condition whether the signal is passed by directly or inverted, is not controlled by the sign of the a.c. signal itself but rather by a noise-free reference a.c. signal, which is derived from the signal generation process. Figure 2.3 illustrates this procedure. Here, the signal generation process is symbolized by a black box delivering the (noisy) signal of interest and a (noise-free) reference signal. It is irrelevant whether a free-running oscillator controls both the primary signal and the reference signal, or whether the periodic signal generation process is free-running and the reference signal comes from the signal generation process. The dashed circles symbolize different typical signal shapes in different

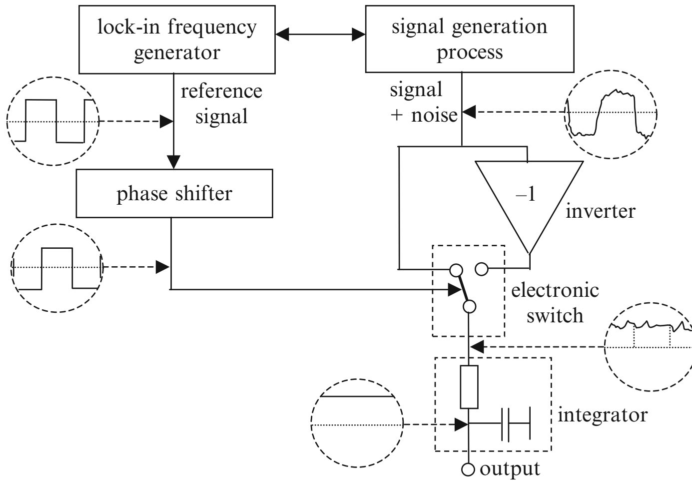

Fig. 2.3 Schematic of an analog wide-band lock-in correlation procedure

positions of the circuit. The actual rectification is performed here via an electronically controlled switch, which connects alternatively the inverted or not inverted signals to the output. Thus, if the reference signal is symmetric (positive period equals the negative one), any d.c. component of the signal is perfectly suppressed by the lock-in process. If the phase of the detected (beneficial) signal coincides with the reference phase, the lock-in procedure behaves to the beneficial signal like an ordinary signal rectification process. Hence, the beneficial a.c. signal is correctly rectified by the lock-in process, leading to a positive d.c. signal at the output. If the phase of the beneficial signal does not coincide with that of the reference signal, both phase positions have to be matched by inserting a phase shifter in the reference path to get the correct signal retrieval. This phase shifter provides a controlled time delay of the reference signal.

The crucial point of the lock-in process is that statistical noise remains statistical even after the rectification process, since it is not correlated with the reference signal. If there are noise components near the reference frequency, after the lock-in procedure they produce another noise signal which, however, has the average value of zero. Therefore, at the final integration stage, which averages the output signal over a certain integration time, this noise averages out and only the beneficial signal passes as a d.c. signal. The longer the integration time, the more efficient is the noise suppression effect, but the longer is the response time for the beneficial signal. In this way it is possible to separate periodic signals, which are embedded in noise being orders of magnitude above the signal level, from the noise. Effectively, the lock-in procedure presents a frequency conversion of the noisy measured signal with the noise-free reference signal towards d.c., where the integration time is inversely proportional to the output bandwidth and thus to the effective detection bandwidth. If the integration stage is a simple RC element, which shows an exponential response characteristic, one speaks of exponential averaging. Averaging the

output over a well-defined integration time t_{int} is called linear averaging. Linear averaging, which can be performed most easily in digital lock-in correlation (see below), has the advantage that there is no cross talk between successive measurements. Choosing the integration time always represents a compromise between the degree of noise suppression and the bandwidth of the output signal.

Mathematically, the lock-in signal treatment (usually called lock-in correlation procedure) can be described as a multiplication of the detected signal $F(t)$ by a correlation function $K(t)$, which is a symmetric square wave function for the case shown in Fig. 2.3. Here, for linear averaging over a certain integration time t_{int}, the output signal S can be written as

$$S = \frac{1}{t_{\text{int}}} \int_{0}^{t_{\text{int}}} F(t)K(t)\,dt \quad \text{with } K(t) = \begin{cases} +1 \text{ (first half period)} \\ -1 \text{ (second half period)} \end{cases} \tag{2.2}$$

If $K(t)$ is symmetric and if a complete number of periods falls into the integration time, the averaged value of $K(t)$ itself is exactly zero, hence (2.2) provides a perfect suppression of any d.c. part of the signal $F(t)$.

Digital lock-in correlation uses an Analog-Digital-Converter (ADC) to digitize the input signal $F(t)$ leading to a set of numbers F_k. Then the whole lock-in correlation procedure is performed numerically. Hence, also the correlation function $K(t)$ has to be replaced by a set of numbers K_k, and (2.2) has to be replaced by a sum. These numbers are also called "weighting factors". They may be positive and negative, and for obtaining an efficient d.c.-suppression their total sum has to be zero. In most lock-in thermography applications the weighting factors follow not a square function as shown in Fig. 2.3 but rather a harmonic function (see below). The digital lock-in correlation procedure consists in averaging the product of the measured values F_k and a set of weighting factors K_k up to the total number of measured values M:

$$S = \frac{1}{M} \sum_{k=1}^{M} F_k K_k \tag{2.3}$$

There are two strategies of performing a digital lock-in correlation: on-line correlation (evaluating the data during the measurement) and off-line correlation (all data are stored and correlated after the measurement). The weighted sum in (2.3) can be summed up during the measurement, but this "standard lock-in correlation" is not the only possible digital correlation technique. Krapez [29] has reviewed different digital signal correlation techniques. Of these the Least Squares Method and also the Fast Fourier Method used by Kaminski et al. [30] have to be performed off-line, since for them all data have to be available prior to the calculation. It is without question that for long integration times and high sampling rates, the storing of all data needs a lot of storage capacity, and the off-line evaluation may become a serious time factor of the whole measurement procedure. This is especially true for lock-in thermography, where whole images have to be stored. Since within the scope of this book we are most interested in highly sensitive measurements requiring

a large amount of averaging, in the following we will consider only standard lock-in correlation, which may be performed on-line.

Note that the (usually equidistant) digitizing or sampling events and the periodic lock-in correlation do not necessarily have to be synchronized. In some cases, a synchronization of the digitization with the experiment is complicated or even impossible to manage. This may hold, e.g., for thermo-elastic investigations, where the sample is treated by a free-running machine independently of the digitizing events. In the following, we will speak of "asynchronous correlation" whenever the lock-in frequency and the sampling rate are not synchronized to each other. It is even possible that the sampling rate is lower than the lock-in frequency. This so-called "undersampling" technique as well as different strategies to organize the timing of lock-in thermography systems will be discussed in detail in Sect. 2.4. Krapez [29] has evaluated some problems connected with a non-synchronized lock-in frequency. For example, in the case of undersampling, there are some "forbidden" lock-in frequencies, which would interfere with the sampling frequency. Under non-synchroneous conditions, due to the usually incomplete number of lock-in periods in one measurement, the d.c. rejection of the lock-in process may not be perfect. Moreover, any frequency drift and phase jitter of both experiment and camera may cause additional noise. Generally, synchronizing the digitizing rate and the lock-in frequency avoids these problems. Synchroneous correlation should therefore be preferred, if technically possible. For the functional diagnostics of electronic components this should always be possible, as electronic components can be triggered via an external signal deduced from the frame trigger of the camera. The main results of Krapez [29] were that more sophisticated correlation methods are advantageous over the standard lock-in method only for a small number of lock-in periods, and if the noise level is below the resolution of the ADC.

In this Section, we always assume synchronization of the lock-in frequency and the digitizing events. Hence, we assume a fixed number of digitizing events n (samples) per lock-in period (which has to be $n \geq 4$, see below), and the weighting factors K_k in (2.3) are the same in each lock-in period. If the measurement is averaged over N lock-in periods, the digital lock-in correlation for a synchronous correlation is given by the sum:

$$S = \frac{1}{nN} \sum_{i=1}^{N} \sum_{j=1}^{n} K_j F_{i,j} \tag{2.4}$$

For function-theoretical reasons, the correlation function optimum to achieve the best signal-to-noise ratio would be the shape of the expected signal. An especially advantageous correlation function, however, is the harmonic (sine or cosine) function. This kind of lock-in correlation is called sin/cos or narrow-band correlation, whereas the square-wave correlation shown in Fig. 2.3 is called wide-band correlation. Typical of the narrow-band correlation is that it evaluates only to the basic harmonic of the signal, which usually carries the dominant information, whereas higher harmonics are suppressed. Electronically, the narrow-band correlation can be

realized either by narrowing the bandwidth of the detected signal prior to the correlation, or by using a sine signal as the reference and an analog multiplier instead of the switches in Fig. 2.3. For the digital lock-in correlation, narrow-band correlation can be realized also either by narrowing the bandwidth of the detected signal or by using the values of a harmonic function for K_j in (2.4). The decisive advantage of the sin/cos correlation is that it allows one to exactly consider the phase of the signal after the measurement (off-line), if the two-channel correlation is used. Two-channel correlation means that there are two sets of weighting factors K_j, one approximating the sine function and the other one approximating the cosine one. The correlation is performed twice in parallel with these two sets of weighting factors. Then the first channel measures the component of the signal in-phase with the sin-function, and the other channel measures the component in-phase with the cos-function, which is 90° phase-shifted to the sin-function. Let us assume that the amplitude of the detected signal is A and its phase (referring to the sin-function) is Φ. Using the addition theorem for the sin-function we get:

$$\begin{aligned} F(t) &= A\sin(2\pi f_{\text{lock-in}}\,t + \Phi) \\ &= A\sin(2\pi f_{\text{lock-in}}\,t)\cos\Phi + A\cos(2\pi f_{\text{lock-in}} t)\sin\Phi \end{aligned} \tag{2.5}$$

If this is inserted into (2.2) with $K^{0^\circ}(t) = 2\sin(2\pi f_{\text{lock-in}} t)$ and $K^{90^\circ}(t) = 2\cos(2\pi f_{\text{lock-in}} t)$ (the factor 2 has to be added to get the correct amplitude), the result of the two correlations over a complete number of periods is:

$$S^{0^\circ} = A\cos(\Phi) \qquad S^{90^\circ} = A\sin(\Phi) \tag{2.6}$$

Exactly the same result is obtained for any even $n \geq 4$, if instead of the integral representation (2.2) the sum representation (2.4) is used for the correlation with K_j being the (doubled) values of the sin and the cos-functions.

$$K_j^{0^\circ} = 2\sin\left(\frac{2\pi(j-1)}{n}\right) \qquad K_j^{90^\circ} = 2\cos\left(\frac{2\pi(j-1)}{n}\right) \tag{2.7}$$

Since the summation in (2.4) goes from 1 to n, j has been lowered by 1 in (2.7) to ensure that the first weighting factor corresponds exactly to a phase position of 0°. S^{0° and S^{90° are usually called the in-phase signal and the quadrature signal. Both signals may be either positive or negative. A negative 0°-signal points to the presence of a signal component 180° phase shifted to the reference, and a negative 90°-signal indicates a 270° signal component. The phase-independent amplitude A (which is always positive) and the signal phase Φ can easily be retrieved from the two results S^{0° and S^{90°:

$$\begin{aligned} A &= \sqrt{(S^{0^\circ})^2 + (S^{90^\circ})^2} \\ \Phi &= \arctan\left(\frac{S^{90^\circ}}{S^{0^\circ}}\right) \left(-180^\circ \text{ if } S^{0^\circ} \text{ is negative}\right) \end{aligned} \tag{2.8}$$

The second term in formula (2.8) for Φ means that an amount of 180° has to be subtracted only if S^{0° is negative. This measure makes the procedure "quadrant correct", since the arctan-function repeats twice within a whole period of 360°. Knowing A and Φ allows one not only to retrieve the in-phase and the quadrature component using (2.6) but also to construct the component of the signal modulation in any phase position Φ':

$$S^{\Phi'} = A\cos(\Phi' - \Phi) \tag{2.9}$$

This situation is illustrated in the complex vector representation of the phase relations occurring in the lock-in process shown in Fig. 2.4. Here, the phase of the reference signal (0°) is the X-axis representing the real part *Re*.

Note that the phase of the cos-function is in advance to that of the sin-function by 90°. In lock-in thermography, however, the surface temperature signals are at best in phase with the periodic power modulation, usually they are more or less delayed. This means that the 90°-signal S^{90° will be essentially negative. In order to have both the in-phase and the quadrature signal essentially positive, the $-$cos-function should be used instead of the +cos one in the quadrature channel.

$$K_j^{0^\circ} = 2\sin\left(\frac{2\pi(j-1)}{n}\right) \quad K_j^{-90^\circ} = -2\cos\left(\frac{2\pi(j-1)}{n}\right) \tag{2.10}$$

Then, the amplitude and the phase are:

$$\begin{aligned} A &= \sqrt{(S^{0^\circ})^2 + (S^{-90^\circ})^2} \\ \Phi &= \arctan\left(\frac{-S^{-90^\circ}}{S^{0^\circ}}\right)\left(-180^\circ \text{ if } S^{0^\circ} \text{ is negative}\right) \end{aligned} \tag{2.11}$$

Throughout this book we will use this definition for the quadrature signal. It will be shown in Sect. 4.5.2 that in some cases, the −45° phase component of the signal

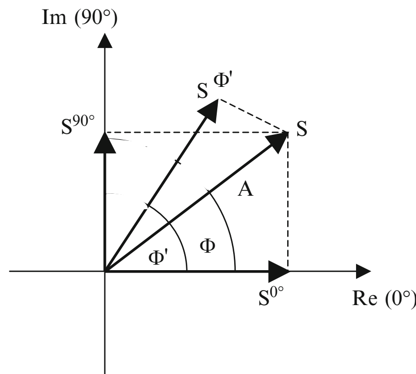

Fig. 2.4 Complex vector representation of the phase relations in the two-channel lock-in process and in retrieving an arbitrary phase component $S^{\Phi'}$

is needed. Applying the addition theorem to (2.9) using $\Phi' = -45°$ and regarding (2.6) leads to the following expression for the $-45°$ phase component:

$$S^{-45°} = \frac{1}{\sqrt{2}}\left(S^{0°} + S^{-90°}\right) \tag{2.12}$$

For a fixed sampling rate f_s the lock-in frequency is given by the number of samples per lock-in period n:

$$f_{\text{lock-in}} = \frac{f_s}{n} \tag{2.13}$$

Synchronization of lock-in and sampling frequency means that the number of samples per lock-in period n is an integer. According to the sampling theorem we need at least two samples per period, and we have to do this twice each period in order to get the in-phase and the quadrature signal. Thus, the minimum possible number of samples per period n is 4, if the two-phase lock-in correlation should be applied. For a fixed maximum sampling rate f_s, this sets an upper limit to the lock-in frequency:

$$f_{\text{lock-in}} \leq \frac{f_s}{4} \tag{2.14}$$

If only 4 signal values are measured within each lock-in period, we will speak of "4-point" correlation. In this case, according to (2.10) the values of the weighting factors K_j are the doubled values of both the sin-function and the $-$cos-function of $0°, 90°, 180°$, and $270°$, respectively. Hence, for the 4-point correlation the two correlation vectors are $K_j^{0°} = (0, 2, 0, -2)$ and $K_j^{-90°} = (-2, 0, 2, 0)$. For a larger number of samples per period the correlation vectors have to be calculated according to (2.10) and the lock-in frequency becomes (2.13).

The higher the number of samples per lock-in period, the more exactly does the sum (2.4) approximate the integral (2.2). Of course, for only 4 samples per period (4-point correlation, maximum possible lock-in frequency) the sine- and cosine-functions are only poorly approximated. Hence, for this case also eqs. (2.6–2.11), which are based on continuous signals, only approximately hold. Thus, in order to preserve the small-band lock-in correlation, the heat signal should actually be harmonic in this case. In serially measuring systems (see Sect. 2.3) this can be managed easily by introducing a band pass filter in the signal path before the ADC. In camera-based systems, however, it is not possible to introduce a filter. Here, the small band correlation may be guaranteed by ensuring that the heat introduction itself is harmonic. This is the reason why harmonic heat introduction is commonly used in NDT [2]. Note that in the early days of NDT in the mid-1990s the computation power was still limited. At that time, for reducing the numeric expense of the correlation procedure, for low lock-in frequencies the digitizing results were averaged over four equidistant periods within each lock-in period. These four averaged values were correlated according to the 4-point correlation procedure described above. In this so-called "4-bucket method" [29] the correlation function also contains higher harmonics, leading to the demand for harmonic heat introduction in NDT. However, for testing electronic devices, the harmonic introduction of heat is seldom

manageable, since in most cases a component has to be tested under well-defined biasing conditions. Hence, usually a certain supply voltage simply has to be switched on and off, leading to a square-wave function of the heat introduction. Possible errors caused by this non-harmonic heat introduction are estimated and discussed in Sect. 2.5. It has been tried by several authors to perform lock-in thermography by applying only a weak modulation to an essentially constant sample bias. In this case the lock-in thermography signal is proportional to the deviation of the locally dissipated power to the bias. However, it has been found that this measure only degrades the signal-to-noise ratio without providing significant advantages. Only in the case of IC failure analysis it may be necessary, for preserving a certain logical condition of the device, to modulate the bias between two values, see Sect. 6.1.

The procedure (2.4) using the weighting factors (2.10) is mathematically called a discrete Fourier transformation [31, 32]. It calculates the complex Fourier component at one single frequency $f_{\text{lock-in}} = f_s/n$ of the measured function $F_{i,j}$. Alternatively, for all measured data F_m also the so-called fast Fourier transform (FFT) procedure can be applied. In simplest form this procedure requires a total number of measurements of $M = 2^i$, i being an integer, but also variants working with arbitrary data format are available [31]. It calculates all Fourier components of this data vector, which belong to the frequencies $f_1 = f_s/M$; $f_2 = 2f_s/M$, etc. up to the Nyquist frequency $f_s/2$ (see Sect. 2.4). So FFT provides a complete harmonic analysis of a signal. The result of this analysis is a vector of complex numbers of length $M/2$ plus the average value. If the data values are real numbers, the imaginary part of the last element belonging to the frequency $f_s/2$ is always zero. This is due to the fact that, with only two samples per period, no two-phase correlation can be performed, see (2.14). Thus, the total number of meaningful values (including the mean value) is M, as can be expected from a mathematical transformation. Of course, this analysis is mathematically more demanding than the discrete Fourier transformation, but the special FFT algorithm is much less demanding than performing all discrete transformations separately. For $M = 2^i$ values per data vector the expense increases only proportional to $M * i$ and not to M^2, as for the discrete Fourier transformation. Hence, the larger the data files the more advantageous is the FFT method. If the measured signal contains only white noise, all Fourier components, which may be positive or negative, should appear with the same average magnitude. However, if it contains harmonic signal components, at the frequencies of these signals peaks appear which represent the magnitudes of the corresponding harmonic components. Just as for the discrete Fourier transformation result in (2.11), the two complex components can be combined to an amplitude, which is always positive, and a phase signal of the corresponding frequency. If the lock-in frequency does not exactly match one of the Fourier frequencies f_m, the amplitude values of both neighboring Fourier frequencies have to be evaluated. In this case, the procedure is equivalent to the asynchronous discrete Fourier transformation (asynchroneous correlation, see Sect. 2.4). Also the FFT procedure is very popular to extract harmonic signals from statistical noise. If it is used in a measurement setup, this procedure has the advantage to the discrete Fourier transform that it does not need any synchronization between the data sampling and the modulation of the signal. Hence, for a

series of measurements the harmonic analysis can be made by FFT after the measurement. The basic limitation of this procedure for lock-in thermography is that it cannot be evaluated on-line (parallel to the measurement, see Sect. 2.3) since all data must be present at once to be evaluated. Thus, in a lock-in thermography measurement all images would have to be stored, which is impractical for long lasting measurements. Another limitation is that the phase signal, which is very important in electronic device testing, is only meaningful if the excitation pulses are synchronized to the measurement events. This condition cancels the above-mentioned main advantage of no needed synchronization procedure. For these reasons, though FFT-based signal correlation is widely used in non-destructive testing, it is not further considered in this book concentrating on electronic device testing.

Another possibility which is not considered here is lock-in detection of higher harmonics. It will be demonstrated in Sect. 2.5 that, even if square-pulse excitation is applied, the basic information of lock-in thermography is lying in the basic harmonic. Higher harmonic detection with harmonic excitation is often used for detecting a non-linear response to an excitation action. In non-destructive testing, for example, second harmonic detection has been used for detecting plastic deformation by vibrothermography [7,33]. Second harmonic detection has been used also by Grauby and Forget [34] for distinguishing resistive from Peltier effects in microelectronic devices under harmonic load. However, we will show in Sect. 5.4 that these two components can also easily be distinguished with asymmetric square-pulse excitation and basic harmonic detection. Also Altes et al. [35] have used second harmonic detection under harmonic load in resistive probe-based scanning thermal microscopy for measuring temperature modulation, and third harmonic detection for the determination of thermal conductivity. Also here, if asymmetric square-pulsed excitation would have been used, basic harmonic detection would have been optimum for temperature modulation measurement, and IR-based lock-in thermography is anyway not feasible for performing thermal conductivity measurements. Therefore, higher harmonic detection will not be considered anymore in the following.

2.3 Lock-in Thermography

All considerations made up to now apply to any lock-in detection system. Lock-in thermography means that the heat in an extended sample is generated periodically and the lock-in correlation process described in the previous section is applied to the temperature signal of each pixel of an image of the surface of the sample under investigation. So lock-in thermography is a kind of active thermography since the sample is actively influenced during the observation [2]. Since the phase of the detected surface temperature modulation may depend on the lateral position, as a rule lock-in thermography uses the two-channel (in-phase and quadrature) lock-in correlation. Following to the previous considerations, the result of a lock-in thermography investigation may be displayed in different ways. The results of the in-phase correlation of all image positions yield the in-phase image (or 0° image), and that of the quadrature correlation yield the quadrature image (or −90° image).

Alternatively, these two images can be used to calculate the phase-independent amplitude image and the phase one if (2.11) is applied to all image positions. With these two images, the image of any phase component of the temperature modulation can be calculated, using (2.9) for all image positions, or systematic phase errors of the detection system can be corrected. Moreover, it is always useful to have a topography image in order to enable some orientation on the surface of the sample. In Chap. 5 (Measurement Strategies) we will discuss and demonstrate which of the different possible images is most appropriate to visualize different signal features.

In principle, performing lock-in thermography would require the parallel operation of one two-phase lock-in detection system for each pixel of an image. Of course, this can no longer be managed physically using analog electronics as shown in Fig. 2.3. This procedure, however, may be converted into a serial procedure. There are two essentially different approaches to perform lock-in thermography: 1. serially probing systems and 2. camera-based systems. In serially probing systems, a T-detector is successively scanned across the sample surface, and in each position a number of lock-in periods are measured and evaluated by a computer. In this procedure only one lock-in correlator is used, hence here either digital correlation or even classical analog correlation can be used. Figure 2.5 shows the general scheme of a serially measuring lock-in thermography system for investigating electronic components. The box called "signal conditioning" represents any kind of converting the temperature signal into a voltage including optional signal filtering. It is obvious that the time efficiency of serial systems is generally very poor, since always only one of many pixels can be probed at any time. For the classical digital lock-in correlation the maximum possible lock-in frequency is given by (2.14). Since the measurement time in each image position has to be at least one lock-in period (undersampling does not imply any advantage for serially probing systems), the minimum possible acquisition time for an image of $X \times Y$ pixel is $t_{acq}^{min} = XY/f_{lock\text{-}in}$. As the following chapters will show, from a technical point of view, in many cases the

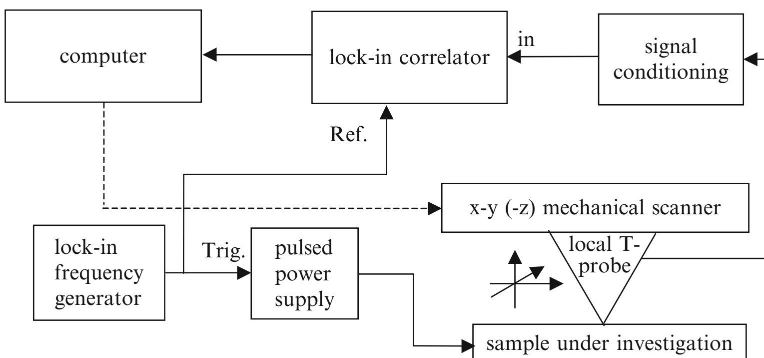

Fig. 2.5 Schematic of a serially probing lock-in thermography system for investigating electronic components. The temperature probing may be either contacting or non-contacting (see Sect. 3.1). Either the sample or the T-probe may be mechanically scanned. The frequency generator and the lock-in correlator may or may not be part of the computer system

highest possible lock-in frequency cannot be applied in practice because of sensitivity limitations, hence a lower lock-in frequency has to be used. For the same reason, it is mostly necessary to average over a number of lock-in periods. Thus, since at least 100×100 pixels are needed to form a meaningful image, serially measuring lock-in thermography systems often require measurement times of several hours to tens of hours (see Chap. 3). The major advantage of serially probing systems is that they are simpler to realize and therefore cheaper than camera-based systems. Moreover, in some cases (e.g. AFM probing) they provide a better spatial resolution than camera-based system do.

In camera-based systems, a camera is running with a certain frame rate f_{fr}, converting the whole 2-dimensional surface temperature distribution into an image containing the temperature information. This frame rate corresponds to the sampling rate f_{s} discussed in the previous section, except that the result of each camera measurement is a 2-dimensional array of T-data for the whole image at once. Thus, the lock-in correlation according to (2.4) has to be performed with all image data, which can be managed only digitally using a frame grabber and sufficiently high computation power.

As any lock-in measurement, lock-in thermography may be performed either with single phase correlation or with two-phase correlation. Single phase correlation means that the procedure (2.3) is performed only once with the phase of the correlation function selected to match the phase of the detected signal. As it is shown in Chap. 4, this is not optimum for lock-in thermography since, depending on the shape of the heat source and on the distance from the heat source, the phase position of the surface temperature modulation varies. If one is only interested to see point-like heat sources, it may be advantageous to display only the in-phase (0°) image, since this provides the best possible spatial resolution (see Sects. 4.3 and 5.1). However, performing only single phase correlation does not allow one to display the phase image or the 0°/−90° image (see Sects. 4.5.2 and 5.1), which are both inherently emissivity-corrected.

It should be mentioned that, if single phase correlation (e.g. 0°) is used, the image shows a 1.4 times better signal-to-noise ratio than the amplitude signal of a two-phase correlation system, since the latter signal contains noise components of both channels. However, also a two-phase system allows to display each single phase component separately, which is equivalent to single phase correlation. Therefore, there is no inherent advantage of single phase systems. In the following we will only consider only two-phase correlation as it was described in Sect. 2.2.

As Fig. 2.6 shows, the 2-channel image correlation procedure consists of multiplying all incoming image information by the two sets of weighting factors K_{j} and adding the results to two frame storages, which had been zeroed before the measurement. Then after the measurement one image storage contains the in-phase (0°), and the other one the quadrature (−90°) image. Of course, also here the data are transferred and treated serially one after the other at a certain pixel rate of the frame grabber of the computer. The basic difference between serially probing lock-in thermography systems and those camera-based is that in serially probing systems the sample is scanned slowly only once during one measurement. In each position,

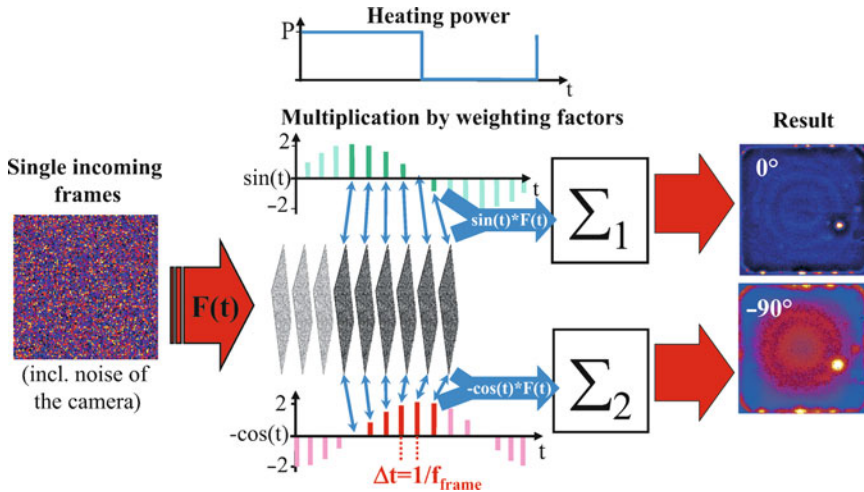

Fig. 2.6 Principle of the sin/−cos lock-in correlation procedure for camera-based systems, here shown for $n = 16$ frames per lock-in period. The images shown result from a real solar cell investigation

many T-measurements for one or several lock-in periods are performed. In camera-based systems, on the other hand, the image scan is performed "quickly" by the camera many times during one measurement, and each data point of each image belongs to one temperature value for a certain position at a certain time. Without using undersampling (see Sect. 2.4), the maximum possible lock-in frequency of camera-based systems is $f_{fr}/4$ (see (2.14)). For lower lock-in frequencies, a larger number of frames has to be used in one lock-in period. Hence, in principle, a complete camera-based two-phase lock-in measurement could be performed using only 4 frames within one lock-in period requiring some 10 milliseconds, which is orders of magnitude faster than any serial system can do. Indeed, it had been shown that, if the detected signal is strong enough, a lock-in thermography image can be obtained within 10 ms [36]. As a rule, however, camera-based systems have to average over many lock-in periods just in order to improve their detection sensitivity. While serial systems may be both contacting and non-contacting, camera-based systems are, of course, always non-contacting. The noise properties of different serial and camera-based lock-in thermography systems will be compared in Sect. 3.1.

Here, a special remark should follow regarding the triggering mode of the sample under investigation. As mentioned above the simplest way of generating an amplitude modulated (a.c.) heat signal in electronic components is to pulse the supply voltage of the component. This measure reveals all heat sources present in this component. However, more complicated components like integrated circuits (ICs) may have a lot of other control inputs, which cause some complex electronic actions within these components. If these control inputs are used for sophisticated triggering, special modes of device testing of ICs become possible. In the simplest case, the supply voltage is permanently applied and the reference trigger is applied to a

certain control input of an IC. Then some current paths (e.g. gates) may become active if the trigger is in "high" position, and passive, if it is in "low" position. Some other gates may behave inversely. If the image in an appropriately selected phase position is displayed, the first class of gates will appear bright (positive contrast), and the second class will appear dark (negative contrast) with respect to the surrounding. Thus, the phase of the signal indicates whether a heat source is switched on or off by the trigger. The signal value of all regions not affected by this trigger will be zero, irrespectively whether continuous heat is generated there, or not. In this way, the action of different control signals on the operation of the circuit can be independently checked. One example of Sect. 6.1 demonstrates an application of this type of sophisticated triggering. Even complex control signals can be applied to one or several inputs, if the circuit under test is connected with an intelligent circuit tester. Whenever these controls are leading to internal circuit actions, which are phase-related to the detecting lock-in reference, these actions and only these can be visualized by lock-in thermography. This sophisticated triggering mode and phase detection greatly enhance the analytical possibilities of lock-in thermography in device testing of electronic components compared to the general imaging of all possible heat sources via simply pulsing the supply voltage.

2.4 Timing Strategies

Beginning with (2.4), only conventional synchronous lock-in correlation had been considered in Sect. 2.2. Hence it had been assumed that the lock-in trigger is derived from the frame trigger of the camera by using a frequency divider. Then each lock-in period contains a number of measurement events (frames, samples) of $n \geq 4$. This condition defines an upper limit of possible lock-in frequencies as $f_{\text{lock-in}} \leq f_{\text{frame}}/4$. It has been suspected that n must be an even number, but it is also allowed to be odd. If the frame rate of the camera is fixed, at least close to the limit $f_{\text{lock-in}} = f_{\text{frame}}/4$ the lock-in frequency can only be varied in certain steps ($f_{\text{frame}}/4$, $f_{\text{frame}}/5$, $f_{\text{frame}}/6$, etc.). Working exactly at a well-defined lock-in frequency is seldom necessary, but the condition $f_{\text{lock-in}} \leq f_{\text{frame}}/4$ often represents a serious experimental limitation. It will be shown in Chap. 4 that the spatial resolution of lock-in thermography improves with increasing lock-in frequency. Today special high-speed IR cameras are available, and for a given camera the frame rate can be further increased by working in sub-frame mode, hence by reducing the used image field. Nevertheless, especially for microscopic investigations, lock-in frequencies in the order of or even higher than the frame rate of the camera are often desirable. It will be shown below that this can be realized by using the so-called undersampling technique. For certain investigations, e.g. for thermomechanical stress investigations, where a sample is deformed by a free-running machine, it is generally not easy to synchronize the lock-in frequency to the lock-in correlation. Another possible case where it is hard to synchronize the lock-in periods to a free-running camera is sophisticated triggering in circuit tester-based IC failure analysis, which had been mentioned at the

end of Sect. 2.3. Here the circuit tester may easily deliver a trigger signal, which is synchronous to the heat dissipation due to certain local circuit activities, but it may be harder to trigger the tester externally from the lock-in thermography system. In this case FFT-based correlation may be used as described at the end of Sect. 2.2. However, as also described there, this kind of correlation has the disadvantage that it cannot be performed on-line. Hence, it is only useful for evaluating a limited number of lock-in periods. In the following, different strategies for organizing the lock-in timing in relation to the timing of the IR camera will be described, leading to different solutions for the lock-in correlation procedure also.

Again, the following considerations hold for any kind of digital on-line lock-in correlation. Let us first consider the simplest case of conventional synchronous lock-in correlation, where the lock-in trigger is derived from the trigger of the free-running digitizing events (camera frames in the case of lock-in thermography) by a frequency divider. Figure 2.7a shows this correlation for the typical case that the sampling rate f_s is considerably larger than the lock-in frequency $f_{\text{lock-in}}$. Here a sine-shaped signal with an amplitude of 2 is assumed to be digitized at certain equidistant measurement (sampling) events. In (a) the signal period is exactly 12 measurement periods long. The dark squares are symbolizing the measurement events, and the vertical dashed line marks the beginning of the second lock-in period. An alternative interpretation of this and the following figure is that the y-values of the dark squares represent the values of the weighting factors $K^{0°}$ of the correlation for the 0° (in-phase) correlation. Note that, according to (2.7) in Sect. 2.2, these factors are the doubled values of the sine function in the sampling moments. The values of $K^{-90°}$ belonging to the corresponding cosine function are not shown here. We always assume that the first measurement starts at $t = 0$, where the signal is at phase position $\Phi = 0°$. We see that in (a) after 12 samples there is the next (13th) sample again exactly at phase position $\Phi = 0°$ of the next period. Here, due to the synchronization of the lock-in trigger to the measurement events, the values of the weighting factors K_k are the same in each lock-in period, as it had been assumed for (2.4). This "synchronous correlation" is definitely the simplest way to perform lock-in thermography. Another advantage is that, if only a complete number of periods is evaluated, the sum of all weighting factors is always exactly zero. This ensures a perfect suppression of the d.c. part of the signal, which is called "topography image" in lock-in thermography.

Alternatively, the measurement events and the lock-in periods may also be not synchronized, which will be called in the following "asynchronous correlation". Note that our denomination "synchronous correlation" should not be confused with the terms "synchronous detection" or "synchronous demodulation", which are often generally used for any kind of lock-in detection and also imply asynchronous correlation. In Fig. 2.7b one lock-in period is somewhat larger than 12 measurement periods, hence there is no measurement event at the starting point of the following sine period. If $K(t)$ is the continuous correlation function in (2.2), which is phase-coupled to the signal to be measured, in (b) the discrete values of the weighting factors K_k in (2.3) have to belong to individual phase positions in each period. Therefore in this asynchronous correlation procedure (b), the weighting factors K_k

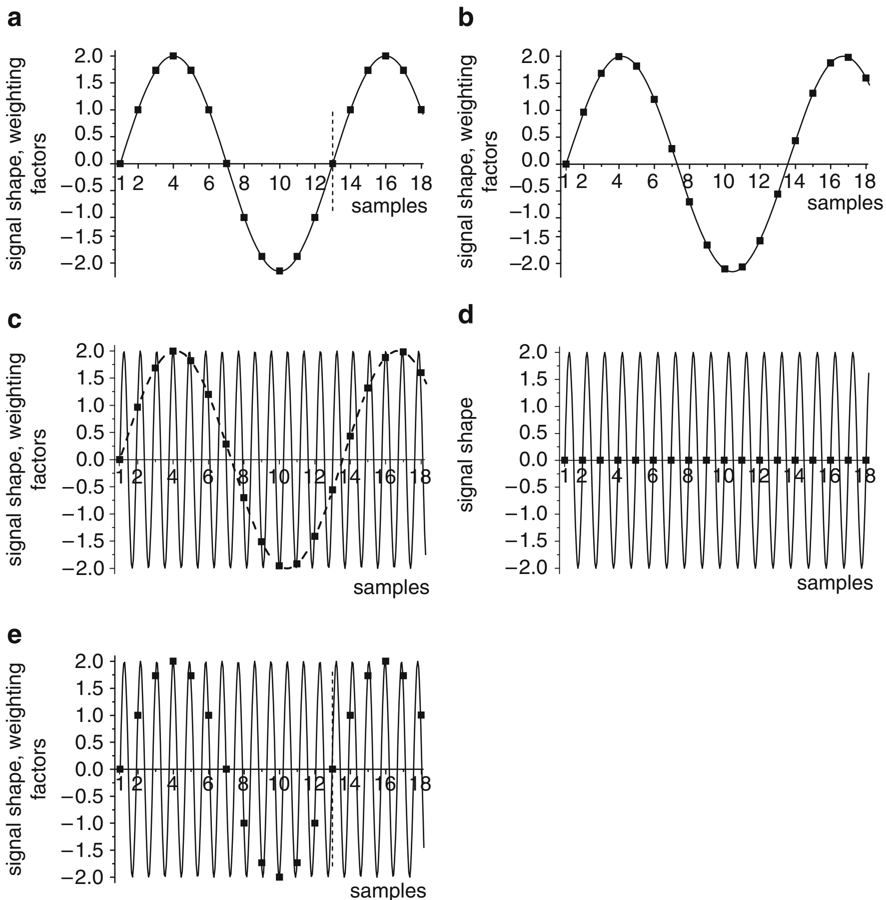

Fig. 2.7 (**a**) Timing diagrams of conventional synchronous correlation, (**b**) conventional asynchronous correlation, (**c**) asynchronous undersampling, (**d**) undersampling at a "forbidden frequency", (**e**) synchronous undersampling

have to change from period to period. This is practically realized by feeding a digital or an analog signal, which is synchronous to the signal generation process, to the computer which organizes the digitizing (sampling, imaging) events. The computer recognizes the frequency of this signal and also its phase, hence it recognizes and may predict the moments when each signal period starts. From these data and the knowledge of the moments of the internal digitizing events, the computer may calculate on-line in which phase position every sampling event is lying. Then the values K_k of the correlation function in (2.3) can either be taken from a look-up table or be calculated on-line for each period separately. In fact, this operation is analog to the operation of a conventional lock-in amplifier (see Fig. 2.3 in Sect. 2.2), where a reference signal of the measurement process is also fed to the lock-in amplifier. It is even possible to digitize an analog waveform, which follows

the expected signal shape, and use these data as the weighting factors for the correlation in (2.3). This also enables non-harmonic or even non-periodic signals to be correlated on-line. One problem of digital asynchronous correlation is that, as a rule, the sum of all weighting factors is not exactly zero. This diminishes the degree of d.c. suppression of the procedure, which is disturbing especially for low acquisition times implying only a limited number of lock-in periods. Therefore, in systems using asynchronous correlation, the d.c. part is usually subtracted from the image data before correlation [29].

The beauty of asynchronous correlation is that, with some restrictions (see below), the lock-in frequency may be arbitrary in relation to the sampling frequency f_s and may be even larger than f_s. For explaining the following terminology, let us make a short excursion to sampling theory. According to the Nyquist-Shannon sampling theorem, at least two samples per period are necessary for detecting a certain frequency. For example, a CD containing frequencies up to 22 kHz uses a sampling rate of 44 kHz. The maximum possible detected frequency being half the sampling frequency is called "Nyquist frequency". Since in lock-in thermography we have to detect two phase components of a signal shape independently, we need at least four samples per lock-in period, as it had been mentioned already several times. It had been demonstrated in Sect. 2.2 in the discussion of (2.14) that 4-point correlation actually consists of two independent 2-point correlations, each using half of the total sampling rate, since here always two of the four weighting factors are zero. Using more than two samples for sampling (or more that 4 for two-phase correlation; e.g. 12 in Fig. 2.7a) is called "oversampling". This measure is also often used in audio technique for improving the signal quality and accuracy. Also in lock-in thermography oversampling improves the accuracy of the harmonic correlation procedure, see Sect. 2.5. If less than two samples per lock-in period are taken (four samples for two-phase correlation), hence if the signal frequency is above the Nyquist frequency, different waveforms may become indistinguishable or "aliases" of each other, as the dashed curve in Fig. 2.7c shows. This curve represents the so-called sub-Nyquist frequency of a waveform having a frequency above the Nyquist frequency. Hence, in this case the frequency analysis of the digitizing procedure is not unique, and in the reconstruction of the signal certain "aliasing frequencies" appear, which have not been present in the original signal. For avoiding these distortions, frequencies higher than the Nyquist frequency have to be filtered out before digitizing by applying so-called anti-aliasing filters. However, if we already know the frequency of interest, we are allowed to sample also a signal with a frequency higher than the Nyquist frequency! Following Krapez [29] this procedure is called "undersampling". In Fig. 2.7c the signal frequency is slightly above the sampling frequency. As this figure shows, the magnitude of a signal with a frequency higher than the sampling frequency may be detected reliably. Here the measurement events occur also successively in 12 different phase positions of the signal period, but the measurements occur in subsequent periods of the signal. The correlation procedure is exactly the same as for asynchronous oversampling with about 12 samples per period, see Fig. 2.7b. However, some restrictions for choosing the signal (lock-in) frequency have to be considered. First, any multiples of the

Nyquist frequency are "forbidden frequencies" for undersampling. As an example, Fig. 2.7d shows sampling of a waveform at $f_{\text{lock-in}} = f_s = 2f_{\text{Nyq}}$. We see that this is a typical interference, hence the samples contain no information as to the amplitude of the periodic signal. For two-phase correlation this first interference occurs already at $f_{\text{lock-in}} = f_s/2 = f_{\text{Nyq}}/4$, since the sampling of each phase component occurs at $f_s/2$ (see Sect. 2.2). Another restriction may hold if the signal contains higher harmonics. Also these harmonics may generate spurious signals if they generate a common sub-Nyquist frequency as the basic harmonic. Frequencies where this may happen are called "aliasing collision frequencies" [37, 38]. In principle, also these frequencies should be avoided for undersampling. Note, however, that for square-pulse heat introduction the basic harmonic has the highest intensity anyway, and higher harmonics of the temperature modulation are naturally strongly damped (see Sect. 2.5). In fact, as long as only the location of local heat sources has to be imaged by lock-in thermography, it does not matter whether the basic harmonic or any higher harmonic is detected. So for electronic device testing aliasing collisions should not be harmful. For strictly harmonic heat introduction there are no aliasing collision frequencies at all, of course. Also therefore harmonic heat introduction is usually preferred in non-destructive testing (NDT), where undersampling is often used. Finally, it has to be mentioned that for undersampling a sufficiently low frame integration time of the IR camera has to be chosen. Note that for modern high-speed IR cameras the frame integration time may be close to the frame period, hence the camera is detecting photons for nearly the whole time between two images. This operation mode may be optimum for achieving a high signal-to-noise ratio, but in the case of undersampling the measured temperature modulation averages out during image integration over more than half a signal period. Therefore a frame integration time below half the period of the signal to be detected has to be chosen for reliably detecting the T signal in the case of undersampling.

Undersampling can also be performed synchronously as Fig. 2.7e shows. Synchronous undersampling has the advantage that, if only a complete number of correlation periods is evaluated, the sum over all weighting factors is exactly zero and the d.c. suppression of the correlation procedure is optimum. In addition, it can be realized relatively easy since the weighting factors are pre-defined and do not have to be calculated on-line. In Fig. 2.7e exactly after 12 sampling periods (at the 13th sample, which already belongs to the next period) the signal is at a phase position of 0° again, see the vertical dashed line. Also here the correlation occurs according to (2.4) and (2.10) with $n = 12$, hence the weighting factors are the same in all correlation periods. The condition that this happens is $f_{\text{lock-in}} = f_s(1 + 1/12)$, which can be realized phase-synchronously only by deriving both the lock-in frequency and the camera trigger from one and the same clock signal by using different frequency dividers. Hence, here the camera is not freely running at its own repetition frequency but is externally triggered by the computer, which also generates the lock-in trigger and thus organizes the synchronous undersampling procedure. If the camera cannot be triggered externally, the realization of synchronous undersampling is more complicated but can also be realized by using a special hardware using PLL (phase-locked loop) techniques [39].

External triggering of the camera opens a number of further timing options. Generally, synchronous undersampling with n samples per correlation period is realized by choosing:

$$f_{\text{lock-in}} = f_s \left(m + \frac{1}{n} \right). \tag{2.15}$$

Here m is an integer, which is sometimes called the order of undersampling [38], and n is the number of frames per correlation period, which has to be $n \geq 4$ for performing two-phase correlation. Undersampling of zeroth order ($m = 0$) is the conventional synchronous correlation procedure with $f_{\text{lock-in}} = f_s/n$. For undersampling of first order, subsequent samples are taken in subsequent periods of the signal, whereas for second order, samples are taken in every third period, and so on. Figure 2.8 shows the timing diagrams of synchronous undersampling of first and second order ($m = 1$ and 2) for $n = 4$ (4-point correlation). Again, the vertical lines mark the beginning of the next correlation period at the fifth sampling event. Synchronous timing with $f_{\text{lock-in}} = f_s(1-1/n)$ is also possible, but then the phase of the signal appears inverted if the evaluation according to Sect. 2.2 is applied (see below).

If the camera is triggered externally, small gaps in the desired frequency (e.g. between $f_s/4$ and $f_s/6$ for $m = 0$) can be closed by reducing the sampling rate, hence the frame rate of the camera, below the maximum possible one. It will be shown in Sect. 2.6 that the signal-to-noise ratio (SNR) increases with the square

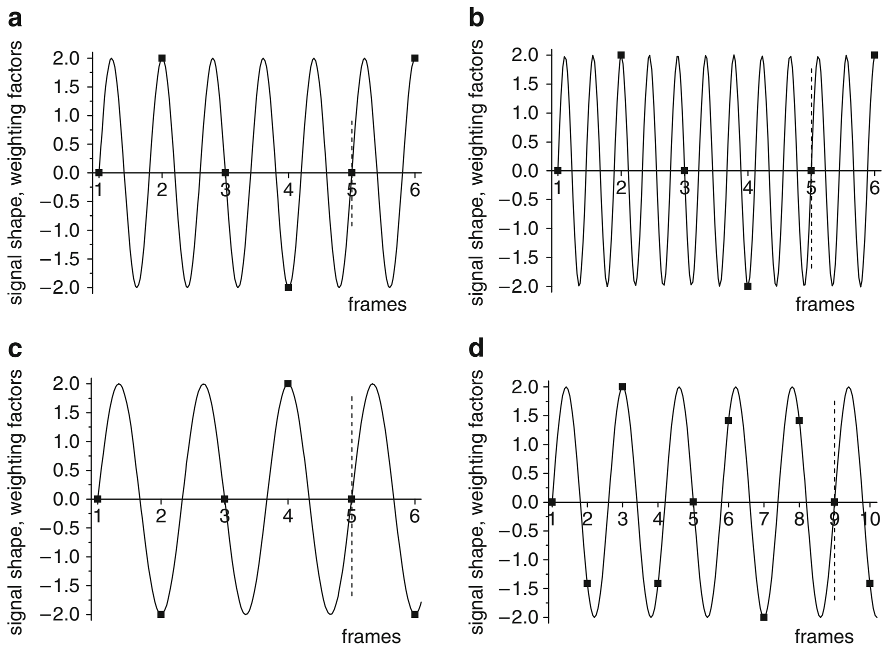

Fig. 2.8 Timing diagrams of 4-point undersampling (**a**) of first order, (**b**) of second order, and of synchronous multi-period correlation with (**c**) $u/n = 3/4$ and (**d**) $u/n = 5/8$

root of the frame rate. Hence, reducing the frame rate by 33% leads only to 18% degradation of the SNR, which usually can be tolerated. However, according to (2.15) there is a larger frequency gap by a factor of four between $f_s/4$ (the highest possible frequency for $m = 0$) and f_s (the lowest possible frequency for $m = 1$). Hence, if e.g. a frequency slightly above 1/4 of the maximum frame rate of the camera should be applied, according to (2.15) only undersampling of first order can be applied with the frame rate of the camera reduced by a factor of 4. This would degrade the SNR already by a factor of 2, which is not negligible anymore.

Fortunately, for filling this frequency gap a special variant of synchronous correlation can be applied, which may be called "synchronous multi-period undersampling". In conventional correlation four or more (generally n) samples are distributed over one signal period. For undersampling according to (2.15), one sample occurs in every one or more (generally m) signal periods. For synchronous multi-period undersampling, four or more (generally n) samples are distributed over two or more (here u) sample periods. Any lock-in frequency exactly fulfilling the condition $f_{\text{lock-in}} = (u/n) f_{\text{frame}}$ with u and n being integers with $n \geq 4$ and $u \geq 2$ can be used to fill the frequency gap between $f_{\text{frame}}/4$ and f_{frame}. The case $u = 1$ is the case of conventional correlation. Figure 2.8c shows the application of this technique for $u = 3$ and $n = 4$ ($f_{\text{lock-in}} = 0.75 f_s$). In this synchronous multi-period correlation procedure, after u periods of the lock-in frequency have passed, exactly n samplings have passed, and the phase relation between both is the same as at the beginning (next sampling at $\Phi = 0°$, see vertical dashed lines). The integers u and n should not be divisible by each other, otherwise the multi-period decays into several equivalent multi-periods, where $n < 4$ may appear. As for synchronous undersampling according to (2.15), also synchronous multi-period correlation has the advantage that the d.c. suppression is optimum if a complete number of correlation periods is evaluated, and that the weighting factors are pre-defined. Assuming again that at $t = 0$, where the first sampling occurs, the signal is at phase position $\Phi = 0$, the sampling moments for multi-period undersampling are in the following phase positions of the signal:

$$\Phi_j = 2\pi(j-1)\frac{u}{n}. \tag{2.16}$$

As in (2.4), j is the index of the samples in each period. Correspondingly, the following weighting factors have to be used in (2.4) for synchronous multi-period correlation instead of (2.10):

$$K_j^{0°} = 2\sin\left(\frac{2\pi u(j-1)}{n}\right) \qquad K_j^{-90°} = -2\cos\left(\frac{2\pi u(j-1)}{n}\right). \tag{2.17}$$

In fact, the case of $f_{\text{lock-in}} = 0.75 f_s$ ($u = 3, n = 4$), which is shown in Fig. 2.8c, corresponds to the above-mentioned case of $f_{\text{lock-in}} = f_s(1 - 1/4)$, which is equivalent to conventional 4-point correlation with inverted phase. Here the weighting factors according to (2.17) are $K^{0°} = (0, -2, 0, 2)$ and $K^{-90°} = (2, 0, -2, 0)$, which are the inverse of the double sin- and the cos-function. Figure 2.8d shows

another case with $u = 5$ and $n = 8$ ($f_{\text{lock-in}} = 0.625 f_s$). Here the values of the weighting factors for the 0° correlation do not follow anymore a simple sine function. For sufficiently filling the frequency gap between $1.1 f_s$ (undersampling with $m = 1$ and $n = 10$) and $0.25\ f_s$ (the highest conventional lock-in frequency), synchronous multi-period undersampling with $u/n = 9/10$ (0.9), 3/4 (0.75), 5/8 (0.625), 4/10 (0.4), 3/8 (0.375), and 3/10 (0.3) can be used. Also the frequency gap between $f_{\text{lock-in}} = 1.25 f_s$ ($m = 1, n = 4$) and $f_{\text{lock-in}} = 2.25 f_s$ ($m = 2, n = 4$) can be filled by choosing $f_{\text{lock-in}} = 1{,}75 f_s$, where the same weighting factors as for $f_{\text{lock-in}} = 0.75 f_s$ are used, see above. For even higher frequencies, undersampling with $n = 4$ is generally most appropriate. By using these possibilities, together with conventional correlation and appropriate reduction of the externally controlled frame rate of the camera, any necessary lock-in frequency should be able to be realized by preserving the advantages of synchronous correlation (pre-defined weighting factors and optimum d.c. rejection) without compromising the signal-to-noise ratio. Remember that in any case of undersampling the frame integration time has to be smaller than half the signal period for avoiding signal averaging effects. This reduces the sensitivity for oversampling of high order and, together with the accuracy of the timing, finally limits the usefully attainable upper limit of the lock-in frequency.

2.5 Influence of Non-harmonic Heating

In the field of non-destructive testing (NDT) nearly all lock-in thermography publications have been based on the assumption that the introduction of heat into the investigated object has to be harmonic. Indeed, the whole theory of thermal waves, which the equations in Sect. 2.2 refer to, is based on the assumption of a harmonic introduction of heat. Therefore, enormous efforts have been made to ensure a most possible harmonic introduction of heat for lock-in thermography used in non-destructive testing. However, as mentioned in Chap. 1, in electronic device testing, as a rule, it is not useful to aspire a harmonic introduction of heat, because of the highly non-linear dependence of the properties of these devices on the supply voltage. Instead, a well-defined bias has to be switched on and off, leading to a square wave shape of the heat introduction. Here the question arises: Does this deviation from the harmonic introduction of heat possibly lead to erroneous results, if the evaluation formulas are based on the assumption of an harmonic heat-introduction? It had been mentioned in Sect. 2.4 that, in the case of oversampling, higher harmonics may lead to aliasing collisions [38], which are not really harmful at least for qualitative electronic device testing. The question remains, how large these errors are for conventional lock-in correlation, if really quantitative results should be obtained.

In this section we will analyze the influence of a non-harmonic (square wave) introduction of heat on the lock-in thermography results for different lock-in correlation conditions. First of all, it has to be emphasized that heat dissipation is an essentially linear process, as long as the thermal parameters of the material can be assumed to be temperature-independent. Hence, since the heat diffusion equation

is of first order (see Chap. 4), its solutions for different boundary conditions (heat sources) superimpose linearly. This also holds for the different spectral components of a square wave heat introduction, which for a basic frequency of $f = \omega/2\pi$ and a power of P_0 during the pulse can be described by a d.c. part and the sum of its Fourier components [32]:

$$P(t) = \frac{P_0}{2} + P_0\left(\frac{2}{\pi}\sin\omega t + \frac{2}{3\pi}\sin 3\omega t + \frac{2}{5\pi}\sin 5\omega t + \dots\right) \tag{2.18}$$

The influence of the time-independent member $P_0/2$ will be treated in Sect. 4.1 and 4.2, discussing the initial heating phase of a lock-in thermography measurement. It will not be considered here. All harmonic members in (2.18) can be treated independently by the thermal wave formalism (see Chap. 4). Hence, for any heat source geometry the temperature field of the square wave heat-introduction is the superposition of different harmonic temperature fields for this geometry, belonging to the different harmonic frequencies f, $3f$, $5f$, etc. Since the square wave signal is symmetric in time, only odd harmonics have to be regarded.

It will emerge that possible errors introduced by a non-harmonic introduction of heat strongly depend on the parameters of the lock-in correlation. In any case, we will consider only standard sin/−cos lock-in correlations based on (2.4) and (2.10) in Sect. 2.2. If the lock-in frequency is small compared to the frame rate of the camera, the weighting factors (2.10) precisely approximate harmonic functions. Then the sum (2.4) is equivalent to the integral representation of the lock-in process. In this case, the sin/−cos correlation really works in the frequency-selective mode with respect to the basic harmonic, hence all higher harmonics are effectively suppressed, since they are leading to members of the kind

$$\int_0^{2\pi} \sin\omega t\,\sin(n\omega t+\varphi)\mathrm{d}t = \int_0^{2\pi} \cos\omega t\,\sin(n\omega t+\varphi)\mathrm{d}t = 0 (n = 3, 5, 7, \dots) \tag{2.19}$$

which holds for any value of the phase shift φ of the T-response. Hence, as long as the number of frames per lock-in period is large and sin/− cos correlation is used, it is absolutely not necessary to manage a harmonic heat-introduction. This statement also holds for any kind of non-destructive testing.

The situation changes if the lock-in frequency reaches the order of the frame rate of the camera, or if the 4-bucket correlation is used. The possible errors caused by a non-harmonic heat-introduction also depend on the geometry of the heat source. The least critical case is a spatially extended heat source, leading to an essentially homogeneous heating of the whole sample. It will be shown in Sect. 2.7 (Calibration) that in this case, the thermal response drops with $1/f$. According to (2.18), the first higher harmonic of a square wave signal is the 3rd one, which itself has only $1/3$ of the intensity of the basic harmonic. Since even for the same power, its thermal response would be only $1/3$ of that of the basic harmonic, in sum the 3rd harmonic of a square wave signal then has a T-response of only 1/9 of the basic one.

Higher harmonics are quenched even more strongly. In fact, as it will be discussed in Sect. 2.7, the T-response then will be of triangular shape, which is close to the sinusoidal one.

The most critical case is, for instance, a point-like heat source at the surface of a 3-dimensional sample, because according to Chap. 4 its T-response in source position is independent of the frequency. Therefore, here the T-modulation in source position is really rectangular. The errors will turn out to additionally depend on the frame integration time of the camera (see Sect. 2.1) and on the phase of the frame integration, referring to the phase of the heating pulse. Hence, it is decisive whether the "electronic shutter" of the camera is open only for a small fraction of each frame period or during the whole frame period, and when the shutter opens, referring to the edge of the heating pulse. The origin of this error is sketched in Fig. 2.9, showing a rectangular T-modulation trace and the frame integration periods for a low frame integration time for a 4-point correlation, depicted for two different phase positions of the frame integration with respect to the pulse edge. It is obvious that the measured data are exactly the same in both cases, in spite of the different phase positions. Hence, the readings in the 0°- and in the quadrature channel are exactly the same. They are no longer linearly independent. This means that, in principle, they do not allow one to calculate amplitude and phase values independently. If the correlation factors are chosen according to (2.10), in both cases, the detected phase will be −45°. This is clearly wrong, since in the left image it is close to 0°, and in the right one it is close to −90°. Hence, in this special case the phase reading is independent on the real phase. For a longer frame integration time, if the integration periods will overlap with the pulse edges, the results will start to react on the real phase position, hence the results will become more realistic.

Now imagine that in the left part of Fig. 2.9 all the frame integration periods are starting even earlier, whereby periods 1 and 3 are crossing the rising and falling edges of the rectangular temperature track. Then the measured values will very sensitively depend on the exact starting position of the integration period with respect to the edges of the signal. In other words: If the edges of the signal are lying within a short integration period t_{int} of the camera, the sensitivity of the phase reading is

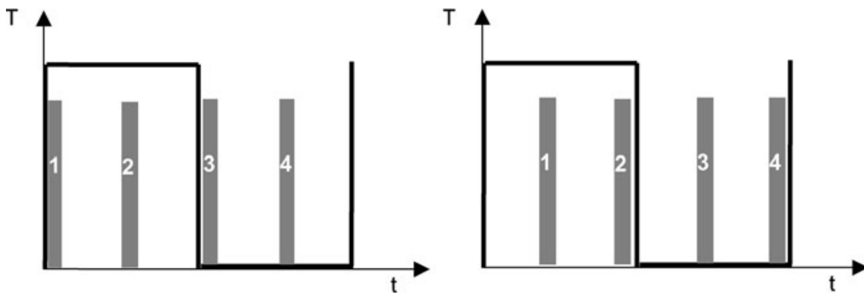

Fig. 2.9 Rectangular temperature trace, as it is measured e.g. in the position of a surface point heat source with a rectangular heat introduction, measured using the 4-point correlation at two different phases between frame integration and heating

increased by an order of $T/4t_{\text{int}}$, with $T = 1/f_{\text{lock-in}}$ being the lock-in period. This effect has been intentionally used by Ramspeck et al. [40] for performing dynamic carrier lifetime imaging of silicon wafers using an infrared-camera-based approach. This technique will be described in more detail in Sect. 3.5.3.

With increasing distance from the source position, the different spectral components are more strongly damped, the higher their frequency is (see Sect. 4.3), leading to a smoothing of the shape of the trace. This is demonstrated in Fig. 2.10, showing the simulation of the a.c. component of one period of the T-modulation at different distances from the considered point heat source. These data have been calculated up to the 99th harmonic. For a better comparison, all traces are independently scaled to the same amplitude of their basic harmonic. The distances r refer to the thermal diffusion length Λ, which in silicon is about 1 mm for a lock-in frequency of 30 Hz (see Sect. 4.1). The smoothing effect and also the expected phase delay with increasing distance are clearly shown. At a distance twice the thermal diffusion length the signal shape is already nearly sinusoidal.

In order to quantify possible errors in the amplitude and phase reading caused by a square-shaped heat introduction, the data of the temperature traces in Fig. 2.10 have been used to simulate different kinds of lock-in correlation. Amplitude and phase values for 4 and 8 frames per lock-in period have been calculated. In all cases, simulations followed for a short frame integration time of $<10\%$ of the frame period, similar to that shown in Fig. 2.9, and for a long frame integration time, filling 100% of the frame period. Note that the 4-point correlation with 100% frame integration time is equivalent to the 4-bucket correlation [29]. Figure 2.11 shows all data referred to the "exact" result, which holds for both a sinusoidal heat introduction and for a square-wave heat introduction and a large number of frames per lock-in period,

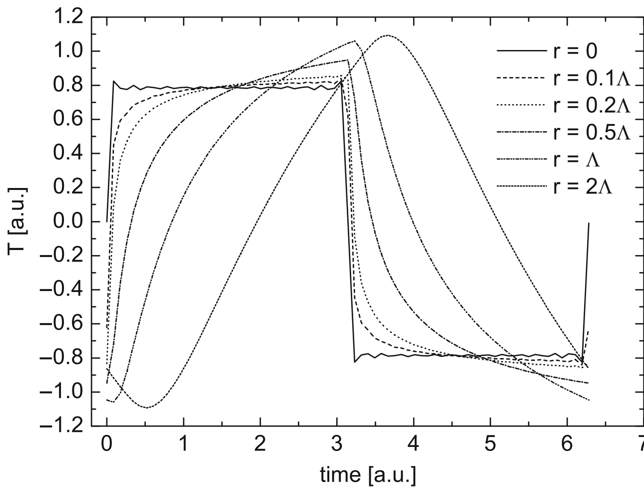

Fig. 2.10 Temperature traces in different distances r from a point source (referred to the thermal diffusion length Λ). All traces are separately scaled to the same amplitude of their basic harmonic

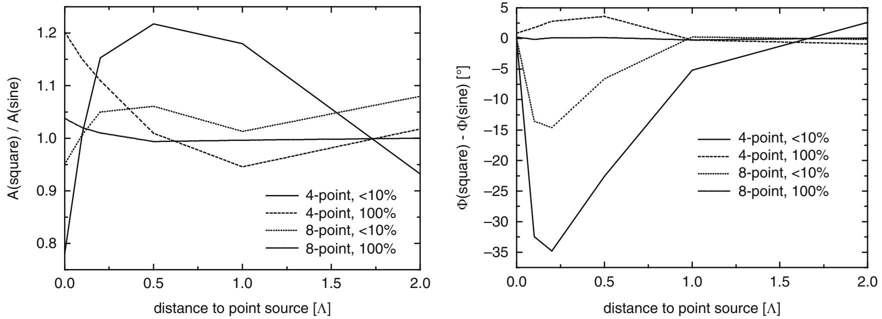

Fig. 2.11 Amplitude error (left) and phase error (right) of square-wave heat introduction referring to sinusoidal one, calculated for 4-point- and 8-point correlations with different percentages of the frame integration time relative to the frame period. The distance from the point source is given in units of the thermal diffusion length Λ

since in both cases the results were exactly the same. As expected, the 4-point correlation with $<10\%$ frame integration time produces the strongest errors ($\pm 20\%$ in amplitude, $-35 \ldots + 5°$ in phase), followed by the 4-point correlation with 100% frame integration time ($+20 \ldots - 7\%$ in amplitude, $-15 \ldots + 4°$ in phase), and the 8-point correlation with $<10\%$ frame integration time ($-5 \ldots + 6\%$ in amplitude, $-1 \ldots + 3.5°$ in phase). The results were best with the 8-point correlation with 100% frame integration time ($-1 \ldots + 3\%$ in amplitude, $\pm 1°$ in phase). With a larger number of frames per period, all these errors are approaching zero.

Note that the amplitude errors found here are always related to the amplitude values measured under the same conditions with a sinusoidal heat introduction. It will be shown in Sect. 4.3 that within the considered distance range the amplitude may vary by two orders of magnitude, depending on the spatial resolution of the system. Hence, the qualitative appearance of amplitude images hardly depends on the fact whether the heat introduction is sinusoidal or square-shaped. Only if results have to be evaluated quantitatively (see Sects. 4.5 and 5.3), or if phase positions have to be determined precisely, or if a signal of a well-defined phase has to be extracted from the measured data, for applying the square-wave heat introduction it is advisable to use >10 frames per lock-in period in order to keep the errors sufficiently small. The following conclusions may be drawn from these simulations:

1. If instead of a sinusoidal heating power a square-wave one is generated in the sample, this may cause quantitative errors in both the amplitude and phase reading.
2. For conventional synchroneous correlation (no undersampling) these errors are largest for the 4-point correlation and quickly reduce with increasing number of frames per lock-in period. Above 10 frames/period they become negligible.
3. Therefore, for low lock-in frequencies, the sin/− cos correlation is clearly superior to the 4-bucket correlation procedure, if square-wave heating is used.
4. The errors are largest in the vicinity of local heat sources, where the T-modulation still has the largest amount of higher harmonics.

5. The errors become lower, if the frame integration time covers the largest possible amount of the frame period. This measure is also advantageous for obtaining a good signal-to-noise ratio (see next section).
6. As long as the results are evaluated only qualitatively, the application of square pulses is equivalent to the sinusoidal heat introduction. Only if the results are to be evaluated quantitatively and a high accuracy is expected, or if a well-defined phase signal has to be displayed, it is advisable to work with $\geq$10 frames per lock-in period.
7. If undersampling is used, higher harmonics may be more disturbing, since they may lead to so-called aliasing collisions. These, however, are also only disturbing for quantitative evaluations.

2.6 Noise Analysis

The noise level of an IR-camera based temperature mapping system as well as of any other one is usually expressed by a "noise equivalent temperature difference" (NETD). The definition of NETD is given by the mean square of the deviation of different values measured of one pixel F_i (measured in digits) from its mean value $\bar{F}$ obtained in k successive measurements ($k \gg 1$):

$$\text{NETD} = \frac{c}{k}\sqrt{\sum_{i=1}^{k}\left(F_i - \bar{F}\right)^2} = \frac{c}{k}\sqrt{\sum_{i=1}^{k}\left(F_i^N\right)^2} = c\sigma_{\text{cam}} \tag{2.20}$$

(c = scaling factor of the camera, given e.g. in mK/digit; F_i^N = noise signal in digits of the ith measured value, related to its mean value $\bar{F}$; σ_{cam} = standard deviation of the camera noise, measured in digits). If the camera signal is given not in digits but in (m)K, as usual for modern thermocameras, c has to be set to 1 in the following. According to (2.20), NETD is given in units of mK. If all pixels of the detector array, in general, have the same noise properties, it does not matter whether (2.20) is calculated from successive measurements of one pixel or from evaluating n pixels of one image nominally showing a homogeneous constant temperature $\bar{T} = c\bar{F}$.

According to Sect. 2.3 ((2.4) and (2.10)), for a synchronous sin/−cos correlation, the 0°- and the −90° images are calculated from the measured values $F_{i;j}(x,y)$ as:

$$S^{0^\circ}(x,y) = \frac{2c}{nN}\sum_{i=1}^{N}\sum_{j=1}^{n}\sin\left(\frac{2\pi(j-1)}{n}\right)F_{i;j}(x,y) \tag{2.21}$$

$$S^{-90^\circ}(x,y) = \frac{-2c}{nN}\sum_{i=1}^{N}\sum_{j=1}^{n}\cos\left(\frac{2\pi(j-1)}{n}\right)F_{i;j}(x,y)$$

(n = number of frames per lock-in period; N = number of averaged lock-in periods). A typical quantity of images used for a lock-in measurement $F_{i;j}(x, y)$ is the sum of three components: 1. a steady-state ("topography") part $F^{\text{topo}}(x, y)$, which is assumed to be noise-free here and should be the same for all images, 2. the actually interesting local temperature modulation signal $\Delta F_j(x, y)$, which is phase-coupled to the periodic heat introduction. This is also assumed to be noise-free here and repeated in each lock-in period, and 3. a statistical noise contribution $F_{i;j}^N(x, y)$, which is related to the NETD of the camera via (2.20):

$$F_{i;j}(x, y) = F^{\text{topo}}(x, y) + \Delta F_j(x, y) + F_{i;j}^N(x, y) \tag{2.22}$$

Here, we have neglected the non-steady-state initial heating period at the beginning of each lock-in thermography measurement, which will be justified in detail in Sects. 4.1 and 4.2. Inserting (2.22) into (2.21) yields:

$$\begin{aligned} S^{0^\circ}(x, y) &= 0 + c\Delta F^{0^\circ}(x, y) + cN^{0^\circ}(x, y) \\ S^{-90^\circ}(x, y) &= 0 + c\Delta F^{-90^\circ}(x, y) + cN^{-90^\circ}(x, y) \end{aligned} \tag{2.23}$$

The first term containing the topography signal becomes zero due to the fact that, at least for the synchronous correlation, the sum of all weighting factors is exactly zero. This property is responsible for the perfect topography rejection of the synchronously working lock-in thermography technique. $\Delta F^{0^\circ}(x, y)$ and $\Delta F^{-90^\circ}(x, y)$ are the local amplitude values of the local temperature modulation signals in-phase and out of phase measured in digits, which we want to measure. $N^{0^\circ}(x, y)$ and $N^{-90^\circ}(x, y)$ are the noise values of the 0°- and −90°-signals (measured in digits) for this measurement:

$$\begin{aligned} N^{0^\circ}(x, y) &= \frac{2}{nN} \sum_{i=1}^{N} \sum_{j=1}^{n} \sin\left(\frac{2\pi(j-1)}{n}\right) F_{i;j}^N(x, y) \\ N^{-90^\circ}(x, y) &= \frac{-2}{nN} \sum_{i=1}^{N} \sum_{j=1}^{n} \cos\left(\frac{2\pi(j-1)}{n}\right) F_{i;j}^N(x, y) \end{aligned} \tag{2.24}$$

Since the values of $F_{i;j}^N(x, y)$ are statistically distributed, also $N^{0^\circ}(x, y)$ and $N^{-90^\circ}(x, y)$ are statistical, hence we cannot calculate these noise values. However, since we know the standard deviation of $F_{i;j}^N$ from (2.20), we may calculate the standard deviations of N^{0° and N^{-90°, with respect to a number of k different positions. We will call the standard deviations of N^{0° and N^{-90° the system standard deviations $\sigma_{\text{sys}}^{0^\circ}$ and $\sigma_{\text{sys}}^{-90^\circ}$. We know that the quantity of $F_{i;j}^N$ is normally distributed with the average value of 0. It has the standard deviation σ_{cam} (see 2.20). According to the laws of statistics [32] the variance (being the square of the standard deviation) of a sum of statistical quantities equals the sum of the variances of the elements of this sum:

$$\frac{1}{k}\sum_{l=1}^{k}\left(N_l^{0^\circ}\right)^2 = \left(\sigma_{sys}^{0^\circ}\right)^2 = \sum_{i=1}^{N}\sum_{j=1}^{n}\left(\frac{2}{nN}\sin\left(\frac{2\pi(j-1)}{n}\right)\sigma_{cam}\right)^2$$
$$= \frac{2\sigma_{cam}^2}{nN} \tag{2.25}$$
$$\frac{1}{k}\sum_{l=1}^{k}\left(N_l^{-90^\circ}\right)^2 = \left(\sigma_{sys}^{-90^\circ}\right)^2 = \sum_{i=1}^{N}\sum_{j=1}^{n}\left(\frac{-2}{nN}\cos\left(\frac{2\pi(j-1)}{n}\right)\sigma_{cam}\right)^2$$
$$= \frac{2\sigma_{cam}^2}{nN}$$

The latter identities hold because of the identity

$$\sum_{j=1}^{n}\sin\left(\frac{2\pi(j-1)}{n}\right)^2 = \sum_{j=1}^{n}\cos\left(\frac{2\pi(j-1)}{n}\right)^2 = \frac{n}{2} \tag{2.26}$$

which holds for each $n \geq 4$ because the average value of both the $\sin^2$ and the $\cos^2$ function is 1/2. Hence, according to (2.20) and (2.25), the system standard deviations of both the 0° and the −90° signals after lock-in correlation are:

$$\sigma_{sys}^{0^\circ;-90^\circ} = \sigma_{sys} = \frac{\sqrt{2}\,\text{NETD}}{c\sqrt{nN}} \tag{2.27}$$

For steady-state imaging techniques (e.g. fluorescent microthermal imaging [41]), the standard deviation between two successively measured frames is often used to give a measure of the noise level. For lock-in thermography, however, we have an even more convenient quantity in the phase-independent temperature modulation amplitude given by (2.11) in Sect. 2.3, which is usually measured in every lock-in thermography experiment. Thus, in order to measure the system noise level of a lock-in thermography system, only a steady-state scene has to be imaged (e.g. a black body at room temperature) in the lock-in mode. Then the image is dominated by the system noise. The phase-independent amplitude signal, averaged over a certain representative region implying $X \times Y$ pixel, is very similar to the definition of the standard deviation of the noise component of each lock-in signal component:

$$\langle A_{noise}\rangle = \frac{c}{XY}\sum_{x=1}^{X}\sum_{y=1}^{Y}\sqrt{\left(N^{0^\circ}(x,y)\right)^2 + \left(N^{-90^\circ}(x,y)\right)^2}$$
$$= \sqrt{2}\,c\,\sigma_{sys} = \frac{2}{\sqrt{nN}}\text{NETD} \tag{2.28}$$

The total number of frames involved in the correlation process $n \times N$ is given by the frame rate f_{frame} and the total acquisition time t_{acq} as

$$nN = f_{\text{frame}}\, t_{\text{acq}}, \tag{2.29}$$

leading to the final result:

$$\langle A_{\text{noise}} \rangle = \frac{2}{\sqrt{f_{\text{frame}}\ t_{\text{acq}}}} \text{NETD} \tag{2.30}$$

Thus, knowing NETD allows us to predict the averaged amplitude noise level after a certain acquisition time according to (2.30). For example, a thermocamera running at $f_{\text{frame}} = 60\,\text{Hz}$ with an NETD of 20 mK, after 30 s acquisition time in a lock-in system, should show an averaged amplitude noise level of $\langle A_{\text{noise}} \rangle = 0.93\,\text{mK}$. Note that the noise level depends on the frame rate of the camera and on the data acquisition time, but not on the lock-in frequency. This prediction, however, is based on the presence of white noise, which needs not be true.

In Chap. 3 a number of different lock-in thermography systems will be compared. This is a non-trivial task, since different measurements have been made using different data acquisition times and different spatial resolutions. For an averaging lock-in experiment, the signal-to-noise ratio improves with the square root of the lock-in integration time t_{int}. This integration time should not be confused with the frame integration time mentioned in Sect. 2.1, which is the time where the electronic shutter is opened to measure one image. In a camera based experiment t_{int} equals the total data acquisition time of the experiment t_{acq}, whereas $t_{\text{acq}} = XY t_{\text{int}}$ holds for an image having Y lines and X rows in a serially measuring experiment. The number of pixels per image $X\,Y$ also determines the noise level to be achieved within a certain data acquisition time. This becomes most obvious in serial experiments with $t_{\text{int}} = t_{\text{acq}}/XY$. But also in camera-based experiments, for a given detector chip size, the number of detected photons for each pixel is proportional to the pixel area. Hence, a larger pixel area is equivalent to a larger integration time. Thus, for comparing different lock-in thermography systems, for each system a universal "pixel-related system noise density" can be defined, which independently of the acquisition time and of the number of pixels describes the noise properties of a certain system:

$$N_{\text{sys}} = A_{\text{noise}} \sqrt{\frac{t_{\text{acq}}}{XY}} \tag{2.31}$$

Here, A_{noise} is the temperature noise amplitude averaged over a representative image region, and $X \times Y$ is the number of pixels of the resulting image. If the noise is measured in mK, this system noise density has the unit $\text{mK}\sqrt{\text{s}}$. This pixel-related system noise density N_{sys} will be used in Chap. 3 as an objective measure to compare the different lock-in thermography systems.

2.7 Calibration

If the temperature measurement system or the thermocamera used in a lock-in thermography system is correctly calibrated, and if there is no cross-talk between successive measurements, the results of the lock-in correlation according to (2.21) are also amplitude values correctly calibrated in units of K or mK. However, in order to check the function of the correlation procedure and to test lock-in thermography systems in general, a simple test device is required, which allows one to perform a functional testing and a quantitative calibration of lock-in thermography systems. Ideally, this test device should provide a homogeneous area, the surface temperature of which can be modulated sinusoidally with a well-defined amplitude. The simplest possible test device is a resistively heated metal stripe. It will be explained in detail in Sect. 4.1 that it is useful to connect this stripe to a heat sink via an insulation layer, providing a well-defined heat resistance between the metal stripe and the heat sink. This insulation layer also provides the necessary electrical insulation between metal stripe and heat sink. Owing to this insulation layer the heat generated by the electrical current in the metal stripe is only slowly fed away to the heat sink. After an initial heating phase the average temperature of the test device is stabilized. If the thermal time constant for this thermal relaxation process is below the inverse of the lock-in frequency, this test device can be regarded to be adiabatic with respect to the lock-in frequency, hence the surface temperature modulation is only governed by the heat capacity of the stripe and the amount of the introduced heat. It is independent of the heat resistance of the insulation layer (for details see Sect. 4.1). If this test device should be used for IR thermography, its surface has to be covered with a thin layer of high IR emissivity (e.g. graphite spray), since any metal is a poor IR emitter. The thickness of this black layer should be so small as to make its heat capacity negligible at the lock-in frequency. Hence its surface should immediately follow the surface temperature modulation of the test device itself. Figure 2.12 shows the cross section through such a resistively heated test device for IR lock-in thermography. The current in the metal stripe is flowing perpendicular to the image plane.

The heat may be introduced into such a resistively heated test device sinusoidally by exposing it to a sinusoidally alternating current. However, here the frequency of the temperature modulation would be double that of the heating current, since

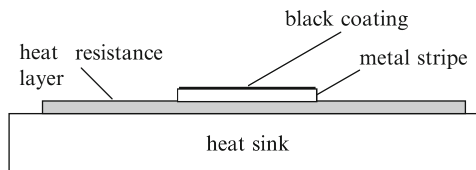

Fig. 2.12 Cross section through a resistively heated IR lock-in thermography test device. The heat resistance layer may be a sheet of paper, glued between the metal stripe and the heat sink

both the negative and the positive half-waves are generating heat. Therefore, it is more convenient to expose this test device to a pulsed d.c. current, hence to realize a square wave introduction of heat as it was discussed in Sects. 2.2 and 2.3. Then, after the initial heating phase, the device is linearly heated up within the first half-period, and in the second half-period, across the heat resistance it cools down linearly to the heat sink. Hence, for a square-shaped heat introduction, the surface temperature modulation in steady-state state has a triangle shape. Cooling begins owing to the steady-state temperature difference, which shows after the initial heating phase between the sample and the heat sink below the device. Therefore, as it will be described in Sect. 4.1 in more detail, the cooling rate is operative over the whole lock-in period and superimposes on the (higher) heating rate within the first half-period, resulting in a lower effective heating rate in the first half-period. Since in the steady-state the amount of heat generated in the first half-period has to be dissipated by the cooling rate operative over the whole period, the effective heating rate in the first half-period is exactly half the "adiabatic" heating rate (see Figs. 4.1 and 4.2 in Chap. 4). Hence, for a constantly dissipated electrical power P during the heating phase, in steady-state the expected real heating rate within the first half-period is exactly half the heating rate to be expected without the continuous cooling effect (m = mass of the metal stripe, c_p = specific heat):

$$\frac{\partial T}{\partial t} = \frac{1}{2}\frac{P}{mc_p} \tag{2.32}$$

Since this heating rate acts within one half of the lock-in period, the peak-to-peak temperature difference of the triangle-shaped temperature modulation of the sample is:

$$\Delta T_{\mathrm{triang}}^{\mathrm{pk-pk}} = \frac{P}{4mc_p f_{\mathrm{lock\text{-}in}}} \tag{2.33}$$

For a triangle-shaped signal having a pk-pk amplitude of 1, its basic harmonic has a pk-pk amplitude of $8/\pi^2 = 0.81$ [32], yielding an amplitude according to the definition in (2.5) of $4/\pi^2 = 0.405$. Thus, the basic harmonic of the temperature modulation amplitude of this calibration test device, if exposed to a pulsed current of I, is expected to be:

$$A_{\mathrm{test}} = 0.405\frac{I^2R}{4mc_p f_{\mathrm{lock\text{-}in}}} = 0.101\frac{I^2R}{mc_p f_{\mathrm{lock\text{-}in}}} \tag{2.34}$$

The correct dimensioning of both the heat resistance layer between the metal stripe and the heat sink, and the thickness of the black coating can easily be checked by measuring the dependence of the measured amplitude signal on the lock-in frequency: Only if both layers are correctly dimensioned the amplitude signal falls with $1/f_{\mathrm{lock\text{-}in}}$ as predicted by (2.34). If the heat resistance is too low, the surface temperature tends to stabilize even within each single heating pulse, leading to a sublinear decay of A_{test} with $f_{\mathrm{lock\text{-}in}}$, and finally for low $f_{\mathrm{lock\text{-}in}}$, to its independence of $f_{\mathrm{lock\text{-}in}}$. On the other hand, if the heat resistance is too large, the duration of the

initial heating phase increases, and the average stabilized temperature of the test device in operation would increase, too. This would not affect the result of the test measurement, since here it is assumed that the measurement time of the calibration measurement is generally large compared to the initial heating phase, or that this temperature drift is correctly compensated, as will be described in Sect. 4.2. If the thickness of the black coating is too large, the heat diffusion resistance from the surface of the test device to the surface of the coating will lead to an additional frequency-dependent quenching of the measured amplitude value with increasing frequency. Hence, instead of the $1/f_{\text{lock-in}}$ dependence expected from (2.34) an even stronger decay of A_{test} with $f_{\text{lock-in}}$ would follow at high frequencies.

2.8 Heat Dissipation and Transport Mechanisms in Solar Cells

Thermal investigations on solar cells are an important application field of lock-in thermography, see Sects. 6.2 and 6.3. The success of this technique in this field relies on the fact that all elementary processes occurring in solar cells are connected with the local heat generation or heat consumption (local cooling). Understanding these processes in detail is the key for understanding the different special lock-in thermography techniques, which have been developed in recent years for the detailed physical investigation of solar cells and modules. Therefore in this section, the elementary electronic processes, which may occur in a dark and illuminated solar cell, are described and related to their heat generation or consumption potential [42]. Reading this section requires basic knowledge in semiconductor physics [43] but is necessary for understanding especially Sects. 5.4, 6.2.2 and 6.3 in detail. Non-thermal processes in such devices, which nevertheless may also be investigated by lock-in thermography, will be described in Sect. 2.9.

The most obvious local heat source is Joule heat, which is generated if any current flows through a material with a finite specific resistance. In the volume the generated local Joule-type power density due to a local current density $J(x, y, z)$ is:

$$p_{\mathrm{J}}^{\mathrm{v}}(x, y, z) = \rho J^2(x, y, z). \tag{2.35}$$

Here ρ is the specific resistance (resistivity) of the material. If the current flows in a thin layer with a specific sheet resistance (sheet resistivity) of ρ_{s}, which happens for example if the current flows in a solar cell horizontally in the thin emitter layer or in a contact grid line on top, the area-related generated Joule-type power density is:

$$p_{\mathrm{J}}^{\mathrm{s}}(x, y) = \rho_{\mathrm{s}}\, J_{\mathrm{s}}^2(x, y). \tag{2.36}$$

Here $J_{\mathrm{s}}(x, y)$ is the sheet current density in units of A/m. Typical resistivities of the bulk material of silicon solar cells are in the range of 1 Ωcm and a typical value of the generated current density under non-concentrated solar illumination (having a

power density of 100 mW/cm^2) is about 30 mA/cm^2. Regarding a typical thickness of a cell of 0.2 mm, this corresponds to an area-related dissipated power density due to the current flowing vertically in the bulk material of about 0.018 mW/cm^2. This is a really negligible value compared to the illumination power density. Thus, the contribution of the volume current in the bulk of solar cells to the generated heat can be neglected for standard solar cells. This does not hold anymore for the horizontal current in the emitter or in the grid lines. Their contribution has to be regarded in any electro-thermal simulation of solar cells according to (2.36) [42]. Note that ohmic shunts, which may be responsible for very dominant local heat sources (see Sect. 6.2.1), also have to be described by (2.35) or, in the case of extended edge shunts, by (2.36).

Solar cells are constructed to feed away typical currents of 30 mA/cm^2 with negligible Joule-type power losses. If the cell does not have any series resistance problems, even the losses according to (2.36) are weak compared to other heat generation mechanisms. Then the dominant heat exchange occurs as a result of the light irradiation and of the vertical current flow across the horizontal p-n junction, which can be illustrated in an energy band diagram. Figure 2.13 shows a simplified band diagram of a p-n junction under forward bias condition, which is exposed to monochromatic illumination with a photon energy of $h\nu$ (h = Planck constant, ν = frequency of light). All important elementary heat generation or consumption mechanisms are indicated in this figure by arrows. Since these arrows symbolize the movement of electrons with the y-axis being their energy, arrows pointing downwards are processes of energy loss, which is generation of heat, and arrows pointing up are processes of energy gain, which is heat consumption, also called Peltier cooling. For holes in the valence band the energy axis is inverted, hence for them an

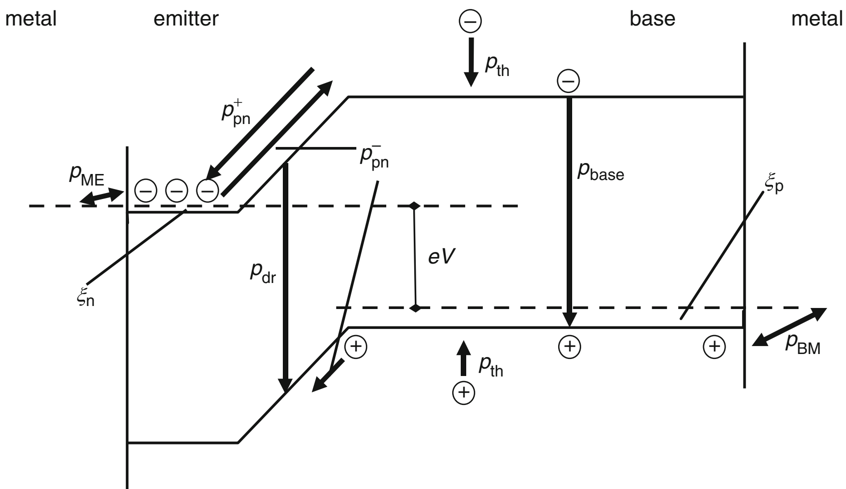

Fig. 2.13 Simplified band diagram of an illuminated p-n junction under forward bias (solar cell in operation) with heat dissipation mechanisms indicated (reproduced with permission of American Institute of Physics)

upward arrow means heat generation and a downward arrow means heat consumption. The dashed lines indicate the majority carrier Fermi levels in the n^+- and the p-side (emitter and base region), respectively, the difference of both being the bias energy eV (e = elementary charge). In the emitter the Fermi level is lying within the conduction band, hence the emitter is degenerately doped. The energy differences between the n- and p-side Fermi levels and the conduction and the valence band edge in these regions are the two Fermi energies ξ_n and ξ_p, respectively. Since the emitter is degenerately doped, ξ_n is negative. The two contacts are symbolized here as vertical lines at the left and right, separating the semiconductor emitter and base from the contact metals. In the following, it will not be considered at which depth in the device (which is the x-axis in Fig. 2.13) an amount of heat is generated or consumed. Hence, the actual solar cell is assumed to be thermally thin, see Sect. 4.1, so all heat generation or consumption mechanisms are assumed to appear at the same lateral position. Exceptions from this assumption will be discussed at the end of this section and especially in Sect. 5.4. Of course, if a thin film solar cell on glass is considered, the whole device may be thermally thick. Nevertheless, also then the active region has a negligible thermal thickness.

If charge is transported in semiconductors by carriers, the electrons in the conduction band and holes in the valence band contributing to this transport have a certain mean energy of ε_e and ε_h above the corresponding band edge. These values depend on temperature T, on the form of the density of states in the two bands, on the doping concentration, and on the nature of the scattering mechanism relevant in the transport process. For a box-shaped density of states, non-degeneracy, and an energy-independent scattering process, the average kinetic energy would be 3/2 kT, which is 1/2 kT for each degree of freedom. A further, purely thermoelectric effect contributes significantly to the kinetic energy term. It is due to the carrier-phonon interaction and is called "phonon drag". The magnitudes of these energies will be discussed in more detail in Sect. 5.4. In the case of non-degeneracy (base region) these are mean kinetic energies, but in the case of degeneracy (emitter region) they also have a potential energy contribution. Here we only will use the quantities ε_e^n, ε_h^n, ε_e^p, and ε_h^p as additional energies for thermalized free electrons and holes in the emitter and in the base, respectively. These kinetic energies were not yet considered in [42] but will be taken into account in the following.

It was assumed in Fig. 2.13 that only in the p-type base excess electrons as minority carriers are generated by irradiation with light with an energy of $h\nu$ being larger than the gap energy (E_g = 1.1 eV for silicon). This excitation event leaves behind a "hot" free hole and a "hot" free electron. By generating phonons, within less than 1 picosecond after the absorption event these carriers loose their excess kinetic energy and thermalize to close to the edge of the bands, where they only have the mean kinetic energy ε_h^p and ε_e^p. Hence, the thermal energy dissipated by this absorption process to the lattice is $(h\nu - E_g - \varepsilon_h^p - \varepsilon_e^p)$. This thermalization energy is indicated in Fig. 2.13 by two arrows, both labelled p_{th} (note that the energy counting for holes is inverse, hence both arrows indicate heat generation). If an electron were excited exactly from the edge of the valence band deeper into the conduction band, this process would leave behind a "cold" hole of zero kinetic energy. Thereby

the number of holes increases by 1 but the kinetic energy of the whole hole ensemble does not increase. Thereby the hole temperature, which is a measure of their mean kinetic energy, slightly decreases. This is equivalent to cooling the hole ensemble by an amount of ε_h^p, which instantly couples to the lattice. In the same way generating a "cold" electron cools the electron ensemble by ε_e^p. Even if $h\nu = E_g$ holds, the two generated "cold" carriers consume a heat energy of $\varepsilon_h^p + \varepsilon_e^p$. Thus, if we assume that all absorbed photons lead to a photocurrent density J_{ph} (i.e. the internal quantum efficiency equals 1), the thermal power per unit area, which is generated by thermalization of absorbed photons in the bulk, is:

$$p_{th} = \frac{J_{ph}}{e}\left(h\nu - E_g - \varepsilon_h^p - \varepsilon_e^p\right). \tag{2.37}$$

The assumption that all absorbed photons contribute to the photocurrent needs not to be true. In reality, a certain fraction of the photo-generated minority carriers recombines before reaching the p-n junction. Since this fraction is independent of the bias, it only leads to another constant heat contribution, which is exactly $h\nu$ for each absorbed photon not leading to a photocurrent. This contribution will be neglected in the following, but it can easily be regarded at the end of the calculation. We also will neglect the influence of photons absorbed in the emitter, since this emitter is usually very thin (about 300 nm) and shows a very low minority carrier lifetime. Moreover, we will neglect hole injection into the emitter, since this process is improbable due to the very asymmetric doping concentrations.

If the electrons photo-generated in the bulk reach the p-n junction, they inevitably "fall down" the barrier, i.e. they are attracted by the electric field in the junction and move to the emitter region. Note that the photocurrent is a reverse current for the p-n junction. By acceleration in the electric field, the electrons gain kinetic energy, which they suddenly loose by emitting phonons. This process, which will be discussed in more detail in Sect. 5.4, is another kind of thermalization and actually a Peltier heating process, which occurs at the p-n junction. The amount of heat per unit area generated by this process is:

$$p_{pn}^{+} = \frac{J_{ph}}{e}\left(E_g - \xi_n - \xi_p - eV + \varepsilon_e^p - \varepsilon_e^n\right). \tag{2.38}$$

Here $(E_g - \xi_n - \xi_p - eV)$ is the value of the energy barrier between emitter and base at a forward bias of V, the other terms in the bracket are a possible difference of the mean kinetic energy of the electrons before and after crossing the p-n junction. Note that the Peltier effect is a pure heat transport mechanism. Hence, a certain Peltier heating is always balanced by a certain Peltier cooling at another position. It will be discussed in Sect. 5.4 where the cooling belonging to the heating in (2.38) comes from. Note also that the two heat sources p_{th} and p_{pn}^{+} are dissipated at the same lateral location where the light is absorbed. This holds exactly for p_{th} and at least approximately for p_{pn}^{+} since, even for a large diffusion length, the electrons may diffuse laterally in the bulk only over a distance in the order of the cell thickness before they flow through the p-n junction. Therefore, these

two heat dissipation mechanisms, together with recombination of photo-generated minority carriers, have been called "local power dissipation" mechanisms [15]. For all other mechanisms involving majority carriers the carriers are free to move laterally between the moment of their generation and that of heat dissipation, which will be discussed later on.

Since this p-n junction is under forward bias, also the electron current opposite to J_{ph} flows from the emitter across the barrier into the base, which is called the "diffusion current" J_{diff}. This current is symbolized in Fig. 2.13 as an upward arrow named p_{pn}^{-}, hence here electrons gain energy. This current would also flow at this bias without any illumination, hence this is a so-called "dark current". According to the detailed balance principle, these opposite current flows (J_{ph} and J_{diff}) can be described independently from each other. Another contribution to the dark forward current is the so-called "depletion region current" J_{dr}, which is also often called "recombination current". It is due to the recombination of electrons and holes in the depletion region between emitter and base region. Since this recombination occurs predominantly in the middle of the p-n junction, both electrons and holes have to gain an energy of approximately half the barrier height. Hence for the diffusion current the electrons have to gain an amount of energy of the barrier height per charge, minus the difference of the mean kinetic energies in both regions. Also for the depletion region current the electrons and holes together have to gain an amount of energy of the barrier height per charge. We will assume that up to the recombination event their kinetic energy is preserved. Since this energy gain consumes thermal energy, this process is a Peltier cooling effect (for details see Sect. 5.4). The amount of Peltier cooling at the p-n junction per unit area is:

$$p_{pn}^{-} = -\frac{J_{diff}}{e}\left(E_g - \xi_n - \xi_p - eV + \varepsilon_e^p - \varepsilon_e^n\right) - \frac{J_{dr}}{e}\left(E_g - \xi_n - \xi_p - eV\right). \quad (2.39)$$

If thermalized electron-hole pairs recombine non-radiatively in the depletion region, they generate a heating power per unit area of $(E_g + \varepsilon_e^n + \varepsilon_h^p)$ per electron:

$$p_{dr} = \frac{J_{dr}}{e}\left(E_g + \varepsilon_e^n + \varepsilon_h^p\right). \quad (2.40)$$

In the same way, if due to the diffusion current electrons reach the base region, they inevitably recombine there or at the base contact, leading to a generated heating power per unit area of:

$$p_{base} = \frac{J_{diff}}{e}\left(E_g + \varepsilon_e^p + \varepsilon_h^p\right). \quad (2.41)$$

Even if an electron-hole pair recombines directly from the band edges, it generates only an energy amount of E_g. However, this process consumes carriers having zero kinetic energy. Then, in the same way as discussed above for the absorption of light with $h\nu = E_g$, the electron–hole ensemble cools down by an amount of $(\varepsilon_e^p + \varepsilon_h^p)$. Here we consider only non-radiative recombination where the whole

recombination energy is converted to heat. The case of radiative recombination will be discussed in Sect. 5.4.

The average absolute energy of the electrons (and holes!) in the contact metals, which contribute to current transport, is close to the position of the Fermi level in these metals. If electrons or holes enter the semiconductor from a contact metal, their energy increases by a potential energy contribution, which is the corresponding Fermi energy ξ_n or ξ_p, respectively, and by a kinetic energy contribution, which for holes entering the base is ε_h^p and for electrons entering the emitter is ε_e^n. If holes or electrons leave the base or the emitter, the same amount of Peltier heat is released. So also at these barriers Peltier cooling or Peltier heating may occur, depending on the current direction. Only if the current flows homogeneously in a cell and the contacts cover the whole area, at each position the net current density between metal and emitter J_{ME} and between base and metal J_{BM} both equal the difference between photocurrent and dark current ($J_{diff} + J_{dr} - J_{ph}$). However, whenever lateral currents are flowing in the device, the local current densities at the contacts may be different. Therefore, the general expressions for Peltier heating or cooling for a current density at the emitter contact of J_{ME} and at the base contact of J_{BM} (both counted positively for a dark forward current and negatively for a reverse current) are [44]:

$$p_{ME} = \frac{-J_{ME}}{e}(\xi_n + \varepsilon_e^n), \tag{2.42}$$

$$p_{BM} = \frac{-J_{BM}}{e}(\xi_p + \varepsilon_h^p). \tag{2.43}$$

This whole set of equations (2.37)–(2.43) describes the heat dissipation and heat transport of the most important mechanisms in a p-base silicon solar cell. In an n-base cell the complementary processes occur. Let us apply these equations to the special case of a current flowing in the dark under forward bias. We will assume here a homogeneous device without any lateral current flow. Joule heating will be neglected. Then only the two dark current contributions J_{diff} and J_{dr} are flowing. The bias dependence of these two currents is described by the following equations [45]:

$$J_{diff} = J_{01}\left(\exp\left(\frac{eV}{kT}\right) - 1\right), \tag{2.44}$$

$$J_{dr} = J_{02}\left(\exp\left(\frac{eV}{2kT}\right) - 1\right).$$

The magnitudes J_{01} and J_{02} are called the "saturation current densities" of the diffusion and the depletion region (recombination) current, respectively. Note that, due the different slopes of these two current contributions, J_{diff} dominates for high forward bias and J_{dr} dominates for medium and low forward bias. J_{diff} is a local measure of the minority carrier lifetime in the bulk. Generally, J_{diff} is an areal current. Regions of low lifetime show a locally increased value of J_{diff} [45]. Local sites of strongly increased J_{dr} are the origin of so-called "non-linear shunts" in solar cells, see Sect. 6.2.1.

For describing the dissipated power density in a homogeneous thermally thin solar cell in the dark, the sum of (2.39)–(2.43) has to be considered with $J_{ME} = J_{BM} = J_{diff} + J_{dr}$, yielding a total dissipated power per unit area of:

$$p_{dark} = p_{pn}^{-} + p_{dr} + p_{base} + p_{ME} + p_{BM} = V\,(J_{diff} + J_{dr})\,. \tag{2.45}$$

As can be expected already from the energy conservation law, the total dissipated power density just equals the product of current density and voltage. All terms containing Fermi energies and kinetic energies, which are related to the Peltier effects, cancel. If the cell contains any kind of inhomogeneity, this holds not anymore locally in any position but only for the whole cell, see below.

If a homogeneous cell is illuminated and a photocurrent J_{ph} flows, also (2.37) and (2.38) have to be added to (2.45), and J_{ph} has to be regarded in (2.42) and (2.43) as a negative current contribution. The result is:

$$p_{ill} = p_{dark} + \frac{J_{ph}}{e}\,(\mathrm{h}\nu - eV)\,. \tag{2.46}$$

Figure 2.14 shows the result of (2.46) using (2.44)–(2.45) for assumed typical values of $J_{01} = 1.5 \times 10^{-12}$ A/cm^2, $J_{02} = 2 \times 10^{-6}$ A/cm^2, $J_{ph} = 30$ mA/cm^2, and hν = 1.4 eV (λ = 880 nm) [42]. It has been assumed here that all absorbed photons are leading to a photocurrent. We see that both under short circuit condition ($V = 0$, $J = -J_{ph}$) and under open circuit condition ($V = 0.6$ V, $J = 0$) the complete amount of irradiated power ($h\nu$ per irradiated photon) is dissipated into heat. In between, there is a minimum of the dissipated power at the so-called maximum power point at about $V = 0.52$ V, which is due to the fact that here the maximum amount of electrical power is generated by the solar cell and fed out to the electric load.

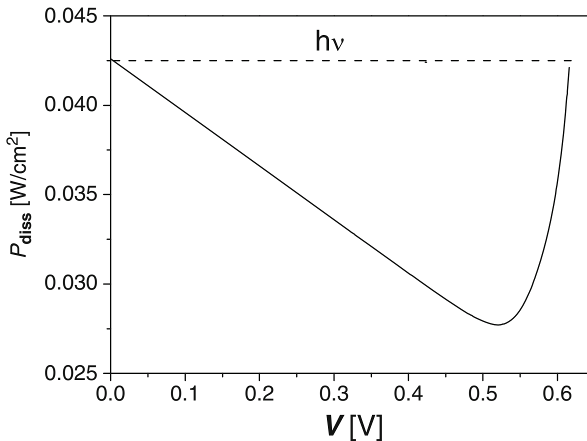

Fig. 2.14 Dissipated thermal power density under monochromatic illumination as a function of the cell bias V (with permission of American Institute of Physics)

Equations (2.35)–(2.43) describing the different elementary heat dissipation and transport mechanisms hold generally, but (2.45) and (2.46) only hold for strictly vertical current flow. If any lateral current flows, e.g. due to local contacts or due to any kind of inhomogeneity in the cell, the elementary mechanisms can be observed separately. For example, the observation of Peltier effects will be presented in Sects. 5.4 and 6.3. The fact that different heat sources may be acting at different sites is the base of lock-in thermography on solar cells. This will be demonstrated in Sects. 6.2 and 6.3.

2.9 Carrier Density Imaging

Until now, only thermal measurements have been considered for lock-in thermography measurements. It had been mentioned in Sect. 2.1 that, according to Kirchhoff's law, the probability of a surface to emit radiation (i.e. its emissivity ε) equals the absorption probability α at this wavelength. Since mid-range radiation in the wavelength range 3–5 μm typically used for lock-in thermography corresponds to a photon energy of 0.25–0.41 eV, which is much smaller than the energy gap of silicon of 1.1 eV, silicon and also most other semiconductors are nominally transparent to infrared light. Hence, in principle, thermography on these materials should be impossible. Fortunately, in doped semiconductors there is another source of IR absorption, which is free carrier absorption. Whenever electromagnetic radiation penetrates a semiconductor having a free carrier concentration of n or p, respectively, the electric and magnetic fields accelerate the free carriers in this body, which is connected with a certain heat generation by absorption of electromagnetic energy. For n-type material having a free carrier concentration of n, the corresponding absorption coefficient can be described by:

$$\alpha_{\mathrm{fc}} = K_n \lambda^2 n. \tag{2.47}$$

Here K_{n} is a material constant, discussed in more detail below, and λ is the wavelength of the radiation. An equivalent equation holds for p-type material. For n-Si, $K_n \approx 10^{-18}\,\mathrm{cm}^2/\mu\mathrm{m}^2$, and for p-Si $K_{\mathrm{p}} \approx (2-2.7) \times 10^{18}\,\mathrm{cm}^2/\mu\mathrm{m}^2$ holds [46]. Hence, free carrier absorption/emission becomes stronger with increasing wavelength and is directly proportional to the free carrier concentration. If both electrons and holes are present in a semiconductor (e.g. under optical excitation), their absorption coefficients simply add up. Only by this free carrier absorption of optically excited or highly doped semiconductor regions, which corresponds to an equivalent free carrier IR-emission, thermal IR-investigations on bare semiconductor devices become possible.

On the other hand, the measurement of free carrier absorption or emission in the IR-range also enables the measurement of the free carrier concentration of semiconductor materials via (2.47). If this measurement is performed by using a thermal camera, images of free carrier concentrations can be obtained. In contrast to actual

temperature measurements, this type of measurements may be called "non-thermal" IR-camera based measurements. Note that "thermal" lock-in thermography is performed on complete electronic devices, whereas "non-thermal" measurements are typically performed on wafers. This section will introduce the physical basics of such measurements; their practical realisation will be described in Sect. 3.5, and typical applications will be introduced in Sect. 6.4.

If we generate excess electrons and holes of density Δn, Δp, respectively, in a silicon wafer, by irradiation with light of an energy $h\nu$ greater than the band gap, they thermalise within picoseconds to a thermal equilibrium with the crystal lattice occupying electronic states above/below their respective band edge. We assume in the following excitation levels which lead to excess carrier densities much smaller than typical doping concentrations of wafers used for solar cells ($10^{16}\,\text{cm}^{-3}$). Then the quasi-Fermi-levels are distant from the band edges (non-degenerate case) and the excess free carriers are distributed over the electronic states given by their respective density of states following a Boltzmann distribution with the temperature T_w of the wafer. If the light irradiation is performed periodically, the weak additional absorption and emission of this excess free carrier distribution can be detected by a thermal camera using the lock-in principle as outlined in Sects. 2.2–2.6. This may be done in a distinct absorption or emission mode, if we select the experimental conditions such that either the absorption or the emission of free carriers dominates. Such a measurement may then be converted to a distribution of the excess carrier lifetime.

As already mentioned, this kind of "non-thermal" investigation is performed on bare wafers, in contrast to the "thermal" lock-in thermography performed on complete electronic devices. Note, however, that in these "non-thermal" investigations also the wafer temperature is modulated (any light absorption also leads to a temperature increase), which leads to a modulation of the thermal IR-radiation even if the free carrier concentration would remain constant. Hence, in reality the IR-camera measures both the "thermal" (temperature-induced) and the "non-thermal" (free carrier-induced) modulation of the device radiation in parallel. It will be described in Sect. 3.5 how these two contributions can be separated from each other.

Historically, single spot infrared absorption of free excess carriers had been used to determine their density and according to

$$\tau = \frac{\Delta n}{G} \tag{2.48}$$

the minority carrier lifetime, where G denotes the generation rate in $\text{cm}^{-3}\,\text{s}^{-1}$. This has been done by methods measuring the decay of carrier concentrations via IR-absorption [47–49] or modulated excitation (Modulated Free Carrier Absorption, MFCA) [50]. This technique was further developed to a setup allowing 2D lifetime mappings [51]. The IR-absorption by free carriers excited in a small spot was measured in this case using a 1,550 nm laser beam transmitting the sample within the generation area. Depending on lateral resolution requirements and wafer size, MFCA maps often took several hours of measurement time per sample. With the

introduction of highly sensitive, fast CCD-cameras, operating in the infrared, the idea to overcome the necessity of scanning the sample was first suggested by Bail et al. [12], developed in parallel by Riepe et al. by implementing lock-in techniques and published in [13].

In this section, we introduce the basic concepts and the two principal measurement modes, absorption and emission of IR-radiation, by free carriers. Calibration and noise considerations will be outlined together with the description of specific measurement setups in Sect. 3.5.

An excess free electron gas in a wafer with temperature T_w interacts with a thermal radiation field by absorption and by emission of photons. If we want to detect excess carriers with a thermal camera, we can in principle make use of both interactions. First, we have to keep in mind that within the detection ranges where suitably sensitive cameras are available, namely the 3–5 (mid-wave) and the 8–10 μm (long-wave) wavelength bands (see Sect. 2.1), there are no pronounced absorption bands of the silicon crystal lattice itself. As mentioned above, a wafer of usual thickness of a few hundred micrometers and low to medium doping concentration is basically transparent to radiation coming from the background. Thus, a big part of the radiation leaving the wafer will be background radiation. If the doping concentration of a wafer is only at about $10^{16}\,\text{cm}^{-3}$, as for typical solar cell material, the free carrier absorption according to (2.47) only weakly influences the background radiation penetrating the wafer. The thermal radiation, which the camera images if focused on a wafer surface, is thus dependent on three factors: (1) the radiation coming from the background, which is influenced by the absorption in the wafer, (2) the free carrier emission in the wafer, and (3) the relation of the temperature of the wafer T_w to that of the background, T_b, which strongly influences the ratio between (1) and (2).

Let us first consider absorption and emission of radiation by free carriers in silicon in some more detail. The radiation transmitted through the sample is proportional to the radiation of the background and the absorption spectrum of the free carriers. In more detail than (2.47), the absorption coefficient of free carriers with density N is given by [52]:

$$\alpha_{fc}(\lambda) = \frac{e^3 N}{4\pi^2 \varepsilon_0 c^3 n\, m^{*2} \mu} \lambda^2, \tag{2.49}$$

where λ is the wavelength, e the elementary charge, ε_0 the real part of the dielectric constant, c the speed of light, n the refractive index, m^* the effective mass, and μ is the mobility. If by periodic irradiation of light the free carrier density N is modulated by an amount ΔN being small compared to N, the steady-state free carrier absorption due to the net doping concentration is modulated by a small amount. If this modulation is detected by lock-in techniques, the steady-state contribution of $\alpha_{fc}(\lambda)$ cancels and only the modulated part due to ΔN is measured. Replacing $\frac{\Delta N}{m^{*2}} = \frac{\Delta n}{m_e^{*2}} + \frac{\Delta p}{m_h^{*2}}$, with $\Delta n = \Delta p$ and m_e^* and m_h^* being the effective masses of electrons and holes, yields the dependence of the free carrier absorption on the modulated excess minority carrier density Δn. Schroder et al. [46] found experimentally a fair agreement of (2.49) and the absorption coefficients for silicon

at room temperature. From (2.49) we note that, in principle, a camera detecting at longer wavelength is of advantage. Whether this advantage can be utilized for CDI/ILM depends on the actual state of the development of IR-cameras for the different wavelength ranges concerning sensitivity and NETD (for an overview of the status in 2009 see Sect. 3.1). Since for thermal lock-in thermography measurements on electronic devices usually mid-wave cameras are preferred owing to their better spatial resolution capability (see Sect. 3.4), these cameras are also often used for non-thermal (carrier density) measurements.

In thermal equilibrium, free carriers also emit infrared radiation. According to the law of detailed balance they have to emit the same amount of power as they absorb at any energy interval to stay at the same temperature. Therefore the absorption coefficient has to equate the emission coefficient (Kirchhoff's law)

$$\alpha_{\mathrm{fc}}(\lambda) = \varepsilon_{\mathrm{fc}}(\lambda). \tag{2.50}$$

If the background with temperature T_{b} can be assumed to emit black body radiation, the number of photons absorbed by free carriers S_{abs} is proportional to the integral of Planck's law (see (2.1)), written for the photon flux density, over the considered range of wavelength which is defined by the spectral range of the camera:

$$S_{\mathrm{abs}} \propto \int_{\lambda_{\min}}^{\lambda_{\max}} \frac{\alpha_{\mathrm{fc}}(\lambda, \Delta n)}{\lambda^4 \left(e^{hc/k\lambda T_{\mathrm{b}}} - 1\right)} \mathrm{d}\lambda. \tag{2.51}$$

The emission by the free carriers depends on their temperature, which is equal to the temperature of the wafer T_{w}, and the emission coefficient of the free carriers is:

$$S_{\mathrm{emi}} \propto \int_{\lambda_{\min}}^{\lambda_{\max}} \frac{\varepsilon_{\mathrm{fc}}(\lambda, \Delta n)}{\lambda^4 \left(e^{hc/k\lambda T_{\mathrm{w}}} - 1\right)} \mathrm{d}\lambda. \tag{2.52}$$

The signal which can be detected by a thermal camera is in general composed of both contributions:

$$\begin{aligned} S_{\mathrm{CDI}} = S_{\mathrm{emi}} - S_{\mathrm{abs}} = d(A_{\mathrm{w}}) \cdot \int_{\lambda_{\min}}^{\lambda_{\max}} \frac{\varepsilon_{\mathrm{fc}}(\lambda, \Delta n)}{\lambda^4 \left(e^{hc/k\lambda T_{\mathrm{w}}} - 1\right)} \mathrm{d}\lambda \\ - d(A_{\mathrm{b}}) \cdot \int_{\lambda_{\min}}^{\lambda_{\max}} \frac{\alpha_{\mathrm{fc}}(\lambda, \Delta n)}{\lambda^4 \left(e^{hc/k\lambda T_{\mathrm{b}}} - 1\right)} \mathrm{d}\lambda, \end{aligned} \tag{2.53}$$

where A_{w} is the surface area on the wafer which corresponds to one camera-pixel and A_{b} is the corresponding surface area on the background. Here d is a positive factor which accounts for the surface dependence of the emission and absorption signal and contains pre-factors of Planck's formula. In a practical setup $A_{\mathrm{w}} \approx A_{\mathrm{b}}$.

With the linear dependence of α_{fc} on Δn and the quadratic dependence on λ from (2.49) and with (2.50), this results in an approximate expression for the camera signal:

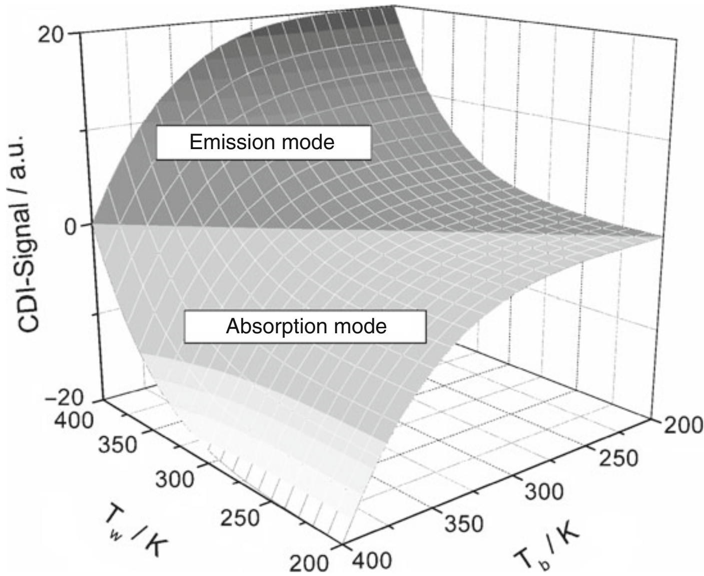

Fig. 2.15 Theoretical dependence of the camera signal on background temperature T_b and wafer temperature T_w according to (2.54)

$$S_\mathrm{CDI} \propto \Delta n \cdot \int_{\lambda_\mathrm{min}}^{\lambda_\mathrm{max}} \left(\frac{1}{\lambda^2 (e^{hc/k\lambda T_\mathrm{w}} - 1)} - \frac{1}{\lambda^2 (e^{hc/k\lambda T_\mathrm{b}} - 1)} \right) \mathrm{d}\lambda . \tag{2.54}$$

In principle, if T_w equals T_b, the absolute value of the absorption signal and the emission signal are equal and a vanishing net signal results. If the background is at a higher temperature than the wafer, an absorption signal can be detected (absorption mode). A cooled background causes a signal which is dominated by the emission of the free carriers, which corresponds to the emission mode. The theoretical dependence of the detected signal on background temperature T_b and wafer temperature T_w is plotted in Fig. 2.15, for an experimental confirmation see Sect. 3.5.

From Fig. 2.15 it is apparent that, in the emission mode, an increase of the wafer temperature T_w results in a strong signal increase, while for lower background temperature T_b the signal increase is asymptotically limited. The signal in the absorption mode, on the other hand, rises strongly with background temperature, while the effect of lowering the wafer temperature is limited.

For the detection of carrier densities the lock-in principle is realised by a chopped optical generation. The thermal radiation coming from the wafer is measured in two different states, first with irradiation of the sample by a light source with $h\nu > E_\mathrm{g}$, generating excess free carriers, and second without any irradiation. If the two images obtained are subtracted from each other, the difference is proportional to the signal related to free carriers, since all other parameters determining the absolute

IR-radiation coming from the sample remain unchanged when switching the generation illumination on/off. This procedure is preferably done with a fast enough sequence of irradiated and unirradiated periods to suppress possible temperature drifts and other changes in the IR background radiation.

Historically, the first realisation of a carrier imaging technique has been to have a black body with emissivity close to 1 and a temperature $T_b > T_w$ behind the wafer [12]. The dominating effect is then that the excess carriers of temperature T_w absorb radiation emitted from the background, the resulting image shows areas with high excess carrier density dark; in areas with low excess carrier density more of the bright background radiation is visible. Figure 2.16, left, shows such an example for a multicrystalline silicon wafer. The sample has been damage etched and SiN-passivated. The displayed area is $100 \times 100\,\text{mm}^2$. The measurement time was 30 s. Compared to the strong background radiation the emission by the colder excess carriers themselves can be neglected.

This "absorption mode" was developed in parallel by two groups, first published in [12] without using the lock-in principle and named "Infrared Lifetime Imaging" (ILM). In a subsequent publication a setup implementing lock-in technique was reported [13, 53] and this variant called "Carrier Density Imaging" (CDI). At first, both terms were used in parallel in literature. Since, however, ILM had included the option to apply the lock-in principle as well and was subsequently developed to this state, later a combined abbreviation was introduced, to clarify, that both terms refer to the same technique. In the following, we will mostly give examples measured with the original "CDI" setup and thus call the technique CDI/ILM.

To use the infrared emission of free carriers instead of their infrared absorption had already been proposed by White et al. [54]. They introduced a scanning method to detect the infrared emission by optically generated free carriers in heated samples. Later Bail et al. [12] used an infrared camera to detect the emission of free carriers.

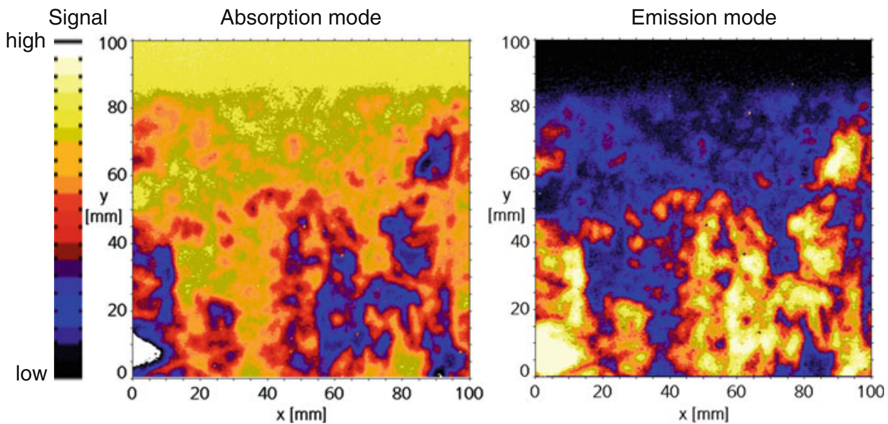

Fig. 2.16 Measured camera image for a surface-passivated multicrystalline wafer in absorption (*left*) and emission mode (*right*)

A high-lifetime FZ wafer was heated with a hot air fan to 350°C to increase the emission of the free carriers and to enable the detection of IR-radiation. Experimental setups which allowed measurements at moderately elevated temperature were introduced in [55] and [56]. In Sect. 3.5 we explain experimental realisations of the different measurement modes in some more detail. For the example of Fig. 2.16, the signal measured in the emission mode is compared to the one measured in the absorption mode (Fig. 2.16, right). As expected, intensities are reversed. Using appropriate calibration (see Sect. 3.5) the excess carrier lifetimes calculated from emission images are in good agreement with the ones calculated from the absorption images. This has been demonstrated e.g. in [55]: The mean lifetime over the total area calculated for two example images was 61 μs for the emission and 65 μs for the absorption measurement. The difference between the absolute lifetime values derived from both techniques was thus only about 6% for this example.

The advantage of emission CDI/ILM is the possibility to increase signal strength by using higher wafer temperatures. As increasing background temperature for absorption CDI/ILM fails because of saturation of the CCD-chip of the camera, the wafer temperature can be raised to moderate temperatures without saturation problems in emission mode since it shows a low emissivity. This allows to retrieve carrier lifetime images with higher signal-to-noise ratio or in a shorter time. If fast measurements are necessary, e.g. for in-line application, the emission mode is an interesting option. Figure 2.17 (courtesy of [57]) shows a comparison of emission CDI measurements realised at different wafer temperatures (40 °C, 59 °C and 100 °C) with a measurement time of only 1 s. The $100 \times 100\,\text{mm}^2$ wafer had been etched to remove saw-damage and is SiN_x-passivated. The mean lifetime averaged over the whole wafer was about 18 μs. Noise dominates the measurement at low temperature

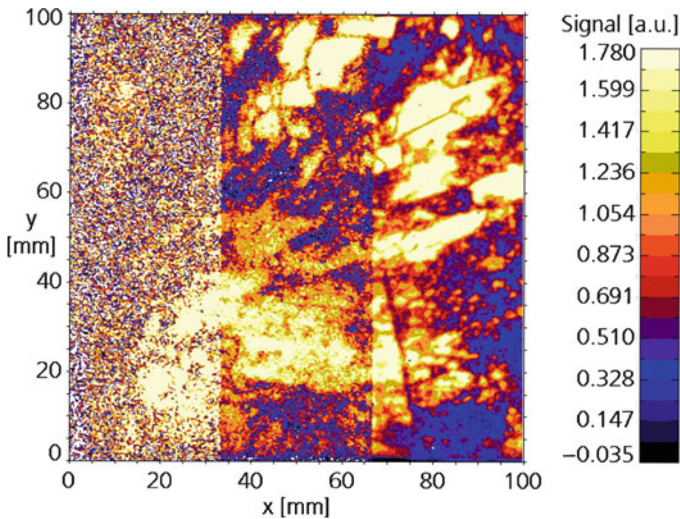

Fig. 2.17 Emission image of a multicrystalline sample with SiN_x-passivation at different wafer temperatures. From left to right: 40 °C, 59 °C, 100 °C. Measurement time was 1 s only

Table 2.1 Quantitative evaluation of the resolution improvement at enhanced temperatures. Over the same homogeneous lifetime area the standard deviation of the signal strength was calculated

Wafer Temperature T_w (°C)	Standard Deviation $\sigma/\sigma_{26°C}$
26	1
40	0.298
59	0.188
100	0.097

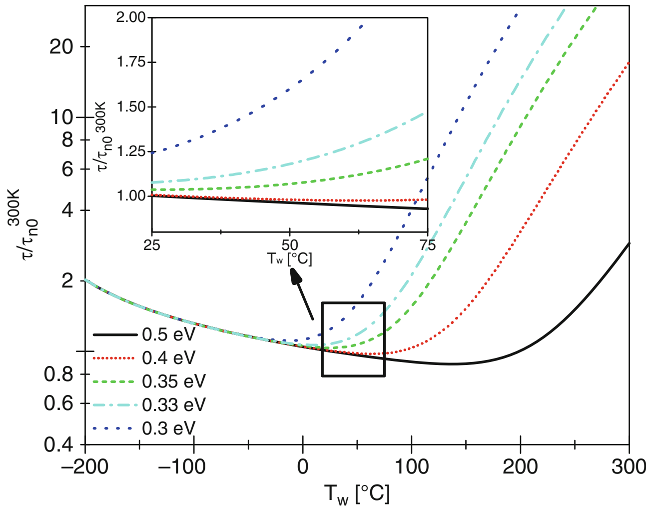

Fig. 2.18 Temperature dependence of minority carrier lifetime limited by Shockley-Read-Hall-recombination for different defect levels. Capture cross sections for electrons and holes are assumed to be equal. τ_{n0}^{300K} is the low injection lifetime for electrons at 300 K. The insert magnifies the most relevant part (*bold square*)

(40 °C), whereas a high signal to noise ratio can be achieved at wafer temperatures of 59 °C and 100 °C.

For a quantitative evaluation of the increase of resolution achieved by an increase of the sample temperature, the variation of the signal from an area of good lifetime was observed for different temperatures (Table 2.1, courtesy of [57]). Compared to the measurement at room temperature the standard deviation at 100 °C reduces to approximately 1/10, already at 60 °C a reduction of more than 1/5 is achieved.

For measurements in the emission mode we have to take into account that the temperature the wafer is heated to may at the same time influence the excess carrier lifetime, which we wish to determine. In Fig. 2.18 (courtesy of [57]) we exemplify the changes in carrier lifetime over the relevant temperature range for recombination limiting defects with defect energy level at various distance ΔE from the conduction or valance band edge calculated according to the Shockley-Read-Hall-recombination mechanism. For shallow defect levels the lifetime varies

significantly, whereas the temperature dependence for deep defect levels is weak in the temperature range under consideration (20–80 °C). Detrimental defects are mostly deep defects, so especially the lifetimes in low performance areas, which are of special interest for material qualification, may be determined at temperatures up to 80 °C and compared with some caution with lifetimes at ambient temperature. Please note in addition, that the temperature of solar cells in operating conditions are mostly above ambient temperature. The measurement of lifetime at these enhanced temperatures allows therefore a reasonable assessment of the expected solar cell performance.

Chapter 3
Experimental Technique

In Sect. 3.1, a number of thermography and lock-in thermography approaches from literature are described and discussed, both steady-state and non-steady-state, showing the large variety of thermography measurement possibilities. Many of these systems are not called thermography but rather thermo-AFM, or photothermal or thermo-elastic investigations. But, in principle, they are all designed to measure lateral surface temperature distributions, and can be used to investigate also electronic components. At the end of this chapter, the figures of merit of different lock-in thermography systems are compared in terms of the pixel-related system noise density, defined in Sect. 2.6. In Sect. 3.2 the design philosopies of different commercial lock-in thermography systems are compared and typical test measurements are introduced. Since many novel techniques for investigating solar cells are working with homogeneous irradiation of light, in Sect. 3.3 different systems for illuminating the sample are compared. In Sect. 3.4 the application of solid immersion lenses for improving the spatial resolution of lock-in thermography investigations is described. Finally, Sect. 3.5 introduces the special demands of the realization of different non-thermal carrier density imaging techniques, which also make use of the illumination systems described in Sect. 3.3.

3.1 Different (Lock-in) Thermography Realizations

In the following, we will consider only thermographic techniques which are at least potentially able to produce an image of electrically generated internal heat sources in electronic components. This rules out any photoacoustic and photothermal techniques which are solely based on measuring the local surface heating produced by a pulsed laser spot. Before infrared (IR) imaging techniques will be discussed, a number of alternative thermography techniques will be reviewed. The most straightforward way of measuring the temperature of a device is to attach a temperature sensor to the surface in contact mode. Therefore, contact thermography is one of the most popular serial thermography approaches. Of course, contact thermography can only be a serially measuring technique, since a large parallel working array of contact sensors is impracticable. Most of the contact thermography approaches in

the literature are microscopic techniques aiming at a spatial resolution of 1 μm or below. Therefore they belong to the category of thermal atomic force microscopy (Thermo-AFM) techniques. The two dominant basic principles of electronic temperature measurements, the thermocouple and the resistance thermometer, have both been used on a microscopic scale. So Williams and Wickramasinghe [58] produced a special AFM tip by separating a metallic coating from the conducting conical tip via an insulating layer. Only at the tip apex these two conductors were in contact producing a thermocouple of about 100 nm in size. This tip actually worked in the non-contact mode with a constant temperature difference between tip and sample. By piezo-modulating the height at around 1 kHz, the thermosignal showed a distance-dependent a.c. signal component, which was used to stabilize the height position. The aim of this development was to establish a non-contacting AFM technique for insulating and soft materials rather than to map surface temperature distributions. Majumdar et al. [59] produced a larger thermocouple between two dissimilar wires by a capacitive discharging and subsequent electrochemical thinning. In a contacting AFM arrangement, they imaged steady-state surface temperature profiles of a GaAs MESFET with a temperature resolution of $<$100 mK and a spatial resolution of a few microns. Also Foster and Gmelin [60] have used a concentric thermocouple tip similar to that in [58] in a variable temperature AFM set-up to investigate the thermal properties of thin films in contact mode. This setup, too, was not used to investigate electronic components. One general problem of thermocouple tips is that they produce a very small d.c. signal. As mentioned above, using lock-in thermography greatly improves not only the sensitivity but also the spatial resolution in thermal investigations. If the tip is in close contact to an electronic device in a lock-in measurement, it is very hard to suppress capacitive coupling between the device driving voltage and the thermal tip signal. This may be one major reason why thermocouple-based AFM systems have rarely been used for investigating electronic components until now.

Resistive thermometers may be loaded and read out with a sufficiently high frequency a.c. current, leading to several advantages in comparison to thermocouples: First, if the resistor read-out frequency and the lock-in one are sufficiently wide apart, a capacitive coupling of the driving voltage into the temperature reading can be avoided. Second, the a.c. principle of measuring the resistance avoids the influence of the so-called $1/f$ noise, which is the dominating noise source in all d.c. amplifiers. Therefore a.c. driven resistors may be read out considerably more sensitively than d.c. driven ones. Finally, at least semiconductor-based NTC (negative temperature coefficient) thermistors show a temperature coefficient ten times higher than metal resistors do, which also favours a higher temperature resolution. Hammiche et al. [61] formed an STM tip from a loop of so-called Wollaston wire. This is a 5 μm diameter platin/rhodium wire embedded in a 75 μm diameter silver wire. At the loop tip, the silver is etched away leaving the Pt/Rh core of 150 μm in length, which may be used both as a micro resistivity temperature probe and as a micro heater. This tip was made commercially available by ThermoMicroscopes and was a part of the Micro-Thermal Analyzer of TA Instruments. After these companies have become part of Veeco [62], Scanning Thermal Microscopy (SThM) using the

Wollaston wire probe is now available for the Nanoscale Thermal Analysis (nTA) mode of the VITA option of the Innova-SPM of Veeco [62]. However, these set-ups are actually intended more for micro-thermal analysis such as differential scanning calorimetry or thermal conductivity mapping on polymers than for investigating electronic components. Nevertheless, a scanning thermal microscope of the Wollaston type has also been used for imaging current-induced heating in microelectronic structures with sub-micron resolution [63, 64]. Since the Wollaston wire does not show a sharp tip, the spatial resolution of this SThM system is limited to a few 100 nm. SThM with sub-100 nm spatial resolution and $<0.1°C$ thermal resolution can be obtained by using a special microfabricated thermal probe, which was developed by Anasys Instruments [65]. Also this high-resolution SThM tip can be used in the VITA option of the Innova-SPM of VEECO [62]. Rangelow et al. [66] have published a thermal nano-probe based on a nanometer-sized filament, which was made by combining focused ion beam etching and a local electron beam deposition technique. The resistivity of this probe was read out in a 10 kHz a.c. bridge, realizing a thermal resolution of 1 mK. Similar to the system of Williams and Wickramasinghe [58], this system works in the non-contact mode with a constant temperature difference between sample and tip. It was used to measure the steady-state surface temperature distribution at the top of an implanted resistor with a spatial resolution below one micron. Although this tip is very fragile, and no details about necessary measurement times have been given up to now, this system also seems to be a promising thermo-AFM solutions for investigating electronic components. Its capabilities can even be improved considerably by using it in the lock-in thermography mode. Note, however, that all piezo-based thermo-AFM solutions imply one decisive problem: They hardly allow one to scan an image field much larger than $100 \times 100\,\mu m^2$. Thus, they usually do not allow one to scan a whole chip or even a larger component such as a solar cell.

In 1994 a macroscopic variant of this technique called Dynamic Precision Contact Thermography (DPCT [67]) was developed. Here a stepper-motor driven x-y-z table was used to scan a spring-loaded miniature thermistor point-by-point in contact mode across a macroscopic device like a solar cell. The spatial resolution of this system was only about 30 μm. The thermistor was read out very sensitively by a self-balancing a.c. bridge, and the two-phase correlation was performed by the computer after digitizing the temperature signal in four equidistant times per lock-in period. With this system, for the first time highly sensitive lock-in thermography investigations were performed at a lock-in frequency of 3 Hz. The thermal noise level, referred to the sample surface, was below 100 μK T-modulation amplitude at an integration time of 1 s per pixel, which was record-breaking at that time [68]. Thus, this system also allowed for the first time to investigate weak shunts in solar cells under forward bias. However, due to the serially measuring principle, the measurement time could not be reduced below several hours per image. Therefore this system has not gained wider popularity and was later replaced by an IR camera based system.

Besides the use of thermocouples and resistance thermometers there are a number of non-contacting techniques to measure surface temperature distributions. One

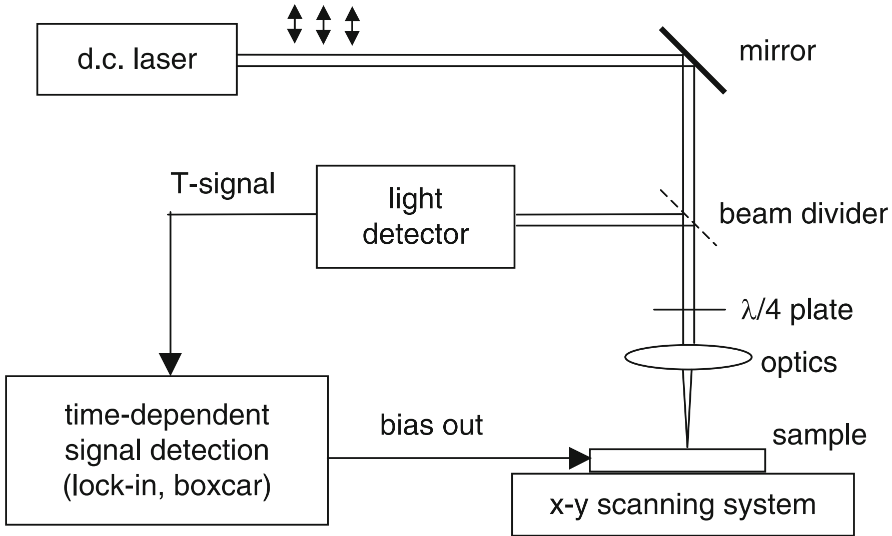

Fig. 3.1 Thermoreflectance measurement set-up for detecting internal heat sources

popular approach is the photothermal or thermoreflectance principle. It is based on the fact that the optical reflection coefficient of a reflecting surface is usually temperature-dependent. Typical temperature coefficients of the reflectivity of metals and semiconductors in the visible range are of the order of 10^{-5}–10^{-4}/K. For a well-defined reflecting surface, the intensity of a reflected laser beam is a measure of the surface temperature. As Fig. 3.1 shows, a typical thermoreflectance experiment on an electronic device comprises a d.c. laser producing a linearly polarized beam, a microscope objective, a beam splitter (usually combined with a $\lambda/4$ plate) for separating the incident and the reflected beam, and a mechanical scanning system. For example, Ju et al. [69] have measured temperature transients with an accuracy of 0.1 K and a spatial resolution of 0.6 μm in different positions of MOS transistors after pulsed biasing. Using a computer-controlled sample scanning system, Voigt et al. [70] performed lock-in thermoreflectance imaging at a modulation frequency of up to 30 kHz on electrically heated microconductors. Sensitivity limits have not been given here explicitly, but the power these structures dissipated was as high as 2 W. A very interesting "stroboscopic" camera-based photothermal imaging system for investigating high-frequency phenomena has been introduced by Grauby et al. [34]. They imaged the local reflectance of the sample surface by using a standard CCD camera operating at a frame rate of 40 Hz. Contrary to Fig. 3.1, however, not a d.c. light source was used for the illumination but an LED, which was amplitude-modulated at a frequency of (2 MHz + 10 Hz). The sample structures were electrically loaded to produce a surface temperature modulation of 2 MHz. Then the reflected optical signal is amplitude-modulated with the difference frequency of 10 Hz due to the heterodyne principle. With the given frame rate of 40 Hz, two-channel lock-in thermography with 4-point correlation has been

performed, yielding amplitude and phase images as described in Chap. 2. Note that this heterodyne technique uses a principle for expanding the time resolution over that given by the frame rate, which is similar to that of the undersampling technique described in Sect. 2.4. Resistive and Peltier heating could clearly be distinguished from each other by their different modulation frequency and their different signal dependence on the driving voltage amplitude (resistive: square dependence; Peltier: linear dependence). The spatial resolution of this system was below 1 μm, but the temperature resolution was obviously only of the order of 0.1–1 K. The spatial resolution of thermoreflectance investigations has been improved to below 50 nm by Goodson and Ashegi [71] by illuminating the sample with a scanning near-field optical microscope (SNOM). However, in this SNOM technique the illuminating light power was limited to some nW, and only a very small fraction of the reflected light could be detected. Therefore typical detected temperature modulation amplitudes were of the order of 50 K, hence the sensitivity of this technique was obviously only of the order of a few Kelvin. The general advantage of photoreflectance methods over the IR detection is its lower price and the possibility to attain a sub-micron spatial resolution. However, photoreflectance needs a well-reflecting plane surface. It can hardly be used e.g. for investigating textured solar cells or 3-D structures. Moreover, the temperature resolution of typically 0.1 K restricts its use for device testing to medium and high-power devices. There are some other techniques related to thermoreflectance such as off-axis thermoelastic deformation measurements (Opsal et al. [72]), optical beam deflection with striking incidence using the mirage effect (Murphy and Aamodt [73]), or photothermal displacement interferometry (Suemune et al. [74]). According to the knowledge of the authors, however, these techniques have been developed and used primarily for investigating thermal diffusion phenomena on layered structures rather than for imaging heat sources in electronic devices. Some of these techniques are only practicable for flat surfaces and cannot be used, e.g., for texturized solar cells or ICs with a surface topography.

Besides IR thermography and photothermal techniques, there are three other camera-based thermography techniques based on visible light microscopy and two based on near IR microscopy, which are widely used in electronic device testing and failure analysis. These are thermal mapping using nematic or thermochromic liquid crystals, fluorescent microthermal imaging (FMI), Moiré imaging, and Schlieren imaging. Nematic liquid crystals show a phase transition between liquid and liquid crystalline, which may be as sharp as 0.1 K. If a sample, covered with a thin liquid crystal layer, is illuminated with polarized light and imaged through a crossed polarizer, it appears dark above the phase transition temperature and bright below that temperature. By carefully adjusting the sample temperature just below the transition temperature, only the regions around local heat sources may appear dark. Within a certain temperature range of thermochromic liquid crystals their spectral reflectivity depends on the temperature. Thus, when illuminated with white light, their colour depends on the temperature. The sensitivity limit of nematic liquid crystal investigations is about 0.1 K, but that of thermochromic ones is even worse. Both techniques are commercially available [75]. Note that working with liquid crystals is somewhat tricky and requires a lot of experience. Especially for investigating ICs it is hard

to guarantee a complete and homogeneous wetting of the surface. This holds especially near wire bonds, since owing to capillary forces, the liquid tends to crawl up the bond wires. Recently, an interesting new technique has been introduced where micron-sized cholestric (thermochromic) liquid crystals droplet are dispersed in a polymer foil, which is loosely attached to the sample [76]. This technique has the advantage that it does not pollute the sample. However, due to the thickness of the polymer films of several 100 μm this method is only applicable to large plane samples such as solar cells, but not to ICs. Based on this principle, a "Shuntometer" for imaging strong shunts in solar cells under reverse bias with a spatial resolution of some millimeters is available [77].

Fluorescent Microthermal Imaging (FMI) investigations are based on the strong temperature dependence of certain organic dyes. A thin dye layer is applied to the surface under investigation and homogeneously illuminated by UV light. Near local heat sources, the luminescence is quenched. Hot spots are revealed by subtracting or dividing two luminescence images, with the heat sources switched on and off. Using a slow-scan CCD camera with 40 s total exposure time and an image of effectively 50×50 points, Kolodner and Tyson achieved a thermal resolution of 10 mK at a spatial resolution of 15 μm [41]. These data allow one to calculate the pixel-related system noise density, defined in (2.31) of Sect. 2.6 to be $N_{sys} = 1.26\,\mathrm{mK}\sqrt{\mathrm{s}}$ for this measurement. FMI can easily be realized with a fluorescence microscope and a sensitive CCD camera (usually cooled slow-scan CCD cameras are used) and is widely used in semiconductor research. Although especially FMI has established itself as a standard technique in IC testing, also its thermal resolution is not yet sufficient for imaging weak heat sources in the μW range, which may produce temperature contrasts well below 1 mK in silicon components (see Sect. 6.1). This has recently been improved by performing FMI in lock-in mode also [78, 79]. By this measure both the spatial resolution and the detection limit of FMI considerably improve. However, according to the experience of the authors, the detection limit of lock-in FMI is still about an order of magnitude worse than that of lock-in IR-thermography under comparable conditions. In [79] the name "Stabilized FMI" has been used for single phase (0°) lock-in FMI.

Another relatively simple thermography technique is Moiré thermal imaging. This technique is performed for backside imaging of integrated circuits (ICs) under non-coherent laser light illumination at about 1064 or 1400 nm. At this wavelength the silicon substrate is essentially transparent. Since the polished backside of the IC is never exactly parallel to the front plane (it may be prepared even deliberately at a certain angle to the front plane), the monochromatic illumination generates a pattern of interference fringes (so-called Moiré pattern) at the surface. If a local heat source is present, the dimensions of the sample slightly vary, leading to a lateral movement of the Moiré pattern. If the heat source is modulated and the Moiré pattern is lock-in correlated, the local amplitude signal is a measure of the locally dissipated power density. This technique was called "Moiré Stabilized Thermal Imaging" [79]. The sensitivity of this technique is about a factor of 5 worse than that of lock-in FMI and the spatial resolution is only in the order of the sample thickness. Nevertheless, it

allows the localization of stronger local heat sources and the identification of entire array blocks with low power consumption [79].

Schlieren thermal mapping uses the angular deviation of a near-IR beam (1060 nm) caused by local heating [80]. This investigation is usually performed from the back side of an IC. Topside Schlieren imaging requires a suitable coating. For the OptoMetrix Schlieren thermal mapper a spatial resolution below 1 μm and a thermal resolution better than 10 mK have been reported [80].

It should be noted that two other very successful optical imaging technique for IC testing are photon emission microscopy in the visible and near IR range and thermal laser stimulation techniques. Light emission microscopy is also commercially available e.g. from Hamamatsu [20]. With this technique it is possible to visualize internal breakdowns in the semiconductor components due to electrostatic discharge (ESD) failure, leakage, hot carrier generation, and latch-up effects. However, purely resistive heat sources such as short circuits in metallizations usually cannot be imaged. Also defects below metallization layers remain invisible in emission microscopy, unless it is performed upside down by looking "through the chip". Moreover, the light emission dramatically drops with decreasing supply voltage of the components, since this emission is based on high field phenomena. Hence, highly sensitive microscopic lock-in thermography may reveal more phenomena than emission microscopy does, but it does not have the spatial and temporal resolution of emission microscopy. Therefore, microscopic lock-in thermography may be at least a valuable supplement to photon emission microscopy. For investigating components having low supply voltages, where emission microscopy more and more fails, lock-in thermography may be substituted for emission microscopy for IC testing.

Thermal laser stimulation techniques like OBIRCH (Optical Beam Induced Resistance Change [81]) and TIVA (Thermally Induced Voltage Analysis [82]) are based on the temperature coefficient of any kind of leakage current in an IC. Hence, the supply current or the supply voltage (at constant current) of an IC is monitored, and the active region is scanned by a focused laser beam of up to 100 mW power. In order to avoid optical absorption, a wavelength of about 1360 nm is used, which also allows to perform this investigation from the back side of the sample. As soon as the laser beam hits a leakage site, the detected current or voltage signal changes, which allows one to image these leakage sites. OBIRCH and TIVA can also be used in lock-in mode, which improves their detection sensitivity [83, 84].

Note that (lock-in) thermography and thermal laser stimulation techniques are imaging the same type of defects. In both the cases a resistance-limited current of a certain magnitude, which also generates a certain local heating power, can be imaged. If a current flows through a low-ohmic line, it can be imaged neither by lock-in thermography nor by laser stimulation techniques. Systematic differences of the detectability of different defects by lock-in thermography and laser stimulation techniques will be discussed at the end of Sect. 6.1.

Infrared (IR) thermography can be applied as a serially scanning measurement and using an IR camera. The first commercial system for thermo-elastic imaging (vibrothermography) was a serially measuring system, where a slow mirror scanner

was used to scan the image point by point during the whole investigation (SPATE 8000/9000 [7]). The minimum spatial resolution was about 0.5 mm. The IR light was detected by a sensitive IR detector, and a commercial two-channel analog lock-in amplifier (SPATE 9000) was used to perform the lock-in correlation. The output of the lock-in amplifier was digitized and processed to obtain both the amplitude and phase images. The minimum necessary measurement time for imaging a 100×100 pixel field was 1000 s (17 min) assuming the use of only one 10 Hz-period per image point, resulting in a thermal resolution of the order of 0.1 K. In a real thermomechanical measurement, however, averaging over many periods is necessary to obtain a satisfactory signal-to-noise ratio, hence real measurement times of this system are many hours. Thus, for the SPATE technique, a pixel-related system noise density of the order of 10 mK$\sqrt{}$s according to (2.31) can be estimated. Breitenstein et al. [85] also performed serial lock-in thermography on leakage currents of solar cells, using a mechanical x-y drive with a spatial resolution of 0.1 mm and a single liquid-nitrogen cooled MCT detector equipped with germanium optics. With a lock-in frequency of 3 Hz and averaging over 5 periods per position, the measurement time of 100×100 pixel per image was 5.5 hrs and the noise level was about 2 mK. This corresponds to a system noise density of about 2.8 mK$\sqrt{}$s. The improved sensitivity compared to the SPATE system was essentially due to the larger numerical aperture provided by the IR optics used in the latter investigation. Fletcher et al. [86, 87] have introduced a SNOM-type serially scanning IR microscope, which also might be used for electronic device testing. Using a microfabricated solid immersion lens with a numerical aperture of 2.5, they attained a focused spot size of $\Lambda/5$ for $\Lambda = 9.3\ \mu$m IR light. However, no data as to the thermal resolution have been cited.

The classical technique of the thermographic inspection of electronic devices is to use an infrared (IR) camera as described in Sect. 2.1. Standard (steady-state) IR thermography is the method of choice to detect, for instance, critical hot components within extended electronic equipments (ICs, line regulators, etc.), which may limit the long-term reliability of these equipments [88]. But also within single components thermography can be used to detect "hot spots", which mark the location of leakage currents. Thus, Simo and Martinuzzi [89] have imaged hot spots in heavily dislocated regions of multicrystalline silicon solar cells. Although their pixel resolution was well below 1 mm, their real spatial resolution was only in the range of several mm due to the large lateral heat conductivity of silicon. Also their sensitivity of about 0.1 K did not suffice to detect hot spots under forward bias conditions. Only after applying >10 V reverse bias, leakage sites were detected. Kaminski et al. [30] have averaged 1000 images of silicon solar cells under forward bias and have subtracted the average over 1000 images without applied bias, thereby reducing the statistical noise and subtracting the topography contrast in the thermograms. Using this static averaging and topography subtraction technique, they improved their thermal sensitivity to below 10 mK, which was sufficient to image strong shunts under forward bias conditions. However, also their images showed a strong degradation of the effective spatial resolution due to lateral heat spreading. The same holds for the very low frequency (0.05 Hz) lock-in thermography approach of Rappich et al. [90]. Gross et al. [9] thermographically imaged shunts at interconnects of thin-film

solar cells also under forward bias conditions using a PtSi FPA camera with a spatial resolution well below 100 μm. Note, however, that these solar cells are made on glass substrates, which show a weak heat conductivity. Thus, here the thermal contrasts are considerably stronger and better localized than in silicon components. For investigating integrated circuits (ICs) commercial IR microscopes are available, for instance at Hamamatsu [20] and Quantumfocus Instruments [91]. The latter system also provides emissivity correction (see Sect. 5.3) as well as time resolved measurements for a bandwidth of 250 kHz. However, the temperature resolution of both systems is only 0.1 K, since both do not yet use any signal averaging techniques. Hence, the application of these systems is restricted to medium and high-power devices, which produce surface temperature contrasts well above 0.1 K. Recently, Hamamatsu has launched the new "THEMOS mini" system, which also provides real two-phase lock-in thermography (see Sect. 3.2). Note that, for investigating microscopic heat sources in ICs, usually 3-dimensional heat diffusion has to be considered since these heat sources have small sizes. Therefore, even if a low lock-in frequency or even steady-state imaging is used, the spatial resolution for investigating ICs may be significantly better than for investigating solar cells (see Chap. 4).

Lock-in thermography in the sense described in Sect. 2.3 was proposed already by Carlomagno et al. [92], but it could not be realized yet at that time. The first camera-based lock-in thermography realization was described by Beaudoin et al. [93]. Here the lock-in correlation occurred off-line, hence after the measurement, on saved images of only 4 measured lock-in periods. According to the knowledge of the authors, Kuo et al. [4] have published first details of an IR-camera based lock-in thermography system with on-line image correlation. In this system, two commercial digital graphics processors in a VME bus workstation are used for digitizing and processing the output of a mirror scanner IR camera. The camera was running in interlaced mode at a full frame rate of 30 Hz. A fixed lock-in frequency of 15 Hz was chosen, always two successive frames were subtracted from each other, and the difference was summed up in the video processor boards. This procedure was performed separately with the two half-frames in the two image processors. Since the two half-frames are time separated from each other by 1/60 s, corresponding to a phase difference of 90° for $f_{\text{lock-in}} = 15\,\text{Hz}$, the processed results of the two half-frames correspond to the in-phase (0°) and the quadrature (90°) signal. Hence, this procedure is equivalent to the 4-point correlation procedure described in Sect. 2.2. In fact, this was the first IR camera-based lock-in thermography system employing the two-phase on-line image correlation. This system was used for imaging current-induced heating in thin copper films evaporated on a Kapton foil forming a resistive microbridge. Hence, this was also the first application of lock-in thermography to electronic device testing. No sensitivity values have explicitly been cited, but the expected $1/\sqrt{t_{\text{acq}}}$ dependence of the noise voltage has been demonstrated.

The first commercial IR-camera based lock-in thermography system was a lock-in option to the AGEMA Thermovision 900 mirror scanner thermocamera, which was developed on the basis of the work by Busse et al. [94,95]. This camera worked in the long-range with a frame rate of 15 Hz at a resolution of 272 × 136 pixels. The lock-in correlation occurred off-line in this system, hence all frames of

a measurement were captured and stored in the computer. After the measurement the correlation was performed with the "4-bucket" method (see Sect. 2.2). The maximum possible number of stored frames was 1000, corresponding to a maximum possible data acquisition time of roughly one minute. After this time, the amplitude noise level of this system was of the order of 15 mK [85]. According to (2.31) this corresponds to a system noise density of $N_{sys} = 0.63\,mK\sqrt{s}$. Note, however, that this noise density does not yet take into account the off-line data evaluation time, which was even longer than the actual measurement time for this system. This system, which was a synchronously working system in the sense discussed in Fig. 2.7, was used primarily for non-destructive testing purposes, but also electronic devices have been tested [96]. It is no longer available. Meanwhile, AGEMA have moved to FLIR systems [21]. An off-line working lock-in thermography system (IrNDT-LockIn), which is similar to the AGEMA one but based on a special multifunctional frame grabber board and equipped with additional analytic functions, is available at Automation Technology [22]. Now this company is also offering a system implying on-line correlation (see Sect. 3.2).

The first commercial lock-in thermography system based on a highly sensitive focal plane array camera and on the on-line sin/cos correlation was the ALTAIR LI system developed by CEDIP [17]. This originally French company is now also part of FLIR systems [21]. The frame capturing and lock-in correlation are performed by a special frame grabber board and a DSP (digital signal processor) board, which were both developed by CEDIP. This system was designed for the asynchronous correlation, since it was developed for thermomechanic (vibrothermography) investigations. As has been discussed in Sect. 2.4, the asynchronous correlation has the advantage that without any modifications the lock-in frequency may be higher than the frame rate (asynchronous undersampling). However, it has the disadvantage that phase jitter and an incomplete number of acquired lock-in periods may induce additional noise. Therefore, the DSP software of the CEDIP system was designed to subtract the mean level of the signal before the correlation procedure, which reduces this additional noise. On the other hand, this subtraction introduces another numerical step in the on-line correlation procedure, which limits the processing speed of the DSP. The first system of this type worked with a 128×128 pixel resolution, but meanwhile systems offering 320×256 pixels are available both for the long range and for the mid range. For the latter system, a noise level of 1 mK peak-peak was reported after an acquisition time of 200 s [17]. According to (2.31), these data correspond to a pixel-related system noise density of about $51\,\mu K\sqrt{s}$, which is an improvement by a factor of 12 compared to the Agema 900 system. A similar system with a similar technical concept for different resolutions is also available from Stress Photonics [18]. Their presently highest resolution version DeltaTherm 1550 has also got a spatial resolution of 320×256 pixels, reaching a full-field thermal resolution of 2 mK after 30 s of acquisition time, corresponding to a noise density of $38\,\mu K\sqrt{s}$.

Since 1992 shunting phenomena in solar cells have been investigated at the Max Planck Institute of Microstructure Physics in Halle (Germany). Right from the beginning, thermal methods have been considered to detect local shunts, but the temperature sensitivity of conventional IR cameras turned out to be clearly

insufficient for this purpose. Note that a solar cell in operation is forward-biased to about 0.5 V (see Sect. 6.2). In order to detect local sites of increased forward current, which are usually called "shunts" even if they are no real short circuits, a bias of only 0.5 V has to be applied to simulate real operation conditions. Shunt currents below 1 mA, already interesting to investigate, produce a local heating in the 100 μW range, which cause a local heating in the range of 100 μK (see Sect. 4.3). The first system allowing to image temperature modulations below 100 μK was the Dynamic Precision Contact Thermography (DPCT), which was a serially measuring system [67]. Hence, for attaining this thermal resolution, for 100 × 100 pixels a measurement time above 5 hrs was necessary, corresponding to a system noise density of 0.082 mK$\sqrt{}$s. Since 1997, an IR camera based lock-in thermography system was being developed at MPI Halle, which was straightforwardly designed to reach an ultimate thermal sensitivity. With a 128 × 128 pixel resolution, its noise level of 0.03 mK after an acquisition time of 1000 s corresponded to a system noise density of 7 μK$\sqrt{}$s. This was also the first system to demonstrate the advantages of microscopic lock-in thermography for integrated circuit testing down to a spatial resolution of 5 μm [97]. Based on this development, Thermosensorik GmbH Erlangen has developed the commercial system TDL 384 M 'Lock-in' [19, 78]. With a resolution of 384 × 288 pixel and a noise level of 0.072 mK after an acquisition time of 1000 s (corresponding to a system noise density of 7 μK$\sqrt{}$s), this system was the highest sensitive commercial lock-in thermography system with the highest resolution at that time. This system was especially designed to meet the demands of diagnostics and failure analysis of electronic components. Meanwhile also systems implying a 256×256 pixel high speed MCT camera (TDL 256 HS) as well as implying a 640 × 512 pixel InSb detector (TDL 640 SM) are available. In the following section, the design philosophy of these systems will be compared with that of other commercially available lock-in thermography systems. Table 3.1 summarizes the major technical data of several lock-in thermography systems, of which the pixel-related system noise densities are known. For comparison, also the corresponding data of steady-state Fluorescent Microthermal Imaging (FMI) from [41] are given, which before the advent of IR-based lock-in thermography systems was the most

Table 3.1 Technical data of different lock-in thermography systems in comparison with FMI

System	Resolution (pixel)	Noise level (mK)	Acquisition time (s)	Noise density (mK$\sqrt{}$s)	Reference
SPATE 9000	100 × 100	100	1000	31	[7]
Agema 900	272 × 137	15	66	0.63	[85]
CEDIP	320 × 240	1	200	0.051	[17]
DeltaTherm 1550	320 × 256	2	30	0.038	[18]
DPCT	100 × 100	0.058	20,000	0.092	[68]
MPI Halle	128 × 128	0.03	1000	0.007	[97]
TDL 384 M	384 × 288	0.072	1000	0.007	[78]
TDL 640 SM	640 × 512	0.092	1000	0.005	this work
TDL 256 HS	256 × 256	0.2	0.9	0.0008	[98]
FMI (steady-state)	50 × 50	10	40	1.26	[41]

sensitive thermal technique of investigating electronic devices. The exceptionally good pixel-related noise density of the TDL 256 HS system is due to two factors: (1) The detector works in "integrate-while-read" mode and the readout circuit is so fast that the camera is integrating photons for more than 80% of the acquisition time. (2) The detector pixels are with $40 \times 40\,\mu$m exceptionally large, hence they are able to collect many photons. On the other hand, the latter property makes this camera less appropriate for microscopic failure analysis on ICs, since here a very high magnification microscope objective would be necessary to obtain a good spatial resolution. However, for microscopic imaging, the brightness of the image inherently reduces with the square of the magnification factor (see Sect. 3.4), hence the advantage of good sensitivity will get lost. It is obvious that the sensitivity of the most sensitive IR-camera based lock-in thermography systems compared to FMI is improved by a factor of 250! This demonstrates the enormous gain in information that can be expected if FMI is replaced by IR lock-in thermography.

3.2 Commercial Lock-in Thermography Systems

In this section the design philosophies of different commercial lock-in thermography systems will be compared and related to their different application fields. It was already mentioned in the earlier section that the first commercial lock-in thermography systems were introduced by AGEMA and CEDIP. The AGEMA system was designed for performing photothermal investigations, hence to investigate the temperature modulation of a surface under the influence of modulated irradiation of light. If there are sub-surface defects in the material, the surface temperature modulation is locally disturbed, which allows to detect such defects [2]. The system allowed to generate a programmable analog waveform synchroneous to the lock-in correlation, which enabled the user to generate a sin-shaped light intensity modulation. As mentioned before, the system was operating synchroneously, hence the lock-in trigger was derived from the frame trigger of the free-running IR camera, and 4-bucket correlation was performed off-line after all images were stored. This has limited the maximum number of evaluated frames to 1000. This system is not available anymore, but several other lock-in thermography systems being specialized to NDT have followed the tradition of this development, like that of Automation Technology [22] and edevis [23]. They are all now based on modern FPA thermocameras, they can be used both for lock-in and pulse thermography, and they can apply different stimulation means like halogen lamps, flash lamps, laser, ultrasonic, eddy current, or mechanical excitation. The correlation type may be synchroneous or asynchroneous at choice, and the correlation may be performed on-line or off-line. However, these systems are not primarily designed for the investigation of electronic components. Of course, here also it is no problem to use an externally controlled power supply as a stimulation mean for applying a pulsed bias to an electronic device. However, e.g. reading back the flowing current, which is a decisive parameter to be measured in electronic device testing, is generally not implemented in the software. Generally, NDT systems are meant for macroscopic investigations,

hence microscope objectives are usually not provided. The use of solid immersion lenses for improving the spatial resolution (see Sect. 3.4) is not even meaningful if other excitation means than internal electric heating are applied. The systems of Automation Technology are now also offered by moviTHERM [28].

The CEDIP Altair-LI system, which is still available from FLIR [21], was the first commercial lock-in thermography system with two-phase on-line lock-in correlation. It was designed especially for thermoelastic investigations. A similar system, also specialized to thermoelastic investigations, is available by StressPhotonics [18]. Here a mechanical device is stressed periodically from compression to expansion in a special deformation machine. Similar to a compressed and expanded gas, in regions of strain, the solid material gets periodically heated and cooled, which is the so-called thermoelastic effect [2]. Hence, lock-in thermography allows to image the local strain rate in the device quantitatively and, for higher deformation amplitudes, also plastic deformation regions. Since, at least in the early days of these investigations, the deformation machines were freely running, the CEDIP system was designed consequently for asynchroneous correlation. Hence, the IR camera is also freely running at its own frame rate and the deformation machine (or any other signal generation means) has to provide a TTL or analog trigger signal which is synchroneous to the expected T-modulation. As described in Sect. 2.5, the system detects in each period the phase of the modulation trigger with respect to the periods of the IR camera and selects the correct values of the correlation vectors from a look-up table. Since for asynchroneous correlation, especially for a small number of lock-in periods, the sum of all weighting factors may be not exactly zero, the d.c. value of the IR-images is generally subtracted before correlation for avoiding additional noise contributions [29]. This system easily allows to operate in the (asynchroneous) undersampling mode, hence the modulation frequency is allowed to be above the frame rate of the camera. However, it has to be avoided to use "forbidden" frequencies (multiples of the Nyquist frequency) as well as, if the excitation contains higher harmonics, aliasing collisions (see Sect. 2.5). In the CEDIP Altair system, the IR camera is connected with a special hardware box (embedded into the camera itself in the newest version), which contains a frame grabber and a separate Digital Signal Processor (DSP) system. The actual lock-in correlation procedure of the image data is performed by this DSP system and only the final results are transmitted to the host PC where the Altair-LI software is running. This philosophy avoids the problems of processing fast continuous data streams, which have been inherent to earlier Windows versions running on computers about 10 years ago. The actual CEDIP Altair-LI software is specialized to stress measurement applications and allows processing periodic and non-periodic (random) mechanical loading. However, CEDIP (now FLIR) offers a developer-kit based on C^{++} under Windows, which allows the user to write his own lock-in thermography application. The NDT systems of Automation Technology and edevis as well as the AescuSoft system (see below) were originally developed based on the CEDIP developer kit.

The first commercial lock-in thermography system, which was consequently specialized to functional diagnostics of electronic components, was the TDL 384 M 'Lock-in' system by Thermosensorik [19] introduced in 2000. Here TDL stands

Fig. 3.2 The Thermosensorik TDL 640 SM 'Lock-in' system

for "Thermosensoric Defect Localization", 384 is the x-resolution in pixels (meanwhile higher resolutions are available), and M means "midwave". This system was developed using the experiences made at the construction of the DSP-based lock-in thermography system at Max Planck Institute in Halle, Germany [97]. In its standard configuration, the camera is mounted on a stable vertical pillar, looking down with variable distance to the sample (see Fig. 3.2). By using a number of wide-angle and microscope-type IR-objectives, this construction allows to apply the system both for microscopic (IC analysis) and macroscopic (e.g. solar cell) applications. Of course, for imaging even larger objects like solar modules, the camera can be mounted horizontally also. Despite being a highly sensitive thermography system, as a lock-in system it does not need a housing. Nevertheless, a housing also implying illumination means is available. The Thermosensorik systems are not based on complete IR-cameras, which contain their own two-point calibration system and can be operated also without a computer. Instead, only the basic camera modules are contained in the camera housing and the two-point calibration and bad pixel correction are

performed by a connected PC under Windows. Also the lock-in correlation procedure is performed under Windows by the PC and not by a separate DSP system. This is a very economic solution, but its programming is very demanding if numeric errors should be avoided. Note that Windows is internally organizing the timing of its own jobs, it is no real time system. Therefore, for this video-type application there is always the danger to loose one or a few images for the correlation. It was explained in Sects. 2.2 and 2.5 that it is essential for the lock-in correlation procedure that the total sum of all correlation coefficients is zero, assuming that all measurement values are present. If one image should be lost, this is equivalent to setting one correlation coefficient to zero, so their total sum is not zero anymore. If this happens, the primary lock-in thermography images (0°- and −90°-image) contain residues of the topography signal. Hence, if single images are lost for the correlation, the perfect d.c.-suppression property of the synchroneous lock-in correlation procedure gets lost. By applying special proprietary means this can be avoided in the Thermosensorik systems also under Microsoft Windows operation. Since the heat generation in semiconductor devices can easily be controlled externally by applying appropriate bias signals, the Thermosensorik systems are generally applying synchroneous correlation, hence the lock-in trigger is derived from the frame trigger of the camera by a frequency divider. As it was discussed in Sect. 2.5, this operation mode ensures optimum d.c.-suppression and minimum noise, but it does not enable to expand the lock-in frequency range above $f_{\text{frame}}/4$ by using undersampling. Undersampling is available also for these systems as a special option, which uses external IR camera triggering (see Sect. 2.5). As the user surface of present Thermosensorik lock-in thermography systems shows (Fig. 3.3), the application of a pulsed bias is integral part of the system (see "Voltage 2", bottom

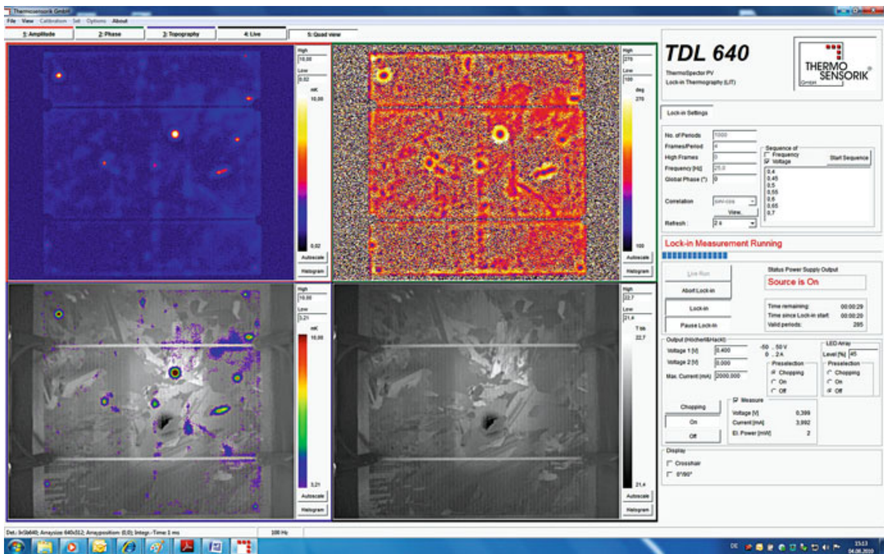

Fig. 3.3 User surface of the Thermosensorik lock-in thermography systems

right region). Depending on the intended application (IC failure analysis, solar cell research, CDI/ILM, solar module investigations, NDT), the system may work with different types of power supplies or other signal generation means such as LED arrays or lasers, which may be controlled by a TTL trigger. For modulation, the sample bias may be switched between on and off (square wave modulation, 100% degree of modulation), or a constant bias may be square-modulated by a certain amount without switching the bias completely off, which is often necessary for IC failure analysis. The bias in the "off" phase can be set in the "Voltage 1" field. Sinusoidal bias modulation is also provided in this software. However, for testing electronic components it is not useful (see Sect. 2.5). An important feature is that the real bias and current values, which are always read by the power supply directly at the sample by using a 4-wire connection at the beginning of each measurement, are displayed in addition to the set voltage and current limit and the polarity settings (see bottom right corner in Fig. 3.3). This display is essential, since the applied voltage and the flowing current are two dominant experimental parameters in electronic device testing. Only by this reading, the operator is informed what really happens with the device, and unintended opens or shorts in the current path to the device or overloading can easily be recognized. The alternative Chopping "ON" and "OFF" buttons at the bottom allow to apply the bias (pulses) to the sample already before the lock-in measurement starts. This allows to prevent the initial heating-up phase at the beginning of a lock-in measurement, see Sect. 4.1. Alternatively, there is the option to include the temperature drift compensation according to Sect. 4.2. The Thermosensorik systems also imply a quick current-voltage (I-V) measurement option for easily finding out the optimum bias setting for the lock-in measurement. The user surface shown in Fig. 3.3 is widely self-explaining and abandons extra windows for performing the lock-in measurement. In the LockIn-Settings the number of frames per period and the resulting lock-in frequency (which can be set also explicitely), the number of lock-in periods to sum up (leading to a certain acquisition time, which is indicated under "time remaining"), the global phase setting, the correlation type (sin/-cos as standard, also sin/cos and square/triangle is possible), and the image refresh time. The global phase setting allows one to correct for any unintended delays between the lock-in pulse-trigger and the photon detection periods of the IR camera. Note that according to Sect. 2.2 (2.10) the lock-in evaluation process assumes that the photon detection period of the first image evaluated in each lock-in period is centered exactly at $t = 0$, where the heating power switches on (cf. also Fig. 2.6 in Sect. 2.3). In reality, due to inevitable delays in the camera control circuits, this is usually not the case. Hence, especially for high lock-in frequencies, where such delays become important, the calculated 0°- and the −90°-image according to (2.4) and (2.10) are not exactly these images but contain a certain phase error. This systematic phase error, as well as additional phase errors caused e.g. by using a black paint on the sample for homogenizing its emissivity, can be corrected by the global phase setting. By applying (2.9) from Sect. 2.2, the system corrects the phase of the results so that the displayed image A is exactly the 0°-image and the image B is exactly the −90°-image. How to find the correct value for the global phase setting will be described in Sect. 5.1. After a lock-in

measurement, the Thermosensorik systems are storing and saving only the topography image and the two primary lock-in images measured by applying (2.4) and (2.10) as floating point data arrays. From the latter, all possible lock-in images, such as the (phase-corrected) 0°- and −90°-image (here called image A and B), the amplitude image, and the phase image, are generated for display. By checking the "0°/− 90°" box, instead of the phase image the 0°/− 90°-image can be displayed (see Sects. 4.5 and 5.1). Four images (e.g. amplitude, phase, overlay of topography and amplitude, and live image) are displayed in full resolution or one of the four images in 2-fold magnification. In the "View" menu it can be selected whether the A or B images (0° and −90° images) or the amplitude and phase (or 0°/−90°) images are displayed. The images can also be zoomed and different colour palettes can be chosen. The scaling means beside the images allow to scale all images separately, which can be done either manually, by using a histogram, or automatically. Either the amplitude or the phase image (or alternatively image A or B or the 0°/−90° image) may be superimposed to the topography image, which is called here "Overlay". In the "Calibration" menu the 2-point calibration for different imaging conditions can be performed and administrated. Alternatively, in any "life" mode also a quick possibility to perform this calibration e.g. by using the lab temperature (objective cap) and the temperature of the palm of the hand is provided. In the "Set" menu the frame mode of the camera (full frame or different sub-frame modes), the image integration time, and different other camera parameters may be set. The four bottoms right of the images allow to choose the life imaging mode of the camera, to start or pause a lock-in measurement, and to abort it. Aborting a measurement is equivalent to finishing a measurement after the programmed time, hence the lock-in data gained up to this moment are ready for display. The field in the rightmost upper part of the user surface allows to define a number of lock-in frequencies or voltages, which are used in a batch measurement. Hence, by pressing "Start Sequence" a number of lock-in measurements with different parameters as defined in the parameter list are performed and saved as different files with the parameter values appended to the file name. As a typical noise measurement, Fig. 3.4 shows the amplitude noise of the system as a function of acquisition time by using a 640 × 512 pixel midwave InSb (indium antimonide) camera. The measurements were performed at a full frame rate of 100 Hz, using a lock-in frequency of 10 Hz (10 frames per period) and a frame integration time of 0.7 ms. For this measurement, the IR-objective was closed by the black plastic lens cap, hence the object was a black body at room temperature (about 25°C), and the amplitude signal was averaged over a representative area. The data in Fig. 3.3 can be fitted by $A_{\mathrm{noise}} = 2.9\,\mathrm{mK}/\sqrt{t_{\mathrm{acq}}}$. Hence, according to (2.31) in Sect. 2.5, this corresponds to a pixel-related system noise density of $0.005\,\mathrm{mK}\sqrt{\mathrm{s}}$, which was also included in Table 3.1 in Sect. 3.1. Figure 3.5 shows the dependence of the noise density of this camera on the lock-in frequency for a fixed acquisition time. It turns out that the noise somewhat increases towards low frequencies. This points to a certain $1/f$ noise contribution in the noise density of the camera, which is typical for electronic noise.

Two other companies, InfraTec [25] and AescuSoft [24], are offering lock-in thermography systems, which are specialized for illuminated lock-in thermography

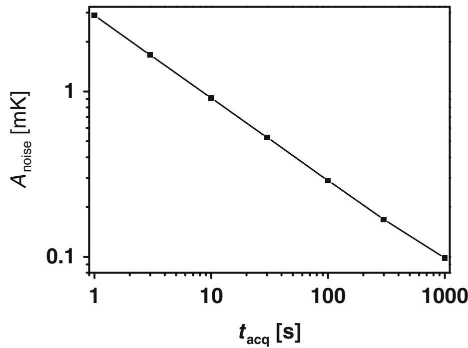

Fig. 3.4 Results of noise measurements of the Thermosensorik TDL 640 SM 'Lock-in' system

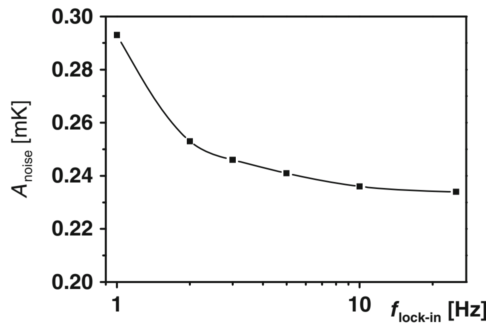

Fig. 3.5 Measured frequency dependence of the noise amplitude

(ILIT) on solar cells (see Sects. 2.6 and 6.2) and on free carrier detection on solar materials (see Sects. 2.9, 3.5, and 6.4). The InfraTec system is based on the developments of University of Konstanz, Germany [14]. They developed a technique called "LimoLIT" ("light-modulated lock-in thermography", which was later called "Voc-ILIT" [16], see Sect. 6.2), where the solar cell is periodically irradiated by an infrared luminescence diode (LED) array (see Sect. 3.3). In order to provide the optimal adaption to the properties of the solar cell material, the changeable LED modules can be selected from a variety with alternative wavelengths (IR, VIS). Alternatively, the InfraTec system supports - additional to the non-contact measurement - also the voltage modulated "VomoLIT" or "DLIT" mode, where the solar cell or module is excited by electrical current. In the InfraTec systems, both the IR camera and the lock-in excitation are triggered by the same clock generator via two independently programmable frequency dividers, as it has been described in Sect. 2.5. However, undersampling is not possible until now. As for other on-line correlating systems, the control software emphasizes continuously visual presentation of the results. Hence, all calculated images as topography, amplitude, phase and single phase image (additional to 0° and 90° also with random selectable angle) are shown and refreshed periodically from begin of the measurement on. A certain

limitation is that the power supply for DLIT uses only 2-wire connection, hence for higher currents the bias reading is inaccurate.

The AescuSoft lock-in thermography system [24] is based on developments of Fraunhofer Institute of Solar Energy Systems (ISE) in Freiburg, Germany [13, 15, 53] and is based on the CEDIP developer kit [17, 21]. The camera and excitation triggering occurs similar to that of the InfraTec systems, hence, the frame rate of the camera can be chosen, synchroneous correlation is used, and undersampling is possible. The specialty of this system is the use of an infrared semiconductor power laser for illuminating the sample. By using a special beam expansion optics, an optical power of up to 110 W can be distributed homogeneously over an are of up to $220 \times 220\,\text{mm}^2$ (see Sect. 3.3). This system is preferentially intended for illuminated lock-in thermography (ILIT) on solar cells and for free carrier detection in solar materials (see Sect. 2.9). Lock-in thermography with electrical excitation is possible as well by using an external power supply. However, the really measured voltage and current values are not brought to the user surface. The basic construction of both systems is made for macroscopic investigations of solar cells and solar materials. Hence, these systems cannot be used for IC failure analysis, where homogeneous light irradiation is not helpful anyway.

Since 2004, FA Instruments, San Jose, CA, USA [26] is offering systems called "Moire Stabilized Thermal Imaging" and "Stabilized FMI" (fluorescent microthermal imaging) for IC failure analysis [79]. Also, "Stabilized" infrared thermal imaging is available in the near IR, midwave, and in the longwave range. The name "Stabilized" is another name for single-phase (e.g. 0°) lock-in square-wave image correlation. It means that here the thermal image establishes already after one lock-in period, whereas for steady-state thermal measurements it may take seconds to minutes till a temperature distribution is stable. Taking the absolute value of the result displays both phases but at the expense of the polarity of the signal. Since the FMI film fades under UV illumination, this time saving is important for sensitivity with up to a factor of 2 improvement in sensitivity per unit time, since the phase information is foregone with single-phase lock-in. The Moire effect relies on interference fringes, which appear under monochromatic illumination at the backside inspection of ICs in the near infrared region, where the silicon material is transparent. If there are local modulated heat sources in the active region, these fringes move laterally as a result of local strain, which can be made visible by lock-in correlation of the IR images. Since Moiré does not fade with time, long acquisition times are possible. It had been already mentioned in Sect. 3.1 that performing fluorescent microthermal imaging (FMI) in lock-in or stabilized modes clearly improves the sensitivity and the effective spatial resolution over traditional background subtract techniques. Since, at least until now, the "Stabilized" thermal methods of FA Instruments comprise only single-phase correlation, a phase image cannot be displayed yet and would be beneficial especially for the Moiré technique to discriminate the thermal signal from the combined background signal seen in the amplitude signal. However, the timing relationship between the bias and the frame capture is manually adjustable to optimize this method (fixed phase adjustment).

In 2005, part of the staff of Thermosensorik has founded a new company called "IRCAM" [27]. Besides manufacturing infrared cameras and systems, IRCAM also offers a software package "IRCAM Works" for scientific and industrial applications, which also contains a functional extension "Lock-in for Works". Similar to the CEDIP system, this system is especially appropriate for thermal stress analysis (TSA) applications. By using the proprietary MIO-interface of IRCAM, both synchroneous and asynchroneous correlation can be applied at any frequency and very compact lock-in thermography systems can be built, even by using a laptop computer.

Since 2007 also Hamamatsu [20] is offering lock-in thermography as an option to their "THEMOS" systems implying a 320×240 pixel midwave InSb camera. The "Themos 1000" and "Themos mini" systems are primarily optimized for microscopic IC analysis (largest object size, which can be imaged in microscopic configuration, is 3×4 cm); however, also macro-optics can be adapted to image large areas. The complete system is mounted vibration-isolated and shielded from external radiation. As a special feature, these systems allow the users to display an "Animation," which is a time-resolved movie of the local heating over one lock-in period. The lock-in timing control is similar to that of the Thermosensorik systems, hence the camera is free running, the lock-in trigger is derived from the camera trigger, and the maximum lock-in frequency is $_{\text{frame}}/4$ (about 35 Hz). Sample biasing up to ±45 V/100 mA is integrated, also enabling a well-defined modulation depth, and internal I-V characteristic measurement and voltage/current reading are provided. This system performs two-phase correlation; hence, it allows the users to display the amplitude or the phase image. Single-phase component image like the 0°-image as well as the 0°/−90°-image can be displayed (see Sect. 5.1). The application of a solid immersion lens (SIL, see Sect. 3.4) for improving the spatial resolution is also supported.

In the basic software, the images can be displayed only in 16 colors, which cannot be changed, they are not quantitatively scaled in units of mK or degrees but rather in digits, the parameters of the IR camera and the 2-point calibration cannot be set by the operator, and no topography image is automatically stored. However, an optional quantitative analysis function is available for absolute temperature measurement. So also there is still some room for improvement. Nevertheless, the lock-in option works reliably and represents a decisive improvement of the THEMOS systems.

3.3 Illumination Systems

In this section different systems for homogeneously illuminating a macroscopic sample like a solar cell or a wafer of solar material by near-IR light, which are necessary for performing different types of illuminated lock-in thermography (ILIT) and free carrier detection will be described (see Sects. 2.9, 3.5, 6.2.2, and 6.4). We will not discuss here any focused laser stimulation techniques, which are used in IC failure analysis e.g. for OBIRCH (Optical Beam Induced Resistance Change [81])

or TIVA (Thermally Induced Voltage Analysis [82]). The optimum wavelength for exciting minority carriers in silicon is the near-IR between 840 and 960 nm, corresponding to a penetration depth in silicon between 20 and 80 μm. If the wavelength is considerably shorter than 840 nm, the increasing photon energy, compared to the energy gap of silicon, leads to a stronger thermalization heat, which is an unwanted homogeneous heat source in the different ILIT experiments, see Sect. 2.8. Moreover, for shorter wavelengths the minority carrier generation occurs very surface-near, which increases the sensitivity of these techniques to surface phenomena. If solar cells are illuminated, too short wavelengths are leading to absorption already in the emitter, what is usually not intended. If, on the other hand, the wavelength is considerably larger than 940 nm, the penetration depth may become larger than the sample thickness. This would improve the depth-homogeneity of the excitation, but then not all irradiated photons would lead to the generation of minority carriers. If larger bandgap materials like amorphous Si, CdTe, or CuInSe should be investigated, a shorter wavelength of, e.g., 700 nm has to be used.

The solar irradiation constant in middle Europe after passing the atmosphere is about 1000 W per square meter (100 mW/cm^2). This is basically white light with a colour temperature of about 6000 K, which is slightly modified by atmospheric absorption and scattering. For irradiating solar cells monochromatically under realistic conditions, the photon flux should be so, that the short circuit current density J_{sc} of the cell equals that under solar irradiation. Since the quantum efficiency of silicon solar cells is close to 1 in the wavelength range between 840 and 960 nm and the maximum possible J_{sc} is about 40 mA/cm^2, this corresponds to a photon flux of about 2.5×10^{20} photons/cm^{2}s. At a wavelength of 850 nm (1.46 eV/photon) this corresponds to an optical irradiation power of 59 mW/cm^2, which is considerably less than the solar irradiation power. Nevertheless, even this is a considerable illumination intensity, which is not trivial to generate over a typical area of a solar cell, which presently is 156×156 mm^2. For having also the possibility to work with an increased excitation intensity, many monochromatic light irradiation means are designed to illuminate at an intensity of up to 100 mW/cm^2. For these experiments, the irradiation is always assumed to be homogeneously across the whole area. Since a certain inhomogeneity of, e.g., $\pm 10\%$ can hardly be avoided without wasting too much of optical energy, in some experiments the local inhomogeneity of the irradiation field is mapped before and the measured results are corrected for this inhomogeneity after the measurement [53].

The first illumination system published for carrier density imaging (CDI) and later on also for ILIT was using a semiconductor laser delivering about 20 W optically at 917 nm from a glass-fiber output [13, 15, 53], see Fig. 3.6. An illumination system of this type with an output power of now up to 110 W is a part of the lock-in thermography systems of AescuSoft [24]. The laser is pulsed on/off by the lock-in system and its radiation is expanded and homogenized over the sample area by a special optics implying a microlens array. The main advantage of this solution is that here the irradiation is performed from a larger distance ($\approx$1 m) without wasting too much optical power. However, due to the high power density of the laser, special laser safety requirements have to be fulfilled in these systems.

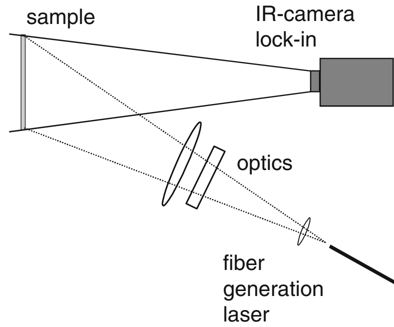

Fig. 3.6 Semiconductor laser-based illumination system of AescuSoft [24]

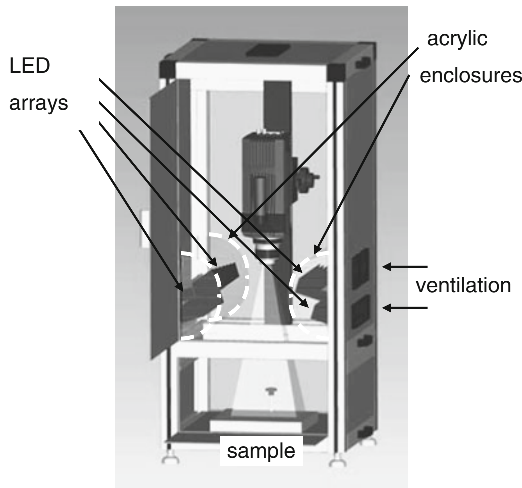

Fig. 3.7 The LED-array illumination system of InfraTec [25]

The “Limo-LIT” systems of InfraTec [25] use four LED-arrays for illumination, see Fig. 3.7. For this LED-illumination no special safety requirements have to be fulfilled. The two main problems for using LEDs for generating such a high illumination power are (1) to dissipate the heat from the LEDs and (2) to screen the sample from thermal radiation of the LEDs. Note that the LEDs are getting warm during operation. If they are operated in pulsed mode, their temperature also oscillates, leading in addition to the LED light oscillation to an oscillating thermal radiation in the wavelength range above 3 μm. The sample has to be screened from this radiation because otherwise this thermal radiation, reflected by the sample to the IR camera, would be misinterpreted as a temperature modulation of the sample. Here this screening is provided by two acrylic enclosures, which contain two LED-arrays each, irradiating downwards. Acrylic is transparent to the LED light but blocks thermal radiation. The SMD-type LEDs are mounted on heat sinks for dissipating

the generated heat. By forced cooling through special ventilation slits the heat is transported to outside the enclosures.

A certain limitation of the illumination system in Fig. 3.7 is that, due to the relatively wide irradiation angle of the LEDs of $+/-30°$ and the big distance to the sample, an essential part of the radiation does not reach the sample area but is irradiated outside it. This loss is essentially avoided in the backside LED illumination scheme for solar cells sketched in Fig. 3.8, which was developed at Max Planck Institute (Halle). Here the "legs" of the LEDs are used in their full original length for dissipating the generated heat. The LEDs are mounted between two printed circuit boards (PCBs). In the room between these boards, where the LED legs are, an air stream flows for cooling, which is generated by a row of fans on one side of the construction. Here the solar cell is facing towards the LED array (downwards) and its back contact is directed to the IR camera (upwards). This is no serious limitation for thermal investigations since a silicon solar cell can be considered as "thermally thin", hence the temperature at its front side is essentially the same as that at its backside (see Sect. 4.1). Thermal waves easily penetrate the back contact of conventional solar cells, which is made by sintered Al-paste and even exhibits a relatively good and homogeneous IR-emissivity. Since the back contact of a solar cell is opaque to thermal radiation, an acrylic window is not necessary here. Instead, the cell is lying here on a thin transparent plastic foil (not shown in Fig. 3.8). Thin film solar cells made on a glass substrate, which are illuminated from the top rather than through the glass substrate, cannot be investigated by this setup of illumination, since this substrate is "thermally thick", hence the thermal waves generated at the active region at the bottom do not easily penetrate the glass substrate facing to the camera. Note that glass is essentially opaque to thermal radiation. On the other hand, superstrate-type thin film cells on glass like CSG-modules (crystalline silicon on glass, [99]), where the light passes the glass substrate and the IR camera may look at the active layer, can be investigated. Here the metallized surface has to be covered by an IR emitter foil, see Sect. 6.2. This setup is also less appropriate for free carrier detection (see Sect. 2.9), since these experiments require illumination from the same side where also the IR camera views. The decisive advantage of the arrangement in Fig. 3.8 is that the LEDs are positioned very close to the sample here. Thus the loss in optical

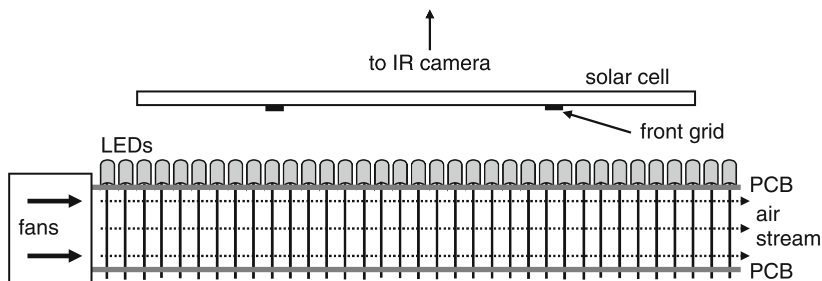

Fig. 3.8 Backside LED illumination scheme

power due to the divergence of the LED radiation is low here. This system is able to illuminate with an intensity equivalent to more than 200 mW/cm^2 (two suns).

A common problem of all LED-based illumination systems is that LEDs are traditionally low power devices. The maximum optical output power of a conventional "high power" IR-LED is about 45 mW at a current of 100 mA (SFH 4258, [100]). Hence, for generating tens of watts optical power, many hundreds of such LEDs have to be used, which may become quite cumbersome to fabricate. Illuminating even larger devices like solar modules by small LEDs becomes too expensive. However, in the last years, decisive advantages in developing high power LED modules have been made. Thus, the SFH 4740 "Ultra High Power Infrared Emitter" by Osram Opto Semiconductors generates 3.6 W optical power at 850 nm at a current of 1 A at 18 V [100]. Figure 3.9 shows an illumination system using such devices, which was also developed at Max Planck Institute (Halle). Here the IR emitter devices, which contain their own cooling plate, are mounted on a metal plate, which, on its opposite side, carries several CPU-coolers. These coolers are actually designed for cooling the central processing unit (CPU) of PCs and are working very efficiently and quietly. In the middle of the metal plate a hole for the wide-angle objective of the IR camera exists, and the IR emitters are distributed evenly around this objective. In front of the IR emitters there is an acrylic plate for

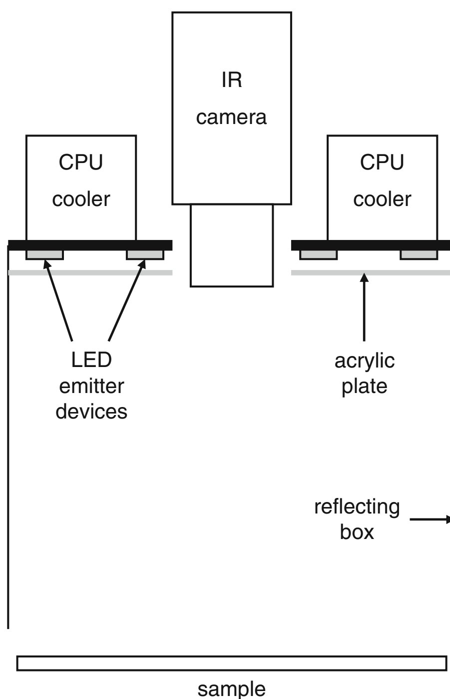

Fig. 3.9 Illumination scheme using "Ultra High Power Infrared Emitter" devices

filtering out the thermal radiation of the IR emitters. Since these emitters are radiating at a wide angle of $+/-60°$, a reflecting box is used to guide the light to the sample and to minimize optical losses. An illumination system employing 16 SFH 4740 devices and four CPU coolers was found appropriate to illuminate an area of $210 \times 210\,\text{mm}^2$ homogeneously well above $60\,\text{mW/cm}^2$ optical power at 850 nm, which is equivalent to sun light above $100\,\text{mW/cm}^2$. The major advantages of this solution are that it is easy to assemble, that there are minimum light losses, that the illumination occurs at the same side as the IR camera views (which enables e.g. free carrier detection in emission mode, see Sect. 2.9), and that this system can easily be expanded to illuminate arbitrarily large areas. This illumination system, used for backside illumination, as well as an illumination system combining the geometry of the InfraTec system (Fig. 3.7) with lens-focused ultra high power light emitters for frontside illumination are available for different wavelengths from Thermosensorik (Erlangen) [19].

3.4 Solid Immersion Lenses

If lock-in thermography is applied for failure analysis of integrated circuits, a decisive limitation is its limited spatial resolution. Note that the decisive point is not the resolution of the lock-in images, which anyway may appear more or less blurred due to lateral heat spreading or because the actual heat source may lay at a certain depth below the surface. Even in such a case, if a heat source is point-like, the position of its center can often be estimated up to an accuracy of 1 pixel by finding the center of gravity of the blurred spot. The main problem with spatial resolution is that the operator still needs to be able to navigate on the surface of the IC! Today the layout pattern may be so small that no details can be resolved anymore with a conventional microscope objective in the mid-IR range. Therefore the challenge for improving the spatial resolution is to get a meaningful topography image, which enables an orientation on the surface. Only then local peaks in the lock-in images can be related reliably to the layout of the IC.

The resolution Δx of any optical system is physically limited by diffraction, which is governed by the wavelength λ of the radiation used for imaging. According to the so-called Sparrow Criterion [101], the optical resolution is limited to:

$$\Delta x = \frac{0.5\lambda}{n\sin(\theta)}. \tag{3.1}$$

Here θ is the half-angle of the light-cone to the objective and n is the refractive index of the medium surrounding the sample. The product $n \times \sin(\theta)$ is also called "numerical aperture" (NA). For a given magnification factor of the objective, the brightness of an image increases with the square of $\sin(\theta)$, since the number of photons reaching the detector increases with an increasing solid angle used by the objective. Even for high brilliance microscope objectives, θ can hardly be

larger than 30–45° for technical reasons, therefore $\sin(\theta)$ is at best between 0.5 and 0.7. Hence, in air ($n = 1$) the optical resolution can be only slightly better than the wavelength λ used for imaging. Therefore midwave IR cameras working in the 3–5 µm range may show a better spatial resolution than longwave cameras working at 8-12 µm. Unfortunately, for samples being close to room temperature, in the mid range the light intensity exponentially increases with wavelength, as can be seen in Fig. 2.1. So the dominant part of the light is concentrated close to 5 µm and only a negligible part appears at 3 µm. Therefore, for a good microscope objective with NA = 0.7 (+/− 45° light acceptance angle), according to (3.1) the diffraction-limited spatial resolution for $\lambda = 5\,\mu\text{m}$ is $\Delta x = 3.6\,\mu\text{m}$, independent of the magnification factor of the objective and the pitch size (pixel distance) of the detector. On the other hand, the so-called pixel resolution is the pitch size divided by the magnification factor of the objective. It may be well below this diffraction-limited optical resolution, if the magnification factor of the objective is chosen large enough. In this case all images appear naturally blurred, therefore this magnification is sometimes called an "empty" (useless) magnification.

Here some remarks to the definition of the spatial resolution should follow. Note that the term "diffraction-limited spatial resolution" refers to the minimum distance of two neighboring small spots or lines (i.e., a "line pair"), which can be separated from each other. If more than two parallel lines are used, the right line of the left line pair coincides with the left line of the right pair, hence, e.g., "288 line pairs/mm" actually means 288 lines/mm, corresponding to a line distance (center-to-center) of $X = 1/288\,\text{mm} = 3.47\,\mu\text{m}$. If such a periodic arrangement is imaged with an objective close to its resolution limit, the brightness is sine-modulated with a spatial frequency of $f = 1/X$, which is the basic spatial harmonic, see Fig. 3.10a. All higher spatial frequencies are suppressed since we have assumed that these details are below the diffraction-limited spatial resolution. The decisive point is that the spatial frequency f is only dependent on the center-to-center distance of the lines X but not on the line width w or the line distance $X - w$. Only the intensity of the basic spatial harmonic compared to higher harmonics depends on w. It is highest if $w = X/2$ holds, hence if the lines have a distance equal to their width. This is realized, e.g., in the elements of the well-known USAF resolution target, one of them sketched in Fig. 3.10b. Here three lines with a center-to-center distance X are displayed with a distance of $X/2$ in between. For 288 line pairs/mm, this distance is

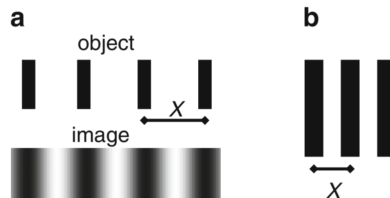

Fig. 3.10 (**a**) Line object and its image close to the resolution limit; (**b**) USAF pattern showing the spatial resolution X

about 1.74 μm. If these lines can be observed separately, the thereby proven spatial resolution is not $X/2$, but it is the center-to-center line distance X! Some authors consider the "line and space distance" $X/2$ as a measure of the resolution [102], but this overestimates the spatial resolution by a factor of 2.

Another interesting question is which magnification factor M of the lens must be used for making use of the diffraction-limited spatial resolution. One might think that a lens leading to an object pixel distance of Δx according to (3.1) should be sufficient ($M > 4.2\times$ for a pitch size of 15 μm and $\Delta x = 3.6$ μm), but this is wrong. According to Shannon's sampling theorem, at least two samples are necessary per spatial wavelength in order to have at least one pixel at the maximum and one at the minimum of the contrast, see Fig. 3.10a. Thus, for a pitch size of 15 μm and $\Delta x = 3.6$ μm, the lens must have a magnification of at least $M = 8.4\times$ for reaching the diffraction-limited spatial resolution. An even higher magnification factor may still improve the visual image quality, but for lock-in thermography, it also degrades the signal-to-noise ratio, which reduces with $1/M^2$ [101].

It is common in light microscopy to use high-NA objectives only for high magnification factors m, where this NA is necessary for obtaining the desired diffraction-limited spatial resolution. For low magnification factors, objectives of low NA are generally used. This has the advantage of a larger depth of field for low m, moreover low-NA objectives are cheaper than high NA ones, and the image brightness (which is proportional to the square of NA$/m$) may become independent on the magnification factor m. However, for thermal imaging of plane samples, this philosophy is clearly wrong. Here one is always interested in creating images with maximum possible brightness, and the depth of the field is not so important. For objectives, as well as for IR cameras, often instead of the NA the so-called f-number called $f/\#$ is given, which is the ratio of the distance to the diameter of the entrance pupil of the camera. This number governs the amount of light which can be fed through the objective to a camera. Values between $f/2 = 0.5$ and $f/1.5 = 0.666$ are typical for IR cameras. Ideally, the objective and the camera should have the same f-number. If the objective has a smaller f-number than the camera, the camera entrance angle is not fully exploited. Then, the thermal radiation that is not coming through the objective may enter the detector, which leads to an increased noise level. For a microscope objective having a magnification factor of m and a numerical aperture NA, the f-number is approximatively $f/\# = \frac{2}{m}$NA. Since the NA of an objective can hardly be larger than 0.7, for a magnification factor of $m > 2$, the lens anyway has a smaller f-number than the camera, hence it cannot fully exploit the sensitivity potential of the camera. Therefore, for any microscope objective with a magnification factor down to $m = 1$, the objective of a thermal imager should show an NA as large as possible for obtaining an f-number and thus a thermal sensitivity as good as possible. This means that, for magnification factors larger than 2, the diameter of the entrance lens of a microscope objective should at best have a diameter double of its working distance for obtaining NA $= 0.7$! If the magnification factor is small against 1 (conventional demagnifying objective), the f-number of the objective can and should always be chosen to match that of the camera.

One could ask now, why the refractive index n of the medium surrounding the sample stands in the denominator of (3.1). The reason is that the wavelength in a medium is proportional to $1/n$. Hence, immersing the object in a medium with high n is equivalent to imaging it in air with a lower wavelength. This is the reason why special immersion objectives, where the sample is embedded e.g. in an immersion oil having $n = 1.5$, are leading to a considerably improved spatial resolution in light microscopy. In principle, the same could be done for thermal microscopy. Unfortunately, water and also immersion oil is transparent neither in the mid nor in the long IR range. However, for samples with a plane surface (as ICs usually are) so-called solid immersion lenses (SIL) can be applied [103]. These are truncated bowls made from a transparent high-refractive index material, which are directly placed on top of a flat surface containing the structure to be imaged (see Fig. 3.11). Since only the innermost part of the truncated bottom face is optically used, the originally hemispherical SILs are often cone-shaped towards the bottom. This allows e.g. to place the SIL closer to bond wires. In the infrared region, silicon ($n = 3.5$) is an especially appropriate material for SILs, but also GaAs ($n = 3.4$) is often used. Gemanium ($n = 4$) would be even better, but since it absorbs radiation with a wavelength below 1.6 µm it can be used only for thermal imaging and not for near-IR investigations. If the gap between the sample surface and the plane bottom face of the SIL is negligibly small, the surface can be assumed to be "immersed" in the material of the lens. The SIL works as a magnifying glass for the following optical imaging system, which explains the gain in spatial resolution. Depending on the thickness of the lens, there are two basic types of SILs, namely "hemispherical" or "centric" SILs and "aplanatic" or "super"-SILs (a and b in Fig. 3.11). The

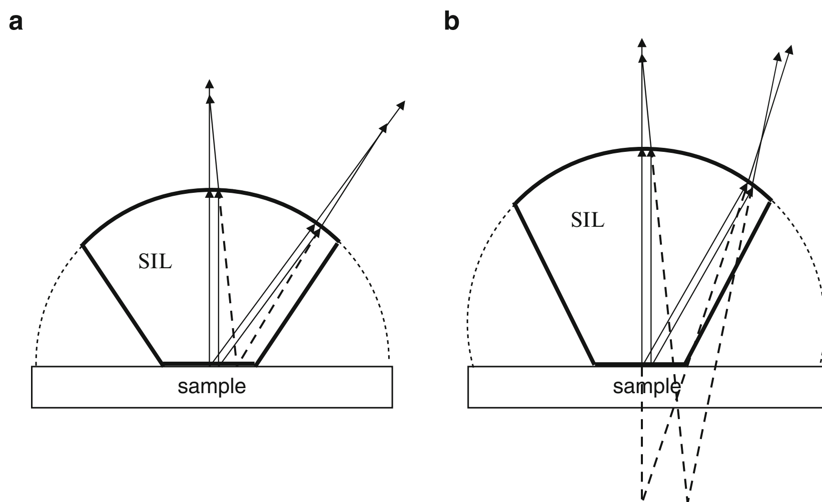

Fig. 3.11 (**a**) Hemispherical SIL and (**b**) "Super"-SIL with path of rays of a central point source (left) and an off-center one (right). Dotted lines: original bowl-shape before cone-grinding. Dashed lines: virtual path of rays (not to scale)

thickness d of the hemispherical SIL equals the radius R of the lens, whereas the optimum thickness d of the Super-SIL is [104]:

$$d = R\left(1 + \frac{1}{n}\right) \tag{3.2}$$

At this thickness the optical aberrations of a SIL are minimum, which is the basic advantage of the Super-SIL. However, there are more differences between both SIL types. As the path of rays in Fig. 3.11 shows, for a hemispherical SIL the virtual image is at the same depth as the object, whereas for the super-SIL it is lying considerably deeper. Also the magnification factors differ. For the hemispherical SIL, it is equal to the value of the refraction index n of the SIL material, but for the super-SIL it is about n^2. Nevertheless, in both cases the spatial resolution is limited by (3.1), whereby the angle of the light-emission within the SIL material is essential. For a hemispherical SIL the light emission angle within the SIL is the same as outside, but the super-SIL reduces it by a factor of $1/n$. So the following optics for a hemispherical SIL should work with a high NA, whereas that for a super-SIL is allowed to have an NA reduced by $1/n$. Of course, a SIL can also be used with a height smaller than its radius. In this case, its magnification factor and thereby its potential to improve the spatial resolution is smaller than n, and the virtual image is lying within the SIL-material.

Both super-SILs and hemispherical SILs may be integrated into a special SIL-objective, or they can be used as an add-on to a conventional microscope objective [105]. In this case, a special challenge is the positioning of the SIL in the middle of the image field. If an SIL is not cone-shaped towards the bottom as in Fig. 3.11, it can be slid into the desired position by using a mechanical aperture on top, which is connected to a micromanipulator [106]. As an alternative, Fig. 3.12 shows an SIL positioning facility, which can be used also for cone-shaped SILs and is available as an add-on to the 5× microscope objective of Thermosensorik (Erlangen) [19]. By using this facility, the user may first localize a hot spot without SIL and then, if the spot is in the middle of the image field, lower the SIL for a detailed inspection and remove it afterwards on demand. Since this is a hemispherical SIL, the focus position is at the same depth for working with and without SIL, and the high NA of the microscope objective is exploited. Meanwhile also other SIL positioning facilities are offered both by Thermosensorik [19] and Hamamatsu [20]. In Sect. 6.1 some results of the application of this SIL in IC failure analysis are presented.

An SIL can also be used for backside inspection by looking through the silicon bulk material of an IC. As Fig. 3.13 shows, there are different possibilities for doing that. In the simplest case (a) the backside is thinned down (for reducing the effect of free carrier absorption at high-doping levels of the bulk), carefully optically polished, and the SIL is placed on top of this backside. Since the remaining silicon substrate is also optically active, the desired thickness d of the silicon SIL has to be reduced for this application by the thickness of the bulk. This geometry has been called "Numerical Aperture Increasing Lens" (NAIL) [104]. This variant has the advantage that the SIL can be shifted to any position. However, the problem is to

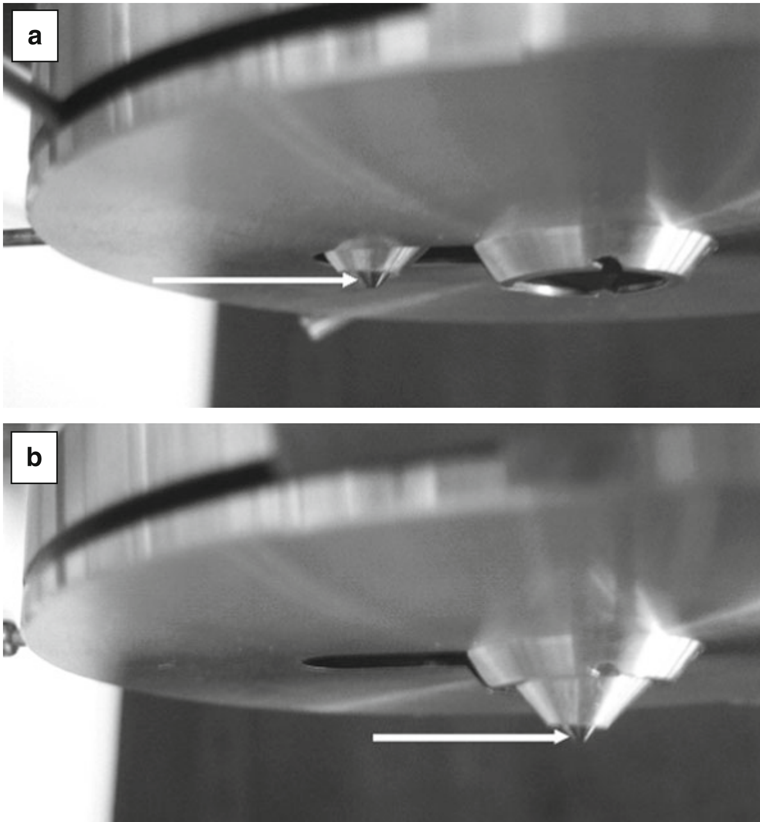

Fig. 3.12 (**a**) SIL positioning facility with SIL (see arrow) retracted and (**b**) in working position

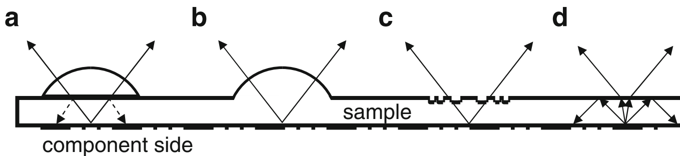

Fig. 3.13 SIL backside inspection: (**a**) NAIL, (**b**) FOSSIL, (**c**) diffractive SIL, (**d**) no SIL

flatten and polish the surface so accurately that the slit between surface and SIL is really negligible. If this slit is wider than a small fraction of the wavelength, total reflection prevents imaging with a high NA (see dashed arrows in a). Filling the slit with an immersion oil helps a little, but does not solve the problem completely since the refractive index of any immersion oil (typ. 1.5) is much lower than that of silicon ($n = 3.5$). This problem is avoided by machining the lens directly into the backside of the silicon wafer (b), as it was proposed by Koyama et al. [107]. The authors named this type of SIL "FOSSIL" for "FOrming Substrate into Solid

Immersion Lens". The basic limitation of this approach is that the position of a fault has already roughly be known by other investigations. Moreover, due to the finite thickness of the original substrate, the SIL can have only a certain maximum size, which limits the area that can be investigated. If the substrate is so highly doped that free carrier absorption becomes dominant, this approach is also not feasible. A similar SIL has been etched into the backside of a device by Scholz et al. by local Focused Ion Beam (FIB) etching with subsequent gas-assisted cleaning of the surface [108]. Since this technique does not allow the removal of large quantities of material, here a relatively shallow lens having a magnification factor of only 1.8 was produced. Another approach, which is also practical only for sufficiently transparent substrate and if the position of the fault is roughly known, is to machine a diffractive (zone) lens into the surface of the backside (c), as proposed by Zachariasse and Goossens [109]. By using local FIB etching and subsequent plasma etching, they produced a series of concentric ring-shaped grooves into the surface, which acts as a SIL. Though the light efficiency of this diffractive SIL was only about 15–20%, the gain in spatial resolution was impressive. Since the geometry of the diffractive structure depends on the imaging wavelength, and avoiding light losses is much more important for thermal imaging than for laser analysis, it still has to be proven whether this approach is feasible for thermal imaging also.

Even for backside inspection through a plane surface (Fig. 3.13d) the interesting region of an IC is immersed in silicon material, where the wavelength of light is considerably smaller than in air. Therefore one could argue that even in this case the spatial resolution could be improved compared to front side investigation. Unfortunately, this is not the case. As Fig. 3.13d shows, due to the high refractive index of the bulk, only light from a narrow cone within the material may exit the surface, whereas light emitted at a larger angle is totally reflected back. This completely compensates the effect of a smaller wavelength in the bulk material. In fact, regarding the law of refraction, in this case $\mathrm{NA} = n \times \sin(\theta)$ is the same inside and outside of the bulk material. Therefore backside inspection without an immersion lens (d) does not lead to any improvement of the spatial resolution. The use of solid immersion lenses (SILs), however, allows a decisive improvement of the spatial resolution by a factor of 3.5 (for a silicon SIL) for thermal imaging. Only this improvement allows to obtain a meaningful lock-in thermography results for failure analysis of modern integrated circuits.

3.5 Realization of CDI/ILM Systems

3.5.1 Absorption Mode

The first carrier density image published [12] was taken with an IR-camera without using the lock-in principle. Since this technique is not used anymore, we will here first discuss the setup published later including the lock-in technique [13] in some more detail.

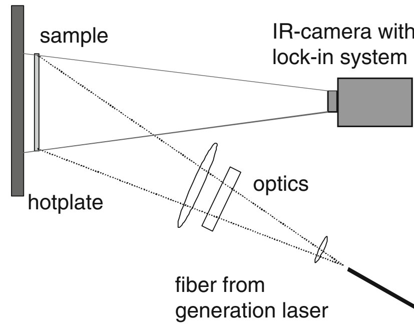

Fig. 3.14 Experimental setup for CDI/ILM measurements in absorption mode

This setup consists of a source emitting infrared radiation (hotplate), the sample under investigation exposed to this IR-radiation and an IR-camera (thermocamera) that measures the amount of IR-radiation transmitted through the sample (see Fig. 3.14). Additionally, a short-wave IR irradiation source is needed to generate excess free carriers, see Sect. 3.3. For a lock-in procedure a light source was needed that can easily be chopped with frequencies around 1–40 Hz and at the same time has a rise/fall time-constant below 0.5 ms. In the first version published, a fiber-coupled semiconductor laser with an optical output power of above 10 W was used to ensure an injection level in a $100 \times 100\,\text{mm}^2$ sample that is about equivalent to the one obtained by full solar illumination (often called "1 sun" illumination). Present setups use lasers with a minimum optical output power of 2×30 up to 2×100 W and are able to homogeneously illuminate areas up to $21 \times 21\,\text{cm}^2$. The illumination has to be as homogenous as possible. A semiconductor laser combined with optics that homogenize the irradiation to 5–10% non-uniformity and with a measurement of the generation distribution and a respective correction (see below) is appropriate. In newer systems, a non-uniformity of a few percent over large areas can be realized without rendering corrections. In the first setup, the homogenization was done in a similar way as in a solar simulator, present setups use commercially available homogenizers supplied e.g. by the company Limo [110]. The wavelength of the laser was chosen to be 917 nm (penetration depth $\alpha^{-1} = 40\,\mu\text{m}$) to assure that only a negligible fraction of the light is transmitted to the rear surface of a typical wafer (thickness around 200 μm). A more efficient generation is obtained e.g. with a 940 nm diode laser, the penetration depth of 55 μm is still appropriate. Note that this illumination system for wafers (without the hotplate) is the same that can also be used for illuminated lock-in thermography (ILIT) on solar cells, see Fig. 3.6 in Sect. 3.3. Hence, by using such an illumination system, both ILIT on solar cells and CDI/ILM on wafers can be performed by one and the same system.

As the IR-source for the absorption mode a hotplate was used, that was homogenized by a thick copper plate on top coated with a black finish that has an IR-emissivity of about 0.96. The radiation intensity can thus be easily varied by adjusting the temperature of the hotplate. The camera detecting the IR-transmission

through the sample was in the first setup a mid-wave IR-camera based on a cadmium-mercury-telluride (CMT) focal plane array of 288×384 pixels. The noise equivalent temperature (NETD) was about 20 mK and frame rates of about 150 Hz were reached under typical measurement conditions. The camera was integrated in a Thermosensorik TDL 384 system (see Sect. 3.2), which connects the camera to a PC and allows the parallel application of two correlation functions to the data collected by the camera. The system also provides a square pulsed trigger signal with a fixed phase relative to the correlation functions, which can be used to trigger the light source. More recent realizations use e.g. a CEDIP Silver camera with 400 Hz frame rate [24].

In common to all setups is that, as for lock-in thermography, the correlation functions are chosen to be $K^{0^\circ} = 2\sin(\omega t)$ for the 0° Image and $K^{-90^\circ} = -2\cos(\omega t)$ for the −90° Image (see Sect. 2.2). This allows for the separation of the non-thermal (CDI/ILM) and the thermal signal. The non-thermal signal, which is proportional to the density of excess free carriers $\Delta n(t)$, has a response-time to the excitation $G(t)$, which is of the order of the carrier lifetime, thus about 1–1000 μs. So the non-thermal signal is fast compared to the lock-in cycle duration which is typically of the order of 25–1000 ms and the time interval between two pictures taken by the camera (typically about 6 ms for a frame rate of 166 Hz). Thus it can usually be assumed that the excess carrier density $\Delta n(t)$ is in-phase with the modulated excitation $G(t)$. Hence, this type of measurement is performed under quasi-steady-state conditions. If a thermocamera that takes images in a time distance in the order of microseconds would be available, then a small phase shift between the excitation $G(t)$ and the electric signal $\Delta n(t)$ could be observed, which could be used to obtain time-dependent free carrier information. A frame rate of the camera of about 10^5–10^6 Hz, that corresponds to this requirement, is at the moment far away from any technical possibilities. So at present, the non-thermal signal $\Delta n(t)$ and thus also the IR absorption of free carriers is generally taken to be exactly in-phase with the excitation $G(t)$ and to completely contribute to the 0°-image only. An approach, which nevertheless uses the build-up time of the carrier density in a square wave-shaped generation sequence will be discussed in Sect. 3.5.3.

The thermal signal, on the other hand, is 90° out-of-phase with its excitation, because the energy flow into the sample $P(t)$, which is in-phase with the generation $G(t)$, is essentially proportional to $\frac{\partial T}{\partial t}$ (with $T(t)$ the sample temperature), resulting in $T(t)$ being delayed by 90° compared to $P(t)$ for a periodic signal (see discussion of a spatially extended homogeneous heat source in Sect. 4.4). Thus the thermal signal of a homogeneously heated sample contributes to the −90° image and does not contribute to the 0° image.

Thus, using two correlation functions which produce a 0° and a −90° image allows separating the thermal and non-thermal (CDI/ILM) signal. In contrary to the thermal imaging, for CDI/ILM the 0°-image is exclusively used for calculating $\Delta n(x, y)$.

3.5.2 Emission Mode

An initial realisation of the emission mode was reported using a black background which was homogeneously cooled by Peltier elements [55] using the setup depicted in Fig. 3.14 with temperature of hotplate lower than wafer temperature.

To ensure that emission of the free carriers was dominating for the chosen background temperature of 1 °C, the power of the emitted radiation of the background at 1 °C was estimated and found to be only 36% of the emission of a background at room temperature and only 13% of the emission of the background used for the absorption CDI/ILM, which was usually at around 60°C. By this means infrared transmission through the sample is suppressed to a low level to prevent a superposition of the absorption signal and the signal coming from the emission of excess carriers. With this setup the transition between dominating absorption and dominating emission as theoretically calculated in Fig. 2.15 was quantitatively confirmed. A measured dependence of the camera signal on the temperature of the background T_b with the temperature of the wafer T_w kept constant was reported in [55] for a surface-passivated silicon wafer with a carrier lifetime of approximately 50 μs and is given in Fig. 3.15a.The fit was calculated from (2.23) with T_w (and thus the emission term) kept constant. The theoretical curve is confirmed by the measurement except for minor deviations attributed to condensation and ice on the sample. The result for the variation of the wafer temperature T_w and T_b kept constant also follows the emission part of (2.24) (Fig. 3.15b), with minor deviations for the range with small temperature differences.

A different approach to realise the emission mode was suggested in [57], with a respective setup presented in [56]. In this setup the wafer is placed on a metal surface having a high reflectivity and thus a low emissivity in the IR-range detected by the camera (see Sect. 2.1), e.g. a gold-plated mirror. This setup has distinct advantages compared to the low temperature background plate. By heating the mirror chuck, the wafer may be heated and at the same time a low IR emission from the background is maintained. In addition, the emission of the free carriers themselves is intensified by the back-reflection of the emitted radiation by the mirror surface. A scheme of a respective setup is given in Fig. 3.16 [56]. Here the focal plane array infrared camera used had a maximum sensitivity at 8.3 μm (long-wave), a frame rate of 38.9 Hz and an array size of 640 × 486 pixels. Excess carriers were generated by an array of 700 light-emitting diodes (LEDs) emitting at 880 nm and providing an excitation level equivalent to 1 sun. In [56] also a detailed treatment to quantify the sensitivity of the measurement with the setup in Fig. 3.16 by defining a noise equivalent lifetime (NEL) may be found.

3.5.3 Lifetime Calibration

To calculate lifetimes from the data obtained in a steady-state measurement, it is necessary to convert the camera signal that comes in "*digits*" or in units of

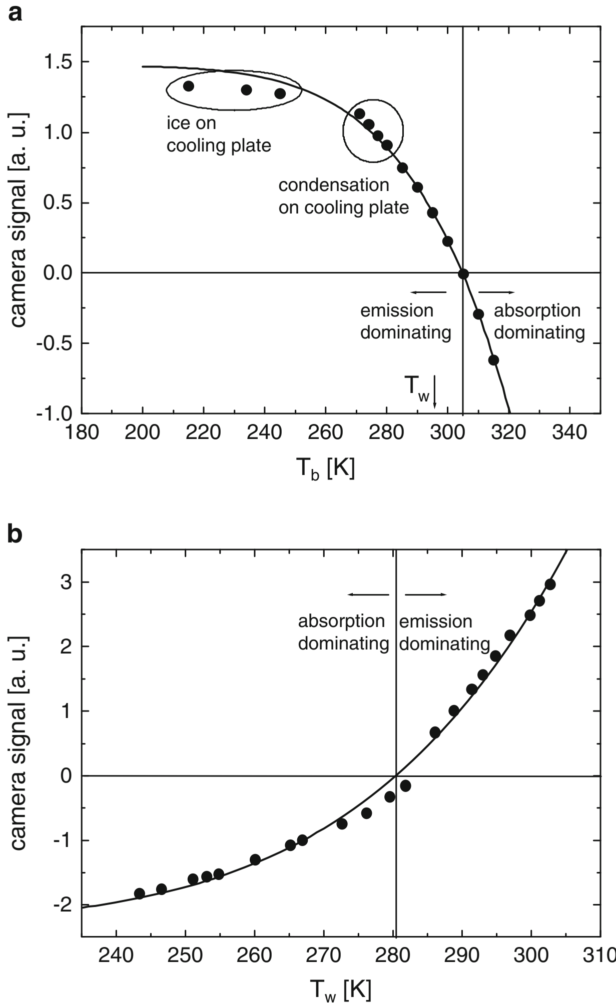

Fig. 3.15 Experimental confirmation of the transition between emission and absorption mode for (**a**) variation of the background temperature T_b with the temperature of the wafer T_w constant and (**b**) variation of T_w and T_b constant. Calculated lines are according to (2.23) and (2.24)

millikelvin to excess carrier densities Δn. These are then transformed to excess carrier lifetimes using (2.20) and the local generation density G determined experimentally (if non-uniformity is pronounced) for the respective setup. For this lock-in technique, a differential calibration transforming Δ *digits* to Δn is sufficient. The general approach to do this was developed by Bail et al. [12]. The practical details given in the following are for the setup shown in Fig. 3.14 and taken from [53].

The basic calibration idea is to use a set of FZ-wafers which have different doping levels but are otherwise identical between each other and also identical to the

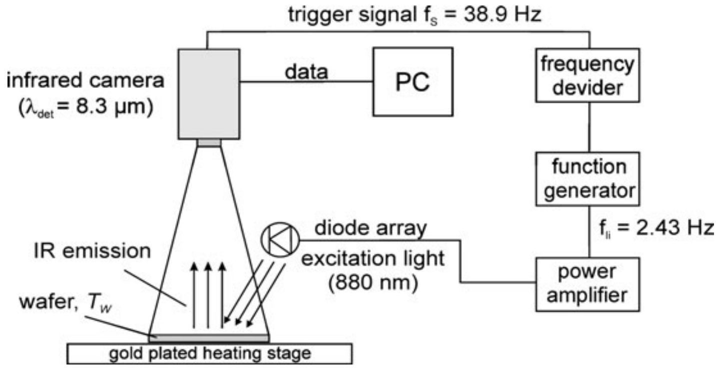

Fig. 3.16 Setup to obtain a lifetime image in emission mode using a gold-plated heating stage [56]

wafer to be measured. This regards not only the wafer thickness but also the state of roughness of the surface. Note that this roughness, by determining the degree of light scattering, also determines the average length of the light paths in the wafers. These wafers are successively put between the camera and the hot plate for measuring their transmissivity in steady-state mode. The differences observed are then due to the differences in free-carrier absorption of the samples. The obtained data can be fitted linearly, since the changes in transmissivity due to free-carrier absorption are small. An example of a plot of the transmissivity in camera digits over wafer doping density for an absorption-CDI setup is given in Fig. 3.17. Here the calibration results in a slope of the linear fit of $m = -(3.82 \pm 0.16)10^{-13}$ digits cm^2 for the camera module used. This slope can then be used to transform the camera signal Δ *digits* into excess free carrier concentrations by the relation:

$$\Delta n(x, y) = \frac{\Delta\, digits(x, y)}{m\sigma W}\zeta. \tag{3.3}$$

Here W is the wafer thickness and σ is a correction factor taking account of the fact that in the calibration procedure p-type wafers were used and thus only the IR absorption of holes has been measured, but that in a real measurement due to electron hole pair generation the free carrier absorption of holes and electrons has to be taken into account (see (2.20)).

The free carrier absorption in silicon was experimentally found to be [46]:

$$\begin{aligned} \alpha_\text{n} &\approx 1 \times 10^{-18}\lambda^2 n, \\ \alpha_\text{p} &\approx 2.7 \times 10^{-18}\lambda^2 p. \end{aligned} \tag{3.4}$$

Here $\alpha_{\text{n,p}}$ is the absorption coefficient for electron/hole free carrier absorption, respectively, λ the wavelength and n/p the free electron/hole density. Thus σ is given by $\sigma = \frac{2.7+1}{2.7} = 1.37$. ζ is another correction factor taking into account the difference between the “real” camera contrast between illuminated and

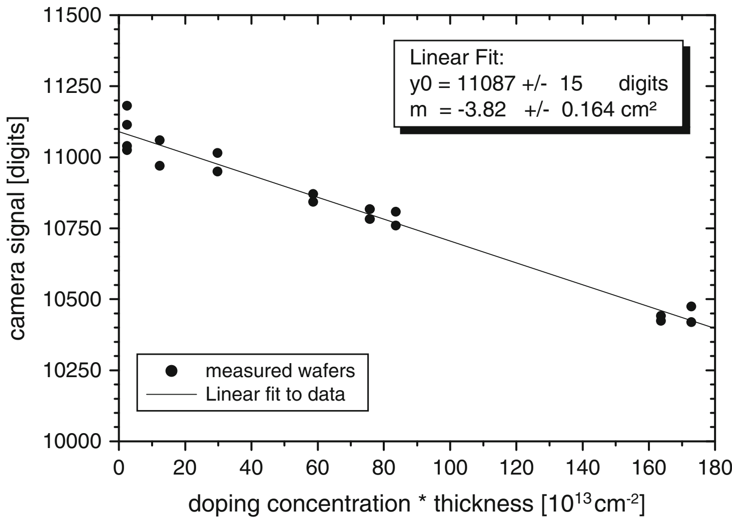

Fig. 3.17 Calibration of the camera signal for excess carrier densities Δn via a set of differently doped mono-crystalline wafers

unilluminated state and the signal given by the lock-in correlation. In the case of a correlation function of $K^{0^\circ} = 2\sin(\omega t)$ it results in $\zeta = \pi/2$. In (3.4) it is assumed that sensitivity differences between the camera pixels are already corrected, e.g. by a 2-point correction procedure.

Actual diode laser irradiation systems reach already uniformed irradiation with deviations of a few percent only, which may then be included in the measurement uncertainty. If the inhomogeneity of the irradiation is significant compared to the desired measurement accuracy, the local excess carrier lifetime calculated from the measured $\Delta n(x, y)$ images from (2.19) written for each pixel $p(x, y)$ has to be corrected in addition accounting for the variable $G(x, y)$. The semiconductor lasers used for irradiation are in general very stable sources. Thus it is possible to map the generation irradiation $G(x, y)$ once during the setup phase of an individual system and use it for subsequent measurements.

A calibration with a set of planar wafers results in absolute carrier lifetimes for measurements on a planar (untextured) wafer. With the same calibration, measurements on textured wafers lead to unrealistically high lifetimes and a blurred appearance of the image. This may be interpreted as follows: for a planar wafer, the radiation emitted by an excess carrier can leave the silicon only within in a small cone of about 17° width. Due to the high refractive index ($n_{\text{Si}} = 3.4$ for $\lambda = 4\,\mu\text{m}$), radiation emitted under higher angles is internally reflected and not detected by the camera. A rough surface allows a larger part of the total radiation emitted by free carriers to exit the silicon toward the camera aperture. For a certain carrier density, a higher signal results as compared to the calibration situation, which mimics a higher carrier lifetime. In addition, at a specific position, radiation not only from this wafer

segment but also from neighbouring parts of the wafer may be detected, which leads to blurring.

A solution for the spurious lifetime increase would be the calibration with a set of wafers with the same type of surface roughness as the one of the sample under test, which is tedious to do and sometimes not possible. Another solution was proposed in [111]. A local emissivity correction is deduced from the slope of the increase with temperature of the emitted photon density compared to blackbody radiation. For the emissivity correction, only the topography images at room temperature and at the elevated measurement temperature are needed.

As a second correction step, in [111] a deconvolution is suggested, in order to convert the blurred measured lifetime distribution to the actual distribution. In [111], a suitable point-spread function and a Fourier transformation with a Wiener filter were used. The procedure was found to be fairly insensitive to the exact shape of the point-spread function. The shape given in [111] was based on an experimentally determined distribution.

With both steps, emissivity correction and deconvolution, the carrier lifetime image obtained from a textured wafer was demonstrated in [111] to closely resemble the one obtained from a neighbouring wafer (within a multicrystalline block) prepared with planar surfaces. An extensive treatment of deconvolution techniques with emphasis on thermal images is given in Sect. 4.5.2.

Although the time resolution of thermal cameras is at present not sufficiently high for directly measuring the time-dependence of free carrier generation, the lag in build-up and decay of the carrier density compared to the rise and fall of a fast-switching generation source can be used for a direct dynamic determination of the carrier lifetime. This allows a lifetime calibration of CDI/ILM images independent of signal intensity, i.e. especially of optical sample properties ("dynamic ILM" [40]). The method to retrieve this information from a sample subject to a square-shaped generation G is sketched in Fig. 3.18. Here images with a short integration time are taken, which allow to compare the local carrier concentration during the build-up (first image) with the steady "on"-state (second image). The third and the fourth image are used for background correction within a lock-in procedure. To achieve a sufficient difference between the first two images, which directly relates to the accuracy in determining the carrier lifetime, a sufficiently short integration time t_{int} has to be chosen. The sequence plotted in Fig. 3.18 is used for an implementation of a lock-in procedure. For details, how the carrier lifetime is deduced, we refer to [40]. Using the 4-point correlation (see Sect. 2.2) a relation of the phase Φ (see (2.8)) with the carrier lifetime is deduced [40]:

$$\Phi = \arctan\left\{\frac{t_{\text{int}} - 2\tau_{\text{eff}}\left[\exp\left(-\frac{T}{4\tau_{\text{eff}}}\right) - \exp\left(-\frac{T+4t_{\text{int}}}{4\tau_{\text{eff}}}\right)\right]}{t_{\text{int}} - 2\tau_{\text{eff}}\left[1 - \exp\left(-\frac{t_{\text{int}}}{\tau_{\text{eff}}}\right)\right]}\right\}. \quad (3.5)$$

For a reasonable integration time $t_{\text{int}} = 300\,\mu\text{s}$, an approximately linear relation of phase Φ and lifetime τ_{eff} is found for carrier lifetimes below about $200\,\mu\text{s}$. With a lock-in frequency of 40 Hz (period length $T = 25\,\text{ms}$) dynamic ILM images on

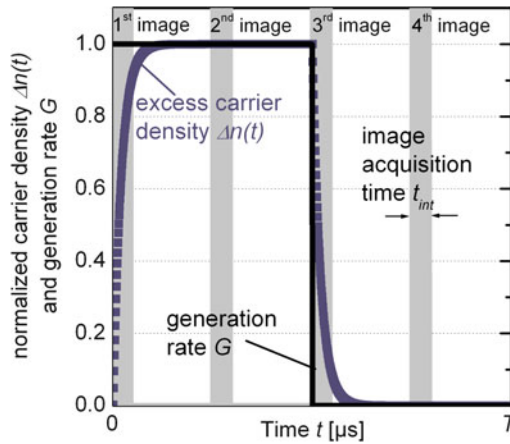

Fig. 3.18 Timing sequence used in dynamic ILM (courtesy of K. Ramspeck, ISFH Hameln)

surface-passivated multicrystalline wafers could be obtained within 1 s, with absolute values agreeing well with microwave detected photoconductance decay maps. The image obtained from the method presented in [40] was found to be hampered by blurring. In a successive publication [112], the higher sensitivity to blurring effects was attributed to the stronger impact of laterally guided radiation on the dynamic evaluation as compared to standard CDI/ILM. The main application of this technique is seen in an independent scaling procedure for conventionally measured CDI/ILM images, which show a better spatial resolution. The approach to use combined dynamic and steady-state images was exploited further in [112]. Phase effects due to the heat signal induced by the optical excitation have to be corrected. Otherwise they may lead to high errors especially for lifetimes approaching the detection limit of the technique (about 10 μs stated in [112]). If the areas of highest lifetimes (50 μs in the example) of a heat-signal-corrected dynamic ILM measurement are used to calibrate a steady-state CDI/ILM image, excellent agreement with a (area averaged) QSSPC measurement was demonstrated. Note that this approach intentionally exploits the irregularity of the phase measurement for 4-point correlation and square-shaped signal, which was mentioned already for Fig. 2.9 in Sect. 2.5.

Chapter 4
Theory

The following sections will outline the heat diffusion theory underlying lock-in thermography experiments. First, in Sect. 4.1, the effects of the heat conduction on the surrounding of the sample will be discussed, presenting the definitions of a thermally thin and a thermally thick sample, and of the quasi-adiabatic state of a measurement. In Sect. 4.2, a simple method is being introduced of compensating the temperature drift in the initial heating-up phase of lock-in thermography experiments. These considerations should also be of interest when interpreting non-destructive testing experiments. Then, the following two sections will review the theory of the propagation of thermal waves for different heat source geometries. Based on these results, in Sect. 4.5 follows a summary of the most important relations for the quantitative interpretation of lock-in thermography measurements in terms of power sources for simple heat source geometries. In Sect. 4.5.1, the image integration/proportionality method is being introduced, which allows a quantitative interpretation of lock-in thermography results also for an arbitrary distribution of heat sources. Finally, Sect. 4.5.2 describes recent advances in the software-based correction of the effect of the lateral heat conduction within the sample on lock-in thermograms, implying also a quantitative interpretation of lock-in thermography results.

4.1 Influence of the Heat Conduction to the Surrounding

The "Theory of heat conduction in solids" is described most minutely in the "Bible" for thermographers with this title by Carslaw and Jaeger [113]. Since here our main interest is focussed on lock-in thermography, only those parts of this book dealing with the solution of the heat diffusion equation for periodically oscillating heat sources should be of interest. However, especially at the beginning of each lock-in thermography measurement there is a period when the thermal equilibrium conditions have not yet established, which in the following will be called the "initial heating-up phase". In this section, after summarizing the basic concepts of thermally thin and thermally thick samples, we will discuss the influence of this heating-up phase on lock-in thermography. Throughout this section, the location of the heat sources will be assumed solely at the surface of the sample.

The non-steady-state heat diffusion equation in a 3-dimensional homogeneous and isotropic solid is:

$$c_p \varrho \frac{\partial T}{\partial t} = \lambda \, \Delta T + p \tag{4.1}$$

(T = temperature, t = time, c_p = specific heat, ϱ = density, λ = heat conductivity, p = dissipated power density). For calculating the temperature distribution in a solid while heat is being introduced, this differential equation has to be solved accounting for given temporal and geometric boundary conditions. One of the analytical solutions can be achieved for the propagation of a plane thermal wave into the depth of a semi-infinite solid. Here, harmonically oscillating heating and cooling activities are assumed at a certain frequency of $f_{\text{lock-in}} = \omega/2\pi$ at the surface of a solid. Within the solid, the dissipated power p is assumed to be zero. Hence, within the solid (4.1) reduces to a one-dimensional homogeneous differential equation in z-direction:

$$c_p \varrho \frac{\partial T}{\partial t} = \lambda \, \frac{\partial^2 T}{\partial z^2} \tag{4.2}$$

The solution to (4.2) in an isotropic and homogeneous material, which vanishes for $z \to \infty$, is the plane thermal wave in z-direction:

$$\begin{aligned} T(z,t) &= A \exp\left(-z\sqrt{\frac{\mathrm{i}\omega c_p \varrho}{\lambda}}\right) \mathrm{e}^{\mathrm{i}\omega t} \\ &= A \exp\left(\frac{-z}{\Lambda}\right) \exp\left(\mathrm{i}\left(\omega t - \frac{z}{\Lambda}\right)\right) \\ \text{with} \quad \Lambda &= \sqrt{\frac{2\lambda}{\varrho c_p \omega}} \end{aligned} \tag{4.3}$$

The quantity Λ, having the dimension of a length, is the so-called thermal diffusion length, which according to (4.3) reduces with $1/\sqrt{f_{\text{lock-in}}}$. It can also be expressed as $\Lambda = \sqrt{2\alpha/\omega}$ with $\alpha = \lambda/(\rho c_p)$ being the so-called thermal diffusivity [2]. For silicon, at a frequency of 3 Hz, the thermal diffusion length is about 3 mm, for copper it is nearly the same, but for insulators such as glass or plastics it is one to two orders of magnitude lower. In the appendix, the thermal properties will be given as well as typical thermal diffusion lengths for several common materials. The amplitude factor A of the oscillating temperature signal can be gained from the amplitude of the oscillating areal surface power density p_0 by calculating the heat flux through the surface at z = 0:

$$\begin{aligned} p_0 \mathrm{e}^{(\mathrm{i}\omega t + \mathrm{i}\varphi)} &= -\lambda \left. \frac{\partial T}{\partial z} \right|_{z=0} \\ &= A\sqrt{\lambda \omega c_p \varrho} \; \mathrm{e}^{(\mathrm{i}(\omega t + \pi/4))} \\ \text{with} \qquad A &= \frac{p_0}{\sqrt{\lambda \omega c_p \varrho}} \end{aligned} \tag{4.4}$$

Here φ is the phase shift between the modulated power and the surface temperature modulation, which here is $\pi/4$ (45°). Equation (4.3) represents a strongly damped plane wave in z-direction, the amplitude of which decays by $1/\mathrm{e} = 0.37$ over the distance of Λ, and by a factor of $\mathrm{e}^{-2\pi} = 0.0019$ over the distance of one wavelength being $2\pi\Lambda$! This strong natural damping of thermal waves, which is frequency-dependent via Λ, is the physical reason why the spatial resolution of lock-in thermography investigations is improved relative to steady-state thermography. It is interesting to note here that the amplitude factor A is proportional to $1/\sqrt{f_{\text{lock-in}}}$, and not to $1/f_{\text{lock-in}}$ as it can be expected for a homogeneously heated body (see discussion in Sect. 2.7). The reason for that is that in this geometry, actually only a surface layer of a (frequency-dependent!) thickness Λ is heated and cooled down. The material below can be assumed to be essentially thermally insulated from the thermal oscillations of this surface layer. Hence, for a sample of a thickness above Λ and with heat generation at the surface, it does not matter for the surface temperature oscillations whether it is mounted on top of a heat sink, or not. With respect to lock-in thermography it can be regarded to be thermally insulated. Therefore, for theoretically describing the oscillating heat conduction on top of such a sample it is reasonable to model it as if infinitely thick.

In real samples, the heat seldom spreads solely as plane thermal waves. Nevertheless, as the next sections will show, the thermal diffusion length Λ has a universal meaning governing also the two- and three-dimensional spreading of thermal waves, since at a certain distance from the source all thermal waves are approaching plane waves. Therefore, this quantity Λ may help in distinguishing between the two basic sample geometries found for lock-in thermography investigations, which are thermally thin and thermally thick samples. A plane sample is generally called "thermally thin" whenever its thickness is small against Λ and "thermally thick" if it is large against Λ. A thermally thin sample can be described as an infinitely thin foil. In a thermally thin sample, the heat flux in vertical direction can be neglected compared to that in horizontal (in-plane) direction, hence the temperature field at the top surface can be assumed to be the same as that at the bottom surface. Thus, the heat diffusion problem reduces from a 3-dimensional one to a 2-dimensional one. For thermally thin samples, their possible mounting onto a heat sink may affect their thermal behavior as will be described below.

On the other hand, if 3-dimensional heat spreading has to be regarded, a sample is called "thermally thick". Actually, one has to distinguish between "thermally finitely thick" and "thermally infinitely thick" samples. If the thickness of a sample clearly exceeds the thermal diffusion length, it can be considered as thermally infinitely thick. Note that also the spatial resolution of an investigation determines whether 2-dimensional or 3-dimensional heat spreading has to be regarded. If, for example, a point heat source at the top of a 300 μm thick sample is investigated with a spatial resolution of 10 μm, the heat diffusion problem has to be treated 3-dimensionally, even if the thermal diffusion length exceeds the sample thickness. On the other hand, for an overview image of the same sample using the same lock-in frequency, but a resolution of 1 mm, the same sample can be described to be thermally thin, since depth-dependent processes are no longer influencing this image. In the

Sect. 4.3, the technique of introducing mirror heat sources will be presented, which allows one to describe the heat conduction also for samples of medium thickness.

In the following, the influence of the heat conduction from the sample under investigation to its surrounding, on the results of lock-in thermography investigations will be discussed. The simple initial question is: Oscillating (sinusoidal) heat introduction actually means subsequent heating and cooling. However, in electronic device testing we only introduce heat, by applying a pulsed bias (except for having Peltier effects), hence the sample is becoming warmer and warmer during the measurement. Where should the cooling come from? It comes from the steady-state heat conduction to the rest of the sample, which is still at lower temperature, and finally to its surrounding. Even if the sample is mounted thermally insulated, with increasing sample temperature, finally, the surrounding air or thermal radiation will lead away the heat so that after a certain measurement time, the average sample temperature will get stabilized at a higher level than before. We will call this the "quasi-steady-state" of the mounted sample. The time to reach this state is called the "thermal relaxation time". We have added the term "quasi", because the non-steady-state periodic temperature modulations resulting from the periodic heat introduction we are actually interested in the lock-in thermography, are still superimposed on the generally increased temperature of the sample in the quasi-steady-state.

This situation is outlined in Fig. 4.1, which is drawn for a thermally thin sample, but which qualitatively also holds for thermally thick samples. Here, the surface temperature of an object under investigation is shown as a function of the measurement time after the beginning of a lock-in thermography experiment. For reasons of simplicity, here we are considering a thermally thin sample, which is homogeneously heated and connected to its surrounding via a major heat resistance, as for instance, for the lock-in thermography test object described at the end of Sect. 2.7. At the beginning of the experiment, the sample temperature T equals the surrounding temperature T_0. Within the first bias pulse, the temperature increases linearly. After this pulse, this increased temperature remains constant in first approx-

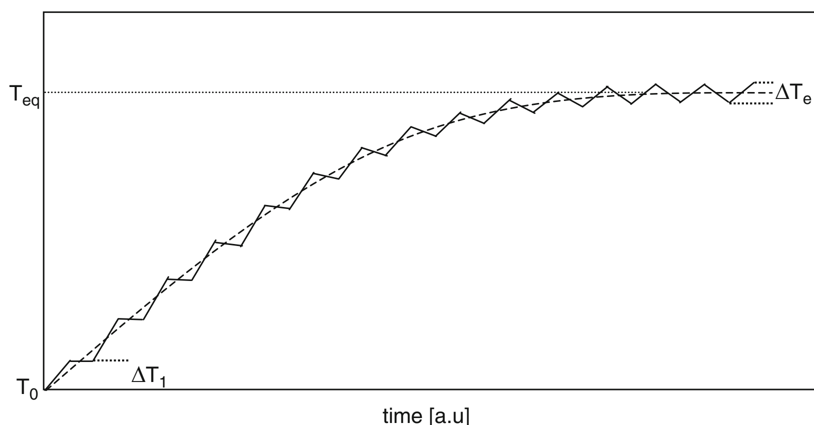

Fig. 4.1 Qualitative temperature trace at the beginning of a lock-in thermography experiment

imation, since the device has a certain heat capacity, and we have assumed a major heat resistance to the surrounding here. This cycle repeats several times, leading to a staircase-like temperature increase, until the sample temperature has increased to such an extent that the heat flow to the surrounding becomes significant. Since this heat flow is continuous and proportional to the temperature increase $(T - T_0)$, the mean sample temperature (dashed line in Fig. 4.1) will exponentially relax to its new "quasi"-equilibrium value T_{eq}, as will be shown in detail below. In the quasi-equilibrium state, the amount of heat introduced during each heating cycle equals the loss of heat to the surrounding in each whole lock-in period. Since the two heat fluxes superimpose, also the two temperature gradients (heating and cooling) can be assumed to superimpose. However, the heating is acting only within the first half of each lock-in period, but the cooling is acting over the whole periods, thus reducing the heating slope in the first half of the lock-in period in the quasi-equilibrium. Therefore, the heating and cooling temperature slopes in the quasi-equilibrium are exactly half the heating slope at the beginning of the experiment. Hence, as discussed briefly at the end of Sect. 2.7, the periodic temperature modulation amplitude in quasi-equilibrium ΔT_e is exactly half of ΔT_1 at the beginning of the experiment. This had been regarded in calculating the expected T-modulation signal of the resistively heated test device introduced in Sect. 2.7.

For Fig. 4.1, the thermal relaxation time constant was assumed to be large against the lock-in period. As long as this condition is fulfilled, the equilibrium temperature modulation amplitude ΔT_e is always half the adiabatic temperature increase within one heating cycle ΔT_1, independently of the value of the heat resistance to the surrounding. A varying heat resistance to the surrounding affects the equilibrium temperature T_{eq} and the thermal relaxation time only, but not the T-modulation ΔT_e. In the following, this condition will be called "quasi adiabatic". The term "quasi" is added here to point out that this condition is adiabatic (heat-insulated) only with respect to the lock-in frequency. Only under quasi adiabatic conditions, the temperature modulation amplitude depends solely on the introduced power distribution and on the thermal properties of the sample, but not on the heat resistance to its surrounding. In general, this makes the quantitative interpretation of lock-in thermography investigations much easier than steady-state thermography ones, where the resulting temperature contrast usually depends on the heat flow to the surrounding. It has been discussed above that any solid of a thickness well above Λ can be regarded as quasi-adiabatic, since the material below a layer of thickness Λ is more and more unaffected by the periodic temperature modulation. Therefore it is most interesting to find out whether thermally thin samples are mounted quasi-adiabatically, or not. Note that in non-destructive testing, especially in the field of thermoelastic investigations (vibrothermography, [2, 7]), the term "adiabatic conditions" is used for the case that no lateral heat exchange appears. This is the case if the lateral details to be measured are larger than the thermal diffusion length in the material. This definition is clearly different to our definition of "quasi adiabatic conditions" where the thermal diffusion length may be much larger than the size of the details to be investigated.

As a rule, below a thermally thin sample there will be a support or a heat sink with a large heat capacity or being even thermostatted, leading away the heat generated in the sample. It will be shown to be advantageous in some cases to artificially increase the thermal resistance between the sample and its support, e.g. by inserting either a woven wire net (if the electrical contact to the base has to be preserved) or a sheet of an insulator such as paper. Let us assume here that we have a homogeneously heated two-dimensional planar thermally thin sample such as a solar cell or the resistively heated test object in Sect. 2.7 of mass m and specific heat c_p, which is mounted on top of a thermostatted metal base kept at a constant temperature T_0. For calculating the thermal relaxation time constant, only the averaged temperature of the sample is of interest. Hence, for this modelling we will assume a constant heating power P starting at $t = 0$. The heat resistance between sample and thermostatted base, which can be influenced by an inserted heat insulation layer, should be R_h in units of (K/W). Then the sample temperature follows the differential equation:

$$m c_p \frac{\partial T}{\partial t} = P - \frac{T - T_0}{R_\mathrm{h}} \tag{4.5}$$

The solution to this under the starting boundary condition $T(0) = T_0$ is:

$$T(t) = T_0 + \Delta T \left(1 - \mathrm{e}^{-t/\tau}\right) \quad \text{with} \quad \begin{aligned} \Delta T &= P R_\mathrm{h} \\ \tau &= m c_p R_\mathrm{h} \end{aligned} \tag{4.6}$$

The important result is that the thermal relaxation time constant τ depends not only on the heat resistance R_h, but also on the heat capacity (hence: on mass m or the thickness, respectively) of the sample. An important question is: Is it allowed to suck a solar cell by vacuum to a metallic chuck, which is usually made by gilded copper or brass? It was discussed already in the first edition of this book that for increasing the heat resistance between sample and chuck, a thermally insulating but electrically conducting layer (like a thin woven metal net) should be inserted between cell and chuck. This question was now investigated more systematically with the following result: due to the natural roughness and the thermal properties of the screen-printed back contact of usual solar cells, the thermal contact conductivity between a solar cell and a metallic chuck in intimate contact is relatively low, in the order of 1000 $\mathrm{W/m^2K}$. If a solar cell with a thickness of 200 µm is directly sucked to a metallic base, its thermal relaxation time constant has been measured to be in the order of $\tau = 300$ ms. The corresponding corner frequency, where the T-modulation amplitude drops by $1/\sqrt{2}$, is $f_\mathrm{c} = 1/(2\pi\tau) = 0.53$ Hz. Only if the lock-in frequency is far above this corner frequency, the sample can be considered as quasi-adiabatic. Recent experiments have shown that for lock-in frequencies of 10 Hz and above, there is no measurable degradation of the lock-in thermography signals (amplitude or phase) by the direct contact to a metallic base. At a frequency of 3 Hz, the phase starts to depend on whether an additional heat resistance is inserted below the cell, but the amplitude signal still remains unaffected. Hence, for frequencies of 3 Hz and below, such a heat resistance should be inserted

for ensuring quasi-adiabatic conditions, but for frequencies of 10 Hz and above, the cell is allowed to be in direct contact to the chuck. Note, however, that according to (4.6), this condition depends on the heat capacity of the sample. If the thickness of solar cells should reduce, e.g., from 200 to 100 μm, these frequencies would increase by a factor of 2. Also if another back contact would be used (e.g., sputtered Al), these considerations might change.

If, instead of a thermally thin sample, a thermally thick one is used, a square root dependence of the averaged surface temperature is expected in the initial heating-up phase instead of an exponential one (see, e.g., Wu [114]). Hence, an infinitely thick sample will never reach really steady-state conditions. Fortunately, no real sample is infinitely thick so that, finally, the whole sample warms up and behaves like a thermally thin one. In any case the initial heating-up phase may easily be corrected, as will be shown in the following section.

4.2 Temperature Drift Compensation

The next question is to which extent the initial heating-up phase shown in Fig. 4.1 affects the results of a lock-in thermography measurement. As mentioned in Chap. 2 the whole lock-in technique (based on (2.2)–(2.11)) is actually based on the assumption that the sample is right from the beginning in a quasi-equilibrium state. Hence, we are dealing with only periodic temperature modulations, but not with a transient temperature relaxation over many lock-in periods. More precisely, the Fourier algorithm underlying the two-phase lock-in technique actually assumes an infinitely long data acquisition time. This is fulfilled in good approximation, if the data acquisition time is large against the thermal relaxation time. For example, for investigating silicon solar cells with the sample holder implying no thermal resistance, the thermal relaxation time is of the order of 300 ms. As long as the lock-in frequency is well above 3 Hz and the acquisition time is of the order of many minutes, the number of evaluated lock-in periods is large and the initial heating-up phase plays only a minor role, here. However, in many cases, one may be interested in results from only a small number of lock-in periods, obtained for an acquisition time even shorter than the thermal relaxation time. This may, for example, happen if lock-in thermography has to be used in the production control, where it is essential to have a low measurement time. In this case, the thermal relaxation at the beginning of each lock-in thermography measurement has to be considered explicitly. Moreover, it has to be checked whether, for instance, the measurement of a phase would still be reasonable for a low number of lock-in periods.

Wu [114] as well as Mangold [115] have considered the influence of the initial heating-up phase on lock-in thermography results for non-destructive testing (NDT). For example, Wu has proposed to reduce the duration of this phase by switching on a continuous cooling together with the pulsed heating, or to pre-heat the sample up to its equilibrium temperature [114]. Mangold has explicitly regarded the temperature drift within each single lock-in period by fitting the measured

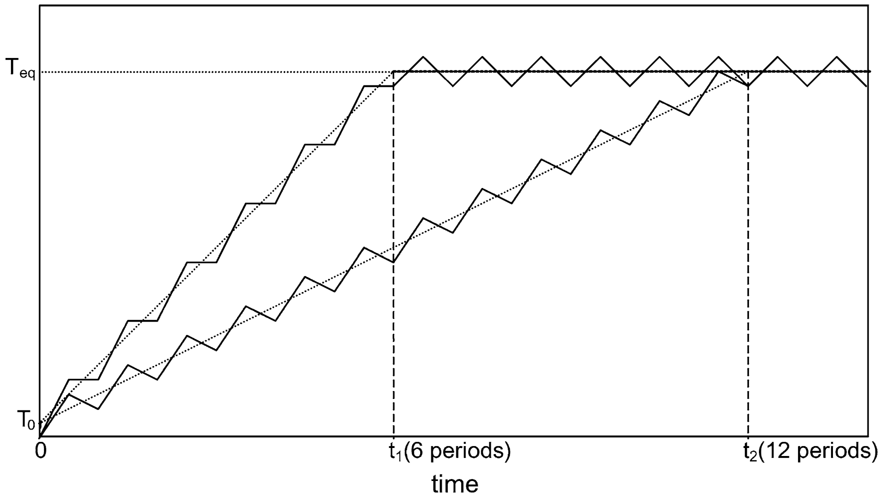

Fig. 4.2 Two hypothetical linear temperature ramps in the heating phase (Gedankenexperiment, see text)

temperature trace with an oscillating function superimposed to a slowly varying function [115]. This, however, can be realized only off-line if all measured frames are stored in the computer. In the following we will perform a "Gedankenexperiment", allowing the conclusion to be drawn that none of these expenses are necessary. Instead, it is sufficient to store just one IR image before and one immediately after the lock-in thermography measurement, and to correct the whole result afterwards for the entire temperature drift, but using only these two images.

The "Gedankenexperiment" shown in Fig. 4.2 works as follows. Let us assume two lock-in thermography experiments on a thermally thin sample similar to that shown in Fig. 4.1. During the first experiment, at the beginning a totally adiabatic behavior is assumed, hence the sample is assumed to be mounted thermally insulated. Then, after starting the experiment, at the starting temperature T_0 the pulsed bias is applied to the sample, leading to the staircase-like increase in temperature obvious already at the beginning of the trace in Fig. 4.1. If T_{eq} is reached at t_1, the heat resistance is thought to be switched on, instantly causing quasi-adiabatic and quasi-steady-state conditions. In the second experiment too, the sample is assumed to be kept thermally insulated at the beginning. In addition, a continuously constant cooling is thought to act on the sample (e.g., via a cool air-stream), the effect of which should exactly be half the average heating rate of the lock-in experiment itself. Thus, we again have a linear heating ramp at the beginning, but having a slope of half of that of the first experiment. The duration of this ramp is double ($t_2 = 2t_1$). Again, after T_{eq} is reached at t_2, the additional cooling is thought to be switched off and the heat resistance is thought to be switched on, again inducing instantly quasi-adiabatic and quasi-steady-state conditions.

The advantage of the linear temperature ramps used in these Gedankenexperiments is that the effect of the heating-up phase on the lock-in results is very easy to calculate. The two experiments sketched in Fig. 4.2 are characterized by the two temperature signals $F^a(t)$ (No.1) and $F^b(t)$ (No.2). They are lasting $N = 14$ lock-in periods each. Thus, according to 2.4 and 2.10, the two-phase lock-in correlation comprises the calculation of:

$$S_{a,b}^{0°;-90°} = \frac{1}{nN}\sum_{i=1}^{N}\sum_{j=1}^{n} K_j^{0°;-90°} F_{i,j}^{a;b} \tag{4.7}$$

with

$$K_j^{0°} = 2\sin\left(\frac{2\pi(j-1)}{n}\right) \qquad K_j^{-90°} = -2\cos\left(\frac{2\pi(j-1)}{n}\right)$$

Now, we may split the digitized temperature signals $F_{i,j}^{a;b}$ within each lock-in period i into three components: one d.c.-component $Fd_i^{a;b}$ (which is constant within each single period but differs from period to period in the linear slope parts of $F^a(t)$ and $F^b(t)$), one oscillating component $Fo_j^{a;b}$ (which is phase-coupled to the heating power and corresponds to the quasi-steady-state signal, which we are interested in, and which is the same in all periods), and one linear slope component $Fl_{i,j}^{a;b}$, having an average value of zero within each period and a constant slope in the linear slope parts of $F^a(t)$ and $F^b(t)$, but being zero in the quasi-equilibrium phases starting from periods 7 and 13, respectively:

$$F_{i,j}^{a;b} = Fd_i^{a;b} + Fo_j^{a;b} + Fl_{i,j}^{a;b} \tag{4.8}$$

with
$$\begin{aligned} Fd_i^{a;b} &= \frac{1}{n}\sum_{j=1}^{n} F_{i,j}^{a;b} \\ Fl_{i,j}^{a} &= \frac{j-\frac{n}{2}-\frac{1}{2}}{6n}\Delta T \quad [1 \le i \le 6] \quad Fl^a = 0 \quad [i > 6] \\ Fl_{i,j}^{b} &= \frac{j-\frac{n}{2}-\frac{1}{2}}{12n}\Delta T \quad [1 \le i \le 12] \quad Fl^b = 0 \quad [i > 12] \end{aligned} \tag{4.9}$$

As mentioned above, according to (4.9) the linear slope part of experiment No.1 has double the amplitude of that of experiment No.2, but it lasts for only half the number of periods. If (4.8) with (4.9) is inserted into (4.7), all sums containing the d.c. part are vanishing because of the d.c. rejection property of the lock-in routine, and the sums containing the linear part have to be performed only over the linear slope parts of $F_a(t)$ and $F_b(t)$, respectively, leading to:

$$S_a^{0^\circ;-90^\circ} = \frac{1}{Nn}\sum_{i=1}^{N}\sum_{j=1}^{n} Fo_j^a K_j^{0^\circ;-90^\circ} + \frac{1}{Nn}\sum_{i=1}^{6}\sum_{j=1}^{n} \frac{j-\frac{n}{2}-\frac{1}{2}}{6n}\Delta T K_j^{0^\circ;-90^\circ} \tag{4.10}$$

$$S_b^{0^\circ;-90^\circ} = \frac{1}{Nn}\sum_{i=1}^{N}\sum_{j=1}^{n} Fo_j^b K_j^{0^\circ;-90^\circ} + \frac{1}{Nn}\sum_{i=1}^{12}\sum_{j=1}^{n} \frac{j-\frac{n}{2}-\frac{1}{2}}{12n}\Delta T K_j^{0^\circ;-90^\circ}$$

This result can be written as:

$$S_a^{0^\circ;-90^\circ} = S_{\mathrm{eq}}^{0^\circ;-90^\circ} + \frac{\Delta T}{N} M1\left(K^{0^\circ;-90^\circ}\right) \tag{4.11}$$

$$S_b^{0^\circ;-90^\circ} = S_{\mathrm{eq}}^{0^\circ;-90^\circ} + \frac{\Delta T}{N} M1\left(K^{0^\circ;-90^\circ}\right)$$

Here, $S_{\mathrm{eq}}^{0^\circ;-90^\circ}$ are the steady-state 0° and −90° lock-in signals coming only from the oscillating signal component, which would appear if the system were in quasi-equilibrium for the whole acquisition time. This would be the result of an infinitely long measurement, which we are actually interested in. $\mathrm{M1}(K^{0^\circ})$ and $\mathrm{M1}(K^{-90^\circ})$ are the first moments of the correlation vectors $K_j^{0^\circ}$ and $K_j^{-90^\circ}$, expressed in a standardized sum representation:

$$M1\left(K^{0^\circ}\right) = \frac{1}{n^2}\sum_{j=1}^{n}\left(j-\frac{n}{2}-\frac{1}{2}\right)K_j^{0^\circ} = \frac{1}{n^2}\sum_{j=1}^{n} jK_j^{0^\circ} \tag{4.12}$$

$$M1\left(K^{-90^\circ}\right) = \frac{1}{n^2}\sum_{j=1}^{n}\left(j-\frac{n}{2}-\frac{1}{2}\right)K_j^{-90^\circ} = \frac{1}{n^2}\sum_{j=1}^{n} jK_j^{-90^\circ}$$

Here, all elements not containing j are vanishing because the sum over all weighting factors is zero. Equation (4.11) shows that the result of these lock-in experiments implying an initial heating-up phase can be described by the result of a measurement without this heating-up phase and a correction term. The decisive result of (4.11) is that for the linear temperature ramp chosen here this correction term does not depend on the slope of the temperature ramp but only on the difference between initial and final temperature $\Delta T = T_{\mathrm{eq}} - T_1$. If this holds for a linear ramp, it also holds for an arbitrary-shaped one, which can always be thought to be composed of a number of linear fractions. Since for each of these fractions, (4.11) holds and the single temperature differences are adding up, also for the whole measurement (4.11) holds, with ΔT being the total temperature drift from the beginning to the end of the lock-in thermography measurement.

Of course, since the steady-state temperature field after the lock-in measurement may be inhomogeneous owing to an inhomogeneous distribution of the heat sources, this initial heating effect has to be considered separately for each image position. Hence, (4.11) yields the final instruction how to extract the steady-state lock-in signal from the measured one for a limited number of lock-in periods measured under (at least partly) non-steady-state conditions, thus correcting a lock-in thermography result for any temperature drifts occurring during the measurement:

$$S_{\mathrm{eq}}^{0^\circ;-90^\circ}(x,y) = S_{\mathrm{meas}}^{0^\circ;-90^\circ}(x,y) - \frac{\Delta T(x,y)}{N}\, M1\left(K^{0^\circ;-90^\circ}\right) \tag{4.13}$$

For the number n of frames chosen per lock-in period the first moments of both correlation vectors $\mathrm{M1}(K^{0^\circ})$ and $\mathrm{M1}(K^{-90^\circ})$ have to be calculated according to (4.12), which are simply two different numbers. Before the lock-in measurement and immediately after it, at least one image has to be measured and stored. The difference between these two images $\Delta T(x,y) = T^{\mathrm{after}}(x,y) - T^{\mathrm{before}}(x,y)$ has to be multiplied by the corresponding moment and divided by the total number of averaged lock-in periods N to obtain the local correction values for $S^{0^\circ}(x,y)$ and $S^{-90^\circ}(x,y)$. It is obvious that, if the sample temperature stabilizes during the measurement, for large N the correction in (4.13) becomes smaller and smaller, finally being negligible. For the same reason, as a rule, there is no risk that the signal-to-noise ratio decreases by this correction process. Note that according to (2.28) in Sect. 2.6, the temperature noise level drops with $1/\sqrt{N}$, but the noise introduced by the drift correction according to (4.13) drops faster with $1/N$, provided that the quasi-steady-state equilibrium is reached during the measurement. Hence, except for very small N, no additional noise is introduced by the procedure (4.13). Note that according to (4.13) the temperature drift disturbs most for low lock-in frequencies, since here for a given acquisition time the number of averaging periods N is lowest.

It can easily be calculated which maximum possible error is to be expected, if the initial heating-up phase is not corrected, and how effectively this error can be corrected by the procedure described. The most critical case is that of a thermally thin homogeneously heated sample, which is totally heat-insulated as had been assumed at the beginning of the Gedankenexperiment No. 1 of Fig. 4.2. Here, no quasi-equilibrium is reached within the acquisition time, and the whole experiment is performed in the linear heating-up phase. As Fig. 4.2 shows, in this case the temperature drift ΔT is proportional to the number of lock-in periods N, hence here, the correction term in (4.13) is independent of the acquisition time. Regarding the fact that the equilibrium temperature modulation ΔT_{e} would be half of one temperature step in one lock-in period under adiabatic conditions ΔT_1 (see Fig. 4.1), worst, there will be a total temperature drift of:

$$\Delta T = 2N\Delta T_{\mathrm{e}} \tag{4.14}$$

Since homogeneous heating is assumed here, under quasi-steady-state conditions the phase of the temperature modulation relative to the periodic heating should be

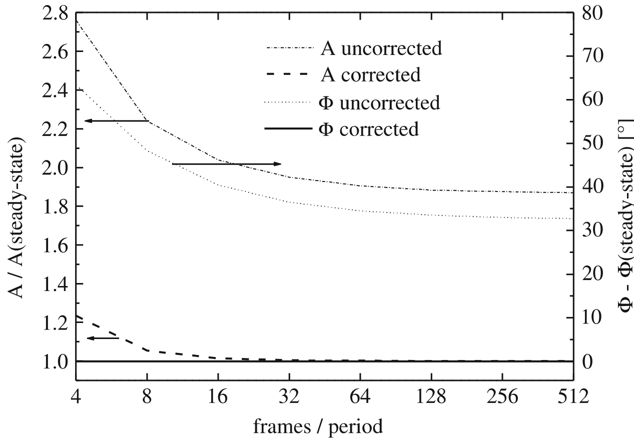

Fig. 4.3 Amplitude and phase errors of the simulation of the action of a measurement induced temperature drift under adiabatic conditions with and without T-drift correction

exactly $-90°$, hence the in-phase signal $S^{0°}$ should be zero, and the amplitude of the basic harmonic of the quadrature signal be for this sawtooth-signal should be $S^{-90°} = 4/\pi^2 \, \Delta T_e = 0.41 \Delta T_e$ (see discussion for (2.34) in Sect. 2.7). This worst case was simulated using (4.7) and (4.12)-(4.14) for different numbers of frames per lock-in period starting from $n = 4$ up to $n = 512$ in steps by a factor of two. As mentioned above, the result of this simulation does not depend on the number of averaged lock-in periods N. Respective results are summarized in Fig. 4.3.

This simulation shows that in this most dangerous case of a thermally insulated and homogeneously heated body the measurement error due to measurement-induced temperature drift is indeed striking. The uncorrected results are considerably corrupted by the temperature drift, whereby the difference to the equilibrium values becomes even larger for a lower number of frames per lock-in period. The values corrected by using (4.12) and (4.13), however, are most reliable. Especially the phase angle is perfectly retrieved even down to $n = 4$. Note that the amplitude errors shown in Fig. 4.3 are referring to the amplitude of the basic harmonic in the steady-state case. The slightly larger amplitude of the corrected signal for lower n is due to the inherent inaccuracy of the digital lock-in procedure, as the harmonic function can be modelled accurately only to a certain extent with a low number of sampling points (see Sect. 2.5). However, as we see from Fig. 4.3, if the T-drift is properly corrected this inaccuracy does not generate any phase error, and even for $n = 4$, the amplitude error is only about 20% and quickly reduces, with the number of frames increasing per lock-in period. In fact, the 4-point correlation procedure does not measure the amplitude of the harmonic component of the oscillation but rather the pk-pk amplitude of the staircase temperature curve, which is indeed exactly ΔT_e here (see Fig. 4.2), causing formally an amplitude value of 0.5 ΔT_e instead of 0.41 ΔT_e. It is interesting to note that with increasing number of frames per period (hence with increasingly accurate approximation of the harmonic

correlation function), the first moment of $K^{-90°}$ converges to zero. Hence, for large n, only the 0°-signal has to be corrected, but the −90°-signal is not influenced by the temperature drift. This is due to the fact that the first moment of the cos-function is zero, but that of the sin-function is not.

It should be noted that the case modelled in Fig. 4.3 (homogeneously heated thermally insulated sample) is the very case where the highest possible temperature drift can be expected. Whenever the heat is led away, the surface temperature ramp becomes shallower than assumed in Fig. 4.3, and the error in the uncorrected results becomes smaller. Heat conduction may appear e.g. into the depth of a thermally thick sample, or laterally, if there are local heat sources, which also happens in a thermally thin sample. It should also be noted that, although this result has been demonstrated for a thermally thin sample, it is applicable to any sample and any heat source geometry. The correction procedure using (4.12) and (4.13) just formally corrects the result of any lock-in thermography experiment for a temperature drift, which is assumed to be linear only within one period. Thus, it can also be applied to non-destructive testing or to thermomechanical investigations, whenever some temperature drift has to be regarded. It may even be applicable to undersampling (see Sect. 2.4) and asynchronous lock-in experiments, commonly used for thermomechanical investigations (vibrothermography). Also here, for the same physical reasons, it can be assumed that the T-drift induced error only depends the total local T-drift $\Delta T(x, y)$, but not on its time dependence. Hence, also here the drift-induced error may be corrected by correlating a linear T-ramp from 0 to $\Delta T(x, y)$ over the whole measure time, and substracting the result from the measured one.

The interesting result of this investigation is that, in general, lock-in thermography can be performed even with a small number of lock-in periods down to one period, if the results are drift-corrected using (4.12) and (4.13). The drift-corrected results even of a one-period measurement are equivalent to that of a long lock-in measurement, at least for a homogeneously heated body considered here, whith no lateral heat conduction taking place. Of course, it has to be assumed that a one-period measurement will differ from longer-lasting lock-in measurements whenever in the image thermal waves are running in lateral direction over a longer distance. It is plausible that thermal waves cannot run over a longer distance within only one lock-in period. Nevertheless, the improved spatial resolution and the fact that the result does not depend on the heat flow to the surrounding (leading to quantitatively interpretable results) are preserved also for a low number of lock-in periods down to $N = 1$. This paves the way for high speed lock-in thermography e.g., in production control. Indeed, meanwhile it has been demonstrated both by the simulations and experimentally that optically excited lock-in thermography (noncontacting, forward bias, see Sect. 6.2.2) can be used for detecting ohmic shunts in real solar cells at an acquisition time below 1 s [98]. If the cell can be contacted and a reverse bias of about 10 V can be applied, ohmic shunts can be detected by lock-in thermography implying only four image frames even within 10 ms [36]. In this case, drift correction was not applied and also not necessary since this was DLIT and not Voc-ILIT as for [98], where the influence of homogeneous heating had to be corrected.

4.3 Thermal Waves of Point Sources

Since in the previous section, it was shown how measurement-induced (and also other) temperature drifts can be compensated by lock-in thermography, in the following, we will generally assume that the measurement is performed under quasi-steady-state conditions. Hence, we will again assume only a harmonic heat introduction. In Sect. 4.1 the plane thermal wave was introduced as the one-dimensional solution to the heat diffusion equation in a homogeneous and isotropic medium (4.3). Another even more general solution is the thermal response of a harmonically oscillating point heat source in 3-dimensional space, which is a spherical thermal wave expressed in spherical coordinates ($r = \sqrt{x^2 + y^2 + z^2}$):

$$T(r,t) = \frac{A}{r}\,\mathrm{e}^{-r\sqrt{\mathrm{i}\omega c_p \varrho/\lambda}}\,\mathrm{e}^{\mathrm{i}\omega t} = \frac{A}{r}\,\mathrm{e}^{-r/\Lambda}\,\mathrm{e}^{\mathrm{i}(\omega t - r/\Lambda)} \tag{4.15}$$

The thermal diffusion length Λ is that defined in (4.3) of Sect. 4.1. The amplitude factor A can be calculated from the oscillating power of amplitude P_0 by calculating the heat flow through a spherical surface with a diameter approaching zero. In this approximation ($\Lambda \to \infty$), the thermal wave can be described by

$$T(r,t) = \frac{A}{r}\,\mathrm{e}^{\mathrm{i}\omega t} \tag{4.16}$$

leading to a heat flow of:

$$P_0\mathrm{e}^{\mathrm{i}\omega t + \mathrm{i}\varphi} = 4\pi r^2 \lambda - \frac{\partial T}{\partial r} = 4\pi\lambda A\mathrm{e}^{\mathrm{i}\omega t} \tag{4.17}$$

Here, there is no phase shift between the oscillating power and the temperature oscillations ($\varphi = 0$). According to (4.17) the amplitude factor A is $A = P_0/4\pi\lambda$. However, if the power source is on the top surface of a semiinfinitely extended solid, which usually occurs in investigating electronic components, the heat can diffuse only into one half space, leading to a doubled amplitude factor of:

$$A = \frac{P_0}{2\pi\lambda} \tag{4.18}$$

A radial profile of the temperature field around a point heat source will be shown in Fig. 5.1 in Sect. 5.1. As (4.15) shows, the temperature field around a point heat source diverges in the source position. Of course, in real physics this divergence does not appear, since there are no ideal point heat sources in nature. Any heat source has a finite extension, otherwise its energy density would be infinite. Nevertheless, the point source model is very useful for modelling real heat sources, as will be shown also in the following sections. Whenever the real extension of a heat source is smaller than the spatial resolution of the thermal imaging system, this source can be described as a point source. As will be shown below, the divergence in source

position can easily be cancelled by averaging the thermal signal across one pixel area, which is done also in reality by the IR camera.

The next question is how this temperature field changes, if not a semiinfinite solid but a plate of a certain thickness d is considered, which is no longer large against Λ. This problem, as any other diffusion problem dealing with external and internal surfaces, can be solved by using the technique of mirror sources. In a diffusion problem, an outer surface is by definition a plane, with no diffusion occurring in the direction perpendicular to this plane. If this surface is a flat plane, a body containing this plane and a certain heat source distribution can be modelled as an extended body without this plane, but having additional heat sources of the same size as the original ones in positions mirrored in the surface plane. Then, in the plane position, the heat flows of the source and of the mirror source in the direction perpendicular to the plane cancel out in any position, which is equivalent to the insertion of a surface. If this plane is not flat, the construction of the heat sources becomes more complicated, but the principle remains the same. This mirror source technique works if diffusion barriers are regarded in any steady-state and non-steady-state diffusion problem. In the following, it will be applied to model the thermal waves emerging from an oscillating point heat source at the surface of a homogeneous and isotropic infinitely extended solid plate of thickness d.

The geometrical situation of this problem is sketched in Fig. 4.4. For a better demonstration, the point heat sources are displayed as bowls of certain dimensions. As mentioned above, for calculating the amplitude factor of the thermal wave at the top of a semi-infinite body, this temperature amplitude is double that of an infinite body. This is exactly the introduction of the first mirror source of quantity $P_1 = P_0$ in the very position of the original heat source, which was assumed to be located at the upper surface. In the same way, the lower surface can be regarded by introducing a second mirror source P_2, which compensates the vertical heat flow of P_0 and P_1 through the lower surface of the sample. Hence, the power of this source has to be $P_2 = P_0 + P_1 = 2P_0$. However, also this mirror source has to be mirrored by the upper surface again, leading to $P_3 = P_2$ at the top and so on, just as two

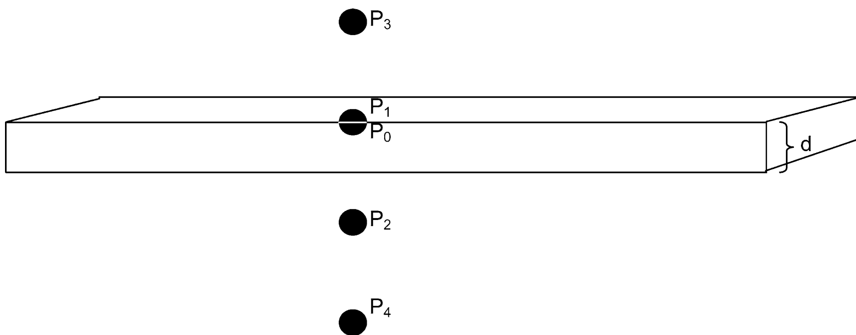

Fig. 4.4 Point heat source on the surface of a body together with mirror sources

parallel-lying optical mirrors generate an infinite multiple reflection of any object positioned in between.

It depends on the ratio d/Λ how many mirror sources have to be regarded for a realistic modelling of the temperature field at the upper surface. P_1 always has to be regarded, since it is in the same position as P_0. If d reaches the order of Λ, also P_2 and P_3 have to be regarded. If the temperature field at the surface is given in cylindrical coordinates, with the origin being in source position, the surface temperature field is calculated by using (4.15) as:

$$T(r,t) = \frac{P_0}{2\pi\lambda}\left(\frac{1}{r}\mathrm{e}^{-r/\Lambda}\mathrm{e}^{\mathrm{i}(\omega t - r/\Lambda)}\right) + \frac{2}{\sqrt{r^2+4d^2}}\mathrm{e}^{-\sqrt{r^2+4d^2}/\Lambda}\mathrm{e}^{\mathrm{i}(\omega t-\sqrt{r^2+4d^2}/\Lambda)}. \tag{4.19}$$

For an even lower thickness of the sample, also P_4 and P_5 have to be regarded, and so on. If the sample is thin against Λ the sample is thermally thin as defined in Sect. 4.1. For the limit $d \to 0$ an infinite number of mirror sources had to be regarded, if the calculation were carried out in 3-dimensional space. However, in this case the geometrical problem reduces from a 3-dimensional problem to a 2-dimensional one. The chain of mirror sources yields an infinitely long heat line source, and the heat spreads only radially from this vertical line, revealing a cylindrical symmetry here. Then the heat diffusion equation has to be solved in cylindrical coordinates. Its solution for a harmonically oscillating line source in isotropic and homogeneous materials, converging to zero for $r \to \infty$, is the modified BESSEL function of second kind of order zero $K_0(z)$ [113]. This complex function can be described by the so-called Kelvin functions ker(x) and kei(x):

$$\begin{aligned} T(r,t) &= A\ K_0\left(r\sqrt{\frac{\mathrm{i}c_p\varrho\omega}{\lambda}}\right)\mathrm{e}^{\mathrm{i}\omega t} \\ &= A\left(\ker\left(\frac{r\sqrt{2}}{\Lambda}\right) + \mathrm{i}\ \mathrm{kei}\left(\frac{r\sqrt{2}}{\Lambda}\right)\right)\mathrm{e}^{\mathrm{i}\omega t} \end{aligned} \tag{4.20}$$

Again Λ is the thermal diffusion length (4.3). The functions ker(x) and kei(x) are not analytical. Usually, within certain argument ranges they are approximated by polynoms [116]. In Fig. 4.5, their shape is displayed together with the absolute amplitude value of the corresponding thermal wave ($\sqrt{\ker(x)^2 + \mathrm{kei}(x)^2}$) assuming $\Lambda = 3$ mm.

Both ker(x) and kei(x) are oscillating functions the amplitudes of which strongly reduce with increasing x. For $x \to 0$, ker(x) diverges as $-\ln(x/2)$, whereas kei(x) approaches the finite value of $-\pi/4 \simeq -0.79$. These analytic approximations allow us to calculate the amplitude factor A of (4.16) for an oscillating power source of an amplitude P_0:

$$\begin{aligned} P_0\mathrm{e}^{\mathrm{i}\omega t+\mathrm{i}\varphi} &= 2\pi r d\lambda - \frac{\partial T}{\partial r} = 2\pi d\lambda A\mathrm{e}^{\mathrm{i}\omega t} \\ \text{with}\quad A &= \frac{P_0}{2\pi d\lambda} \end{aligned} \tag{4.21}$$

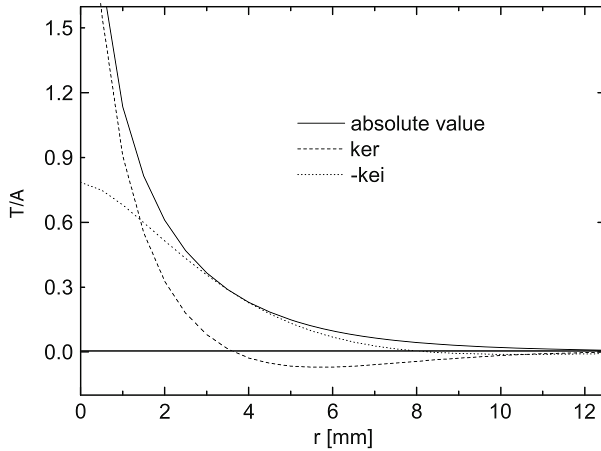

Fig. 4.5 Profiles of the Kelvin functions ker and -kei together with the absolute value of $K_0(z)$, describing a cylindric thermal wave, thermal diffusion length 3 mm

As in the 3-dimensional case, there is no phase shift between the oscillating heat introduction and the temperature modulation in source position ($\varphi = 0$). For $x \to \infty$, the functions ker and kei describe the real and the imaginary part of damped radial waves, the amplitude of which exponentially decays with the thermal diffusion length Λ.

As described in Sect. 2.3, the result of a lock-in thermography measurement can be presented in different ways: Either the images belonging to a well-defined phase are displayed (0°- and −90°-image), or the phase-independent amplitude and phase-images are calculated from these images using (2.11). We will use the results of this section and the following one in Sect. 5.1 "Measurement Strategies" to discuss which conditions of measuring and displaying are most effective for visualizing certain types of heat sources. As Fig. 4.5 shows, the 0°-image (described by the ker-function) shows a sharp maximum in the position of a point source and a considerable overshoot into the negative for $r > \Lambda$. The −90°-image described by the kei-function, on the other hand, shows only a weak maximum in source position, and a pronounced "halo" around, extending up to a distance of $2\,\Lambda$. The oscillations of this phase component towards longer r are already so strongly damped that they remain nearly invisible. The phase-independent amplitude, which is composed of both components, contains both the sharp maximum in source position, and the halo around the source. It does not show any oscillations for a single point source. The spherical thermal wave around a point heat source in a thermally thick sample (4.15) behaves qualitatively similarly, except that its divergence at $r = 0$ is even more strongly pronounced.

Note that for both thermally thin and thermally thick samples, the thermal response around a point heat source shows a distinct peak in source position even in the limit $\Lambda \to \infty$, which corresponds to steady-state measurement conditions ($f_{\text{lock-in}} \to 0$). Hence, even if the thermal diffusion length Λ is well above the

aspired resolution of a lock-in thermography experiment, point heat sources remain visible down to steady-state conditions, as all previous steady-state thermographic device tests have shown. A physical analogy to this is the old discussion whether the minority carrier diffusion length is a spatial resolution limit for EBIC (electron beam-induced current) measurements and CL (cathodoluminescence) imaging. Practical experiences as well as the simulations of Donolato [117] have shown: If the defect to be observed is lying at the surface (what we are also assuming here), the spatial resolution of these methods may be much better than the minority carrier diffusion length. In fact, the maximum temperature signal measured in the position of a point heat source (where the approximations of (4.16) and (4.21) for $\Lambda \to \infty$ hold) should be independent of $f_{\text{lock-in}}$ for thermally thick samples and nearly independent for thermally thin samples, but the disturbing "halos" around each local heat source are strongly reducing with increasing lock-in frequency. As the following section will show, this prediction does not hold for spatially extended heat sources, where the thermal diffusion length really represents a spatial resolution limit.

4.4 Thermal Waves of Extended Sources

The simplest case of an extended heat source is a homogeneously heated area, which extends over a certain region. If the size of this region is well above the thermal diffusion length Λ, within this region the solutions for an infinitely extended heated area can be applied. For example, an extended heated area on a thermally thin sample behaves like a homogeneously heated sample, which was discussed in Sect. 2.7. For simulating the temperature signal of such a sample, we only need the definition of the heat capacity:

$$P(t) = mc_p \frac{\partial T}{\partial t} = P_0 \mathrm{e}^{\mathrm{i}(\omega t + \pi/2)} \tag{4.22}$$
$$T(t) = \frac{P_0}{mc_p\omega} \mathrm{e}^{\mathrm{i}\omega t} = \frac{p_0}{\varrho d c_p \omega} \mathrm{e}^{\mathrm{i}\omega t}$$

(p_0 = areal power density, ϱ = mass density, d = sample thickness). Hence, with respect to the power the temperature is delayed by 90° ($\pi/2$), and the amplitude factor here is proportional to $1/f_{\text{lock-in}}$. This strong frequency dependence of the amplitude factor of a 2-dimensional heat source in a thermally thin sample affects the visibility of such heat sources significantly. As shown in the previous section, the temperature signal in the position of a point source is almost independent of the lock-in frequency. Hence, if both strongly localized heat sources and spatially extended heat sources are present in one sample, which usually occurs in investigating solar cells, the spatially extended signal can often be observed solely by using a low lock-in frequency. On the other hand, if the measurement is performed at a high frequency, the strongly localized heat sources usually remain visible, whereas the spatially extended signal is often embedded in noise. It will

be shown in the simulations at the end of this Section that, for spatially extended heat sources, the spatial resolution is indeed limited by the thermal diffusion length.

In Sect. 4.1 we discussed that the 1-dimensional thermal wave in 3-dimensional space emerges from an infinitely extended, flat heated surface into the depth. Equation (4.3) correctly describes the thermal signal for a heat source, which is spatially extended over more than Λ on the surface of a thermally thick sample. As described there, with respect to the power modulation, the thermal signal is delayed by 45° ($\pi/4$), and the amplitude factor is:

$$A = \frac{p_0}{\sqrt{\lambda \omega c_p \varrho}} \tag{4.23}$$

As discussed in Sect. 4.1, this amplitude factor is only proportional to $1/\sqrt{f_{\text{lock-in}}}$. Hence, the difference between the visibility of spatially extended and localized heat sources at high lock-in frequencies in thermally thick samples is lower than in thermally thin samples. Of course, if $f_{\text{lock-in}}$ becomes so small that Λ reaches the order of the sample thickness d, any thermally thin sample becomes thermally thick.

The 1-dimensional solution also holds for a line heat source lying in a thermally thin sample (2-dimensional case), which can be imagined to be a vertical cut through a 3-dimensional body. In the 2-dimensional case, the wave runs laterally into both directions, i.e. left and right from the heated line into the plane, like in the 3-dimensional case away from a heated plane, which is embedded within an infinitely extended body. Thus, the thermal wave of a line source in a thermally thin sample can be described by (4.3) in Sect. 4.1, with z being the lateral distance from the heated line. If p_0^l is the amplitude of the oscillating power density per unit length, the amplitude factor here is:

$$A = \frac{p_0^l}{2d\sqrt{\lambda \omega c_p \varrho}} \tag{4.24}$$

This amplitude factor is only half of that of (4.4) since here the wave is running into both directions, hence we do not have to regard the mirror source at the surface. Only if the line heat source coincides with a lateral edge of the sample, a lateral mirror source has to be regarded and the amplitude factor doubles compared to (4.24). In any case, the phase of the temperature modulation in source position is delayed by 45° (π/4), to the power modulation phase (see 4.4). The decisive difference between the behaviour of the point source and the line source in thermally thin samples is that the temperature signal of the line source does not diverge in source position. Its amplitude only exponentially decays with the distance to the line source having the decay length of Λ (see 4.3). Thus, the visibility of a line source in a thermally thin sample, which may be, for instance, the edge current of a solar cell, strongly depends on the thermal diffusion length Λ, and thus, via (4.3), on the lock-in frequency.

A line heat source on top of a 3-dimensional thermally thick sample behaves qualitatively differently to that in a thermally thin sample. As Fig. 4.6 shows, this geometry is equivalent to the cylindrical symmetry, which has been discussed for

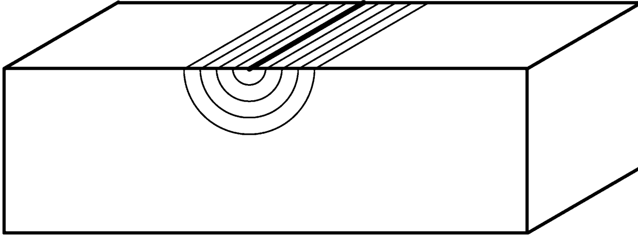

Fig. 4.6 Oscillating line heat source at the surface of an extended body

the point heat source in a thermally thin sample. Here, the heated line is lying at the top surface. The cylindrical waves are running into the depth parallel to the line, and at the surface they run into both directions from the heated line. Hence, for describing the thermal wave at the surface, (4.20) of the previous section can be used, with r being the distance from the line source. If p_0^l again is the amplitude of the oscillating power density per unit length, in analogy to (4.21), the amplitude factor then is:

$$A = \frac{p_0^l}{\pi \lambda} \tag{4.25}$$

This amplitude factor is a factor of two larger than that of (4.21), since here the heat is running only into one half-space. Hence, here again we have to regard the mirror heat source at the surface. The general properties are as described for the point source in thermally thin samples, hence the phase shift between heat introduction and temperature modulation in source position is zero, with the thermal signal diverging in source position. Hence, in thermally thick samples, thermal line sources lying at the surface can be observed at both high and low lock-in frequencies and even in steady-state thermography, which is in contrast to the case of thermally thin samples discussed above. As for the point heat sources discussed in the previous section, the signal in the very position of a line source in a thermally thick sample should almost be independent of $f_{\text{lock-in}}$ for thermally thick samples and nearly independent for thermally thin samples, but the halo around this source becomes smaller with increasing lock-in frequency.

Only for some special cases of extended heat sources, a complete solution to the non-steady-state heat diffusion equation can be given. In the following we will use the point spread function algorithm to model spatially extended oscillating heat sources in a finite element approximation as a superposition of the thermal waves of elementary point sources. This model is based on the fact that heat diffusion is a linear process. Hence, the sum of two solutions of the heat diffusion equation is also a solution to the heat diffusion equation. Thermal waves linearly superimpose. Of course, in order to correctly regard the phase relations between different thermal waves, which cause interference phenomena, this superposition has to be described in complex space. Hence, if all different local heat sources within the sample are oscillating in-phase (which usually happens since all are driven by the same oscillating bias), the real and the imaginary parts of all emerging thermal waves have to

be superimposed separately to get the resulting oscillating temperature field. In our model, extended heat sources are modelled by an ensemble of point sources lying in the centers of the meshes of a square network spanning across the surface of the sample. For modelling lock-in thermography images, as a rule, this network corresponds to the pixels of the thermocamera used. Hence for modelling a 128×128 pixel image, up to 16384 elementary heat sources can be used to model extended heat sources within the imaged area. In the following, we will assume that the heat sources are all lying either at the surface of the sample, or within one plane at a well-defined depth of a 3-dimensional sample. We will also restrict our simulations to isotropic and homogeneous materials.

Finite element simulations are a standard method to model complex geometries, where no complete mathematical solution is known. There are commercial programs available (e.g. ANSYS [118], COMSOL [119]), which allow one to perform also non-steady-state thermal simulations. In a usual finite element model, the sample is divided into a network, with the knots being the active elements. Hence, the temperatures in the knots are the variables, the power is introduced into these knots, the knots are characterized by a certain heat capacity, and the thermal conduction in the sample is described by heat resistances between neighboring knots. The particular advantage of this model is that it easily allows one to describe bodies of complicated symmetry as well as thermally inhomogeneous bodies such as layered structures.

The point spread function (PSF) based finite element model described in the following, however, works differently. It was developed by Konovalov and Breitenstein [120, 121] for enabling the spatial deconvolution of thermograms in homogeneous and isotropic bodies (see Sect. 4.5.2). This model works in real space and is based on the exact solution of the thermal diffusion equation for an oscillating point heat source. The basic idea of this model is to replace extended heat sources by a regular array of point sources, and to use the exact description of the temperature field of these point sources for describing the complex temperature field of an extended heat source.

In the following, we will deal only with the local parts of the thermal signal $T(r)$, which are the values of the time-dependent thermal signal $T(r,t)$ for $t = 0$. Since $\exp(\mathrm{i}\omega t)$ is 1 for $t = 0$, the local part of T is simply obtained from the complete T-signal by skipping the factor $\exp(\mathrm{i}\omega t)$, and vice versa. Let us assume that the number of rows of our image is R, the number of lines is L, and the pixel distance (referring to the position at the sample) is D. Then (r,l) are the indices of one pixel with $1 \leq r \leq R$ and $1 \leq l \leq L$. The so-called point spread function (PSF, sometimes also called Green's function) is given by two matrices $Tp_{i,j}^{\mathrm{re,im}}$ for both the real and the imaginary part of the temperature signal in real space, of an oscillating point source of one unit power in position (0,0). These matrices are square-shaped of $1 - M \leq i; j \leq M - 1$ in dimension. Hence, the point heat source is assumed to be positioned in the center of the matrices. For symmetry reasons, it is sufficient to describe each matrix by the data of one quadrant (including the center point), which is a square matrix of dimension M. The pixel distance of the image and that of the PSF matrix are assumed to be the same. The elements of the PSFs are calculated for thermally thick and thermally thin samples from the real and the imaginary parts of

(4.15) and (4.20), respectively, using $r = D\sqrt{i^2 + j^2}$, $t = 0$, and z as the depth of the assumed heat sources below the surface in the 3-dimensional case. Again the thermal diffusion length Λ according to (4.3) is used. For the amplitude factors (4.18) and (4.21), respectively, one unit power has to be inserted for calculating the PSF matrices. As mentioned above, since the data in these matrices are rotation-symmetrical, only one quarter of the PSF has to be calculated, and the others are obtained by symmetrical mirroring of the solution. Beyond the definition range of the PSF matrices, the thermal signal of the central point source is assumed to be zero. Hence, depending on Λ, the dimension M of the PSFs has to be chosen large enough to fulfil this requirement to a sufficient degree. One approximation of this model is that the thermal signal within each pixel of the PSF is assumed to be constantly that of its central value. This is a good approximation as long as the pixels are small against the thermal diffusion length Λ and are sufficiently distant to the point source. The only mathematical problem arises from the two elements $Tp_{0,0}^{\mathrm{re,im}}$ in the center of the two PSF matrices, which describe the action of the point heat source in very source position. At least the real parts of (4.15) and (4.20) are diverging, and the variations of the functions across this pixel are definitely strong, so that we cannot use the values of the functions in source position directly. Hence, we use an approach outlined at the beginning of the previous section: For calculating the temperature signal measured by a thermocamera in the position of a point source, we have to simulate the operation of the camera. The camera averages the total irradiation across one pixel. Therefore, also here the two matrix elements $Tp_{0,0}^{\mathrm{re}}$ and $Tp_{0,0}^{\mathrm{im}}$, where the variations within the pixel are strongest, are calculated as the average of the corresponding functions across the pixel $(0, 0)$. For further simplification, since the thermal waves are radial-symmetrical, we replace the square integration field by a circular one having the same area:

$$Tp_{0,0}^{\mathrm{re}} = \frac{1}{D^2} \int_0^{D/\sqrt{\pi}} 2\pi r \,\mathrm{Re}(T(r, t = 0))\, dr \tag{4.26}$$

$$Tp_{0,0}^{\mathrm{im}} = \frac{1}{D^2} \int_0^{D/\sqrt{\pi}} 2\pi r \,\mathrm{Im}(T(r, t = 0))\, dr$$

In our model, the matrix $P_{r,l}$ describes the distribution of the assumed elementary power sources across the image field. If p(x,y) is the lateral distribution of the power density, the matrix elements $P_{r,l}$ are the product of the local power density times the pixel area. Then, the complex local temperature signal in the position (r, l) is given by the summation over the contributions of all elementary heat sources in the surrounding:

$$T_{r,l} = \left(T_{r,l}^{\mathrm{re}} + \mathrm{i}T_{r,l}^{\mathrm{im}}\right) \tag{4.27}$$

$$\text{with} \quad T_{r,l}^{\text{re}} = \sum_{r'=1-M}^{M-1} \sum_{l'=1-M}^{M-1} P_{r-r',l-l'} \, Tp_{r',l'}^{\text{re}}$$

$$\text{and} \quad T_{r,l}^{\text{im}} = \sum_{r'=1-M}^{M-1} \sum_{l'=1-M}^{M-1} P_{r-r',l-l'} \, Tp_{r',l'}^{\text{im}}$$

If the phase image or the phase-independent amplitude image has to be simulated, this can be done using the real (0°) and the imaginary (90°) image and (2.8) of Sect. 2.2. The −90°-image is the inverse of T^{im}. Mathematically, (4.27) is equivalent to the convolution of the power density distribution $p(x, y)$ with the two-dimensional PSF. Note that $P_{r,l}$ is defined only within the indices $1 \leq r \leq R$ and $1 \leq l \leq L$. In (4.27), however, depending on r and l, the summation may range from $2 - M$ up to $R + M - 1$ or $L + M - 1$, respectively. Hence, for performing the convolutions (4.27) we need matrix elements beyond the borders of our image, which have not been defined yet. Physically, these elements belong to heat sources, which are possibly outside the imaged region and which may still influence the thermal image owing to the lateral heat conduction in the sample. There are two alternative options to fill these elements. One option is to set them generally at zero, assuming that there are no heat sources outside the image field. This, however, may cause errors in the simulation whenever there are heat sources outside the image field. For example, if the whole sample contained a homogeneous heat source and only some part of it were imaged, this option would cause errors in the simulation of the border region, as will be demonstrated below.

These errors can be avoided by our second option, in which lateral mirror sources are introduced outside the image field. This option is illustrated in Fig. 4.7. First, the four outer stripes of the width of $M - 1$, separated by dotted lines, are mir-

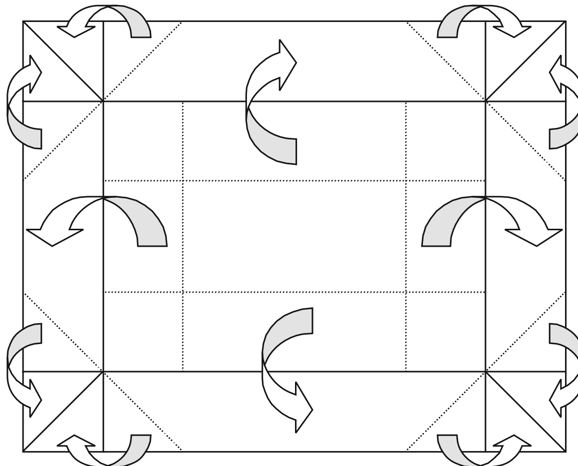

Fig. 4.7 Introduction of mirror heat sources outside the image field of a simulation

rored to outside the image field (large arrows). Then, also the corner areas are filled with triangle-shaped data fields as symbolized by the smaller arrows. In this way, the data fields are connected at the boundaries without any steps, except for the four diagonal-lying boundaries in the outer corners, which should be least critical. Another physical motivation to mirror the border-near heat sources to outside is given if the area investigated has exactly the same lateral size of the sample investigated, i.e. if the borders of the image region are also the edges of the sample. Then, the outer edges prevent any lateral heat flow out of this area. As discussed in the previous section, this has to be regarded mathematically by introducing mirror sources outside the considered area, what we are exactly doing in our second option. Without these mirrored heat sources, for instance the simulation of the thermal signal of edge shunts of solar cells would be too weak by a factor of 2, since the model would assume a heat flow out of the image region. If the image region coincides with the whole sample region, the option to mirror the border-near heat sources to outside has to be employed for a realistic simulation of lock-in thermography results.

As an example of such a lock-in thermography simulation, Fig. 4.8 shows the 128×128 pixel image of an assumed ensemble of differently shaped heat sources together with the lock-in simulation of both the 0°-image and the −90° image. These simulations, as well as the image deconvolutions presented in Sect. 4.5.2, were performed by using the software "DECONV", which is available from one of the authors (O. B.). One line source segment was located at the border of the area

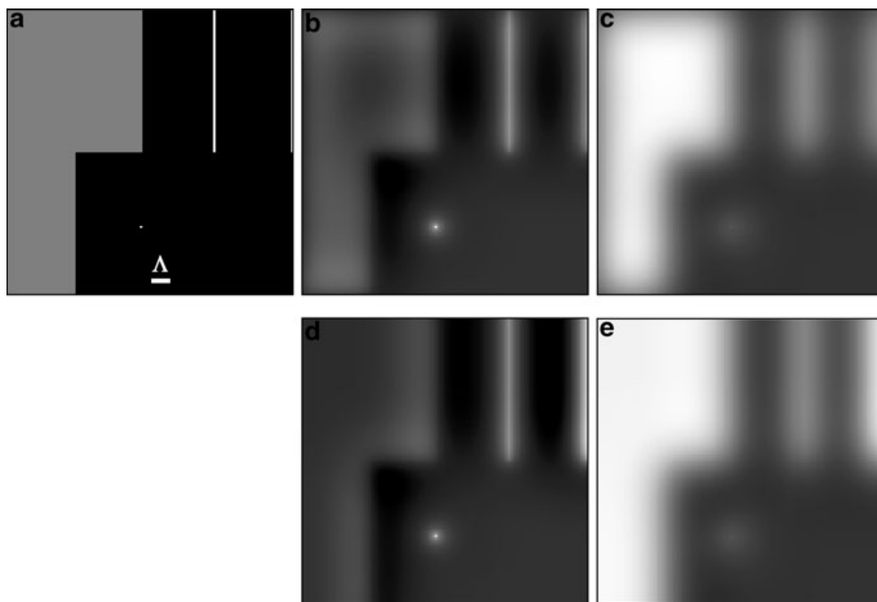

Fig. 4.8 Assumed power distribution (**a**) and simulated 0°-image (**b**) and −90°-image (**c**) without assuming mirror heat sources, and assuming mirror sources (**d**, **e**). All thermograms are displayed in the same scaling, the zero signal is in dark grey (as shown in the bottom right corner)

in order to check the influence of the heat mirroring at the border. A thermally thin sample was assumed, with the thermal diffusion length being $\Lambda = 10$ pixel, and the dimension of the PSF matrix was chosen to be $M = 40$, hence the PSF was defined up to a distance of four diffusion lengths from the power sources. The pixel-related power source amplitudes of the 2-dimensional area, of the lines, and of the single dot were chosen to be in the relation of $1:10:80$ in order to lead to comparable maximum signal amplitudes of all heat sources. Figure 4.8 shows the results of the simulations both without and under the assumption of mirror heat sources outside the image field. The scaling of all thermograms is the same, turning slightly to the negative, hence the zero signal is a dark grey here. The line sources and the point source clearly appear more contrasted in the 0°-image than in the −90° one, which is due to the divergence of the 0°-signal in source position. Moreover, there is a measurable "overshoot" of the thermal waves into the negative only in the 0°-images, which is more strongly pronounced at the borders of the extended heat sources than around the point source (cf. Fig. 4.5). The effect of the mirror sources at the borders is also evident. Although both line sources have the same amplitude, for the simulation implying mirror sources the signal of the line source at the border is higher than that in the middle, which is most obvious in the −90°-image (e). Moreover, without this mirroring the thermal signal of the extended heat sources drops at the borders of the region, except for the 0°-signal of the extended heat source. As described above, an infinitely extended heat source would have zero 0° signal. However, at the sharp border of such a region there will be an S-shaped 0° signal with an overshoot into the negative due to the lateral heat conduction across this boundary, as these simulations show. Using the heat source mirroring at the border simulates the situation of extended heat sources extending to outside the region, or that there is really the outer edge of the sample. In both cases, no lateral heat diffusion across the border is expected, hence here the border of the extended heat source behaves like its interior. Therefore, only in Fig. 4.8 (d) the 0° signal in the upper left corner is approaching zero, since only there an infinitely extended heat source is approximated.

4.5 The Quantitative Interpretation of Lock-in Thermograms

If internal heat sources are imaged by lock-in thermography in electronic devices, the quantitative interpretation of lock-in thermograms means to conclude the distribution of the local dissipated power density e.g. in units of W/cm^2 from lock-in thermograms. Since heat dissipation is a linear process, the local value of the surface temperature modulation should be generally proportional to the local value of this power density, provided that the heat is dissipated at the surface or in a well-defined depth below. So, in principle, any lock-in thermography image, except a phase image which is independent on the value of the power density, should be able to be interpreted quantitatively as a measure of the local power density. However, there are some limitations regarding the accuracy of this procedure. The first limitation is due to the IR emissivity ε. Only if ε is homogeneous and well-known, the

Table 4.1 Amplitudes of the 0° and −90° temperature signals in source position of simple source geometries, referring to the power dissipated during the bias pulse

Sample type	Point source	Line source	Extended source
thermally thin: $S^{0°}$	$\frac{P}{\pi^2 d\lambda}\ln\left(\frac{2}{D}\sqrt{\frac{\pi\lambda}{\varrho c_p \omega}}\right)$	$\frac{p^l}{\pi d\sqrt{2\lambda\omega c_p \varrho}}$	0
thermally thin: $S^{-90°}$	$\frac{P}{4\pi d\lambda}$	$\frac{p^l}{\pi d\sqrt{2\lambda\omega c_p \varrho}}$	$\frac{2p}{\varrho\pi d c_p \omega}$
thermally thick: $S^{0°}$	$\frac{2P}{\pi\sqrt{\pi}D\lambda}$	$\frac{2p^l}{\pi^2\lambda}\ln\left(\frac{4}{D}\sqrt{\frac{\lambda}{\varrho c_p \omega}}\right)$	$\frac{\sqrt{2}p}{\pi\sqrt{\lambda\omega c_\mathrm{p}\rho}}$
thermally thick: $S^{-90°}$	$\frac{P\sqrt{\varrho c_p \omega}}{\pi^2\lambda\sqrt{2\lambda}}$	$\frac{p^l}{2\pi\lambda}$	$\frac{\sqrt{2}p}{\pi\sqrt{\lambda\omega c_\mathrm{p}\rho}}$

signal of the IR camera can be uniquely attributed to a local temperature modulation amplitude. In Sect. 5.3, we will discuss in detail the way in which different IR emissivities can be regarded in lock-in thermography measurements. In this and the following sections, we will generally assume a constant emissivity of $\varepsilon = 1$. Of course, the thermal signal also depends on the thickness and the thermal properties of the material. In Table 4.1 the quantitative values of the temperature modulation in source position will be summarized for different geometries of heat sources. This geometry is another important factor influencing the relation between the magnitude of a heat source and the value of the induced temperature modulation. It has been shown in the earlier sections that heat always diffuses laterally over a distance in the order of the thermal diffusion length Λ. If the heat source is e.g. a point source at the surface, its 0°-signal even diverges in source position (as the power density does), but nearly the complete field of the temperature modulation is lying essentially outside of the heat source position. In this case, the shape of any lock-in thermography image considerably deviates from that of the local power density. On the other hand, if the spatial dimensions of local heat sources are large compared to Λ, hence if the heat sources can be approximated as large planes, lateral heat conduction can be neglected. In this case, the proportionality between power density and T-modulation amplitude exactly holds. In fact, for spatially extended plane heat sources (larger than Λ) both a single phase signal like the –90°- or the –45°-signal and the amplitude signal are proportional to the local power density. Note, however, that for such heat sources on a thermally thin sample the 0°-signal is zero, as is the +45°-signal on a thermally thick sample, so these single phase signals are inappropriate to display such a local power density. The question is: Which signal has to be displayed that, in spite of a reduced spatial resolution, at least the signal average over a certain region is exactly proportional to the averaged power density in this region, independent of the shape of the heat sources? It will be justified in Sect. 4.5.1 that this signal is the –90°-signal for thermally thin samples and the –45°-signal for thermally thick samples.

A completely different approach to calculate the local dissipated power density from lock-in thermograms is to mathematically remove the influence of lateral heat spreading, which is called image deconvolution. Different variants of this technique will be described in Sect. 4.5.2. In the following, the expected magnitudes of the lock-in thermography signals for heat sources of three well-defined geometries will be summarized.

Whenever a local oscillating heat source in a homogeneous and isotropic body can be considered a surface-near point source, or a line source, or a laterally homogeneous heat source having an extension well above Λ, its thermal signal can be described by one of the formulas given in the previous sections, provided the sample can be uniquely regarded to be "thermally thin" or "thermally thick" (see Sect. 4.1). In these cases, the amplitude of the thermal signal in source position is proportional to the power of the heat source with a predictable proportionality factor. In the following, we will summarize the amplitudes of the temperature signals for these simple heat source geometries. The only problem is to describe those cases of the temperatures in source position diverging. Just as in the finite element model described in the previous section, we will solve this problem by averaging the signal across one camera pixel. Therefore, in these cases the formulas will contain the pixel width D (referring to the sample surface). In general we have assumed D to be small against the thermal diffusion length Λ so that we can use the analytical approximations of the temperature fields for large Λ in cases of divergence. Then, all averaging procedures can be performed analytically. For point sources, the same approximation as for (4.26) has been used that the squared averaging area is replaced by a circular one having the same area. Hence, in these cases the radial integration will go from zero to $D/\sqrt{\pi}$. For calculating the 0°-signal in the position of a line source on top of a 3-dimensional body, however, a square-sized pixel was assumed. Hence, here the averaging perpendicular to the line source goes from $-D/2$ to $+D/2$. The amplitudes of the 0° and of the −90°-signals of all simple source geometries are summarized in Table 4.1. From these values the phase-independent signal amplitude and the phase of the signal can be calculated using (2.11). Note that for the results in Table 4.1 an ideal operation of the IR optics was assumed. In reality, however, owing to inevitable errors of real optics there is a certain degree of additional blurring, which spreads the light coming from one position, over more than one pixel. Therefore, in reality there will be some deviations from the predictions of Table 4.1, especially for highly localized heat sources.

Note also that in Table 4.1, the −90° component is given, which is the inverse of the imaginary part of the complex T-modulation amplitude. In the formulas of the previous sections, P_0 denoted the amplitude of a sinusoidal point power source, p_0^l was the power amplitude density of a line source (power per unit length), and p_0 the areal power amplitude density (power per unit area) of a homogeneously heated area, all referring to a sinusoidal power introduction. However, as discussed in Sects. 2.5 and 4.1, in a real lock-in thermography experiment on electronic devices no sinusoidal power introduction is used (harmonic heating and cooling) but rather a pulsed heating superimposed on continuous cooling. Hence, in reality, we have to do with a symmetrical square wave power introduction with a peak-to-peak amplitude

of P, being the power electrically dissipated in the sample during the pulse. The amplitude of the basic harmonic component of such a square wave is $P_0 = 2P/\pi$ [32]. Hence, in Table 4.1, the really dissipated power P, the real areal power density p and the real line power density p^l are used, and the factor $2/\pi$ is added to the formulas given in the previous sections. For example, the formula given in Table 4.1 for extended heat sources in a thermally thin sample thus exactly corresponds to (2.34) in Sect. 2.7, which was not derived from (4.22) based on a harmonic heat introduction but directly from (2.32) based on a constant heat introduction, but regarding the continuous cooling in quasi-thermal equilibrium and the basic harmonic component of triangular waveform. All cases assume a sample laterally extended over more than Λ from the source position. Whenever a point or a line source is located directly at the outer edge of a sample, the lateral mirror heat sources described above have to be regarded, leading to a temperature signal twice as large as that given in Table 4.1. If, however, a local heat source is located at a certain distance $< \Lambda$ from the edge, its signal height cannot be predicted by using Table 4.1. It can only be simulated by using the simulation procedure introduced in the previous section. On the other hand, if an extended heat source extends up to the outer edge of the sample, or if a line heat source crosses the edge under 90°, the thermal signal always remains constant up to the edge, as the simulations of Fig. 4.8 have shown. The physical reason for this is that in these cases, there is no lateral heat flow within an extended homogeneously heated area or along a line heat source, which would be reflected by the outer edge of the sample.

Since power dissipation is a linear process, the signals given in Table 4.1 always depend linearly on the power or the power density, respectively. However, the dependence of the signal amplitudes on the lock-in frequency (or ω, respectively) is very different and reaches from proportional to $\sqrt{\omega}$ up to proportional to $1/\omega$. We will use these different dependencies in Sect. 5.2 for discussing the optimum lock-in frequency to detect different heat source geometries.

The formulas given in Table 4.1 can be used to estimate the detection limit of lock-in thermography for a given heat source geometry and a given lock-in thermography system. For example, according to Table 3.1, the TDL 388 M'Lock-in' system shows a noise level of about 0.072 mK after 1000 s (17 min) of acquisition time. Note that this noise level was measured using the 28 mm objective having an aperture ratio (referring to the camera side) of $f/1.5$. If the detection limit is of interest for a point heat source in silicon imaged through a microscope objective, we have to regard the different aperture ratio of $f/2.0$ of the (×2.5) microscope objective. Since the light intensity is proportional to the square of the aperture ratio, the thermal noise level expected for the microscope objective is about 0.128 mK. According to Table 4.1, in a thermally thick silicon sample of a detector width of $D = 10\,\mu\text{m}$ (referring to the sample surface) a point heat source of 1 μW produces a frequency-independent 0° signal of about 240 μK (which is the dominant one here). Hence, if a signal level 3 times the noise level is assumed to be reliably detectable, the detection limit of a microscopic point heat source can be estimated to be 1.5 μW for an acquisition time of 1000 s (17 min). In the same way, for a two-dimensionally extended heat source having a power density of 1 mW/cm^2 at a frequency of 20 Hz

on top of a thick silicon body, the 0°- and the −90° signals are both 24 μK, hence its amplitude signal is about 34 μK. Hence, producing a signal 3 times the noise level of 128 μK requires a power density of more than 10 mW/cm^2. Note that this detection limit depends on frequency and only holds for heat sources spatially extended over more than the thermal diffusion length, being about 1.2 mm for $f_{\text{lock-in}} = 20$ Hz. Note also that here an IR emissivity close to 1 was assumed, and that estimating the detection limit of point sources presupposes the ideal operation of the IR optics. Owing to the aberrations of real IR optics, the realistic detection limit of a point heat source in silicon can be estimated to be about 3 μW [97]. For a low emissivity the detection limit may rise to some 10 μW [78].

4.5.1 The Image Integration/Proportionality Method

In many cases, local heat sources cannot be regarded as point sources or sufficiently large line or extended heat sources. For example, an extended heat source having dimensions smaller than Λ cannot be described by any of the formulas given in Table 4.1. The formulas of Table 4.1 also require the knowledge of the thermal parameters of the material investigated and of the scaling factor (mK/digit) of the camera used, which may depend on the settings of the camera parameters or on the IR objective used, which sometimes may not be known at all. Moreover, these formulas cannot be applied at all if the sample cannot uniquely be considered "thermally thin" or "thermally thick", hence if its thickness is of the order of the thermal diffusion length. Fortunately, also in these cases lock-in thermography results may be evaluated quantitatively under favorable conditions using the so-called image integration or proportionality techniques [122, 123], which will be outlined in the following. These techniques are based on the property of thermal waves to be strongly damped. Hence, the main information about a localized heat source is contained in the surrounding of one or maybe a few thermal diffusion lengths Λ around the source. Therefore, we can expect that plane-integrating an appropriately chosen thermal signal across a limited surrounding of a local heat source represents the amount of its dissipated power. This will be called in the following "image integration technique". Regarding the fact that the average of a signal is its plane integral divided by the integration area, this method can also be expressed as: The average of the thermal signal within a certain area is proportional to the averaged power density in this area. This will be called in the following "proportionality technique". As it had been discussed already in the earlier section, for a sufficiently homogeneous heat source this proportionality exists in any position. For local heat sources smaller than the thermal diffusion length, this proportionality holds at least for the averages across a certain area. The actual image integration technique will be described at the beginning. It is most appropriate for measuring the power of local isolated heat sources, whereas the proportionality technique, which will be described afterwards, is more appropriate for quantitatively evaluating heat sources distributed across the whole sample. In the following, which

lock-in thermography signal is most appropriate for these techniques and how the averaging area influences their accuracy will be checked. The basic argument for these techniques is the linear character of thermal waves, which had already been used in the finite element simulations of the previous section: Any phase component of thermal waves of different heat sources superimposes linearly. This property also holds if a plane integral of a certain phase component around the heat source is calculated. Note that the average is the plane integral divided by the integration area. Here, too, the plane integral across the thermal signal (e.g. the 0° or the −90°-signal) of two neighbored local heat sources equals the sum of the corresponding plane integrals of the signals of each of these heat sources separately, which also holds for a larger number of heat sources. Thus, if we can show that the plane integral of a certain phase component of the T-modulation of a single point source is proportional to its power, this property should also hold for an arbitrarily extended heat source, which can be thought as an accumulation of point sources.

It should be noted that this property does not hold if, instead of a certain phase component the phase-independent amplitude signal is used. The reason for this is that the amplitude represents a non-linear combination of the 0° and the −90°-component, being always positive (2.11). Note that any phase component may be both positive and negative, whereby interference phenomena between different thermal waves from different sources are correctly described. Amplitude images, on the other hand, do not superimpose linearly, since this would not take into account the interference between different thermal waves.

Let us first calculate the plane integral of the 0°- and the −90°-signal around an oscillating point heat source in polar coordinates up to a certain integration boundary R in a thermally thin sample, see (4.20):

$$I^{0^\circ}(R) = \int_0^R 2\pi r S^{0^\circ}(r)\,\mathrm{d}r = A\int_0^R 2\pi r\,\mathrm{ker}\left(\frac{r\sqrt{2}}{\Lambda}\right)\mathrm{d}r \tag{4.28}$$

$$I^{-90^\circ}(R) = \int_0^R 2\pi r S^{-90^\circ}(r)\,\mathrm{d}r = -A\int_0^R 2\pi r\,\mathrm{kei}\left(\frac{r\sqrt{2}}{\Lambda}\right)\mathrm{d}r$$

Here, A is the amplitude factor defined in (4.20). Figure 4.9 shows that $I^{-90^\circ}(R)$ converges on a well-defined value (π for $\Lambda = 1$), but $I^{0^\circ}(R)$ converges towards zero. This is due to the fact that the ker function is more strongly oscillating than the kei one, visible already in Fig. 4.5. Indeed, it can be shown that the plane integral of $\mathrm{ker}(x)$ over the whole area ($R \to \infty$) is exactly zero, whereas that over $\mathrm{kei}(x)$ is not.

$$A\int_0^\infty 2\pi r\,\mathrm{ker}\left(\frac{r\sqrt{2}}{\Lambda}\right) = 0 \tag{4.29}$$

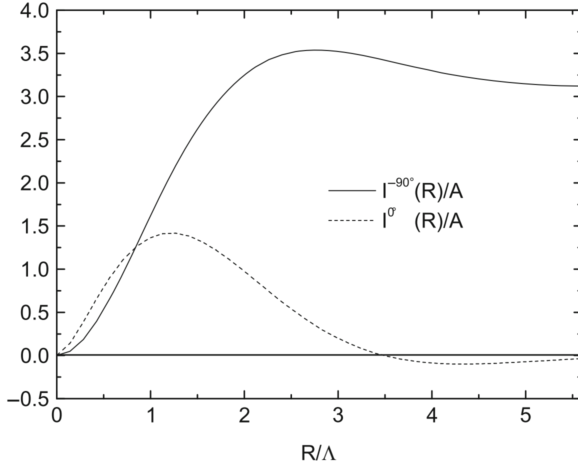

Fig. 4.9 Value of the integrals in (4.28) as a function of the integration boundary R for a thermally thin sample

$$-A\int_{0}^{\infty} 2\pi r \operatorname{kei}\left(\frac{r\sqrt{2}}{\Lambda}\right) = \pi A \Lambda^2 = \frac{P_0}{\varrho d c_p \omega}$$

This means that for thermally thin samples the plane integral over the $-90°$ component of the temperature modulation carries the information about the power of a point source. As Fig. 4.9 shows, this integral has to be calculated at least up to $R = 2\Lambda$, where the integral value crosses its limiting value for $R \to \infty$ for the first time. If the integration is carried out for a larger R, the integral value shows a slight overshoot of about 10% and converges on its limiting value for $R > 5\Lambda$. If this uncertainty of 10% may be tolerated, for a thermally thin sample, for any value of the integration boundary of $R \geq 2\Lambda$, the integral (4.28) may be said to converge with a sufficient accuracy. Hence, in order to measure the power of a local heat source, we have to calculate the plane integral of the $-90°$ signal around this heat source up to a distance of at least 2Λ and apply (4.29). The plane integration can be done most easily using the "mean value" function being implemented in most image processing softwares: The plane integral is the mean value multiplied by the selected area. Since in this case the integration plane is always rectangular and the applicability of (4.29) is not restricted to a circular integration area, the procedure is now transferred from polar coordinates into Kartesian ones, with the local heat source assumed in position $(0, 0)$:

$$P_0 = \varrho d c_p \omega \int_{\leq -2\Lambda}^{\geq 2\Lambda} \int_{\leq -2\Lambda}^{\geq 2\Lambda} S^{-90°}(x, y) \mathrm{d}x \, \mathrm{d}y \tag{4.30}$$

If (4.30) holds for a point heat source, which it was derived for, it also holds for an arbitrary-shaped local heat source, provided that it is surrounded by a region at least 2Λ wide containing no other heat source. This is the basic limitation of the image integration technique described. However, there are three important exceptions from this rule. One is that (4.30) is also valid for a homogeneously distributed heat source, hence the integration boundary is allowed to cross a spatially extended homogeneous heat source. In this case, the temperature modulation in any position is the superposition of all contributions of the corresponding phase components of all elementary heat sources in the surrounding. With an oscillating power density of p_0 (referring to the area) this will lead exactly to (4.29), with the power P_0 of the point source in the amplitude factor replaced by the power density p_0. It is not surprising that this is the temperature modulation amplitude of the homogeneously heated body, which in (4.22) had been derived for a sufficiently large heated area. Since everywhere in a homogeneously heated area the temperature modulation amplitude is constant, there is no lateral heat flow, and the integration in (4.30) is trivial and holds for any size of the integration plane. Even if a local heat source is embedded in a homogeneous heat source (such as a local shunt within a solar cell, with also some homogeneous injection current flowing), the image integration technique using (4.30) can be applied if the integration boundary is more than 2Λ away from the local heat source. In this case, the result is the sum of the local and the homogeneous power in the region considered. The local power itself can be obtained by subtracting the result of another region not containing a local shunt.

In the same way, a linear heat source of constant amplitude is allowed to cross the integration boundary, if this crossing is mainly perpendicular. The physical reason is the same as for the homogeneously heated area: Also in this case there is no lateral heat flow across the integration boundary. The simulations of Fig. 4.8 at the end of Sect. 4.4 present such an example.

Finally, the third exception from the rule that the image integration method needs a 2Λ wide region without any heat source around the one under investigation, is given if one fraction of the integration boundary, or even the whole one, coincides with the lateral edge of the sample. As discussed in Sect. 4.3, the edge of a sample may be described by mirror heat sources. As shown in Fig. 4.7 of Sect. 4.4, this is equivalent with the lateral mirroring of the temperature field across the edge. Hence, if one or several integration boundaries coincide with the edge of the sample, it will be equivalent to the extension of the integration region across this boundary. If the local heat source is near the edge and the plane integration extends up to the very edge, the “missing part” of the thermal wave folds back into the integration plane and is correctly regarded, even if the integration boundary is closer than 2Λ to the heat source. If the integration area coincides with the whole sample area (4.30) always exactly holds, independent of the value of Λ. This third exception will be required for the following.

Equation (4.30) may also be formulated as: The average value of the $-90°$ component in a sufficiently large area is proportional to the average value of the power density of this area. This is the basis of the proportionality technique, which will be described below. The corresponding proportionality factor is contained in

(4.30), hence it depends on the thickness d of the sample, on the lock-in frequency $f_{\text{lock-in}} = \omega/2\pi$, and on both the density and the specific heat of the material. Moreover, the thermal signal has to be given in units of (m)K, the phase position has to be $-90°$, and it still has to be regarded that the power P_0 in (4.30) is the amplitude of the harmonic component of the actually dissipated power during the bias pulse P, which is $P_0 = 2P/\pi$ (see discussion of Table 4.1). Thanks to the discussion above there is, however, a simple possibility of obtaining quantitative results also from an arbitrarily scaled image if neither any data nor the exact phase position are known. The unknown proportionality factor between the mean power density and the mean thermographic signal may easily be determined by evaluating the image of the whole sample area, from which we know the totally dissipated power. Hence, the easiest way of measuring the power of a local shunt comprises three steps:

1. Measuring an image of the whole sample in a well-defined phase position close to $-90°$.
2. Calculating the mean signals in this phase position over the whole sample area $S^{-90°}_{\text{whole}}$ and over a region containing the local shunt in the middle $S^{-90°}_{\text{shunt}}$.
3. With the total dissipated power P_{whole}, the whole sample area A_{whole}, and the selected area A_{shunt}, which $S^{-90°}_{\text{shunt}}$ was measured for, the power of the shunt may be obtained by:

$$P_{\text{shunt}} = \frac{S^{-90°}_{\text{shunt}}}{S^{-90°}_{\text{whole}}} \frac{A_{\text{shunt}}}{A_{\text{whole}}} P_{\text{whole}} \tag{4.31}$$

Note that according to (4.29) the plane integral of the 0°-signal over a sufficiently large area is zero. Thus, even if the phase of $-90°$ is not exactly met, the result of both averagings (across the whole area and across the selected area containing the shunt) would be diminished by only the same factor, which does not affect the validity of (4.31) as long as the phase is not exactly 0°. It is also not necessary that the temperature scaling of the camera is correct or the emissivity is known, since they influence both the shunt and the whole signal in the same way. It is only necessary that the emissivity is essentially homogeneous. Note also that, even if there are local heat sources near the border of the integration region, the error in calculating the averaged power density is the smaller the larger the integration area is. This technique has been successfully applied to measure the bias-dependent leakage current flowing across the edge of solar cells and across local shunts in the cell area ([122, 124]).

The proportionality technique is based on the same physics as the image integration technique, except that not the plane integrals of the power density or of the lock-in thermography signal are considered but rather their local values. For a thermally thin sample, this technique can be expressed as: Within a certain local accuracy, the $-90°$ signal is proportional to the local power density and thus, for a given constant bias and vertical current flow, to the local current density. Our next question is: What is the local accuracy of this technique? The profile of the $-90°$ signal of a point heat source, which is a δ-function, was shown for $\Lambda = 3$ mm in Fig. 4.5. It shows that the signal decreases to half of the maximum value at a

distance of something below Λ. Hence, the signal of a point source is blurred to a size of nearly 2Λ. Also in the 2-dimensional thermal simulations in Fig. 4.8 the edge of the homogeneously heated area is blurred in the $-90°$ images to an amount of about Λ. Hence, the spatial resolution of the proportionality technique is generally in the order of Λ. Also here, the scaling factor can be easily determined by evaluating the image of the whole sample area. So the local current density J_{loc} in a thermally thin sample can be expressed from the local $-90°$ lock-in thermography signal $S_{loc}^{-90°}$ as:

$$J_{loc} = \frac{S_{loc}^{-90°}}{S_{whole}^{-90°}} \frac{I_{whole}}{A_{whole}} \tag{4.32}$$

Here again, $S_{whole}^{-90°}$ is the $-90°$ signal averaged over the whole sample area A_{whole}, and I_{whole} is the current flowing through the whole cell. This formula, which assumes that the bias V is everywhere in the cell the same (no series resistance problems), is the base of many quantitative lock-in thermography techniques on solar cells, such as ideality factor and saturation current density mapping (see Sect. 6.2.1), local emissivity correction (see Sect. 5.3), and different variants of illuminated lock-in thermography (see Sect. 6.2.2). Note that it is assumed here that the current flows vertically due to a constant bias, hence Joule heat due to horizontal current flow cannot be described by (4.32). However, if the total dissipated power P_{whole} is known, the local dissipated power density p_{loc} including any Joule contribution can be expressed as:

$$p_{loc} = \frac{S_{loc}^{-90°}}{S_{whole}^{-90°}} \frac{P_{whole}}{A_{whole}}. \tag{4.33}$$

All the above calculations in this section refer to a thermally thin sample. However, the argumentation is the same for a thermally thick sample, except that the optimum phase position for the averaging is different. As shown in Table 4.1, for a homogeneous (infinitely extended) heat source on top of a thermally thick sample the phase of the temperature modulation at the surface is $-45°$ instead of $-90°$. Hence, for a thermally thick sample, the $-45°$ phase component can be expected to carry the plane integral information about the dissipated power. According to (4.15) and (4.18), the complex local part of the temperature field across a harmonic point heat source of amplitude P_0 in a thermally thick sample is given by

$$T(r) = \frac{P_0}{2\pi\lambda r} e^{-r/\Lambda}\, e^{-ir/\Lambda} = A\frac{1}{r} e^{-r/\Lambda}\, e^{-ir/\Lambda} \tag{4.34}$$

Hence, the phase of the temperature modulation at distance r is $-r/\Lambda$ (measured in rad). Here, A is again the amplitude factor of the point source given in (4.18). The complex $-45°$ phase component may be obtained from (4.34) by adding $\pi/4$ to the imaginary argument:

$$T^{-45°}(r) = A\frac{1}{r} e^{-ir/\Lambda}\, e^{i(-r/\Lambda+\pi/4)} \tag{4.35}$$

The real part of (4.35) is the local amplitude of the $-45°$ component, and the imaginary part is that of the $+45°$ one. Regarding the addition theorems for the trigonometric functions, this can be written as:

$$T^{-45°}(r) = A\frac{1}{\sqrt{2}r}\mathrm{e}^{-\mathrm{i}r/\Lambda}\left(\cos\frac{-r}{\Lambda} - \sin\frac{-r}{\Lambda}\right) \tag{4.36}$$

$$T^{+45°}(r) = A\frac{1}{\sqrt{2}r}\mathrm{e}^{-\mathrm{i}r/\Lambda}\left(\cos\frac{-r}{\Lambda} + \sin\frac{-r}{\Lambda}\right)$$

Again, the plane integrals over both components appearing in (4.35) have been calculated in polar coordinates up to the integration boundary R for $\Lambda = 1$. Respective results are shown in Fig. 4.10. Here, the $+45°$ component converges on zero and the $-45°$ one on $\sqrt{2}\pi$. The overshoot of the $-45°$ integral is about 10%, but here, the integral converges within this accuracy for an integration boundary of only $R \geq 1.5\Lambda$.

Using arbitrary values of Λ we obtain analytically [32]:

$$\int_0^\infty 2\pi r\, T^{-45°}(r)\,\mathrm{d}r = \frac{P_0\Lambda}{\sqrt{2}\lambda} = \frac{P_0}{\sqrt{\lambda\varrho c_p\omega}} \tag{4.37}$$

As discussed already for (4.29), this integral represents also the value of the homogeneous temperature modulation for a homogeneous heat source given in (4.23), which may be thought to consist of a dense array of elementary point sources of power density p_0, replacing P_0 in (4.37). Thus, if a local heat source of arbitrary shape on top of a thermally thick sample is surrounded by a region of at least 1.5

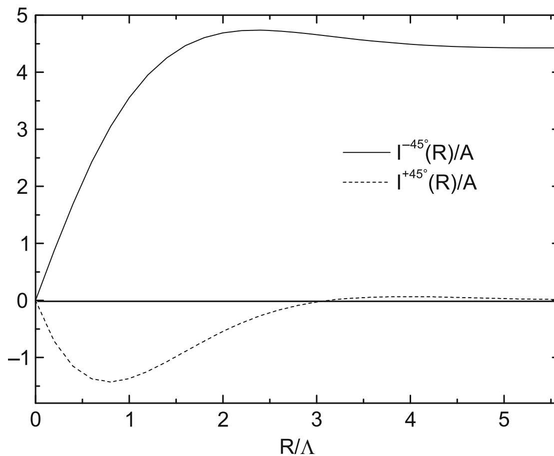

Fig. 4.10 Values of the plane integrals over (4.34) as a function of the integration boundary R for a thermally thick sample

Λ in width and free of other power sources, in analogy to (4.30), its power may be "measured", within an accuracy of 10%, by using:

$$P_0 = \sqrt{\lambda \varrho c_p \omega} \int_{\leq -1.5\Lambda}^{\geq 1.5\Lambda} \int_{\leq -1.5\Lambda}^{\geq 1.5\Lambda} S^{-45^\circ}(x, y)\, \mathrm{d}x\mathrm{d}y \tag{4.38}$$

As for a thermally thin sample, a homogeneous heat source is allowed to cross the integration boundary, and the empty region around the source is allowed to be smaller than 1.5Λ if the integration boundary coincides with the lateral sample edge. This procedure, too, may essentially be simplified by using the whole sample as a "scaling object" for measuring the proportionality factor between the mean power density and the mean value of the amplitude of the temperature modulation within a certain region. Then again (4.31) may be applied, with S^{-90° (for a thermally thin sample) replaced by S^{-45° (for a thermally thick sample):

$$P_{\text{shunt}} = \frac{S_{\text{shunt}}^{-45^\circ}}{S_{\text{whole}}^{-45^\circ}} \frac{A_{\text{shunt}}}{A_{\text{whole}}} P_{\text{whole}} \tag{4.39}$$

The corresponding formula for the proportionality method applied to thermally thick samples is:

$$J_{\text{loc}} = \frac{S_{\text{loc}}^{-45^\circ}}{S_{\text{whole}}^{-45^\circ}} \frac{I_{\text{whole}}}{A_{\text{whole}}}. \tag{4.40}$$

Due to the somewhat stronger localization of local temperature fields in thermally thick samples, the spatial resolution is slightly better in thermally thick than in thermally thin samples. Also this formula can be expressed as a local power density:

$$p_{\text{loc}} = \frac{S_{\text{loc}}^{-45^\circ}}{S_{\text{whole}}^{-45^\circ}} \frac{P_{\text{whole}}}{A_{\text{whole}}}. \tag{4.41}$$

The decisive advantages of the independently scaled image integration method according to (4.31) and (4.39) and the proportionality method according to (4.33) and (4.41), over the exact solutions given in (4.30) for thermally thin samples and in (4.38) for thermally thick samples are the following:

- The exact values of the thermal data of the material need not be known.
- The phase needs not exactly match −90° or −45°. A phase error as large as 45° may be tolerated, but it should be constant over the whole image.
- The scaling of the camera needs not be correct and the emissivity should be homogeneous, but needs not be known.
- Most importantly, this technique is also applicable to cases between thermally thin and thermally thick samples. All arguments presented here also hold if a certain sample thickness is considered using the mirror source technique described in Sect. 4.3. Then, the optimum phase is somewhere between −45° and −90°,

but any phase selection between these two values leads to good results because of the phase tolerance of this procedure. The only restriction is that an image with a well-defined phase position has to be used instead of an image with a phase-independent amplitude according to (2.11), because these amplitude images of different heat sources do not superimpose linearly.

4.5.2 Deconvolution of Lock-in Thermograms

In this section, we will use $T(x, y)$ for the lock-in thermography image (thermogram), and $P(x, y)$ for the lateral distribution of the oscillating dissipated power, having in mind that both quantities refer to one image pixel. Hence, actually $P(x, y)$ is the product of the power density in position (x, y) times the pixel area. According to (4.27) in Sect. 4.4, the oscillating temperature field $T(x, y)$ on the surface of a sample with its oscillating heat sources $P(x, y)$ in a certain lateral distribution can be described by a convolution of the lateral power distribution with the complex point spread function $T_p(x, y)$. Accordingly, the lateral power distribution may be derived from the measured temperature field by performing the inverse mathematical transformation, which is called deconvolution. If this so-called "inversion" procedure is successful, the problem of quantitatively interpreting the thermograms is solved for our purpose, since the lateral power distribution is exactly the quantity we are interested in for the functional diagnostics of the electronic components. Image deconvolution has widely been used in astronomy and light microscopy for "deblurring" optical images, hence to enhance their spatial resolution and to correct imaging errors [125]. Deconvolution procedures have also been used in non-destructive testing (NDT) to improve the usually blurred images of sub-surface defects, which are the main objects of investigation in NDT [126, 127].

However, while a convolution is a straightforward mathematical operation, the deconvolution (sometimes also called "inversion") is not. Especially if statistical noise is present in the images, the inversion may be an "ill-posed" problem. Hence, there may be no unique mathematical solution, and the latter may only be approximated [125]. A general property of all deconvolution procedures is that they tend to increase the degree of statistical noise of the image. Therefore, high-quality image data are required for the deconvolution to work effectively. In most deconvolution procedures, some data filtering (called "regularization") is implemented, or the "degree of deconvolution" may be chosen, which allows one to make a compromise between the noise increase and the spatial resolution obtainable. Note also that another presupposition to a successful deconvolution of lock-in thermograms is that they do not show any emissivity contrast. Hence, it is necessary that the images contain the information of the true temperature modulation, which may be guaranteed, for instance, by covering the surface with a strongly IR emitting layer, or by correcting the IR emissivity prior to the deconvolution (see Sect. 5.3).

As mentioned above, lock-in thermography results are of a complex nature, hence each measurement generates an in-phase (real, 0°) image and a quadrature

(imaginary, 90°) one, which may be combined to yield the amplitude and the phase image. Thus, in principle, both images are necessary to reconstruct the power source. In non-destructive testing (NDT) experiments, the signal phase carries the important information about the depth position of a defect below the surface. Therefore, here the inversion procedure has to be performed using the complex data set in order to correctly retrieve the depth position [126]. However, for the functional diagnostics of electronic components the local heat sources are mostly lying at the surface or in a well-defined depth below the surface. Here, even one image uniquely reflects the lateral power distribution we are interested in. Then the deconvolution may also be performed with one image of a certain phase position, hence by using a scalar data set instead of a complex one. Therefore, in the following, we will concentrate ourselves on deconvoluting scalar images.

The commercially available deconvolution programs for deblurring optical images are usually based on scalar images. Note, however, that there is a decisive difference between the deconvolution of lock-in thermography images and of common optical ones: Optical images display local intensities, representing the square of the phase-independent amplitude values. Since optical images are generated by using non-coherent light, they usually do not contain any phase information, and intensities are superimposing linearly. The point spread function (PSF) of optical systems refers to intensities and is always positive, since there is no negative intensity. In lock-in thermography, on the other hand, all heat sources are modulated synchronously, hence their thermal waves are coherent. As mentioned in Sect. 4.4, this may lead to interferences between thermal waves from different sources, which are correctly described by the negative parts of the PSFs. Therefore, in lock-in thermography, the deconvolution actually has to be performed either with the complex result of the measurement [126], or with an image of a well-defined phase, but not with the phase-independent amplitude image and a corresponding amplitude-PSF. If commercial programs are used for deconvolution, they must be able to employ the negative parts of the PSF also. However, it will be shown below that even the amplitude image may be used for deconvolution, provided small errors can be tolerated.

If one phase component is used for deconvolution, the question arises which phase component is optimum. As the discussion of the thermal waves of point sources in Sect. 4.3 proved, highly localized heat sources show a strong 0° signal in source position and a narrow PSF, whereas the maximum of the −90° signal is much less pronounced, with its PSF much broader. This suggests to use the 0° signal for deconvolution. However, at least for thermally thin samples, it was shown in Sect. 4.5.1 that the 0° signal does not contain any information about homogeneous heat sources. This rules out the use of the 0° signal for deconvoluting thermograms, at least of thermally thin samples. It will be shown below that, for thermally thin samples, the −45° signal (which according to (2.12) in Sect. 2.2 is the sum of the 0°- and the −90°-signal, divided by $\sqrt{2}$) is optimum for scalar deconvolution, since it contains the dominant information of both local heat sources and homogeneous ones. For thermally thick samples the 0°-signal can also be used for deconvolution. A homogeneous heat source at the top of the latter leads to a −45° signal, hence

here also the 0° signal contains information about homogeneous heat sources (see Sect. 4.4). Unfortunately, the phase image, which is by nature free of any emissivity contrast, is not able to be deconvoluted by the usual procedures, because this signal is not additive for different heat sources at all. Note that the phase image is actually a measure of the time delay between modulated power and temperature modulation. For isolated local heat sources, it is even independent of the power of the source (see Sect. 5.1). Especially for microscopic lock-in thermography failure analysis on integrated circuits, where blackening the surface is most critical, both the 0° and the −45° signals are modulated by the local emissivity. Since the local emissivity of ICs is highly inhomogeneous, these two signals, just as the amplitude and the phase signals, cannot be used directly for deconvolution. It will be shown in this section that, especially in this case where the improvement of the spatial resolution by image deconvolution is most desirable, the 0°/− 90° signal is most appropriate for becoming deconvoluted (see also Sects. 5.1 and 5.3).

There are two main approaches to perform a deconvolution, which are Fourier transform based techniques and iterative procedures working in real space. In Fourier space, the convolution of a power distribution $P(x, y)$ with a point spread function $Tp(x, y)$ just comprises the multiplication of the respective two-dimensional Fourier transforms $p(u, v)$ and $tp(u, v)$ of both functions:

$$t(u, v) = p(u, v)\, tp(u, v) \tag{4.42}$$

Hence, in principle, dividing the Fourier transform $t(u, v)$ of the measured image $T(x, y)$ by the Fourier transform of the PSF $tp(u, v)$ should lead to the Fourier transform $p(u, v)$ of the power distribution $P(x, y)$, which itself could be retrieved by an inverse Fourier transformation from $p(u, v)$. In general, this procedure, however, does not lead to useful images because of the strong (spatial) frequency noise as well as the limited accuracy of the digitization, which cause divisions by zero. Therefore, some kind of filtering or smoothing is usually necessary, which may be performed either in space domain or in the Fourier domain. One of the most popular filters is the so-called Wiener filter, which essentially replaces the division in the Fourier domain by the following expression:

$$p(u, v) = \frac{tp^*(u, v)\, t(u, v)}{|tp(u, v)|^2 + K} \tag{4.43}$$

Here, $tp^*(u, v)$ is the complex conjugate of $tp(u, v)$, and K is an adjustment parameter, which effectively determines the radius of the filter in the frequency domain. Note that $|tp(u, v)|^2 = tp(u, v) \times tp^*(u, v)$ holds, hence $K = 0$ corresponds to a simple division $p(u, v) = t(u, v)/tp(u, v)$. For high-spatial frequencies u and v, $tp(u, v)$ generally becomes small. If $t(u, v)$ contains high-frequency components due to white noise contributions, this noise would become strongly amplified for $K = 0$. Equation (4.43) can also be written as:

$$p(u,v) = \frac{t(u,v)\ F(u,v)}{tp(u,v)}. \tag{4.44}$$

Here $F(u,v)$ is a filter, which is unity for small values of the spatial frequencies u and v where $tp(u,v)$ is large, and approaches zero for high-spatial frequencies where also $tp(u,v)$ approaches zero:

$$F(u,v) = \frac{|tp(u,v)|^2}{|tp(u,v)|^2 + K}. \tag{4.45}$$

It can be shown that for suppressing white noise this filter is the optimum filter [31]. Thus, $K > 0$ in (4.43) avoids the possible division by small numbers in the deconvolution. Hence, here, the adjustment parameter K allows one to choose the "degree of deconvolution". Note that even if $T(x,y)$ and $Tp(x,y)$ are scalar images, their Fourier transforms $t(u,v)$ and $tp(u,v)$ as well as the result $p(u,v)$ are complex, since the Fourier transform itself is a complex procedure. The inverse Fourier transform of $p(u,v)$ finally retrieves a complex lateral power distribution, of which only the real part has to be interpreted as the wanted deconvoluted power distribution $P(x,y)$. We will demonstrate the application of this Fourier procedure later in this section.

The most popular alternative procedure to the Fourier transform technique is the iterative deconvolution method working in real space (see e.g. [128]). This is mainly a scalar procedure which, however, may also be performed in parallel using both phase components [120,121]. The algorithm of this technique is shown in Fig. 4.11. First, the power distribution $P_1(x,y)$ is guessed, which, in the simplest case, is proportional to the measured temperature image $T(x,y)$. From this assumed power distribution the resulting temperature distribution $T_1(x,y)$ is calculated by performing a convolution according to (4.27). At the beginning of the procedure this image will considerably differ from the measured one $T(x,y)$. The difference between both images $\Delta T_1(x,y)$ is then used to correct the power distribution $P_1(x,y)$, leading to the second iterative of the power distribution $P_2(x,y)$. Here, parameter m is the "loop gain", which strongly affects the convergence of the procedure. If m is chosen too small, the procedure will converge only slowly. If m is chosen too large, on the other hand, the result will oscillate from iteration to iteration, never converging. $P_1(x,y)$ may be subject to the condition of so-called "positivity constraint" [128], setting all values of $P_1(x,y)$ appearing negative to zero. This option is based

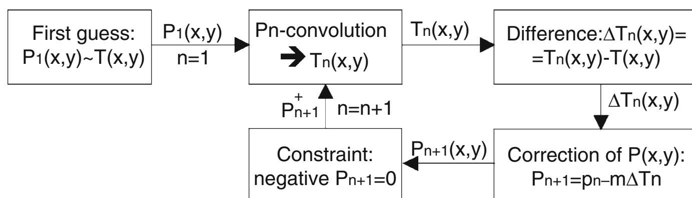

Fig. 4.11 Iterative deconvolution algorithm

on the fact that there are only positive heat sources (without any Peltier effects). In regions without any power sources, it helps reduce the noise to avoid oscillations of the solution in these regions and, thus, to speed up the convergence of the procedure. In the next iteration cycle, the whole procedure is repeated using $P_1(x, y)$ etc. In each iteration cycle, the power distribution approaches the real one. This is due to the fact that the PSF has its maximum in source position, hence the corrections in the positions desired are dominating over the inevitable corrections not desired in the procedure. The sharper the maximum of the PSF is pronounced, the faster is the convergence of the iteration procedure, and the better will be the quality of the deconvolution result. If $P_n(x, y)$ is sufficiently close to the original power distribution $P(x, y)$, the convoluted temperature distribution $T_n(x, y)$ equals the measured one $T(x, y)$, the temperature difference $\Delta T_n(x, y)$ becomes zero everywhere, and the deconvolution procedure has converged with $P_n(x, y)$ being its final result. However, with statistical noise present, the procedure also tries to fit the noise, considerably enhancing the noise of the result, with the number of iterations increasing. The "degree of deconvolution" may easily be set here by selecting the number of iterations $n_{\max}$ as an adjustment parameter, which allows one to make a compromise between an improvement of resolution and a noise increase.

Based on the work of Konovalov and Breitenstein [120,129], an easy-to-use Windows program called "DECONV" is now available from one of the authors (O.B.). This program allows the deconvolution of lock-in thermograms by the Fourier transform or by the iterative technique based on the internal generation of the thermal PSFs for thermally thin and thermally thick samples. In the latter case, even a (constant) depth of the power sources below the surface may be assumed. In addition, external user-defined PSFs may be implemented. DECONV also allows one to perform simulations of lock-in thermography results of a given power distribution, used already in Fig. 4.8 of Sect. 4.4. It is optional to apply the condition of "positivity constraint" and to consider lateral mirror heat sources outside the region of interest according to Fig. 4.7. The program allows one to deconvolute lock-in thermograms taken at a definite phase angle (0°, −45°, and −90°) as well as 0°/−90° and phase-independent amplitude images. In the latter case, the iteration procedure is performed in parallel with both the real and the imaginary part of $T(x, y)$. Only because of the power correction in each iteration step, the phase-independent T-modulation amplitude in each position is calculated according to (2.11). Therefore, this really is a vectorial deconvolution with the interferences between thermal waves of different power sources correctly regarded. Nevertheless, as the simulations below will show, in some cases, unwanted spurious "ghost heat sources" may occur if the amplitude signal is used for deconvolution. However, in practice this option mostly works well [129]. Using amplitude images for deconvolution is advantageous as the exact phase position of the image need not necessary to be known.

One example of the deconvolution of really measured thermograms will be shown in Sect. 6.1. In the following, the above two deconvolution procedures (Fourier based deconvolution using (4.43), and iterative deconvolution according to Fig. 4.11 both using the DECONV software) will be compared by applying

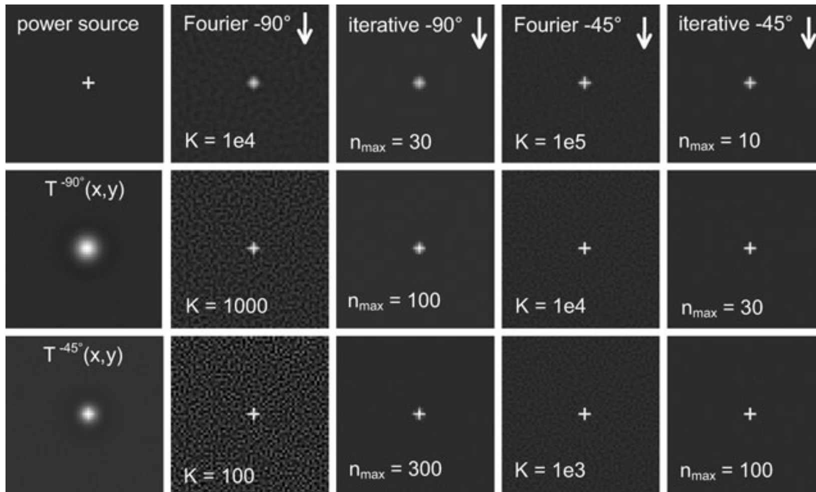

Fig. 4.12 Assumed cross-shaped power source, simulated $-90°$ and $-45°$ lock-in thermograms (both containing 1% statistical noise), and different stages of deconvolution of these thermograms performed by the Fourier method and the iterative technique. The arrows above mark the images belonging together for different values of the corresponding adjustment parameter

them to simulated thermography results, to demonstrate their different properties. Figure 4.12 demonstrates the deconvolution of a $-90°$ thermogram and a $-45°$ thermogram of a cross-shaped heat source in a thermally thin sample applying both deconvolution methods, however, using different values of the corresponding adjustment parameter. Deconvoluting this example should be particulary simple, since here, only one local heat source is in the middle of the image, hence the thermal signal at the border of the image is zero. All simulated signals and all deconvoluted results are displayed on a comparable scale with the zero signal in dark grey to mark also all overshoots into the negative black. The assumed thermal diffusion length was 3 pixels. In order to simulate realistic conditions, a statistical noise contribution of 1% of the maximum signal level was added to both simulated thermograms.

Without noise, both techniques precisely revealed the original source geometry of both the $-90°$ and the $-45°$ thermogram. As expected, the cross shape of the power source can be recognized more clearly in the $-45°$ thermogram, which thus can be deconvoluted more easily than the $-90°$ one, applying both techniques. There is a distinct increase of noise with rising accuracy of the deconvolution (lower K for the Fourier technique and larger n_{max} for the iterative technique). Note that for this power source, both deconvolution techniques allowed the reconstruction of the source shape from both the 0° image and the amplitude image (see below). However, a decisive difference between both techniques is the amount of noise increase for a given degree of deconvolution. Although both techniques were working with exactly the same input images and point spread functions, the results of the iterative method are clearly less noisy than that of the Fourier method. It will become obvious below

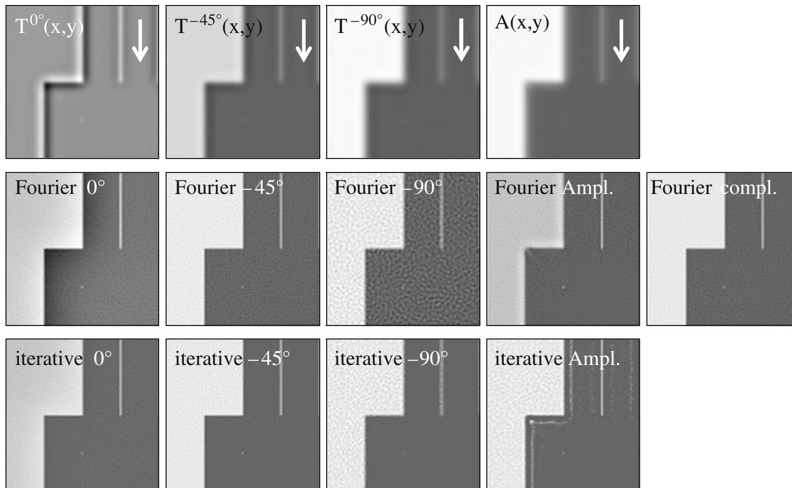

Fig. 4.13 Different thermograms (top) and power distributions deconvoluted using the Fourier method (middle) and the iterative technique (bottom). The arrows on top mark images belonging together (thermogram and two different deconvolutions). The complex deconvolution on the right was made using both the 0° and the −90° thermogram

why the iterative deconvolution technique tolerates the statistical noise more than the Fourier method does. On the other hand, the numerical expense differs between both techniques by a factor of at least 100. Since for the Fourier method, Fast Fourier Transform (FFT) techniques are applied, these calculations are performed in less than a second, whereas the iterative calculations may take some 10 s to minutes, depending on the number of image pixels and the number of iterations.

The differences between both techniques become more distinct if a more complicated power source distribution is assumed as shown in Fig. 4.13, also containing a plane heat source. Here, a power distribution is assumed similar to that in Fig. 4.8, except that all power sources have the same value of the pixel-related power here. Hence, in the deconvoluted images all power sources should show the same brightness. As in Fig. 4.12, a thermal diffusion length of 3 pixel is assumed, and again all simulated thermograms contain a statistical noise contribution of about 1% of the maximum signal value. However, since here the maximum signal (in the homogeneously heated region) is considerably larger than in Fig. 4.12, the statistical temperature noise level in Fig. 4.13 is larger by a factor of 3 than that in Fig. 4.12. Figure 4.13 solely shows the results of the optimum choice of the adjustment parameter. In addition to the –45° and the –90° deconvolutions of Fig. 4.12, Fig. 4.13 also shows deconvolutions using the 0° thermogram and the amplitude image. For the Fourier deconvolution, the amplitude PSF was used, whereas the iterative deconvolution was performed using the vectorial amplitude option of the DECONV program mentioned above. Additionally, the result of a complex Fourier deconvolution using both the 0° image and the –90° one is shown at the right of Fig. 4.13. For all deconvolutions the mirror source option at the borders was applied. As for Fig. 4.12, all

iterative deconvolutions have been performed using the positivity constraint option provided by the DECONV program.

The general results presented in Fig. 4.13 confirm the results of Fig. 4.12: The $-45°$ deconvolution is again yielding the most reliable results for both scalar procedures, and the noise in the regions outside the power sources is considerably lower for the iterative deconvolution than for the Fourier one. The $-90°$ image, which is most strongly blurred, cannot be perfectly inverted. However, here also the noise level outside of power sources is lower for iterative deconvolution. On the other hand, on the left of the images in Fig. 4.13, being the spatially extended heat source, the noise levels of both procedures are comparable. This explains why the noise level of the iterative technique is lower than that of the Fourier one: This is an effect of the condition of "positivity constraint", which can only be implemented into the iterative procedure. With no power sources present, statistical noise of the power distribution would consist of an equal amount of positive and negative power sources. If negative power sources are excluded by the "positivity constraint", also the resulting amount of positive sources has to be vastly reduced, since otherwise the average thermal signal value in this region would increase. Indeed, if the condition of "positivity constraint" is disabled, the noise level of the power distribution in the regions outside of the power sources is comparable to the results of the Fourier technique.

As expected, the complex Fourier deconvolution, using both the 0° image and the $-90°$ one, reveals a more perfect reconstruction of the power distribution than any of the scalar Fourier deconvolutions do. Nevertheless, also here the noise level outside the power sources is still higher than in the $-45°$ constraint iterative deconvolution. Therefore, the scalar $-45°$ constraint iterative deconvolution has to be regarded to be best of all possibilities shown in Fig. 4.13. It is interesting to note that, at least in principle, the deconvolution works even with the 0° and the amplitude signals. As discussed above, actually both signals should not be suited to perform deconvolutions: The 0° signal should hardly be able to reveal extended heat sources, and the amplitude signal should be unable to describe interference phenomena. Indeed, in the 0° Fourier deconvolution the power density of the homogeneously heated region is inhomogeneous and at the border to this region, the power density assumes negative values. Also in the iterative deconvolution of the 0° signal, the local heat sources are correctly reconstructed, but the levels of the homogeneous source and also outside the sources are drifting. Thus, although the 0° deconvolution is generally applicable to thermally thin samples, it cannot be used for quantitative evaluations. For thermally thick samples, on the other hand, the deconvolution of the 0° signal is as good as that of the $-45°$ signal. Also the amplitude deconvolution in general is applicable, but it may imply certain errors. In both the iterative and the Fourier deconvolution, in the actually source-free regions some spurious "ghost sources" appear (especially in the inner corner of the homogeneously heated region), which are even more strongly pronounced in the iterative procedure. In the Fourier deconvolution, this is due to the missing interference action, whereas in the iterative procedure, the ghost sources are of different origin: They are appearing mainly in regions where the phase of the measured T-signal is about 180°. Obviously, the

iteration procedure tends to overcompensate this signal by introducing the ghost sources, which locally causes the same amplitude values. While both procedures allow a more or less correct retrieval of the quantities of the point and line sources from the amplitude image, the Fourier procedure leads to an underestimation of the quantity of the homogeneously extended heat source. This can be explained by the absence of interference in the (scalar) Fourier procedure using the generally positive amplitude PSF, which also contains the 0° signal. This leads to an overestimation of the temperature response in homogeneously heated regions, where the 0°-signal should entirely be compensated by the interference between different elementary power sources. In the iterative procedure, used by the DECONV program for deconvoluting amplitude images, this interference is correctly regarded, leading to the correct amplitude of also the homogeneous heat source here.

It had been mentioned before that for failure analysis of ICs neither any of the single phase images nor the amplitude image can be directly used for deconvolution, since they are all influenced by the strong emissivity contrast of such samples. In Sect. 5.3, a method to blacken the surface of ICs is presented, but this method also slightly degrades the spatial resolution, and surface layers are generally unwanted in IC failure analysis. Also the phase image, which is inherently emissivity-corrected, is not able to be deconvoluted since it does not react additively to nearby-lying heat sources. Fortunately, it has been found that the 0° image divided by the −90° image (the so-called 0°/−90° image) can be deconvoluted, provided that the thermal diffusion length is at least in the order of the dimensions of the image [130, 131]. Hence, this technique is most effective for microscopic investigations, where it is also most desirable. Figure 4.5 has shown that for thermally thin samples the −90° signal decays to only half of its maximum value at a distance of one thermal diffusion length. Qualitatively the same will be shown also for thermally thick samples in Sect. 5.1. Hence, from all possible thermal signals, the −90° signal has the worst spatial resolution and is most strongly blurred. Therefore, as long as microscopic regions being small against the thermal diffusion length Λ are considered, the −90° signal can be considered to be "nearly homogeneous" across the area. Nevertheless, like the 0° signal showing the best possible spatial resolution, it is accurately proportional to the local emissivity. Therefore, the −90° signal can be used to correct the 0° signal for its local emissivity by calculating the ratio between both, which is the 0°/−90° signal. The advantages of this kind or representation of lock-in thermography signals compared to the phase signal will be outlined in more detail in Sect. 5.1. Here we will only mention that this signal is inherently emissivity-corrected and nevertheless sufficiently additive to be deconvoluted, in contrast to the phase signal. This will be demonstrated in the simulations in Fig. 4.14. Here the same model power distribution as for Fig. 4.13 was used, except that a thermally thick sample was assumed and the thermal diffusion length Λ was assumed to be the image size (128 pixel). Hence, for a lock-in frequency of 30 Hz, leading in silicon to a thermal diffusion length of $\Lambda = 1$ mm, the image displays an area of $1 \times 1\ \text{mm}^2$, which belongs to a pixel size of 7.8 μm. An emissivity contrast of 50% was simulated by inserting horizontal stripes where the signal is only 50% of its value outside of the stripes. A noise level of 0.1% of the maximum thermal signal

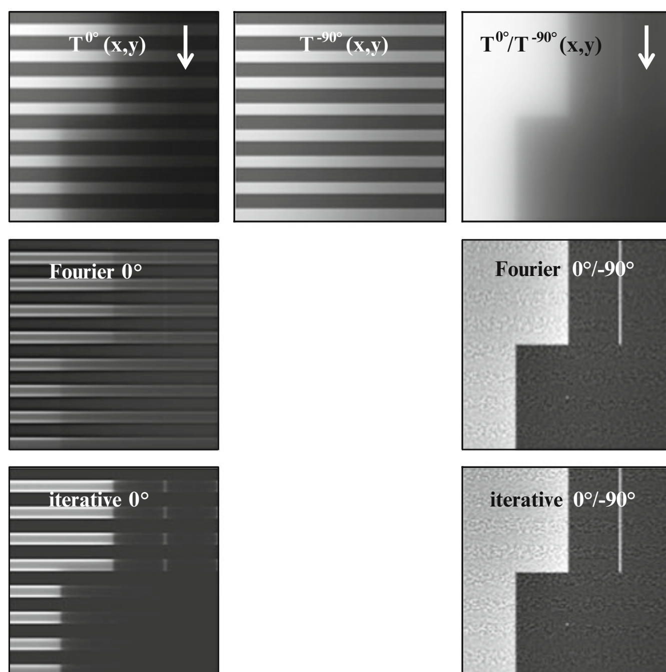

Fig. 4.14 Different simulated thermograms of a test pattern on a thermally thick sample in the presence of horizontal stripes of emissivity contrast (top) and results of the deconvolution of the 0° and the 0°/ − 90° images by using the Fourier method (middle) and the iterative method (bottom)

was added to the thermograms. The PSF used for the deconvolution was that of the 0° signal. Results of the Fourier and iterative deconvolution of the 0° and the 0°/–90° image are shown below the thermograms. As expected, the deconvolution of the 0° image with emissivity contrast is dominated by the emissivity contrast. There are some differences between Fourier and iterative deconvolution caused by the negativity constraint option of the iterative procedure, but generally the images are useless. In contrast, in the 0°/–90° signal the emissivity contrast is removed and the generated images are looking very useful. The power line and the power spot are correctly retrieved, but the homogeneous region becomes somewhat inhomogeneous. This is a result of the approximative nature of this procedure, since the –90° signal is not exactly homogeneous. As could be expected, the noise level in the regions of low emissivity is higher than that in regions of high emissivity, since there the signal-to-noise ratio of the thermogram is degraded. Interestingly, in this case there is no difference of the noise level between the Fourier and iterative deconvolution. The reason is that, again due to the approximative nature of this procedure, a small homogeneous positive power density comes out of the calculation in regions where there is no power density originally. Hence here the positivity constraint option did not work. Altogether, for deconvoluting microscopic lock-in

thermograms in IC failure analysis, the deconvolution of the 0°/–90° image is a very efficient option.

The result of this section regarding the mathematical deconvolution of lock-in thermograms for revealing lateral power distributions summarizes as follows:

- Spatial deconvolution (inversion) is a promising tool of reconstructing the laterally oscillating power distribution from measured thermograms, hence to "deblurr" the thermograms or to remove the halos around local heat sources, which are caused by the lateral heat conduction in the sample. Only high-quality thermograms showing a good signal-to-noise ratio and containing no emissivity contrast are appropriate to be deconvoluted successfully.
- The constraint iterative deconvolution technique is superior to the classical Fourier based deconvolution, because it allows one to apply the condition of "positivity constraint", which considerably reduces the noise in the regions free of power sources.
- If the heat sources are at the surface or at a well-defined depth, there is no need to perform the deconvolution in complex space. The most appropriate scalar signal for performing the deconvolution in thermally thin samples is the signal −45° phase shifted to the modulated power. The other signals are less appropriate, since the 0° signal does not allow the reconstruction of homogeneous heat sources in thermally thin samples. In general, the −90° signal causes a degraded spatial resolution and an increased noise level. The amplitude signal may give rise to spurious "ghost" heat sources. In thermally thick samples, the 0° signal, too, can be used for deconvolution.
- For microscopic investigations, if the image size is in the order of the thermal diffusion length or below, the 0°/–90° signal is most useful to become deconvoluted, since this signal is inherently emissivity-corrected and nevertheless sufficiently additive in microscopic regions to become deconvoluted.

Chapter 5
Measurement Strategies

In the following sections some practical aspects of using lock-in thermography in the functional diagnostics of electronic components will be discussed and illustrated by measurement examples of a typical, thermally thin sample (solar cell) and a thermally thick one (integrated circuit). All these discussions are based on the theoretical findings presented in Chap. 4. Section 5.1 discusses the question which of the images available from a lock-in thermography experiment (0° image, −90° image, amplitude image, phase image, or 0°/−90° image) is most appropriate to display certain details of different heat source distributions. In Sect. 5.2, the influence of the lock-in frequency on the obtained signal amplitude and lateral resolution of the thermograms will be discussed and demonstrated for different heat source geometries. In Sect. 5.3, the influence of a spatially varying IR emissivity will be discussed (emissivity contrast), and different ways to overcome this influence will be introduced and demonstrated. Section 5.4 describes the technique of measuring local I-V characteristics thermally (LIVT). In addition, it will be shown there how a non-destructive mapping of the so-called n-factor of exponential I-V characteristics is possible. Finally, in Sect. 5.4 a simple technique will be introduced to distinguish Joule type heating from Peltier effects in lock-in thermography experiments on resistive samples.

5.1 Which Signal Should be Displayed?

According to Sect. 2.2 it is possible to display four different images resulting from a lock-in thermography experiment: the 0° (in-phase) image $T^{0^\circ}(x, y)$, the −90° (quadrature) image $T^{-90^\circ}(x, y)$, the phase-independent amplitude image $A(x, y)$, and the phase image $\Phi(x, y)$. As mentioned there, for the functional diagnostics of electronic components it is generally useful to display the −90° image instead of the +90° one, since the latter is essentially negative. In Sect. 4.5.2 another kind of representation of lock-in thermography signals was introduced, which is the 0°/−90° signal. It will be justified in this section why this signal is useful only for microscopic investigations. In the following, examples will be presented of these thermograms of both a typical thermally thin and a microscopic thermally thick sample according

to the definition in Sect. 4.1. Of course, all these images are scalar images, hence their natural presentation would be grey-scaled. Nevertheless, it has become most popular to publish thermograms in a false-colour presentation, since this allows one to distinguish finer signal differences, and, visually, it is more appealing. We will use the colour table "fire 2" for presenting our images, which goes across black-blue-magenta-red-yellow-white. Intuitively, this colour table can be interpreted most clearly in terms of increasing heat or brightness, while still being colourful enough. It is based on the "hot metal" scale (black-red-yellow-white) by inserting blue at the "cold end" of the scale. Contrary to the "rainbow" scale (magenta-blue-green-yellow-red), which is also often used in thermography and other imaging techniques, in the "fire 2" scale the brightness is monotonically associated with the signal value so that even a grey copy of the images is still uniquely interpretable. If lock-in thermography is used for non-destructive testing (NDT) experiments, the phase image has yielded more unique information about subsurface defects than the amplitude one has done [2]. The reason is that, contrary to the amplitude image, the phase image is not affected by the local emissivity and less by the local illumination intensity. In NDT it is generally not popular to display images of a definite phase like the 0°- and the $-90°$ image. The situation is somewhat different if lock-in thermography is used for the non-destructive testing of electronic components. Of course, also here the emissivity contrast is disturbing, which will be discussed in detail in Sect. 5.3. However, since in our case the quantity of the detected heat sources is a decisive result of the investigation, here the amplitude signal is more interesting than the phase one, since only the amplitude signal carries the information as to the amount of the dissipated power. Within the limit of the spatial resolution of the technique (see Sect. 5.2) the amplitude image can be interpreted as a map of the power distribution, provided there is no emissivity contrast. Therefore, as a rule, amplitude images are presented, if lock-in thermography is used for the functional diagnostics of electronic components. It will be demonstrated below that only in special cases (weak heat sources besides strong ones, or strong emissivity contrast) it may also be useful here to display the phase image. Moreover, the 0° signal turns out to be most useful for displaying highly localized (point-like) heat sources.

The special properties of the 0° and the $-90°$ signal compared to the amplitude signal were discussed in Chap. 4. Especially, Fig. 4.5 in Sect. 4.3 displays these three signals around a point source in a thermally thin sample. For comparison, Fig. 5.1 displays the same profiles together with the profile of the phase signal for a thermally thick sample (cf. (4.15)), here calculated for a thermal diffusion length of $\Lambda = 0.58$ mm. These profiles look very similar to that in Fig. 4.5 of a thermally thin sample, except that for a thermally thick sample the divergence of the 0° and of the amplitude signal in source position is even stronger, the overshoot of the 0° signal into the negative is less distinct, and the profiles are generally somewhat narrower. Both figures show that the $-90°$ signal is considerably more extended than the 0° one, and that the maximum of the $-90°$ signal in source position is well-defined and by far not so well pronounced as that of the 0° and the amplitude profile. This is due to the fact that for a point source in both thermally thin and thick samples, the 0° signal actually diverges in source position, whereas the $-90°$ signal does

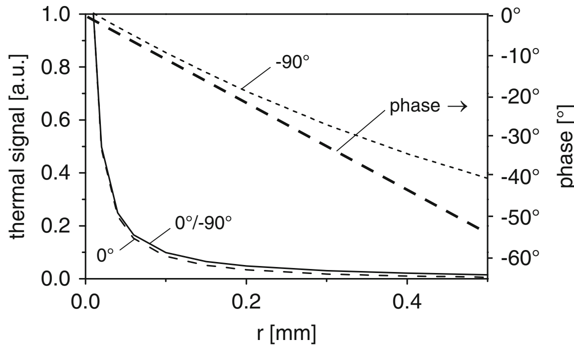

Fig. 5.1 Profiles of the 0°, the −90°, the 0°/−90°, and the phase signal around an oscillating point source in a microscopic region of a thermally thick sample, thermal diffusion length 0.58 mm

not (see Sect. 4.3). The amplitude profile contains both the 0° and the −90° signal, hence it shows the distinct maximum in source position, having nevertheless a broad base. In contrast to the 0° signal and the −90° one, the amplitude signal is always positive and does not show any residual oscillations. Therefore it is usually chosen for displaying lock-in thermography results in electronic device testing. Note that the phase linearly drops with the distance from the source position (which holds generally for a homogeneous body), and that the phase profile is neither affected by the IR emissivity nor by the power of the heat source. Hence, if there are several local (point-like) heat sources with different intensities present in the investigated area, in the phase image they all appear in a comparable brightness.

In Fig. 4.5 macroscopic dimensions and a thermal diffusion length of 3 mm was assumed, which belongs to a lock-in frequency of about 3 Hz for investigating silicon samples. If lock-in thermography is used for failure analysis in ICs, typical image sizes are in the order of 1 mm, and a higher lock-in frequency is often used for reducing thermal blurring. Figure 5.1 shows lock-in thermography signals in a microscopic region of a thermally thick sample simulated for a lock-in frequency of 88 Hz, where the diffusion length is 0.58 mm, which is about the image size here. In addition to the "classic" lock-in thermography signals, in Fig. 5.1 also the 0°/−90° signal is shown. All thermal signals are separately scaled to meet each other at a distance of about 10 μm from the source. We see that the shape of the 0° signal is very similar to that of the 0°/−90° signal. While these two signals diverge in source position, hence they allow a spatial resolution much better than the thermal diffusion length, the −90° and the phase signal only shows a single maximum here. Therefore, the −90° and the phase signals show a low spatial resolution, which is in the order of the thermal diffusion length. Since the phase signal is given by $\Phi = \arctan(-S^{-90^\circ}/S^{0^\circ})$ (see (2.11)), the divergence of the 0° signal at $r = 0$ explains why the phase is always 0° in the position of a point source, independent on the magnitude of its power. This is the reason why the phase signal shows its "dynamic compression" feature and is not able to become deconvoluted

meaningfully. On the other hand, if two point sources of different powers are lying side-by-side within a smaller distance compared to the thermal diffusion length, their −90° signals superimpose and are nearly the same in both positions. Their 0° signals, however, are both proportional to their power, so that their 0°/−90° signals are also still proportional to their individual power. Both the phase and the 0°/−90° signal are inherently emissivity-corrected, but they show two different properties: (1) The 0°/−90° signal shows a better spatial resolution than the phase signal. (2) For nearby-lying point-like heat sources, the phase signal is nearly independent from the individual power of the sources, but the 0°/−90° signal is still proportional to it. This enables the 0°/−90° signal to become mathematically deconvoluted for removing residual thermal blurr (see Sect. 4.5.2). Note that all the described properties of the 0°/−90° signal become meaningless whenever image dimensions considered are larger when compared to the thermal diffusion length. At a distance of about 3.14 diffusion lengths from a point source, the −90° signal crosses zero. Hence, latest in this distance the 0°/−90° signal becomes infinite and there is no similarity to the 0° signal anymore.

The properties discussed above are shown in the measured images of Fig. 5.2, with the different scaling intervals cited in the caption. All scaling intervals have been extended by 10% into the negative in order to display also some overshoot

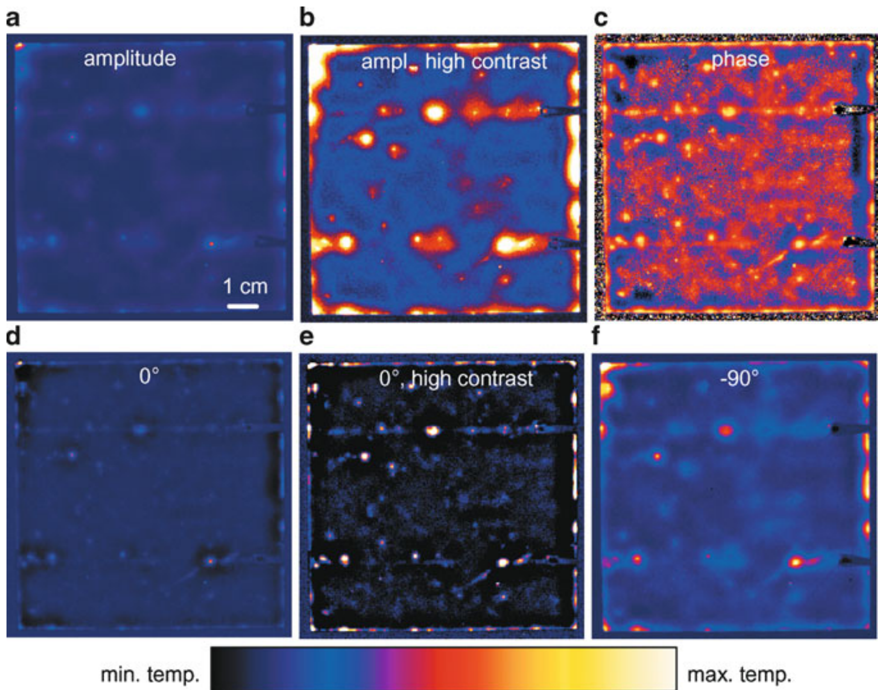

Fig. 5.2 Multicrystalline silicon solar cell measured at $f_{\text{lock-in}} = 4\,\text{Hz}$: (**a**) amplitude image −0.7 … 7 mK, (**b**) amplitude image −0.07 … 0.7 mK, (**c**) phase image −150 … 0°, (**d**) 0° image −0.5 … 5 mK, (**e**) 0° image −0.05 … 0.5 mK, (**f**) −90° image −0.2 … 2 mK

of the signal, which is especially pronounced in the 0° images. The "fire 2" colour scaling bar (black-blue-magenta-red-yellow-white) at the bottom of Fig. 5.2 refers to all coloured images (except CDI/ILM) in this book. All these thermograms are the result of one lock-in thermography measurement of a multicrystalline solar cell $10 \times 10\,\mathrm{cm}^2$ in size, which during the measurement was covered with a black IR-emitter foil to avoid any emissivity contrast (see Sect. 5.3). The lock-in frequency chosen was 4 Hz, according to (4.3) corresponding to a thermal diffusion length of $\Lambda = 2.7\,\mathrm{mm}$ in silicon. Note that this length is large against the sample thickness of 0.4 mm, that the pixel distance in the images is about 0.34 mm (close to the sample thickness), and that this sample was mounted on a thermally insulating layer. Therefore, this sample clearly is a thermally thin sample according to our definition in Sect. 4.1.

The solar cell shown in Fig. 5.2 contains both local (point-like) heat sources and a spatially extended current injection over the whole area (leading to a plane heat source), which shows cloudy inhomogeneities. Whenever there are different heat sources of strongly varying power as, e.g., the different point sources in this example, it is useful to display the thermograms in different scalings. We see that the amplitude images (a and b) display both the point sources and the homogeneous heating. Therefore, if it is displayed in different scalings like in Fig. 5.2, the amplitude image shows all the dominant heat sources in a sample. However, if its contrast is strongly enhanced like in (b), the point shunts appear strongly broadened. This strong "halo" around local heat sources is a result of the broad base of the amplitude PSF. This halo-effect is considerably reduced in the 0° images (d and e), which display the point shunts with a clearly better resolution than the amplitude image does. Therefore, the 0° signal is most appropriate to display point-like heat sources. It was mentioned in Sect. 3.5.1 that the 0° signal has to be used also for carrier density imaging (CDI/ILM). On the other hand, the 0° signal shows a pronounced overshoot into the negative, and it does not display the homogeneous heating of the cell. This property holds only for thermally thin samples and was discussed in Sect. 4.5.1. Indeed, the average of the 0° signal across the whole image (d) is zero. The homogeneous heating is displayed predominantly in the −90° image (f), which, on the other hand, displays the point shunts with a low spatial resolution. Therefore, the −90° signal is not so much suited to display the heat sources as an image. Nevertheless, we may need this image for quantitatively measuring the power of certain heat sources via the image integration method (see Sect. 4.5.1). According to Sect. 4.5.2, also the −45° signal (not shown here) may be needed, since this signal is most appropriate to perform an image deconvolution, as had been pointed out in Sect. 4.5.2. The phase image (c) looks especially interesting: It displays all point-like heat sources with nearly the same intensity, independently of their individual power! This "dynamic compression effect" is due to the above-mentioned fact that the phase of the thermal signal is a measure of the runtime of the thermal waves from the source, which is not related to the intensity of the source. For this very reason, outside the sample or in regions without any thermal signal, the phase signal is not zero but displays a strong noise. In the following, some more examples of phase images will be introduced.

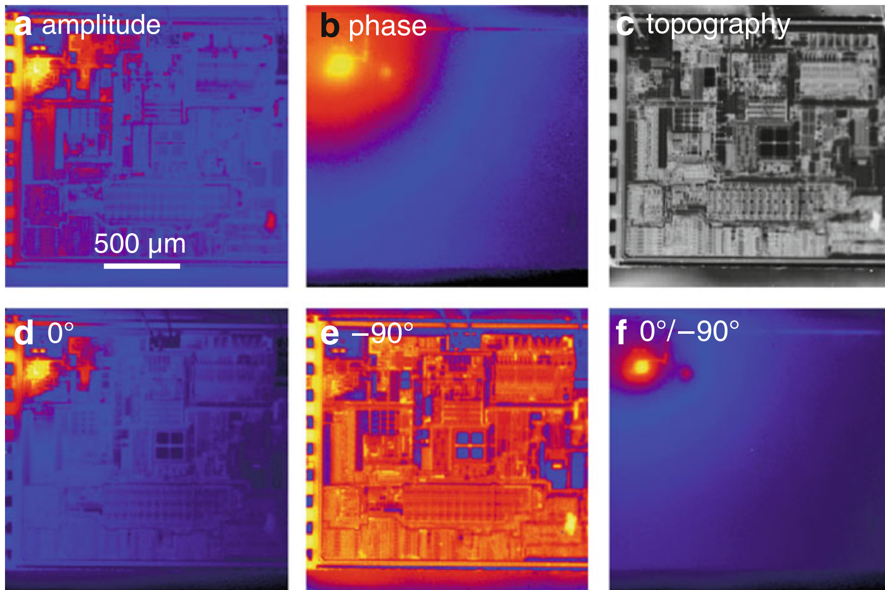

Fig. 5.3 Integrated circuit measured at $f_{\text{lock-in}} = 3\,\text{Hz}$: (**a**) amplitude image 0...8 mK, (**b**) phase image $-80°\ldots 0°$, (**c**): topography image; a.u., (**d**): 0° image 0...8 mK, (**e**): $-90°$ image 0...4 mK, (**f**): $0°/-90°$ image, arbitrary scaling

In principle, the same conclusions can be drawn from the second example in Fig. 5.3, which displays results of a microscopic thermally thick sample. Here, an integrated circuit, which was soldered on a metal plate acting as a heat sink, was investigated by using a microscope IR objective. The pixel resolution was about 7 μm, which is small against the sample thickness of about 500 μm. Though for this measurement a low lock-in frequency of 3 Hz was chosen, leading to a thermal diffusion length as large as 3.14 mm, according to Sect. 3.1 this sample has to be regarded as a thermally thick one. Note that the criterion whether a sample has to be regarded as thermally thin or thick is not only the relation between sample thickness and thermal diffusion length, but also the relation between sample thickness and pixel resolution. Only this relation decides whether for a heat source of one pixel in size, 3-dimensional heat diffusion has to be regarded, or not. If the thermal diffusion length exceeds the sample thickness as in Fig. 5.3, this will primarily affect the halo of the thermal signal around the heat sources at a distance of about the sample thickness and higher.

The results shown in Fig. 5.3 have to be evaluated differently from that of Fig. 5.2. Here, we have a thermally thick sample with a large thermal diffusion length, and moreover, we have a strong emissivity contrast due to the presence of different metallized regions. Therefore, only here it is useful to display also the topography image, which is usually taken at the beginning of each lock-in thermography measurement (see Sect. 2.3). The heat sources in this IC are in the upper left. However, here the thermal contrast is strongly modulated by the local IR emissivity

(emissivity contrast). Therefore, neither the amplitude image (a) nor the 0° one (d) clearly allows one to find out whether there is only one or several heat sources present in this region. Here we see the advantage of the phase image (b), which is independent of the local emissivity. In this image, regions of a low emissivity only show an increased noise level, but the emissivity contrast is totally compensated. In Fig. 5.3(b), there are indeed several heat sources present. The horizontal line source at the top is due to the heating of the current path to the upper left corner. It is interesting to note in Fig. 5.3 that the −90° signal (e) is nearly identical with the topography one (c). This is a consequence of the thermal diffusion length being larger than the image size, here. According to Fig. 5.1, the −90° signal varies only little close to the source position. Therefore it can be used for to correct the local emissivity of the 0° signal, leading to the 0°/−90° signal. Like the phase signal, this signal is perfectly emissivity-corrected, but it shows a clearly better spatial resolution.

Summarizing this section, the different signals to be displayed show the following properties with respect to the functional diagnostics of electronic components:

- The amplitude signal is the most universal one and is the standard to display both thermally thin and thick samples. It shows a distinct maximum in the position of local heat sources, it shows no overshoot into the negative, and it displays also homogeneous heat sources in both thermally thin and thick samples. However, it is characterized by a distinct (lock-in frequency dependent) halo around local heat sources, arising from its −90° contribution. If there is any emissivity contrast, it modulates the amplitude signal, just as the 0° and the −90° ones.
- The 0° signal shows the best spatial resolution, but in thermally thin samples it shows a distinct overshoot into the negative around local heat sources. It is the best choice if different point-like heat sources have to be imaged separately. However, for thermally thin samples, the 0° signal cannot display extended plane heat sources of a size exceeding the thermal diffusion length. For thermally thick samples, however, this signal contains also this information. Therefore, especially if the thermal diffusion length strongly exceeds the pixel distance, for thermally thick samples it may be more appropriate to display the 0° signal than the amplitude one. Moreover, for thermally thick samples, the 0° signal may be used for deconvolution according to Sect. 4.5.2, if there is no emissivity contrast. It also has to be used for carrier density imaging.
- The −90° signal shows only a weak maximum in the position of a point heat source. Besides, it shows only little overshoot into the negative. On the other hand, it shows a pronounced (lock-in frequency dependent!) halo around local heat sources. Therefore, this signal is not very suited to be displayed. However, it has to be used to be evaluated quantitatively via the image integration/proportionality method for thermally thin samples according to Sect. 4.5.1.
- The −45° signal is the sum of the 0° and the −90° ones (see Sect. 2.2). It is not very suited to be displayed, but it is optimum to become deconvoluted for thermally thin samples according to Sect. 4.5.2. Moreover, it has to be used for the quantitative evaluation via the image integration/proportionality method for thermally thick samples according to Sect. 4.5.1.

- The phase signal has the unique property to display local heat sources of different intensity with a comparable brightness. Thus, it is very useful for distinguishing adjacent heat sources of different intensity from each other. Moreover, the phase signal does not contain any emissivity contrast. Therefore, it is especially suited to be displayed for investigating ICs, usually showing a strong emissivity contrast, in order to determine which contrast part is a thermal one and which is an emissivity one. However, it is characterized by a distinct (lock-in frequency dependent) halo around local heat sources. So its spatial resolution is in the order of the thermal diffusion length.
- The $0°/-90°$ signal is only useful to be displayed in microscopic regions, where the image size is not large against the thermal diffusion length. It can be considered as an "emissivity-corrected 0° signal". Like the phase signal, the $0°/-90°$ signal does not contain any emissivity contrast. However, it shows a better spatial resolution than the phase signal, and local heat sources of different intensity are displayed with different brightness. This makes the $0°/-90°$ signal e.g. of integrated circuits appropriate to become deconvoluted by using the PSF of the 0° signal.

5.2 Influence of the Lock-in Frequency

The lock-in frequency, together with the physical properties of the investigated material, determines the thermal diffusion length Λ according to (4.3) in Sect. 4.1. As described in Chap. 4, Λ governs the lateral extension of the halo around local heat sources in lock-in thermography results. As discussed at the end of Sect. 4.3, for local (point-like) heat sources lying at the surface, the spatial resolution is by far not limited to Λ. Instead, it may be of the order of one image pixel owing to the divergence of the 0° signal in source position. Nevertheless, the halo is disturbing also here, since it affects or even prevents the detection of adjacent weaker heat sources. As the simulations of Fig. 4.8 in Sect. 4.4 show, the thermal diffusion length Λ really represents the spatial resolution limit of spatially extended heat sources. Therefore, the general statement about the influence of the lock-in frequency on the result of lock-in thermography used for the functional diagnostics of electronic components is the following: The higher the lock-in frequency, the better the effective spatial resolution, but the poorer the signal-to-noise ratio. Thus, for the sake of a good spatial resolution for local heat sources, the lock-in frequency should always be chosen as high as possible, as long as the signal-to-noise ratio remains acceptable.

However, as Table 4.1 in Sect. 4.4 shows, the temperature modulation amplitude of heat sources of different geometry depends differently on the lock-in frequency, which additionally depends on the sample type (thermally thin or thick). Thus, the question of the optimum lock-in frequency also depends on the question: what is to be seen in the image. The two extreme cases of a source geometry are a point source and a homogeneously extended heat source, whereas the properties of a line source are in between. The difference between these geometries is best pronounced for a

thermally thin sample. Here, according to Table 4.1, the 0° signal of a point source in source position (which dominates its amplitude signal) only logarithmically depends on the square root of the lock-in frequency. Thus, this signal is almost independent of $f_{\text{lock-in}}$. The −90° signal of an extended heat source (which equals its amplitude signal), on the other hand, decays with $1/f_{\text{lock-in}}$. Therefore, the ratio of the lock-in thermography signals of local and extended heat sources depends on the lock-in frequency: At low frequencies, extended heat sources are dominating the image, whereas at high frequencies local heat sources are dominating it. Hence, if both extended and local heat sources are present in a device (which often is the case, e.g. in a forward-biased solar cell), the extended heat source (which is the homogeneous current injection here) will better be visualized at a lower lock-in frequency than it has to be selected for evaluating the local heat sources (shunts).

This is demonstrated in Fig. 5.4 showing images of the solar cell already used for Fig. 5.2, measured at three lock-in frequencies differing by a factor of 100. Here, too, the cell was covered with a black-painted plastic foil to avoid any emissivity contrast (see Sect. 5.3). As the standard for the functional diagnostics of electronic components, the amplitude signal is displayed here, since for a thermally thin sample, this signal contains the information of both local and extended heat sources. All images are displayed in two different scalings: top: the whole dynamic range

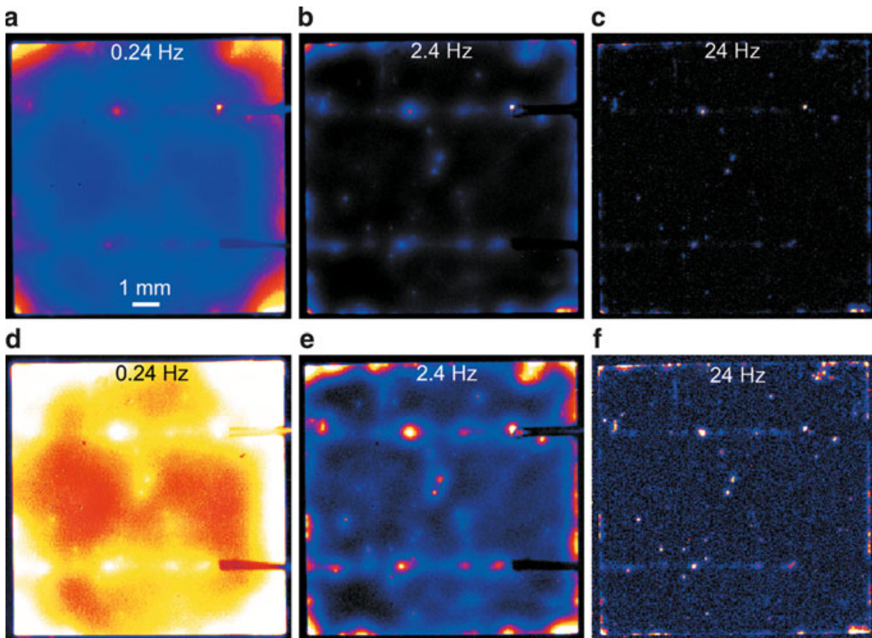

Fig. 5.4 Lock-in thermograms (amplitude images) of a multicrystalline silicon solar cell measured at different lock-in frequencies and displayed in different scalings. (**a**) 0.24 Hz; 0 . . . 15 mK, (**b**) 2.4 Hz; 0 . . . 8 mK, (**c**) 24 Hz; 0 . . . 2 mK, (**d**) 0.24 Hz; 0 . . . 5 mK, (**e**) 2.4 Hz; 0 . . . 2.6 mK, (**f**) 24 Hz; 0 . . . 0.66 mK

of the respective image (a–c), bottom: the contrast expanded by a factor of 3 (d–f). Comparing the different images of Fig. 5.4 allows the following conclusions to be made:

- The halo around local heat sources decreases with frequency, hence the spatial resolution improves.
- The relative contribution of the homogeneous signal decreases with frequency.
- The general signal-to-noise ratio improves with decreasing frequency.

The differences between different heat source geometries are less pronounced in thermally thick samples. As Table 4.1 in Sect. 4.5 shows, the 0° signal of a point source in source position (which dominates its amplitude signal) is independent of $f_{\text{lock-in}}$, whereas the signal of an extended heat source is proportional to $1/\sqrt{f_{\text{lock-in}}}$. Hence, compared to thermally thin samples the visibility of heat sources of different geometry is less frequency-dependent here. As for thermally thin samples, the extension of the inevitable halo around local heat sources, which is proportional to the thermal diffusion length Λ, decreases with $1/\sqrt{f_{\text{lock-in}}}$ (see (4.3) in Sect. 4.1). Figure 5.5 shows lock-in thermograms of an IC used already for Fig. 5.3, measured at three different frequencies varying by a factor of 25. According to the suggestion made in the previous section, the 0° and the phase signal are displayed in Fig. 5.5.

In both the 0° and phase images the halos around the heat sources decreases with increasing frequency, hence the spatial resolution improves. While it is hard to dis-

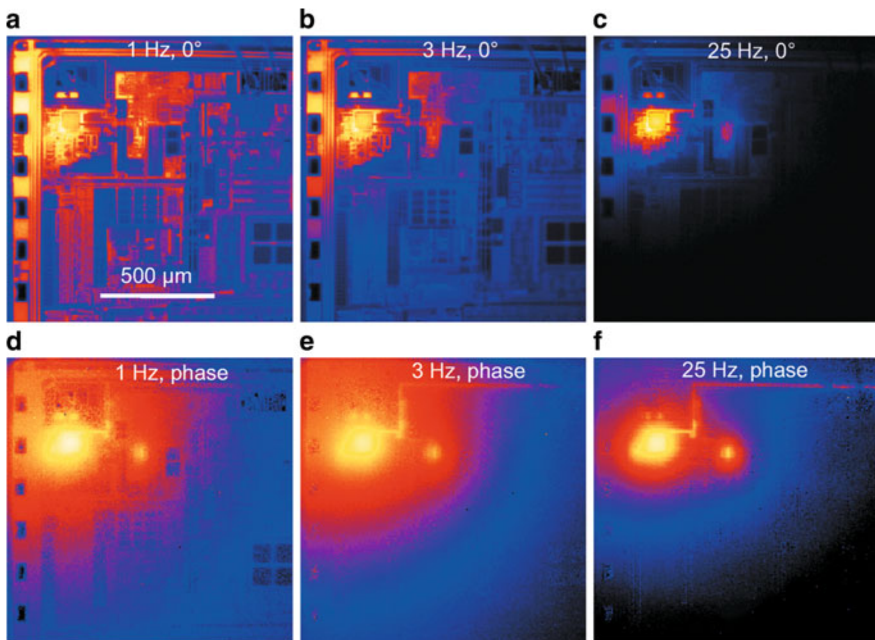

Fig. 5.5 Integrated circuit (0° image and phase image) measured at different lock-in frequencies: (**a**) and (**d**) 1 Hz, (**b**) and (**e**) 3 Hz, (**c**) and (**f**) 25 Hz

tinguish between real heat sources and topography contrast in the 1 Hz/0° image, the phase image displays the real heat sources even at 1 Hz. As expected, at 25 Hz the 0° signal is most strongly confined to the positions of the real heat sources, and it becomes negative (overshoot) at a distance more than 1 mm from the heat sources. Interestingly, the phase image taken at 1 Hz seems to show some "emissivity contrast" in regions where no heat source is expected (e.g. the dark window-like contrast at the lower right). This may be either due to the influence of the temperature drift, which has not been corrected here and disturbs most for low frequencies, or due to a spurious signal resulting from the IR emission of persons moving in the laboratory during the measurement owing to the reflectivity of the sample. Note that all these measurements have been made without shadowing or optically screening the set-up in the lab. Since IR irradiation from the lab shows main contributions in the low-frequency range, its reflections to the sample are disturbing more and more strongly the lower the lock-in frequency is chosen. This is another argument in addition to that of the spatial resolution, also when investigating thermally thick samples to choose a lock-in frequency as high as possible. The highest possible lock-in frequency may be limited either technically, depending on the lock-in thermography system used, or practically by the inevitable reduction of the signal-to-noise ratio with increasing lock-in frequency.

5.3 Influence of the IR Emissivity

As mentioned in Sect. 2.1, the thermal radiation is modulated by the local value of the IR emissivity ε. Besides it may contain components reflected by the surrounding. According to Kirchhoff's law, the emissivity ε equals the absorbance α in the corresponding wavelength range. Only if the emissivity is close to $\varepsilon = 1$ or at least well-known and constant across the investigated area, and if the amount of reflected radiation can be neglected, the real temperature of a surface can be concluded from a thermography measurement. Lock-in thermography inherently compensates the reflected radiation, since it is steady-state, but the primary results (0° and −90° signals) are still modulated by the local emissivity ε. This type of contrast, which modulates both the topography image and lock-in images, is called "emissivity contrast". This effect is most disturbing if a sample is partly covered with metallization layers, which is usual in the functional diagnostics of electronic components. Metallization layers can easily be penetrated by thermal waves, hence local heat sources lying below these layers can also be detected by lock-in thermography. However, since due to the high reflectivity of these layers their emissivity is low, heat sources below them might remain undetected if no measures are taken to increase the emissivity. Furthermore, the IR emissivity should also be increased if bare surfaces of silicon or other semiconductors are to be imaged. Semiconductors (except small gap ones) are nominally transparent to IR radiation, hence their absorbance and therefore also their emissivity are low. A certain amount of IR absorbance is provided by free carrier absorption, which is more effective in the long-wavelength range

(8 ... 10 μm) than in the mid-range one (3 ... 5 μm). Therefore, highly doped semiconductor layers usually lead to a measurable lock-in thermography signal of bare semiconductor samples. Nevertheless, some part of the radiation may also come from deeper regions. Especially for solar cells, the highly doped back side contact, together with the sintered aluminum paste back-metallization, may provide even the dominant IR signal, if they are imaged in the bare state. Indeed, it has been observed that bifacial solar cells, where the back contact is also a grid structure, exhibit only a very weak lock-in thermography signal, since they are essentially transparent to the IR light [132]. The same can be expected if cells with dielectric backside passivation are investigated, which contain a metallic backside mirror. The emissivity contrast is mostly disturbing if lock-in thermography has to be used for the functional testing of integrated circuits (ICs), as already demonstrated by the examples in Figs. 5.3 and 5.5.

There are two possibilities to treat the emissivity contrast: 1. To avoid it by covering the surface with a layer of high IR emissivity, or 2. to compensate it after the measurement by measuring the local emissivity image $\varepsilon(x, y)$. The first possibility is the classical one often performed in standard thermography. Usually, black paint is used to cover the surface of an object under investigation to provide the surface an IR emissivity close to 1. Note that here the emissivity in the wavelength range of the camera (3...5 μm or 8 ... 10 μm) is decisive, and not that in the visible range. As published tables of emissivity show [133] also differently coloured and even white paints may show an IR emissivity above 0.9. There are special black paints available for blackening the interior of optical instruments (so-called Velvet coatings) that are frequently used for IR thermography to increase the IR emissivity.

There are, however, several arguments against the general use of IR-emitting paints in the functional diagnostics of electronic components. If, for instance, the surface of an IC is covered with an efficient IR emitter, the topography image will look very homogeneous so that the orientation on the surface becomes complicated. Sometimes it is also hard to fully remove these paints after the investigation. This is especially true if the component has a rough surface as, e.g., a textured solar cell, or if there are micron-sized slits or gaps on the surface of the component. Moreover, most of these coatings are based on carbon particles, hence, dried they may be more or less electrically conducting. This may lead to the appearance of current bypasses or even shorts, if high-ohmic electronic components are covered and tested in operation. For microscopic investigations, particle size and film thickness can often not be neglected, hence the pigment film may produce spurious contrasts and may degrade the spatial resolution. Finally, often also the heat conductivity within the paint layer cannot be neglected. To obtain a high emissivity, the thickness of the paint layer has to have a certain minimum value. Then the active electronic components are actually buried below the paint layer, and the thermal waves have to diffuse to its surface before being detected. Hence, the paint layer acts as a low pass with a certain internal thermal time constant. For standard thermography, of course, this argument would not hold, since in the limit $f_{\text{lock-in}} \rightarrow 0$ the paint layer can be assumed to behave adiabatic, reflecting the surface temperature without any errors.

Thus, the demands on an optimum IR-emitting paint for lock-in thermography on electronic components are the following:

- It has to provide a large IR emissivity, hence it has to be opaque and not reflecting in the wavelength range of the camera.
- Nevertheless, it should be able to be applied as a thin layer (preferably $<10\,\mu$m) in order to have a low internal thermal time constant and not to degrade the spatial resolution.
- For microscopic investigations its particle size should be as low as possible.
- It should be electrically insulating.
- It has to be easy to remove.
- It should be non-toxic.

Until now, no paint has been found which would excellently meet all these criteria. Velvet coating is electrically insulating, but it cannot be homogeneously applied if thinner than several $10\,\mu$m, and it shows a visible surface roughness. Commercial colloidal graphite spray gives a good emissivity for homogeneously thin layers below $10\,\mu$m, but it shows a distinct sheet resistance of the order of $10^4\,\Omega/\text{sqr}$. Black india-ink is also almost without a structure, it provides a high emissivity for a thickness below $10\,\mu$m, and at least some varieties of it are electrically well-insulating. However, india-ink is usually water-resistant, hence it is not easy to remove. We have made good experiences with water-soluble black aquarelle paint. If correctly diluted, it yields a good emissivity for a layer thickness below $10\,\mu$m, it is reasonably structureless, it is electrically well-insulating, and it can easily be removed with warm water in an ultrasonic bath. We also have made experiments with pure liquids like oil and glycerin and even with magnetic liquids. However, it turned out that with all these liquids, at least in the mid IR range (3–5 μm), a layer thickness well above $10\,\mu$m would be necessary to attain a sufficient IR emissivity.

For commercial IR-absorbers colloidal metals are often used, which are prepared by evaporating metals under a low pressure. However, such "silver black" or "gold black" layers are electrically conducting. In [134], a method of preparing colloidal bismuth films is described. These films with a thickness of about $10\,\mu$m show a high emissivity above 70% and a low electrical conductivity, which vanishes completely after some days of storage in air. Here the bismuth material was evaporated from a tantalum boat at a residual air pressure of 200 Pa in a closed box in the evaporation chamber with an internal radiation shield. These films are very effective for increasing and homogenizing the emissivity since they are structureless and homogeneous even in microscopic regions. Nevertheless, their use has not become popular until now, maybe because there is no commercial source for producing these films available yet. Though these films can easily be removed in an ultrasonic water bath, it must also be considered that, especially for in-circuit testing, any foreign layers at the surface are generally unwanted in semiconductor device failure analysis.

If macroscopic investigations with a spatial resolution well above $10\,\mu$m have to be made on plane samples like solar cells or other wafers, the best way to improve the IR emissivity is to use a "self-supporting IR emitter film" together with the sample holder, which will be introduced in Fig. 6.6 in Sect. 6.2. This solution allows

one to increase the emissivity without applying paint to the sample surface. We use a 23 μm thick black polyethylene foil ("rs 40" from www.ratioform.de), which is originally intended for packaging purposes and shows a transmittance of about 20% in the wavelength range between 3 and 5 μm. As will be shown in Fig. 6.6b in Sect. 6.2, this film is tightly vacuum-sucked to the sample surface, which also keeps the sample in position and presses the electrical leads to its top contacts. It should be noted that this film is most effective for a lock-in frequency of 3 Hz and below. For higher lock-in frequencies the thermal insulation by the plastic film is already so high that it cannot follow the surface temperature modulation immediately anymore. Hence, the amplitude signal starts to decay superlinearly with increasing lock-in frequency, and the signal becomes strongly dependent on the contact properties between solar cell surface and the film. Therefore, for lock-in frequencies of 10 Hz and above, we do not use this black plastic film anymore but rather a transparent one, or we work without any film at the surface. Also if light has to be irradiated to the sample (see Sect. 6.6.2) the black plastic film cannot be used. However, it must be used if thin film cells with metallic top layer are investigated (see Sect. 6.2.2) or if bifacial cells or cells with dielectric backside passivation are investigated, which show a very low IR emissivity. If this foil is used on top of metallized surfaces (e.g. thin film cells with metal contacts, see Fig. 6.21 in Sect. 6.3), its effective thickness doubles. Therefore here it reduces the emissivity contrast from >90% to <5%.

The influence of the opaque IR emitter film on the appearance of the amplitude image and the topography one is demonstrated in Fig. 5.6 using the multicrystalline solar cell used before. In the lower line (c and d) the cell was covered with a transparent polyester film to keep it in position. With the IR emitter film (a and b) the contact leads and the edges of the sample can only be identified by some residual reflections on these edges in the topography image. Without this film the topography clearly shows the grid lines as well as the crystal structure of the material owing to the texture of the surface. Also the amplitude image of the lock-in thermography investigation (which is shown in exactly the same scaling as with the IR emitter) shows the grid lines as dark lines owing to their emissivity contrast. However, the amplitude signal is generally somewhat lower than with IR emitter, and especially the shunts below the grid lines appear clearly weaker without the IR emitter. Therefore, on large plane samples it is generally better to work with the IR emitter film.

The alternative to the covering of the surface is the software-based compensation of the emissivity contrast after the lock-in thermography measurement. Note that the IR emissivity of even metallized surfaces is usually not zero but of the order of $\varepsilon = 10\,\%$. Therefore, metallized surfaces usually appear dark in the topography image, but they still carry their temperature information. The basic idea of the software-based emissivity correction is to use the topography image to construct an image of the local emissivity $\varepsilon(x, y)$ and to correct the thermograms after the measurement using this emissivity map. The number of photons emitted from each pixel of a sample is the sum of the thermally emitted photons (containing the local emissivity ε as a factor) and the reflected photons emitted from the surrounding. The number of emitted photons may be calculated by integrating Planck's formula across the sensitivity range of the camera, regarding $\varepsilon(\lambda)$ and the wavelength-dependent

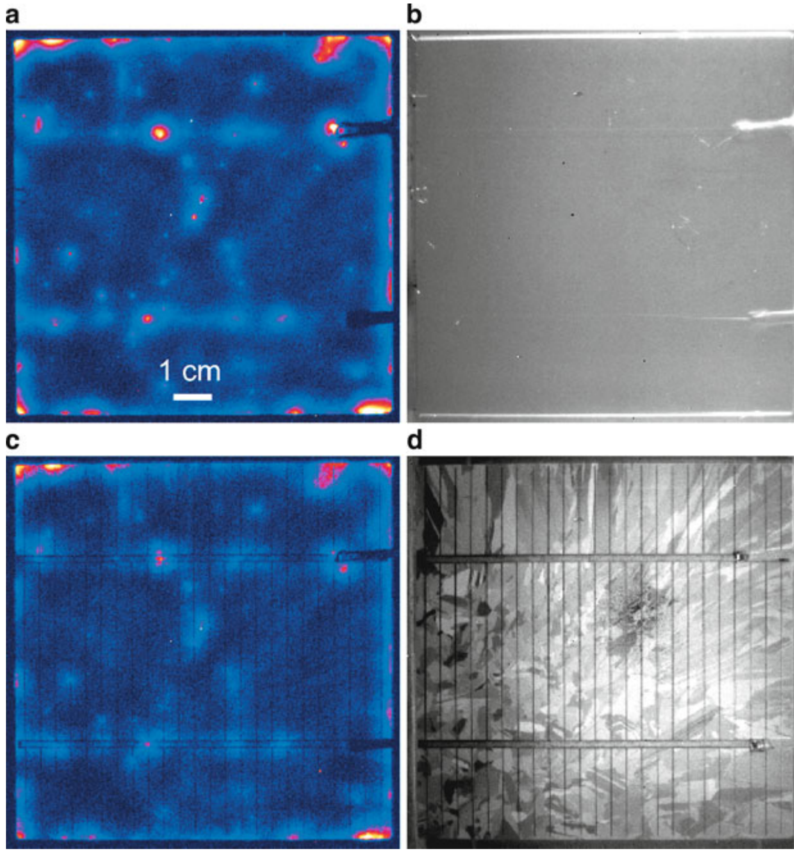

Fig. 5.6 Solar cell investigated with and without a "self-supporting IR emitter film". (**a**) amplitude image with IR emitter, (**b**) topography with IR emitter, (**c**) amplitude image without IR emitter, (**d**) topography without IR emitter

sensitivity of the camera. However, within a limited temperature range of about 10 K this signal can be well approximated to depend linearly on T. Within this limited temperature range, the surface reflectivity may be assumed to be T-independent. Hence, if one thermogram of the (unpowered) sample is taken at ambient temperature T^{amb} and another one with the sample thermostatted at a higher temperature $T^{\mathrm{amb}} + \Delta T$, these two signals will differ only by the increased number of emitted photons:

$$S^{\Delta T}(x, y) = S^{\mathrm{amb}}(x, y) + \varepsilon(x, y)\, \Delta T \tag{5.1}$$

Here $\varepsilon(x, y)$ is the emissivity image and S is the camera reading in units of (m)K, referring to a black body. Thus, the emissivity image may be calculated as:

$$\varepsilon(x, y) = \frac{1}{\Delta T}\left[S^{\Delta T}(x, y) - S^{\mathrm{amb}}(x, y)\right] \tag{5.2}$$

If then the sample is allowed to cool down to ambient temperature and is powered by applying a bias, the emissivity-corrected (true) surface temperature distribution $T(x, y)$ is calculated from the measured signal $S(x, y)$ as:

$$\begin{aligned} T(x, y) &= T^{\mathrm{amb}} + \frac{1}{\varepsilon(x, y)} \left[S(x, y) - S^{\mathrm{amb}}(x, y) \right] \\ &= T^{\mathrm{amb}} + \Delta T \frac{S(x, y) - S^{\mathrm{amb}}(x, y)}{S^{\Delta T}(x, y) - S^{\mathrm{amb}}(x, y)} \end{aligned} \tag{5.3}$$

This is the basis of any quantitative steady-state thermography on objects with unknown and/or inhomogeneous surface properties. If the emissivity measurement and the powered device measurement are made with the same camera settings (e.g. one after the other), the lower part of (5.3) even holds true if the blackbody calibration of the camera was not exact (e.g. done with the heel of the hand, see Sect. 2.1). Once the emissivity map $\varepsilon(x, y)$ is obtained with the unpowered device by using (5.2) or any other means, the first part of (5.3) allows one to display the so-called "true temperature" image of the sample, which is emissivity-corrected. In fact, (5.3) even holds if the camera scaling is not constant across the whole image, hence if the internal 2-point correction of the camera is not correctly adjusted, or if even uncorrected (raw) data would be used (see Sect. 2.1). In principle, the described procedure corresponds to a pixel-by-pixel 2-point scaling procedure of the camera with the object taken instead of a black body. Hence, if the camera system used for lock-in thermography allows to perform the 2-point calibration procedure, and if the sample temperature can be adjusted, this calibration procedure just has to be performed with the sample instead of a black body. Then the IR-image is automatically emissivity-corrected, hence it shows the true temperature. Of course, this "true temperature imaging" only works correctly if the image position for both the calibration measurements and the actual measurement of the powered device are exactly the same. Especially for microscopic investigations it has to be ensured that the sample position does not shift by more than a small fraction of one pixel size due to thermal image drift. Any lateral image drift leads to strong spurious signals especially at sharp boundaries between regions of different emissivities.

In some cases the two-point correction cannot be performed by the user, or the sample can be heated up but the exact sample temperature is unknown. Then, for enabling quantitative lock-in thermography on solar cells, a "relative emissivity correction" procedure can be applied, which has been proposed by Kasemann et al. [135]. This procedure is based on the fact that (5.2) holds both for the local emissivity $\varepsilon(x, y)$ and for the average emissivity of the whole imaged region $\varepsilon_{\mathrm{whole}}$. Then the ratio of both, describing the relative emissivity variations over the sample surface, is:

$$\frac{\varepsilon\,(x, y)}{\varepsilon_{\mathrm{whole}}} = \frac{S^{\Delta T}\,(x, y) - S^{\mathrm{amb}}\,(x, y)}{\left(S^{\Delta T} - S^{\mathrm{amb}}\right)_{\mathrm{whole}}} = \frac{S^{\Delta T}\,(x, y) - S^{\mathrm{amb}}\,(x,y)}{S^{\Delta T}_{\mathrm{whole}} - S^{\mathrm{amb}}_{\mathrm{whole}}}. \tag{5.4}$$

Here, as in Sect. 4.5.1, the index "whole" stands for the average across the whole area. This equation holds independent on the temperature difference ΔT used for the calibration measurement. For obtaining a sufficient signal-to-noise ratio, ΔT should be at least several K [135]. If the ratio (5.4) is used in (5.3) instead of $\varepsilon(x, y)$, the emissivity contrast is indeed removed, but the "true" temperatures are measured too high since the mean value of (5.4) is 1, but $\varepsilon(x, y)$ is always smaller than 1. However, this uncertainty can be removed for lock-in thermography, as will be shown below. For lock-in thermography, any steady-state signal contribution cancels out, and the two primary signals $T^{0°}(x, y)$ and $T^{-90°}(x, y)$ only have to be divided by $\varepsilon(x, y)$:

$$T^{0°}_{\text{corr}}(x, y) = \frac{T^{0°}_{\text{meas}}(x, y)}{\varepsilon(x, y)} \tag{5.5}$$

$$T^{-90°}_{\text{corr}}(x, y) = \frac{T^{-90°}_{\text{meas}}(x, y)}{\varepsilon(x, y)}$$

The relative emissivity correction using (5.4) is very valuable for the quantitative interpretation of lock-in thermograms of solar cells (see Sect. 4.5), if their emissivity is not homogenized by a black surface layer. If in (4.33) all lock-in thermography signals are divided by $\varepsilon(x, y)$, which can be replaced by $\varepsilon_{\text{whole}}\ (\varepsilon(x, y)/\varepsilon_{\text{whole}})$, (4.33) can be re-written as [135]:

$$p\,(x, y) = \frac{S^{-90°}\,(x, y)}{\left(\frac{S^{-90°}}{\varepsilon(x,y)/\varepsilon_{\text{whole}}}\right)_{\text{whole}}}\,\frac{\varepsilon_{\text{whole}}}{\varepsilon\,(x, y)}\,\frac{P_{\text{whole}}}{A_{\text{whole}}}. \tag{5.6}$$

Since the absolute value of the emissivity influences both the local lock-in thermography signal and the signal averaged across the whole area, the absolute value of ε is not needed in (5.6), and it is sufficient to use the relative emissivity change (5.4), which is easier to measure. In this way, quantitatively correct lock-in thermography investigations can also be performed on bare devices like solar cells showing a distinct emissivity contrast.

Thermostatting the sample takes time and is not always possible. It would be much easier if the emissivity correction could also be performed with a sample kept at room temperature. Indeed, under certain favourable conditions this is possible. The procedure of obtaining $\varepsilon(x, y)$ may essentially be simplified if the reflected radiation can be neglected. This is the case if the surrounding of the sample is at a considerably lower temperature than the sample itself, which can be realized most simply by heating up the sample by at least 10 K above room temperature. Alternatively, the influence of reflected light can also be minimized by placing the sample in a hollow enclosure, which contains a hole for the camera to look through and is internally black painted and cooled well below sample temperature. For investigating ICs with a microscope IR objective by using a cooled camera even at room temperature the reflected radiation can usually be neglected. This is because then the object is very close to the objective, hence the reflected light mainly comes

from the cold interior of the camera itself. One can say that in this case the black spot of the “Narcissus effect” (see Sect. 2.1) covers the whole area.

If the reflected light can be neglected, the topography signal $S^{\text{topo}}(x, y)$ of the unpowered object, which is always measured and stored before a lock-in thermography measurement, can be written as:

$$S^{\text{topo}}(x, y) = S_0 + \varepsilon(x, y) S_{\text{em}} \tag{5.7}$$

Here, S_0 is the camera signal offset value, which appears without receiving any photons, and S_{em} is the signal part, resulting from the emission of photons at this temperature. Equation (5.7) comes from the fact that we assume a linear dependence of the camera reading on temperature here, which actually is super-linear. Therefore, even if the object would be at 0 K, the camera reading is at S_0. For a black body, $S_{\text{em}} = S^{\text{topo}}_{\text{black}} - S_0$ would hold, with (5.7) leading to:

$$\varepsilon(x, y) = \frac{S^{\text{topo}}(x, y) - S_0}{S^{\text{topo}}_{\text{black}} - S_0} \tag{5.8}$$

The two parameters S_0 and $S^{\text{topo}}_{\text{black}}$ may be obtained either empirically by minimizing the emissivity contrast of a lock-in thermography result, regarding that S_0 has to be below the lowest and $S^{\text{topo}}_{\text{black}}$ above the highest pixel value of $S^{\text{topo}}(x, y)$. Alternatively, both values can be directly measured by exposing the camera to a sufficiently cool object and a black body at sample temperature. The simplest realization of a cool object is to show the camera its own “cool eye” in a good metallic mirror. Once S_0 and $S^{\text{topo}}_{\text{black}}$ are established and the emissivity map has been calculated from the unpowered topography image $S_{\text{topo}}(x, y)$ according to (5.8), the “true temperature” map of the powered device can be calculated from the measured signal $S(x, y)$ according to:

$$T(x, y) = S_0 + \frac{S(x, y) - S_0}{\varepsilon(x, y)} \tag{5.9}$$

It should be noted that, if the emissivity map is obtained according to (5.8), the unpowered “true temperature” image according to (5.9) looks always homogeneous (no emissivity contrast), independent on whether S_0 has been chosen correctly or not. However, if S_0 has an incorrect value, in the “true temperature” image of the powered device some emissivity contrast reappears, which vanishes if S_0 is correctly chosen. On the other hand, if lock-in thermography measurements are corrected according to (5.5), the emissivity contrast only vanishes if S_0 is correctly chosen. So, in a lock-in thermography system, the easiest way to obtain S_0 is not to measure it but to vary it interactively until in any lock-in thermography result the emissivity contrast vanishes. This option can be implemented in the Thermosensorik lock-in thermography systems.

All previous considerations are valid only in a limited temperature range of less than 10 K, where an essentially linear dependence of the camera signal on temperature can be expected. Over a larger temperature range, however, the intensity of

emitted IR radiation depends super-linearly on temperature, see eq. (2.1) in Sect. 2.2. Then non-linear camera calibration has to be used, which is incorporated in most modern IR cameras. Then a given (homogeneous) emissivity has to be assumed. If the emissivity is inhomogeneous but temperature-independent, it can be measured as for (5.2) and (5.8). However, in contrast to (5.3), here the emissivity correction for true temperature imaging has to be applied not to the temperature reading of the camera but rather to its raw signal, since only this one depends linearly on the emissivity. Then from the emissivity-corrected raw image the true temperature image can be calculated by using the non-linear scaling procedure of the camera calibrated for a black body.

Finally, if lock-in thermography with two-channel correlation is applied, the disturbing emissivity contrast is not present if the results are displayed as the phase image, which is inherently emissivity-corrected. However, as it has been outlined in Sect. 5.1, the phase image only qualitatively displays the local dissipated power distribution. For isolated local heat sources, the phase image is independent on the magnitude of the dissipated power. Therefore the phase image displays the dissipated power distribution with a kind of "dynamic compression". This property also can be taken as an advantage, since it allows to display weak heat sources adjacent to strong sources with a similar brightness. If only microscopic regions have to be imaged, as it is the case in thermal failure analysis of integrated circuits, also the $0°/-90°$ image can be displayed, which is also inherently emissivity-corrected. As it has been explained in Sect. 5.1, this signal preserves the information of the magnitude of local power sources, at least within a microscopic region being small against the thermal diffusion length. This is the reason why the $0°/-90°$ signal can also be mathematically deconvoluted for removing the thermal blurr and obtaining the true lateral dissipated heat distribution in microscopic region (see Sect. 4.5.2).

To summarize this section, the emissivity contrast can be removed by the following measures:

- Covering the surface with a thin layer of high emissivity, like graphite spray (conducting!), aquarelle paint, or colloidal bismuth.
- Sucking on a thin black plastic foil (best for d.c. imaging or lock-in thermography of solar cells at lower frequencies).
- Thermostatting the sample, measuring the local emissivity, and correcting all results correspondingly.
- Thermostatting the sample and performing the 2-point correction of the IR camera with the unpowered sample at two temperatures.
- Thermostatting the sample and performing the relative emissivity correction (for correcting lock-in thermography results).
- If reflected light can be neglected (sample at elevated temperature, cooled environment, or microscopic sample under microscope objective), emissivity correction by using the topography image of the unpowered device at room temperature.
- Display of the phase image (only qualitative measure of the power distribution) or the $0°/-90°$ image (quantitative in regions being small against the thermal diffusion length).

5.4 Influence of the Peltier Effect

It was already mentioned in Sect. 2.8 that several different heat dissipation and transport mechanisms may be active in an electronic device, which all may contribute to a local temperature change detected by lock-in thermography. These are resistive (Joule type) heat generation, heat generated by non-radiative minority carrier recombination, Peltier-type heating and cooling, and thermalization of hot carriers after optical generation.

In this section, we will focus on the physical understanding of the Peltier effect both at ohmic contacts and at the p-n junction. In most textbooks, the Peltier effect is described only for a loop made by two dissimilar metal wires A and B switched in sequence A-B-A in conjunction with the Seebeck effect. If a temperature difference ΔT is established between contacts A-B and B-A, a thermovoltage appears between the two open ends A-A, which is the Seebeck effect. Thus, the Seebeck coefficient Σ has the unit V/K. On the other hand, if a current I flows through this circuit under isothermal conditions, e.g. at junction A to B heating occurs and at junction B to A cooling power, depending on the two materials. Reversing the current direction exchanges the heating and cooling sites. Thus, the Peltier coefficient Π has the unit $\mathrm{W/A} = \mathrm{V}$. It can generally be shown that for any temperature T and for any combination of materials $\Sigma = \Pi / T$ holds, which is known as one of Kelvin's laws.

By the pure Peltier effect (i.e. under isothermal conditions) heat is only transported but not generated. Both the Peltier heating and cooling powers have the same magnitude, and the Peltier process itself does not consume any energy. Only if, due to the Peltier effect, a temperature difference between both contacts is established, which is connected with a Seebeck effect, and the current flows against the thermovoltage, electric energy is consumed by the device. Also the inevitably involved Joule heating in the device consumes electric energy. Both the Seebeck and the Peltier coefficients can be defined also for a single material [44]. In the following section, we will focus only on the Peltier effect and will try to explain its physical nature in some more detail for metals, metal–semiconductor contacts, and also for p-n junctions. Understanding the following paragraphs requires basic knowledge in semiconductor physics.

The Peltier effect can be explained either by using thermodynamic potentials or based on semiconductor physics of quantum particles (electrons and holes). Here, we will use the particle description since it appears to us to be more comprehensible. In the following we will often mention electrons as charge carriers, but the whole discussion can also be performed for holes. We also will restrict ourselves to 1-dimensional current and heat flows and isotropic materials, hence we will consider the Peltier coefficients and the conductivity as scalars.

The Peltier coefficient of a material is a measure of how much energy is transported by its charge carriers if a current flows [44]. This energy is a "latent" heat energy, which is transported by a medium (carriers) at constant temperature. This can be seen in analogy to thermodynamic phase transitions. So the Peltier coefficient Π can also be described as "heat per amount of transported charge", having the units $\mathrm{J/C} = \mathrm{Ws/As} = \mathrm{V}$. As it will be shown later, this energy can have

contributions of potential energy and of kinetic energy. In any material the energy-dependent equilibrium electron concentration is given by the product of the density of states and the Fermi distribution function, which shows an occupation probability of 1/2 at the Fermi level. In metals the Fermi level is lying within a band. Since electrons are Fermi particles, they need empty states for movement, so that they cannot move in energy positions well below the Fermi level where the band is totally occupied. Therefore the current transport in metals occurs mainly by electrons having an energy close to the Fermi level. However, depending on the shape of the band and on the scattering mechanism, the mean energy of the carriers participating on transport may slightly deviate from the position of the Fermi level. For example, if the density of states increases with increasing energy, there are more carriers with higher energy available for the transport, hence here the mean energy of the transporting carriers is slightly above the Fermi level. The scattering process determines the mean free path of the carriers depending on their kinetic energy, which also may increase the mean energy of the carriers contributing to current transport. Since these two effects lead to only small deviations between the Fermi level and the mean free energy of carriers contributing to charge transport in metals, the differential Peltier coefficients for combinations of metals are small, typically in the order of some mV.

This changes if ohmic contacts between metals and semiconductors are considered. In a non-degenerated semiconductor, the Fermi level is lying in the gap where no allowed electron states exist. For entering the band of a semiconductor from a metal, the carriers have to gain an amount of potential energy which equals the Fermi energy ξ of the semiconductor. In addition, as it had been already mentioned in Sect. 2.8, the carriers in the bands carry a certain mean energy. It can be found in [44] how this energy can be calculated both for the case of non-degeneracy and degeneracy. The expected Peltier coefficient between a metal and a semiconductor is $\Pi = \pm(\xi + \varepsilon)/e$ [44]. The sign of the Peltier coefficient depends on the conductivity type; it is positive for holes and negative for electrons, and its magnitude strongly depends on the doping concentration via ξ. Here ε is the mean energy of conducting carriers in a band relative to the band edge. In the case of non-degeneracy ε can be viewed as the mean kinetic energy of the carriers, which depends on the dominant scattering mechanism and is for silicon at room temperature $\varepsilon = (r + 5/2)\mathrm{k}T$. The temperature dependence of the scattering process is given by the scattering parameter r, which for silicon at room temperature is about −0.5 [136]. In the case of degeneracy ξ becomes negative and ε is a function of ξ and r [44].

Another contribution to Peltier-type heat transport in semiconductors needs to be taken into account in addition to the potential and kinetic heat of the electrons. Consider a directed flow of electrons in a high-quality crystal at low temperatures. The electrons are scattered by lattice vibrations. Therefore, in steady-state conduction, a certain amount of energy is conducted through a directed flow of phonons parallel to the electron flow and in equilibrium with it. At a metal contact, the directed phonon flow comes to a sudden stop and the latent heat carried by them is absorbed by the lattice.

This effect known as "phonon drag" [44] always increases the amount of latent heat conducted together with the electronic transport, and can thus be added to the kinetic energy portion ε of the electrons (the same holds for holes).

Although phonon drag is a low temperature effect, it still amounts for some 30–40% of the overall Peltier coefficient $\xi + \varepsilon$ of moderately doped silicon (10^{16} cm^{-3}) [136–138]. It depends critically on crystal quality and on geometry and is therefore hard to predict for a given experiment.

Note that here, in contrast to [44], the Fermi energy ξ is counted positively in the case of non-degeneracy and negatively in the case of degeneracy. The Peltier effect at the contacts was described in Fig. 2.13 in Sect. 2.8 by the inclined double arrows labelled p_{BM} and p_{ME}. Note that, in reality an ohmic contact never is a simple energy step as sketched in Fig. 2.13. Since there are inevitable energy barriers at the semiconductor interface, only a highly doped semiconductor at the interface enables the formation of low-ohmic contacts, since only in this case the barrier is low enough to be overcome or small enough to be tunneled through by the carriers [139]. Fortunately, the amount of the differential Peltier effect at the metal-semiconductor interface does not depend on the microscopic structure of this interface but only on the homogeneous Peltier coefficients of the materials that are left and right of this interface, where the charge is transported away. Only the contact resistance, which governs the resistive loss at the interface, depends on this microscopic structure.

It had been already mentioned in Sect. 2.8 that the current flow across a p-n junction also implies a Peltier effect. While the Peltier effect at metal contacts or at the ohmic contact between a metal and a semiconductor is a majority carrier process, which changes sign if the applied bias is reversed, the Peltier effect at a p-n junction is a minority carrier effect. This phenomenon is known as bias-dependent Peltier effect, bipolar Peltier effect, or internal cooling effect [140]. The additional potential energy of the minority carriers is given by the bias-dependent barrier height at the junction. According to Fig. 2.13, the "thermalization" of photo-generated electrons crossing the p-n junction from the p- to the n-side generates a Peltier heat of p^{+}_{pn} (2.38). In the same way, the dark forward current generates a Peltier cooling of p^{-}_{pn} (2.39). While the effect of Peltier heating can easily be understood by imaging electrons as particles in a gravitation field, which loose their potential energy, it is harder to imagine why the electrons "climb up the hill" (since they move against the electric field) by becoming cooler. This can only be understood by considering the fact that charge is not only conducted by carriers close to the band edge, as it is drawn in most figures and also in Fig. 2.13, but also by hot carriers deep in the band, which exist there also in equilibrium due to the "Maxwell-Boltzmann tail" of the Fermi distribution. Only those "hot" electrons in the n-material having a kinetic energy above the barrier height are able to flow into the p-material. This process is also known as "thermionic emission". Since the carriers are slowed down by the electric field, they arrive at the p-side with a correspondingly lower kinetic energy without having generated any heat. However, by the drain of the highest energy electrons in the n-material, the electron temperature in this material reduces, which instantly couples to the lattice temperature. This is the Peltier cooling power at the p-n junction p^{-}_{pn}.

It is sometimes hard to imagine that also at a p-n junction Peltier heating and Peltier cooling have the same amount. If electrons are injected from the n- to the p-side at an applied forward bias V in the dark, they generate a certain Peltier cooling, as described. Also at the contacts only Peltier cooling occurs. So where is the corresponding Peltier heating which should balance this cooling? It is contained in the recombination heat. Indeed, as (2.45) shows, for the device as a whole the sum of all Peltier contributions is zero and the only dissipated heat is the product of the flowing current and the applied bias. Since the only heating effect considered in this model is recombination heat, the recombination energy has to be split into two parts. This is one irreversible part, which is $e \times V$ per electron, and one reversible part, which is the sum of all contributing Peltier effects. If the recombination should be purely radiative, also the light absorber is part of the whole thermodynamic ensemble. Then the heat is dissipated at the absorber, and in the p-n junction (which is then an LED) only Peltier cooling occurs. This effect is known as "optical refrigeration" [141].

The Peltier effect in an illuminated solar cell is also an interesting consideration. Let us assume a cell under short circuit (having zero dark current) under illumination. Then, according to our explanation, both at the contacts and the p-n junction only Peltier heat is generated, so where is the corresponding Peltier cooling? It can be thought to be generated in an LED at the same temperature illuminating the considered cell. Indeed, the splitting of the photon energy into a reversible and an irreversible contribution is physically related to the Shockley-Queisser model of the maximum possible conversion efficiency of solar cells [142], which also depends on the bias, hence on the illumination intensity: The irreversible fraction of the photon energy is the one that can be converted into electric energy at maximum.

These considerations have the implication that, in the presence of minority carriers, the Peltier coefficient of the semiconductor has to be split into an electron- and a hole-contribution, from which the minority carrier contribution is no material constant anymore but is dependent on the position in the device and on the applied bias [140]. Without going into any more details, the implications of this behavior for the interpretation of lock-in thermography measurements will be presented here. It was already mentioned in Sect. 2.8 that none of the Peltier effects can be observed in the dark for vertical current flow, i.e. that all Peltier effects and the non-radiative recombination appear in one and the same position viewed by the IR camera. In this case the heat generation occurs in analogy to Joule heat generation, which is the base of all approaches for quantitative interpretation of lock-in thermography presented in Sect. 4.5. According to (2.45) in Sect. 2.8, which holds under forward bias without illumination, all three Peltier terms p_{pn}^{-} (at the p-n junction), p_{ME} (at the emitter contact) and p_{BM} (at the base contact) are negative (cooling), and the only heat source is recombination. The pure recombination heat ((2.40) plus (2.41), times cell area) is $P = I \times E_{\mathrm{g}}/e$ (plus the kinetic energy terms), which is much more than the value $P = I \times V$ expected from the energy conservation law. So we can say that the Peltier effect "carries additional heat to the recombination sites", which is consistent with the interpretation of the Peltier coefficient as a measure of how much energy is transported by carriers.

It depends on the sample geometry how much of this effect can be observed separately by lock-in thermography. The bipolar Peltier effect at the p-n junction, for example, could be observed separately if, in a long-length diode, the IR camera is observing the p-n junction from the side. Then, since the minority carriers are recombining in a certain lateral distance from the p-n junction, depending on their diffusion length, the local Peltier cooling at the junction could be observed separately by performing DLIT at this device. If then a strong recombination center was placed between the p-n junction and the base contact, which dominates the whole recombination in this device, the recombination heat on this site would contain all three Peltier heat contributions: the bipolar one from the minority carriers from the junction and the two unipolar ones from both contacts.

In solar cells the p-n junction is lying in the image plane and the minority carriers are moving essentially vertically, therefore recombination and current injection appear here at the same sites. In this case, any lateral current is a majority carrier current. Then only the unipolar Peltier effects at the contacts can be observed separately at local contacts, and the recombination heat only contains the additional Peltier heat from the contacts. Since the top contact of all solar cells is formed as a grid, in the emitter always a lateral current flows, hence under dark forward current the grid lines should show local Peltier cooling and under reverse current (photocurrent) local Peltier heating. It will be shown later in this section that this is indeed the case, but the effect is small, since the emitter doping concentration is very high. The Peltier coefficient at the grid contacts is only about 70 mV, which is small when compared to a typical applied bias. At the base contact the Peltier coefficient is about 350 mV, which is much more pronounced. However, in most present silicon solar cells the base contact covers the whole area and is very low-ohmic. So horizontal electric fields in the base region cannot establish, hence the base current is flowing essentially vertically. Therefore, if the current is fed into the cell through a homogeneous p-contact, no Peltier effects from the base contact can be observed separately and all techniques for quantitative evaluation of lock-in thermography should work correctly. This changes if we have a local base contact, like a grid contact for double-sided cells or an array of point contacts. Here for forward currents, the grid contacts should become cool and the recombination sites should show a correspondingly higher power generation. The latter effect was already mentioned by Kaes et al. [14] who have observed that local recombination sites show a higher lock-in thermography signal under pulsed illumination, leading to a certain pulsed open circuit voltage, than by application of the same pulsed bias in the dark. They have attributed this effect to the missing Peltier effect of the back side at these sites, hence they have assumed lateral majority carrier (hole) transport to the recombination sites in the base. Also a certain amount of lateral minority carrier diffusion to the recombination sites might contribute to this effect. As one example in Sect. 6.3 will show, the Peltier effect is especially pronounced in thin-film CSG (Crystalline Silicon on Glass, [143]) solar cells, since there all contacts are local and the unipolar Peltier effects from both contacts are clearly visible.

Since lock-in thermography may detect very tiny temperature modulations it is especially qualified to detect Peltier effects. Indeed, Grauby et al. [34] have

investigated a resistive network consisting of metal lines and polycrystalline silicon conductor stripes. They have uniquely observed the Peltier effect at the junctions between the metal lines and the poly-Si stripes. However, contrary to our approach of lock-in thermography, they have used a symmetric harmonic signal for loading their structure. Here, the Joule heating has a $\sin^2$-shape, hence the Joule heating oscillates with double the driving frequency, whereas Peltier heating and cooling occur synchronously with the driving frequency. This allowed them to clearly separate these two effects by synchronizing the lock-in detection to these two different frequencies. As mentioned above, Peltier heating increases linearly with the driving current, but the Joule one increases to the quadratical power, which was also experimentally verified. Unfortunately, the lock-in thermography systems described in this book, specialized to investigate electronic devices, are neither intended to provide a symmetric and harmonic driving signal nor to enable a detection at double the driving frequency. Instead, they provide an asymmetric square wave driving signal and detect only at the basic harmonic of this signal. Hence, the question arises how it is possible using the systems described here to detect Peltier signals and to distinguish them uniquely from signals caused by Joule type heat dissipation.

This problem can easily be solved by making two separate lock-in measurements of the sample applying the same bias in both polarities [138]. Joule heating does not depend on the polarity, but Peltier heating and cooling just change their signs for different polarities. In order to distinguish heating from cooling, the polarity of the detected signal has to be detected. Therefore, as the result of the lock-in measurement a fixed phase signal has to be used instead of the amplitude one. The optimum phase, which most clearly allows one to distinguish heating from cooling for any heat source geometry, is the one which gives a maximum signal for a homogeneous heat source and shows a minimum overshoot for point sources. According to the considerations in Chap. 3 this is the $-90°$ signal for thermally thin samples, and the $-45°$ one for thermally thick ones. The problem is that in each of the two measurements (forward and reverse bias) in one and the same position the signals of Joule heating and Peltier heating/cooling may superimpose. Thus, the trick to separate both components is to calculate the sum and the difference of the fixed phase images for both polarities! In the difference-image, the Joule component should cancel, and in the sum-image the same happens with the Peltier one. Hence, the difference-image displays the Peltier signal separately, and the sum-image does the same with the Joule one. While the Joule image should be positive everywhere, in the Peltier image a positive signal corresponds to Peltier heating, and a negative one to Peltier cooling. Altogether, both Peltier components should have the same total amount and should average out across the whole sample area.

This is demonstrated in Fig. 5.7, showing different $-90°$ lock-in thermography images of a piece of a silicon solar cell. The n^+-doped emitter layer of this cell is contacted by silver grid lines having a separation of about 2.5 mm. In normal operation of the cell, all these grid lines are connected together by the bus bars. In this small piece of a solar cell, however, the grid lines are electrically separated from each other. For demonstrating the Peltier effect, the pulsed voltage was applied here between two grid lines. The base voltage was chosen such that the p-n junction was

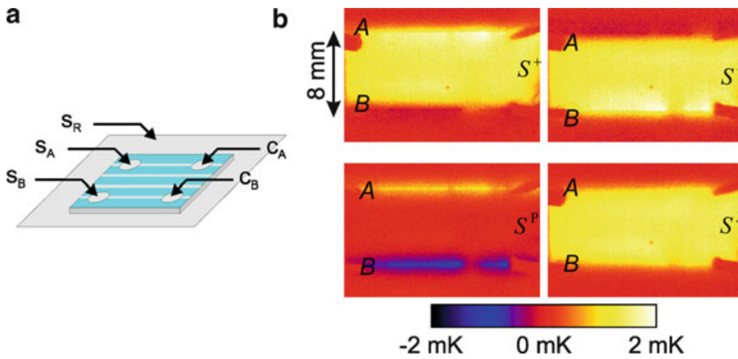

Fig. 5.7 Current flow between two contact grid lines of a silicon solar cell. (**a**): Schematic drawing, $s_{A,B}$ and $c_{A,B}$ are "sense" and "current" leads for contacts A and B, respectively. The p–n junction of the cell is reverse biased using s_R. (**b**) $-90°$ thermograms, S^+: positive at contact A, S^-: negative at contact A; S^P: Peltier signal; S^J: Joule signal

under reverse bias everywhere. Then the current flows from one grid line through the ohmic contact into the emitter layer and leaves this layer through the ohmic contact to the other grid line, as sketched in (a). For reducing the emissivity contrast, the surface of this device was covered by a thin layer of black paint. Figure 5.7b shows the lock-in thermograms of this device under 0.6 V bias applied under both polarities ("+" at the upper and "+" at the lower contact). The main heat is generated in this device by Joule heating in the emitter layer between both contact stripes. This heat is independent of polarity. However, the signals at the two contacts are slightly different and depend on polarity. This becomes more obvious if the Peltier and the Joule component are displayed separately by subtracting the images for both polarities and adding them (both divided by 2 for obtaining the same scaling limits). Indeed, the average value of the pure Peltier signal across the whole device is zero, and the Peltier signal appears only at the contacts. There is no increased Joule signal at the contacts, hence here the contact resistance is negligible compared to the sheet resistance of the emitter layer. Since the amount of Joule heat is well known here by knowing the applied bias and the flowing current, also the Peltier effect can be quantified from the data in Fig. 5.7 by applying the proportionality method (see Sect. 4.5.1). It turns out that in this device the Peltier coefficient of the emitter has a magnitude of -70 mV. This value corresponds well both to measured values from the literature [137] and to the theoretically expected value [44] for an effective emitter electron concentration of about $n = 1 \times 10^{20}\,\text{cm}^{-3}$. A similar investigation of the base of a typical solar cell yielded a Peltier coefficient of about $+350$ mV, which also corresponds well to literature values for a base doping concentration of p approximately $10^{16}\,\text{cm}^{-3}$. In contrast to the value for the emitter, this value for the base is significantly affected by phonon drag (approximately 30% of the Peltier coefficient). For detailed information on the measurement and interpretation of the results cf. [138]. Hence, lock-in thermography provides effective

means to measure the Peltier coefficient quantitatively in simple devices like solar cells having spatially separated ohmic contacts.

It had been mentioned already at the end of Sect. 2.8 that, if the current flows strictly vertically through a device, it is not possible to image the Peltier effect at the contacts separately, since it always superimposes with other heat sources. As Fig. 5.7 shows, such a separate imaging is possible if the contacts are local and the current spreads laterally. Also the result shown in Fig. 6.17a, which was originally attributed to Joule heat, is caused mainly by the Peltier effect. It will be shown in Sect. 6.3 that lock-in thermograms of thin film polycrystalline silicon solar cells are considerably affected by Peltier warming and cooling. Hence, these lock-in thermograms can only be interpreted correctly by considering also the Peltier effect.

Chapter 6
Typical Applications

Some applications of Lock-in Thermography for the investigation of a thermally thin sample (solar cell) and a thermally thick one (IC) were already presented in the examples given in Chap. 5. In the following section we will present some more applications, showing the universal applicability of this technique to different fields of functional diagnostics of electronic components. Here we have restricted ourselves to the most prominent application fields of lock-in thermography in electronic device testing, which are failure analysis in integrated circuits and testing of solar cells, modules, and materials. At the beginning of each section, the physical problem to be solved will briefly be introduced. Of course, also this can only be a small survey of the possibilities of lock-in thermography in this field. Not considered here will be e.g. the application to the fields of non-destructive testing (NDT, see [2]) and of biology and medicine (see, e.g., [144]). In Sect. 6.1 some more investigations of integrated circuits (ICs) will be described, since this is already today one of the most promising applications of lock-in thermography. Especially, we will present the application of a solid immersion lens (SIL), and an application of a more sophisticated triggering mode of imaging sites of a definite logical response of an IC, which was mentioned in Sect. 2.3. Moreover, we present an example of a lock-in thermography investigation from the back-side on an encapsulated chip "through the die". Another example shows how lock-in thermography may detect sub-surface shorts in the mold compound of a device. In Sect. 6.2 some more examples of solar cell investigations will follow. Depending on whether or not the sample is irradiated during these investigations by light, these investigations are divided into dark lock-in thermography (DLIT, Sect. 6.2.1) and illuminated lock-in thermography investigations (ILIT, Sect. 6.2.2). In Sect. 6.3 investigations on solar modules are reported. It will be shown that the interpretation of lock-in thermograms of single solar cells differs somehow from that of solar modules, which consists of an electrical serial and parallel connection of several solar cells. Finally, in Sect. 6.4 some applications of "non-thermal" investigations of carrier density imaging on wafer material (CDI/ILM) are introduced.

6.1 Integrated Circuits

It had been outlined already in Sect. 3.1 that the microscopic thermal inspection of integrated circuits (ICs) has become an established standard diagnostics tool. Some kinds of defects like leakage currents, shorts, or latch-ups, are leading to local heat sources. Also the normal operation of an IC may lead to a characteristic pattern of (usually weaker) local heat sources across the die, which may be used to characterize the correct function of the circuit. The most popular microthermography techniques of IC testing and failure analysis are liquid crystal techniques [75], Schlieren imaging [80], fluorescent microthermal imaging [41] and IR microthermography [20,91]. The advantage of the liquid crystal technique is its ease of operation, whereas its main disadvantage is its limited sensitivity of about 100 mK and the necessity to cover the surface with the liquid crystal layer of homogeneous thickness. Moreover, this technique requires the exact control of the device temperature. Fluorescent microthermal imaging (FMI [41]) may reach submicron spatial resolution and a sensitivity limit down to 10 mK, but it also requires that the surface is covered with a foreign layer. Both techniques cannot be performed from the back side of a flip-chip "through the die", which is possible for IR thermography inspection techniques (see below). Schlieren imaging is only possible from the back side, frontside imaging requires a suitable coating. The basic limitation of microscopic IR thermography is that its optical resolution is limited by the wavelength of the detected light to the order of 5 μm. This limitation can be overcome to a certain degree by using a solid immersion lens (SIL, see Sect. 3.4), which shifts the spatial resolution limit close to 1 μm. Another serious problem is that the image is strongly modulated by the local IR emissivity so that it may be hard to distinguish weak temperature contrasts from the emissivity contrast (see Sect. 5.3). Therefore, if IR thermography is applied in the conventional (steady-state) mode, a special emissivity map has to be measured in addition to the actual thermogram at elevated temperatures in order to correct the thermograms for the emissivity contrast [91]. This procedure had been discussed before (see Sect. 5.3). It has to be pointed out that the lateral heat conductivity may seriously degrade the spatial resolution of any steady-state thermographic investigation, especially in silicon devices, which had been discussed already in Sect. 5.2.

If microscopic IR thermography is performed in the steady-state mode, a temperature resolution of the order of 100 mK may be obtained [91], which is of the same order as that of the liquid crystal technique. With this thermal sensitivity only relatively strong heat sources in ICs can be imaged, like latch-up sites, shorts in the metallization, or gate oxide breakdown sites. Heat sources from the ordinary operation of the circuits, however, usually remain invisible in these investigations, unless a considerable local power of many mW is dissipated. The application of lock-in thermography greatly improves the sensitivity by 3 orders of magnitude from about 100 mK to below 100 μK. We have estimated that a local heat source of below 5 μW on the surface of a silicon die is still detectable after a measurement time of 1/2 hr by microscopic lock-in thermography [97]. This improved sensitivity, combined with the inherently improved lateral resolution of lock-in thermography (see Sects. 5.1

and 5.2), enables a vast number of new applications in thermal IC testing, which have not been accessible before by thermal methods due to the lack of sensitivity. Now also weak heat sources, possibly arising during the normal operation of an IC, may be detected. Another great advantage of lock-in thermography over the steady-state one is the possibility to display a phase image or an "emissivity corrected 0° image" (0°/−90° image, see Sects. 5.1 and 5.3). These two images directly follow from a single lock-in measurement performed at room temperature without any thermostatting. But contrary to the amplitude image, they are not directly influenced by the emissivity contrast, only their signal-to-noise ratio is degraded in regions of low emissivity. The 0°/−90° image may become even numerically deconvoluted to obtain the local power distribution (see Sect. 4.5.2). In the following, some more results of microscopic IR lock-in thermography on ICs will be presented.

The thermocamera used for lock-in thermography may be equipped with different IR objectives. For example, the Thermosensorik lock-in thermography systems [19] may be equipped with a wide range of Macro- and Micro-Objectives up to Micro 10×, corresponding to a pixel size of 1.5 μm. It was discussed already in Sect. 3.4 that the decisive figure of merit of an objective used for lock-in thermography is its brilliance, which is given by its input-NA (numeric aperture) and its f-number. Any IC failure analysis starts with a low magnification image to see in which region of the die the dominant local heat sources are. It is one of the advantages of lock-in thermography, e.g. compared to light emission microscopy, that no defect is too small to be detected even at a low magnification factor. This is due to the inherent lateral blurring of all thermal methods, which leads to a remarkable halo of the thermal signal around the defect. Due to this halo, also very small (point-like) heat sources remain visible at low magnification factor, if their power is above the detection limit (see Sect. 4.5). So the first investigation is at low magnification, where the die can be imaged as a whole. For this investigation, a lower value of the lock-in frequency may be chosen in order to have a large signal height. Only as the second step the interesting details should be investigated using the highest magnification microscope objective at a high lock-in frequency in order to have a good spatial confinement of the heat around local heat sources. Finally, a SIL may be used for detecting the fault position as good as possible.

This procedure is demonstrated in the investigations shown in Fig. 6.1. Here overlay images of the topography image (in grey) with the actual lock-in thermography images (in colour) are shown. Topography images are single images of the IR camera which are taken before the lock-in thermography procedure begins. Figure (a) was taken at a lock-in frequency of 10 Hz by using a 2.5× objective which is able to display the whole die. The point-like power source in the framed region was the fault in this device. For (b) a 5× objective was used and the lock-in frequency was increased to 25 Hz. Finally, (c) shows the region around the fault imaged at the same frequency through a silicon solid immersion lens (SIL), which further increased the magnification by a factor of 3.5. The localization of the fault allowed a focused ion beam (FIB) preparation of a cross-section specimen for a transmission electron microscopy (TEM) investigation, which is shown in (d). This image shows residues

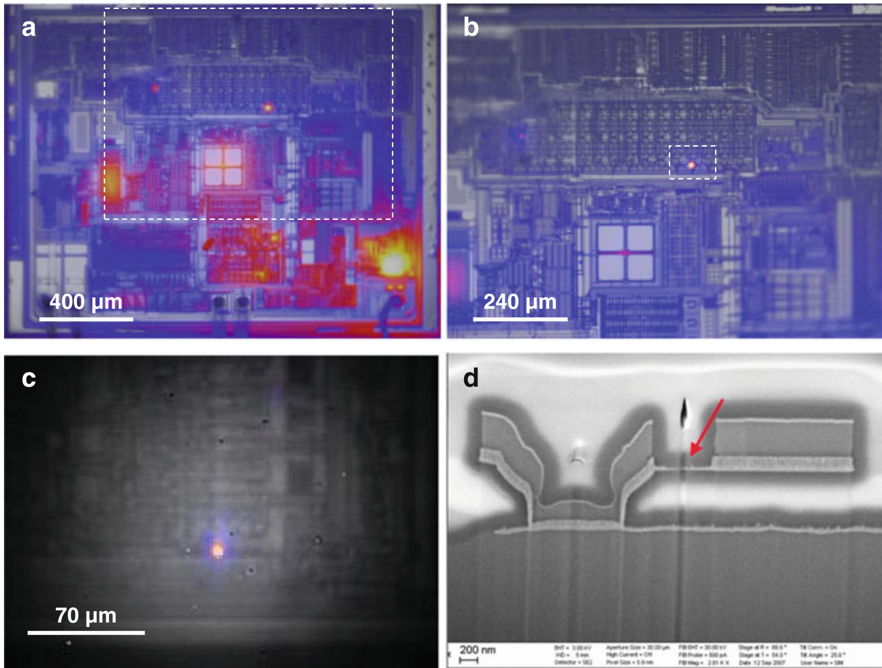

Fig. 6.1 (**a**) Survey image of the whole die (objective 2.5×); (**b**) detailed image of the region framed in (**a**) (objective 5×); (**c**) detailed image of the region framed in (**b**) (objective 5× with SIL); (**d**) TEM image of a cross-section through the fault region (Courtesy of IWMH, Halle)

of a TiN barrier layer which were not completely etched away (arrow) and finally lead to a short (by courtesy of Ch. Schmidt, IWMH, Halle).

The emissivity contrast is especially disturbing whenever spatially extended heat sources are present in an IC. Figure 6.2 shows the amplitude image of a hall sensor circuit (a), the corresponding phase image (b), the ε-corrected 0°-image (0°/−90° image, c, detail), and the power distribution (d) numerically deconvoluted from (c). All details visible in Fig. 6.2 arise during the normal operation of this circuit. The selected region displayed in (c) and (d) is indicated in (b). The measurement was performed at a lock-in frequency of 22 Hz within a few minutes. Similarly to Fig. 5.3 of Sect. 5.1, here we see that the amplitude image (a) is indeed strongly affected by the emissivity contrast caused by the metallization. Note that due to the lock-in technique the steady-state IR image is already perfectly compensated even in the amplitude image (a). Hence, the bright regions outside the heat source positions, modulated by the local emissivity contrast, are caused by the inevitable heat conduction-induced halo of the temperature modulation around the heat sources. This halo is more pronounced for extended heat sources than for point sources, since for extended heat sources the signal does not diverge in source position (see Chap. 4). From the amplitude image (a) it is not possible to judge which of the bright regions are real heat sources and which are regions of high IR emissivity.

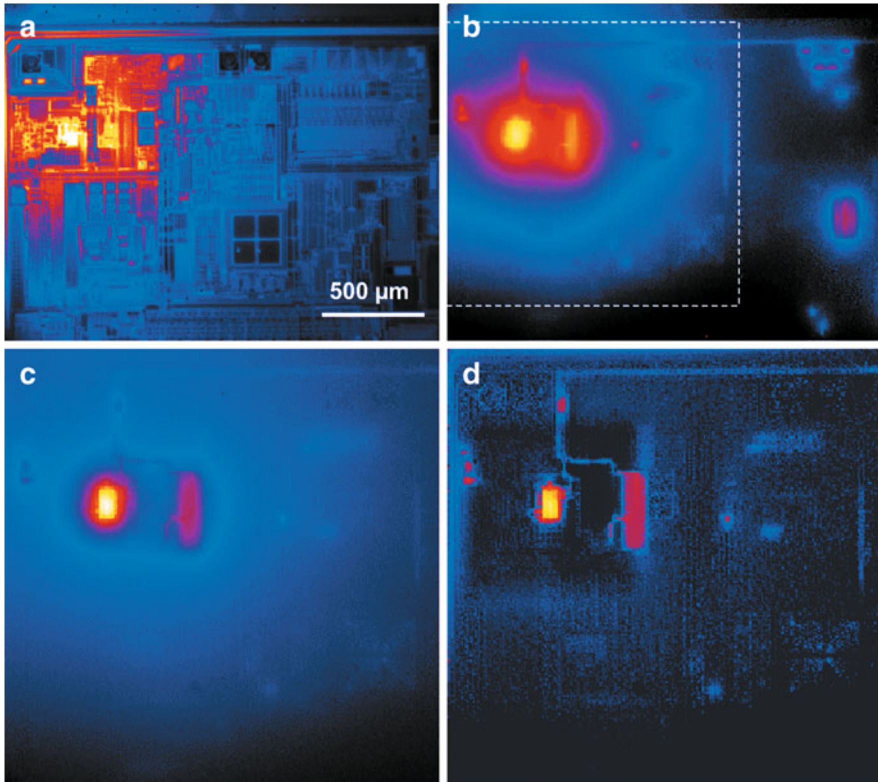

Fig. 6.2 Amplitude image (**a**), phase image (**b**), ε-corrected 0° image (**c**; from the region indicated in b), and power distribution (**d**), numerically deconvoluted from (**c**), of a hall sensor circuit; supply voltage pulsed with 22 Hz

In the phase image (b) and the ε-corrected 0° image (c), however, this emissivity contrast is indeed perfectly removed. This is due to the fact that both images rely on the quotient of the 0° image and the −90° one, which are both modulated by the local emissivity in the same way. Only the signal-to-noise ratio is degraded in regions of low IR emissivity. The differences between the phase image (b) and the ε-corrected 0° one (c), discussed in Sect. 5.3, are clearly revealed also in Fig. 6.2: The phase image shows a stronger halo around the heat sources, and it displays heat sources of different intensity with comparable brightness. Depending on the point of view, the latter property may also be considered an advantage, since it provides a kind of "dynamic compression" visualizing both weak and strong heat sources in one image. On the other hand, the phase image can not be deconvoluted. The reason is that in the phase image the contributions of different heat sources are not linearly superimposing, which at least approximatively holds for the ε-corrected 0° (0°/−90°) image. The power distribution (d), which was obtained from (c) by numeric deconvolution, shows by far the most details of all images in Fig. 6.2.

In the next example of this section the supply voltage was permanently applied to the IC, and the lock-in trigger pulse was applied to one of the control inputs of the circuit (see Sect. 2.3). Under these “sophisticated triggering” conditions, heat sources permanently existing in the IC, which are not affected by this trigger signal, do not appear in the lock-in thermogram. Only heat sources reacting on the trigger signal are detected here. However, there may be two possibilities: In the “high” period of the trigger signal a heat source may be either switched on, or off. If the amplitude signal were displayed here, these two possibilities could not be distinguished from each other. Therefore, here it is advantageous to display not the amplitude signal but rather that of a fixed phase position, which has to be selected for an optimum separation of the two possible signal components. Then complementary acting heat sources appear as a positive or negative signal, respectively. Alternatively, also the phase signal could be used to display the different trigger signal-induced heat sources.

The images shown in Fig. 6.3 are composed of four 128×128 pixel images each. The IC shown contained some power transistors in the centre and some control logic around to drive them. In the fixed phase lock-in thermograms (b) and (c), the red colour corresponds to regions of no thermal reaction to the trigger pulse, yellow-to-white regions correspond to heat sources reacting in-phase to the trigger, and blue-to-black regions correspond to heat sources inversely reacting to the trigger pulse. Hence, two complementary reacting heat sources always produce a yellow/blue pair of dots in the image. While the low-contrast image of Fig. 6.3(b) only shows the two complementary-acting driver transistors, in the contrast-enhanced image (c) these heat sources appear overexposed, but a lot of weaker heat sources in the logic circuitry are visualized. Obviously, this whole control circuit has a widely complementary design, since nearly all appearing heat sources find their complement nearby in the circuit. Whenever the function of this circuit is disturbed, it becomes clearly visible in the lock-in thermogram. Knowing the circuit topography, one can even find out how far away a digital signal passes within the circuit, until

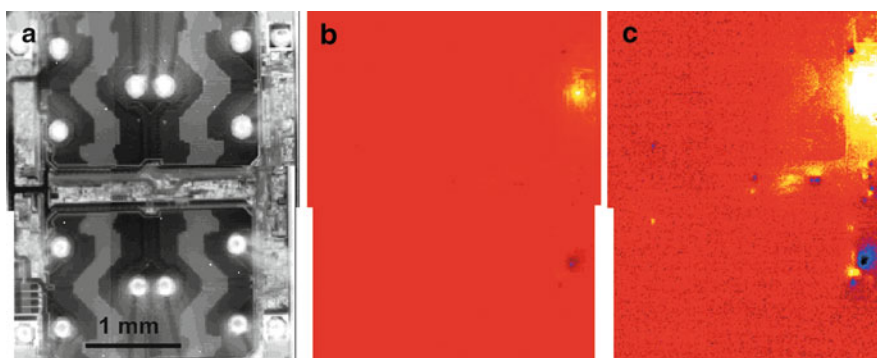

Fig. 6.3 Topography image (**a**) and fixed phase lock-in thermogram: (**b**) and (**c**) of an IC with permanently applied supply voltage and triggered control input. (**c**) is a contrast-enhanced presentation of (**b**)

it is blocked by a possible fault. In the outlook (Chap. 7), we will discuss how this measurement principle can be implemented into sophisticated IC testing stations.

The next example of this section is to illustrate results of investigating an encapsulated circuit, which was mechanically opened from the back side up to the silicon chip and imaged "through the chip". Until now, all reported IC investigations have been performed on originally plastic-encapsulated chips after opening the case from its front side by hot HNO_3-etching. This technique, however, is inapplicable if a chip is mounted in "flip chip" configuration face-down, as it is usually done e.g. for PC microprocessors in order to have a more efficient heat dissipation to the heat sink. Note that in this case liquid crystal investigations as well as fluorescent microthermal imaging (FMI) are no longer applicable, since the active region of the IC is at the bottom of the chip. IR imaging "through the chip" is already well-known for steady-state microthermography [20], and Schlieren imaging [80], but there the above-mentioned limitations regarding the sensitivity, the effective spatial resolution, and the emissivity contrast have prevented a wider application until now. Also here, lock-in thermography significantly expands the field of application of this kind of investigation. For the investigations shown in Fig. 6.4, a plastic-encapsulated 8 Bit microprocessor running at a clock frequency of 12 MHz was used, which was mechanically opened and polished from the back side and imaged through $\approx$400 μm silicon material. The investigation was performed by pulsing the supply

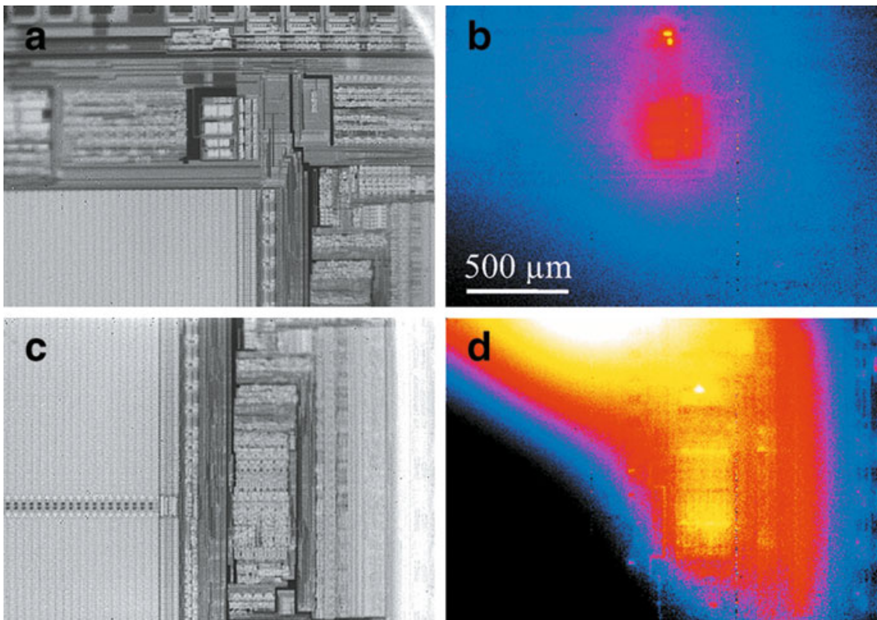

Fig. 6.4 Topography images (**a**), (**c**) and corresponding phase images (**b**); scaling range $-160° \ldots 0°$, and (**d**); scaling range $-120° \ldots -90°$) of two adjacent positions in a dynamically operating microprocessor, imaged from the back side "through the chip"

voltage (5 V) with $f_{\text{lock-in}} = 20\,\text{Hz}$. During operation the circuit was connected with the 12 MHz clock generator, but no ROM for the program code was connected. Hence, the processor was imaged in dynamic standby operation, consuming a supply current of about 8 mA. Figure 6.4 shows the topography and the phase image of two neighbored regions of the chip. Obviously, the optical resolution is not seriously degraded in this back side investigation, compared to an investigation performed from the front side (see, e.g., Fig. 5.3 of Sect. 5.1). A further improvement of the spatial resolution would be possible by using a solid immersion lens for backside inspection, see Sect. 3.4. The heat sources visible in Fig. 6.4(b) showed a temperature modulation amplitude of up to 10 mK, therefore here a measurement time of only 20 s was sufficient to capture this image. The details in a lower-lying region displayed in (d), on the other hand, showed a temperature modulation amplitude which was roughly 100 times lower. Nevertheless, after a measurement time of 45 min and appropriately scaling the phase image, also here some additional details become visible. However, at this relatively low frequency of 20 Hz, which at the time of this measurement was our highest possible lock-in frequency for this spatial resolution, the halo of the above-lying strong heat sources is already seriously disturbing the imaging of the neighbouring weak ones. Hence, in this case the selection of a higher lock-in frequency by working in the undersampling mode (see Sect. 2.4) would have been advantageous.

The final example in this section is the investigation of a short lying in the encapsulation mould compound (by courtesy of Ch. Schmidt, IWMH, Halle). The device shown in Figure 6.5(a) showed a short between the two contacted pins. Figure 6.5(b) is an overlay of the topography (grey) and the lock-in amplitude image (colour), which roughly shows the position of the short. Since here the short is lying a few millimeters below the surface and the mould compound is not transparent to the IR light, the spatial resolution is very poor. For increasing this resolution, the mould compound in the interesting region was carefully thinned down until the first bond wires appeared (c). This device is still fully functional and still contains the short. The overlay image (d) shows the bond wires as dark lines (due to their low emissivity) and the short position with a much better spatial resolution (see arrow). Further cross sectioning and electron microscopy analysis revealed a steel splinter shorting two bond wires in this position. This root source could probably not have been found if the mold compound were chemically etched away.

Already these few examples demonstrate the high potential of lock-in thermography for failure analysis in microelectronic industry. As it was shown in Sect. 3.2, meanwhile several vendors are offering lock-in thermography systems specialized for this type of failure analysis. Since the success rate of lock-in thermography for finding a fault is very high, his technique is especially suitable for a quick and coarse fault localization. If the spatial resolution of about 1.5 μm provided by an SIL inspection is not sufficient for finding the root cause, other fault isolation techniques like light emission microscopy and laser stimulation techniques may be applied [145]. These laser stimulation techniques, which are today standard failure analysis techniques, are called OBIRCH (Optical Beam-induced Resistance CHange) or TIVA (Thermally Induced Voltage Analysis), depending on whether the

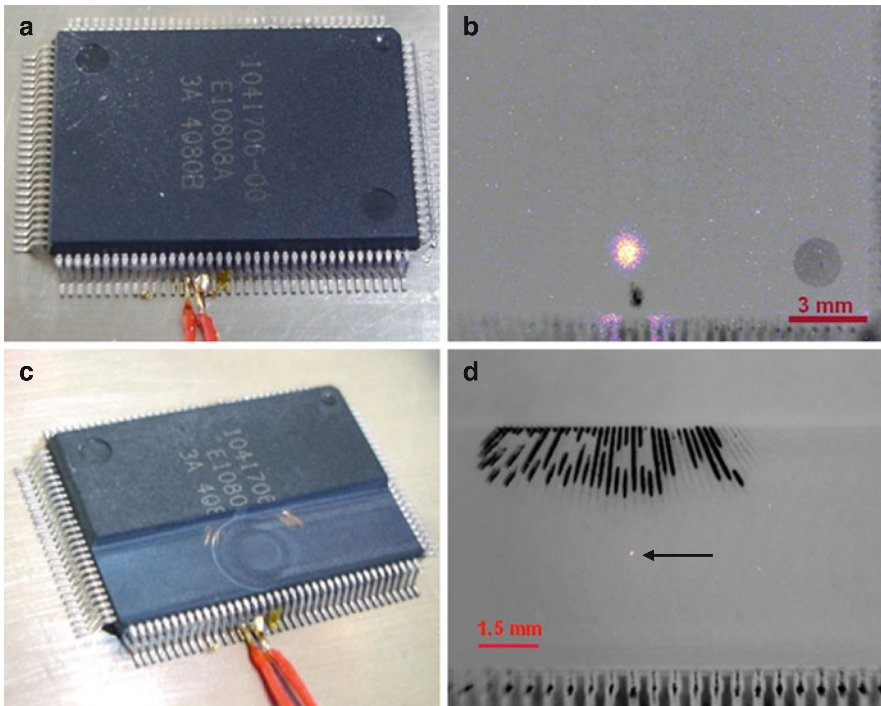

Fig. 6.5 Short in mould compound: (**a**) device image, (**b**) overlay topography + amplitude image, (**c**) thinned device, (**d**) thinned device, overlay topography + amplitude image (courtesy of IWMH, Halle)

device is operated at a constant voltage or current. They are measuring the influence of a scanned focused laser beam in the operation current or voltage of a device, respectively. Since every leakage current has a certain temperature coefficient, be it negative or positive, local heating at a leakage site changes this current and leads to an OBIRCH or TIVA signal.

It was mentioned already in Sect. 3.1 here that OBIRCH and TIVA are detecting the same type of defects as lock-in thermography does, namely resistance-limited local leakage currents. If a current flows in a low-ohmic conductor line without any voltage drop, it can be detected neither by OBIRCH or TIVA nor by lock-in thermography. The method of choice to detect such currents is current imaging using magnetic field sensors [145]. Also an "open" (break of a line) can be detected neither by OBIRCH or TIVA nor by lock-in thermography. It has been shown by the parallel application of OBIRCH and lock-in thermography to one and the same device that most faults can be detected by both techniques [146]. The answer to the question, which of the two methods shows a higher success rate, depends on the special parameters of a fault in a device. For example, if a leakage current is very small (less than a μA) and also the whole device current is only in the μA-range, this fault is more easily detectable by OBIRCH than by lock-in thermography. On

the other hand, if a leakage current of at least some μA is flowing at some V bias and the whole device draws tens of mA current, this fault is easier to detect by lock-in thermography than by OBIRCH. It has been shown that, if a weak leakage current is flowing in close proximity to a large one, the weak one can be detected only by lock-in thermography but not by OBIRCH [147]. Here the special property of the phase image was untilized to display weak local heat sources with a similar brightness as strong ones, see Sect. 5.1. Generally, lock-in thermography is better suited to get an overview about all local leakage currents in a device than laser stimulation techniques [146]. Meanwhile, also the sensitivity and the general image quality of OBIRCH and TIVA have been improved by operating both techniques in lock-in mode [83, 84]. Until now only single-phase lock-in has been applied here. It can be expected that two-phase lock-in correlation should also be advantageous for OBIRCH and TIVA, since only here a phase image can be displayed. As for lock-in thermography, the phase image shows the dynamic compression feature, and it even may enable the observation of different thermal time constants in the device.

6.2 Solar Cells

In this section, we will present more examples of investigating solar cells using lock-in thermography. Thereby we will concentrate on the investigation of crystalline silicon solar cells. Although a lot of research is done on other solar cell materials and techniques, solar cells made from mono or multicrystalline silicon still dominate the market of photovoltaics. The investigation of both silicon and non-silicon thin film modules will be demonstrated in Sect. 6.3.

Silicon solar cells are rather simple electronic devices consisting of a large-area p–n junction diode, which is manufactured by diffusing a thin n-type emitter into a p-doped base. The huge area of typically 243 cm^2 is the outstanding feature of these diodes in comparison to microelectronic devices. In addition, the material used for most of today's solar cells is a large-grained multicrystalline material, which contains far more crystal defects than found in microelectronic devices. Thus, the interesting question with respect to solar cells is the homogeneity of the I-V characteristic across a single device.

As mentioned before, the investigation of inhomogeneities in solar cells was the initial task, leading to the development of the lock-in thermography systems used for testing electronic devices. Lock-in thermography results of a typical multicrystalline solar cell have already been used as practical examples throughout Chap. 5 to illustrate the behavior of thermally thin samples. In this section, we will pay our attention to the physical information to be gained on solar cells. According to our experiences, nearly all solar cells show certain local sites of an increased forward current. These sites are traditionally called "shunts", even if they are not complete shorts in the electrotechnical sense but rather sites of a locally enlarged forward current. They degrade the efficiency of the whole device and have to be minimized. The investigation of the lateral homogeneity of the current flow, which is performed in the dark without irradiating the sample ("dark lock-in

thermography", DLIT), is the dominant application of lock-in thermography in solar cell research and development. In Sect. 6.2.1 the physical background of these investigations is explained in some more details and different variants of DLIT-investigations are introduced and demonstrated. In operation, solar cells are illuminated by light. If lock-in thermography is performed on solar cells under any kind of illumination, we speak from "illuminated lock-in thermography" (ILIT). Sect. 6.2.2 summarizes the physical background of ILIT investigations and introduces and demonstrates several newly developed special ILIT techniques. By using these techniques not only shunts can be detected without electrically contacting the cell, but also information about the local minority carrier lifetime as well as about series resistance problems in solar cells may be obtained and the local avalanche multiplication factor may be imaged.

An important question holding both for DLIT and ILIT is how to mount solar cells correctly for performing lock-in thermography. For performing electrical or optical measurements on wafer-based devices, they are usually sucked by vacuum to a gilded chuck, which is often made from copper or brass for effectively feeding away any generated heat. In Sect. 4.1 the term "quasi-adiabatic condition" was introduced which means that the heat resistance between the sample and a heat sink should be so high that the magnitude of the temperature modulation does not depend on the height of the heat resistance anymore. It was discussed already in Sect. 4.1 that typical industrial silicon solar cells, having a thickness of 200 μm, behave quasi-adiabatic for a lock-in frequency of 10 Hz and above, even if they are directly sucked to a metallic sample holder (chuck). Figure 6.6 shows a sample holder where the cell is sucked to an 8 mm thick brass plate by vacuum. At the back of this plate a heat exchanger allows to control the sample temperature via water flowing through a thermostat. At the edge of the plate a number of sockets is inserted, one row representing the current feeding and the other one the corresponding sense-input of the power supply. The lateral positions of these sockets may be changed according to the cell types to be investigated. By using special contact rails containing spring-loaded contact pins, also high currents can reliably fed in and out

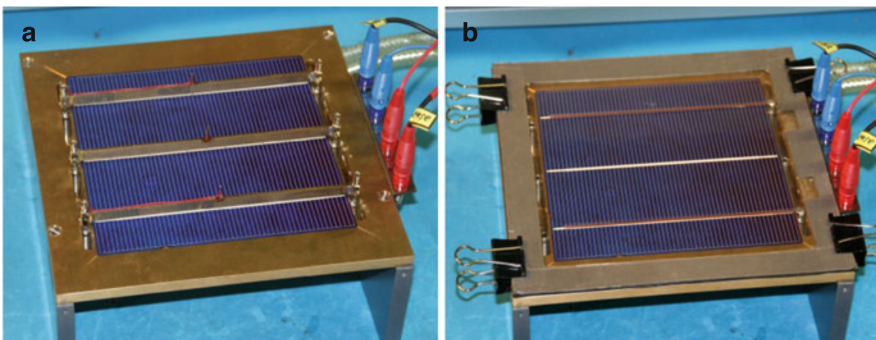

Fig. 6.6 Sample holder used for lock-in thermography in solar cells: (**a**) for investigating bare cells, (**b**) for using a black IR-emitter foil (here shown with a transparent plastic foil for showing the contacting means)

of the bus bars. One of the contacts feeds out the sense-potential. These contact rails can only be used if bare solar cells (without IR emitter foil) are imaged. Alternatively, flexible contact pads can be inserted into the sockets and the whole plate may be covered with a black IR-emitter foil, which is sucked to the surface, see Sect. 5.3. This sample holder is available [19]. Thin film cells on glass substrate can be considered as thermally thick, they are free-standing and do not need any special sample holder, except if they shall be investigated by using the black IR-emitter foil, see Sect. 6.3.

6.2.1 Dark Lock-in Thermography (DLIT)

In operation (under illumination) a solar cell is under forward bias. For silicon solar cells the so-called "superposition principle" holds in good approximation, hence the illuminated current-voltage (I-V) characteristic equals its dark (un-illuminated) characteristic shifted by the bias-independent photocurrent, which is a reverse current (see Sect. 6.2.2). Hence, for any forward bias the dark current reduces the net current which is supplied by the cell to a load. Under open circuit condition (no load current) the photocurrent equals the dark forward current, hence the latter determines the open circuit voltage. It follows that the illuminated I-V characteristic of a solar cell, which governs its efficiency, is strongly affected by the dark I-V characteristic of this cell. Therefore lock-in thermography performed in the dark (DLIT) is a powerful tool to characterize solar cells, since it allows to "see where the dark current flows". Also, under larger reverse bias, new local shunts, which are called breakdown sites, may appear. The investigation of such breakdown sites has attracted special attention recently, since they strongly influence the reliability of solar modules.

In the traditional interpretation of I-V characteristics of solar cells all nonlinear currents were attributed to recombination processes of the whole cell, and only ohmic current paths across the p–n junction have been called 'shunts'. With the availability of lock-in thermography techniques these shunts could be made visible. In the following, all bright features visible in DLIT images were called 'shunts'. However, by later investigations, it has turned out that there are not only ohmic shunts, but also diode-like ones caused, e.g., by local recombination sites. So the question, what is a shunt and what belongs to the undisturbed cell, obtained a philosophical dimension: Should a region of lower crystal quality be called a shunt? This question is still under discussion. Throughout this book, we will use the term 'shunt' for any position in a solar cell showing a dark-current contribution additional to the diffusion current under forward or reverse bias. In this sense, sites with edge leakage currents are shunts, but a region of lower crystal quality, where only the saturation current density of the diffusion current is increased, is not [148]. Future discussions will show whether this definition will survive or has to be replaced by a more precise one.

It was mentioned in Sect. 2.8 that, in the absence of ohmic shunts, the forward bias I-V characteristic of solar cells contains two exponential contributions, which

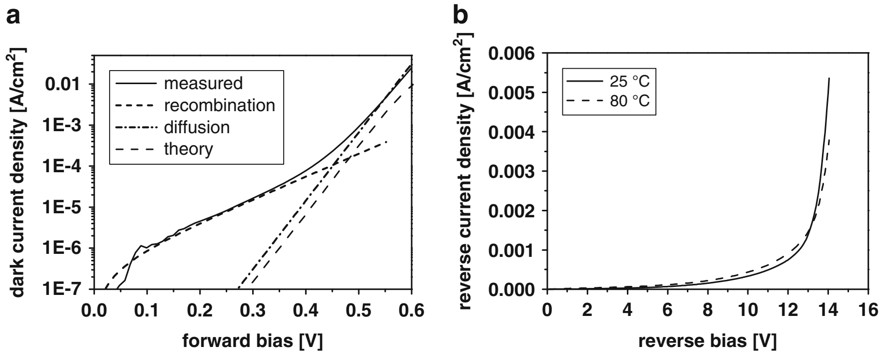

Fig. 6.7 Typical dark current-voltage (I-V) characteristics of multicrystalline silicon solar cells (**a**) under forward bias (half-logarithmic drawing, details see text) and (**b**) under reverse bias (linear drawing) for two temperatures

are the recombination current and the diffusion current. Figure 6.7(a) shows a measured forward I-V characteristic of a typical silicon solar cell not containing any ohmic shunts in half-logarithmic drawing, with the recombination current and the diffusion current contributions indicated separately. The reverse bias characteristics shown in (b) will be discussed at the end of this section. Note that (a) and (b) are scaled in A/cm^2, which is the usual convention to make them independent of cell size. However, it will be shown later that most of these current contributions come from local shunts, so these characteristics usually cannot be interpreted as homogeneous current densities. Also shown in (a) is the expected characteristic of this cell according to established diode theory [45], which was calculated assuming a mean minority carrier lifetime of the material of 100 μs. It is observed that the measured recombination current is many orders of magnitude larger than predicted by theory, and also the diffusion current is significantly larger. The question, which can be answered by DLIT, is: Where do these unexpected current contributions flow? Figure 6.7(a) shows that, due to their different slope, the diffusion current dominates for a forward bias above 0.5 V, whereas for a lower forward bias the recombination current dominates. This property allows imaging these two contributions nearly separately. If DLIT is performed at a forward bias of 0.5 V or below, one may expect the recombination current to dominate in the image. If there are ohmic shunts, they should also dominate at low forward bias. On the other hand, the diffusion current should dominate the image if DLIT is performed at about 0.6 V. This current contribution mainly depends on the local value of the effective minority carrier lifetime in the bulk material [45].

6.2.1.1 Shunt Imaging

For shunt imaging in silicon cells a forward bias as low as +0.5 V has to be applied, since for a higher bias other effects will dominate, see below. Ohmic shunts can be

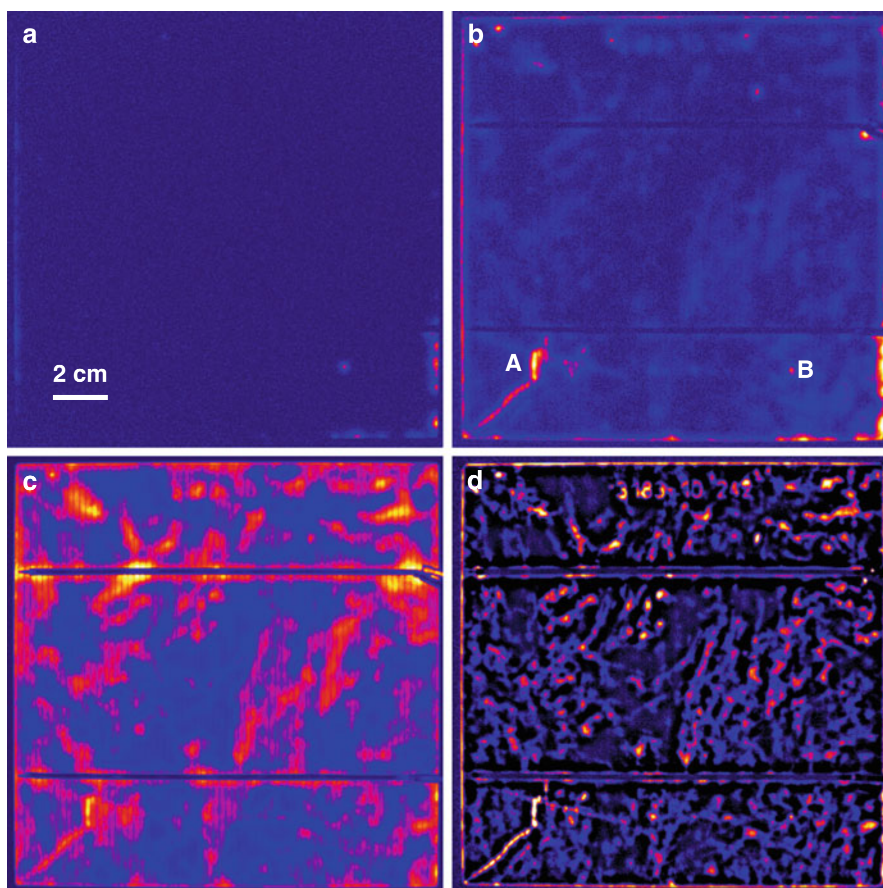

Fig. 6.8 DLIT amplitude images of a multicrystalline solar cell, (**a**) measured at −0.5 V reverse bias (scaled to 1 mK), (**b**) +0.5 V forward bias (scaled to 1 mK), (**c**) +0.6 V (scaled to 5 mK), and (**d**) 0° component of the +0.6 V image (scaled to 1 mK)

identified by comparing the DLIT image recorded at −0.5 V (reverse bias) with a DLIT image recorded at +0.5 V (forward bias). If a shunt leads to the same signal amplitude under both conditions, its characteristic is ohmic (linear). If ohmic shunts are present in a cell, their current usually dominates the whole low-voltage part of the I-V characteristic, hence here the recombination current is hardly visible. In Fig. 6.8 amplitude images taken at −0.5 V (a) and +0.5 V (b) are compared with each other. All examples shown in this section have been measured at a lock-in frequency of 10 Hz on bare cells. In (a) only linear (ohmic) shunts are visible, one of them being in the area and the rest at the edge. The DLIT image (b) taken under +0.5 V forward bias (the so-called "shunt image", taken close to the maximum power point of the cell, see Sect. 6.2.2) additionally shows a large number of other local heating sites, which are recombination-induced shunts showing a non-linear

(diode-like) I-V characteristic. Therefore these shunts do not appear under weak reverse bias (a). This is the reason why reverse-bias shunt investigations are, as a rule, not representative for the shunt behaviour at the working point of the cell. Only if ohmic shunts are dominating under forward bias, they also dominate under reverse bias. The non-linear shunts are the source of the unexpectedly large recombination current. Especially the edge region, where the p–n junction crosses the surface, is a strong source of this current contribution. The irregular line in the lower left is caused by a weak scratch, visible at the surface by the naked eye. One non-linear (A) and one linear shunt (B) are labelled in (b). At this forward bias of +0.5 V the diffusion current just starts to become visible. The weak cloud-like features in the area of (b) are already due to this current contribution, see the discussion of Fig. 6.11. A summary of the different types of shunts, which were identified by a detailed investigation of shunt sites by microscopic and microanalytic techniques in a large number of solar cells, can be found in [148].

6.2.1.2 High-current DLIT

The diffusion current dominates in the high-current DLIT image taken at a forward bias of +0.6 V Fig. 6.8c, where the shunts appear relatively weaker. This image closely anti-correlates to the local lifetime image of the material (not shown here), hence regions with low lifetime correspond to regions with high diffusion current. Note that +0.6 V is already close to the open circuit voltage of this cell. Hence, the forward current at this voltage of about 3.7 A is already half of the short circuit current of this cell. For reliably applying such high currents with minimum series resistance influence, the conductivity of the bus bars has to be increased, e.g. by feeding in the current in different positions for avoiding voltage drops along the bus bars. This can be done by using multi-contact rails as shown in Fig. 6.6 Moreover, 4-point probing has to be applied, hence the bias has to be measured and regulated directly at the cell. In addition to the amplitude images (a-c), which contain both the 0° and the −90° signal contributions (see Sect. 2.1), also the pure in-phase (0°) contribution of the +0.6 V measurement is displayed in Fig. 6.8(d). As it was already discussed in Chap. 4 and Sect. 5.1, the 0° image shows the best possible spatial resolution, and, for this thermally thin sample, it is insensitive to homogeneous heating contributions. Therefore the 0° signal is best appropriate to display local heat sources independent of homogeneous sources. The comparison between (b) and (c) shows that the recombination current flows locally in the positions of certain shunts, whereas the diffusion current is an areal current. The 0° contribution of this image (d) shows an irregular line structure, which stems from recombination-active grain boundaries. Hence, the diffusion current in this cell, which is a typical multicrystalline one, is obviously dominated by low-lifetime regions and recombination-active grain boundaries.

Note that for high-current DLIT (and for J_{sc}-ILIT, see Sect. 6.2.2), due to the high currents flowing, the electrical contact points may heat up. Then these sites are looking like local shunts lying directly below the contact points. Such an effect

will be shown in the J_{sc}-ILIT image in Fig. 6.17(b) at the top right and the bottom left contact points, where the current was injected. Such "pseudo-shunts" may be avoided by feeding in the current in many positions of the bus bar. Note that "pseudo-shunts" may also appear at the back contact. If the cell is not homogeneously sucked to the metallic base by a vacuum but just kept in position by some spring contacts, it contacts the base only in several local positions. In high-current DLIT (and J_{sc}-ILIT) also these positions are becoming warm, thereby looking like local shunts. The characteristic of these "pseudo-shunts" is that they become relatively weaker (compared to the areal signal, which is due to the diffusion current) with decreasing current level. This is in contrast to real shunts (both ohmic/linear and non-linear), which always become relatively stronger with decreasing current.

The electric contacts to standard industrial solar cells are formed by a high-temperature treatment ("firing") of a metal paste. If the firing parameters are not optimal or if there are any other technological problems, this contact formation does not work properly. In this case the whole cell or at least some regions in this cell are not well-contacted, hence there are regions of locally increased series resistance R_s. High-current forward-bias DLIT is also able to image such high-R_s regions, which is demonstrated in Fig. 6.9. Here a monocrystalline cell is investigated where the leftmost region is poorly contacted. The shunt image (a) taken at +0.5 V essentially shows the typical edge recombination and some additional edge shunts at the top. The high-current DLIT image (b), however, clearly images the non-contacted region as a region where less or no diffusion current flows due to the locally increased series resistance. Unfortunately, this technique does not work straightforwardly for multicrystalline cells showing an inhomogeneous lifetime distribution, see Fig. 6.8(c). Here it is difficult to distinguish high-R_s regions from regions with high lifetime, where the diffusion current is reduced as well. It was proposed to correct for these inhomogeneity by yielding the ratio of two DLIT images taken at two different

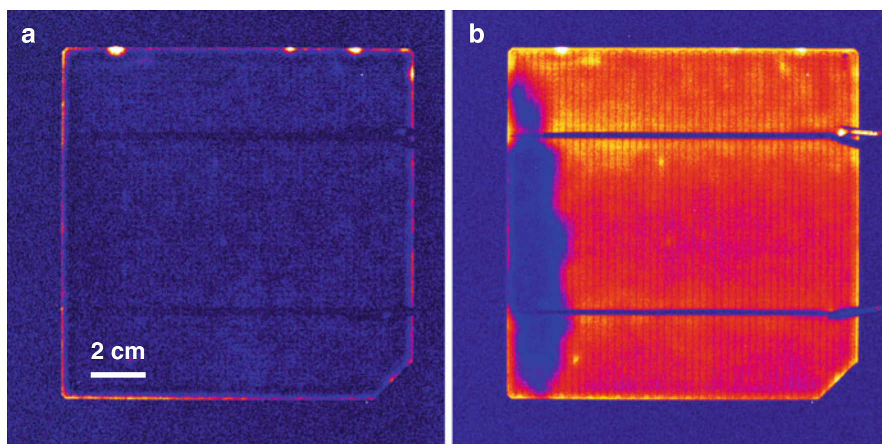

Fig. 6.9 DLIT images of a monocrystalline cell containing a region of high series resistance, (**a**) measured at +0.5 V (scaled to 1 mK) and (**b**) at +0.6 V (scaled to 5 mK)

forward bias conditions (R_s-DLIT, [149]). However, then the high lifetime regions appear very noisy in the resulting image. Therefore, for multicrystalline samples, R_s problems can be detected more reliably e.g. by applying R_s-ILIT, see Sect. 6.2.2.3, or by RESI (see following section).

6.2.1.3 Series Resistance Imaging (RESI)

Another way to correct a high-current DLIT image for inhomogeneities of the lifetime is to combine it with electroluminescence (EL) imaging. Ramspeck et al. developed a technique called RESI (REcombination current and Series resistance Imaging) which even allows to measure the local series resistance quantitatively [150]. Also RESI uses the fact that, when applying a certain forward bias V_{appl} to the cell, the locally dissipated power density P_{loc} (area-related) is measured by DLIT. Neglecting Joule heating and assuming vertical current flow, this local power density equals the local junction bias $V_{loc}(x, y)$ multiplied by the locally flowing dark current density (see also (2.45) in Sect. 2.8). In [150] this dark current density was named local recombination current density J_{rec}, but according to the terminology used here it is the sum of the recombination and the diffusion current densities, whose carriers finally also recombine in the bulk, see Sect. 2.8. Since, at least in multicrystalline cells, J_{rec} may locally vary considerably from location to location even for constant local bias, this information alone is not sufficient yet for calculating the local series resistance. Therefore in RESI the local junction bias V_{loc} is measured independently by EL imaging. It can be shown that $V_{loc}(x, y)$ can be calculated from the local EL signal $S_{EL}(x, y)$ by:

$$V_{loc}(x, y) = \frac{kT}{e} \ln\left[S_{EL}(x, y)\right] + c. \tag{6.1}$$

The constant c is obtained e.g. by extrapolating the EL signal across the grid lines to below the bus bars where the junction bias V_{loc} is supposed to be very close to the applied bias V_{appl} [151]. Finally, the local (dark) series resistance $R_s(x, y)$ is obtained from [150]:

$$R_s(x, y) = \frac{V_{appl} - V_{loc}(x, y)}{J_{rec}} = \frac{V_{loc}(x, y)\left(V_{appl} - V_{loc}(x, y)\right)}{P_{loc}}. \tag{6.2}$$

Figure 6.10 (courtesy of K. Ramspeck, ISFH Hameln) shows typical results of this procedure applied to a monocrystalline cell showing series resistance problems.

6.2.1.4 Ideality Factor and Saturation Current Mapping

Other useful DLIT techniques are ideality factor mapping and saturation current density mapping. Figure 6.7(a) has shown that there are different exponential current

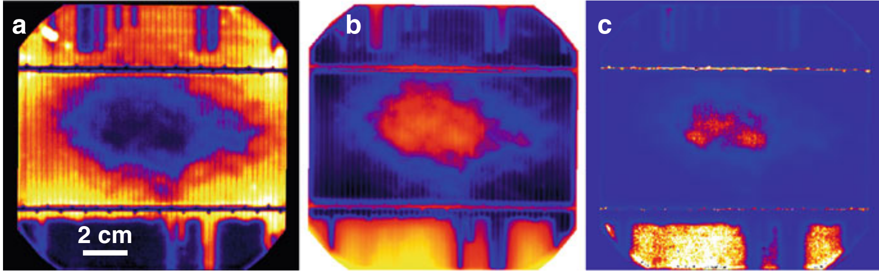

Fig. 6.10 (**a**) P_{loc} after DLIT measurement of a monocrystalline cell with R_s-problems (scaled to 50 mW/cm^2), (**b**) $V_{appl} - V_{loc}$, scaled 0 to 100 mV, (**c**) R_s, scaled to 30 Ω cm^2 (courtesy of K. Ramspeck, ISFH Hameln)

contributions present in a solar cell, having different exponential slopes, which may belong to different positions in a cell. Within a limited bias range it is common to approximate the local characteristics of a solar cell by the general exponential form:

$$J(x, y) = J_0(x, y) \exp\left(\frac{eV}{n(x, y)kT}\right). \tag{6.3}$$

Here $J_0(x, y)$ is the position-dependent saturation current density and $n(x, y)$ is the position-dependent "ideality factor", which is proportional to the inverse of the slope of the logarithmized characteristic. Generally, this ideality factor is also bias-dependent. The diffusion current always has an ideality factor of 1. Theoretically, the ideality factor of the recombination current should be 2 or below [43], but for solar cells it is observed to vary from 1.5 up to 5 and above. Hence, for the identification of the different local conduction mechanisms, especially the local ideality factor $n(x, y)$ is an important information, whereas the local saturation current density $J_0(x, y)$ is a measure of the magnitude of this conduction process. It was described in Sect. 4.5.1 that the −90° image $S^{-90^\circ}(x, y)$, within its spatial resolution of the thermal diffusion length Λ, can be converted to the locally flowing current density $J(x, y)$. Assuming the validity of (6.3), the two parameters n and J_0 can be calculated for each position (x, y) by measuring the local current density $J(x, y)$ for two different biases V_1 and V_2. Then the local ideality factor and the local current density are given by [123]:

$$n(x, y) = \frac{e(V_2 - V_1)}{kT \ln\left(\frac{S_2^{-90^\circ}(x,y)\; V_1}{S_1^{-90^\circ}(x,y)\; V_2}\right)}, \tag{6.4}$$

$$J_0(x, y) = \frac{I_2 V_2}{S_{2\text{whole}}^{-90^\circ} A_{\text{whole}}} \exp\left(\frac{V_2 \ln\left(\frac{S_1^{-90^\circ}(x,y)}{V_1}\right) - V_1 \ln\left(\frac{S_2^{-90^\circ}(x,y)}{V_2}\right)}{V_2 - V_1}\right).$$

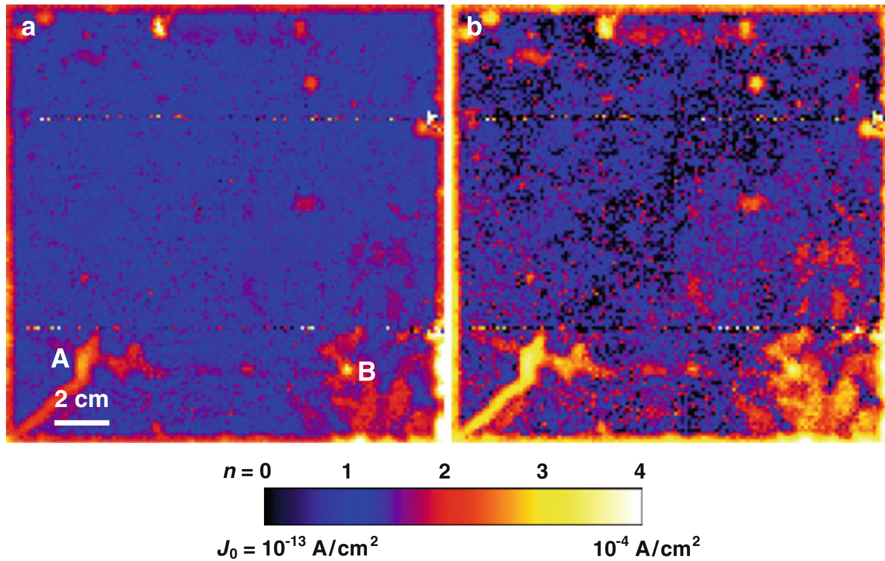

Fig. 6.11 (**a**) Ideality factor (n) map and (**b**) map of the logarithm of the saturation current density J_0 of the cell used in Fig. 6.8

As in Sect. 4.5.1, A_{whole} is the whole cell area, and $S_{2\text{whole}}^{-90°}$ is the $-90°$ signal of the second measurement, averaged over the whole cell area. Figure 6.11 shows the results of this procedure for the cell previously used in Fig. 6.8, based on measurements at $V_1 = 0.5$ V and $V_2 = 0.55$ V. Hence, these parameters are valid only in the limited bias range between 0.5 and 0.55 V. One might argue that high values should be used for V1 and V2, leading to a good signal-to-noise ratio, but for high-forward bias the ideality factor everywhere approaches 1 since then the diffusion current dominates. Moreover, at high forward bias, corresponding to a high current density, also the series resistance becomes important, which effectively increases the measured ideality factor again. Therefore ideality factor imaging should be performed for biases as low as possible. On the other hand, for too low biases also the currents are getting low, hence the signal-to-noise ratio will become insufficient. So 0.5 and 0.55 V are a good choice for V_1 and V_2 for crystalline silicon solar cells since the local current density is already remarkable, but the diffusion current does not yet dominate. The results in Fig. 6.11(a) show that the ideality factor is close to 1 (blue) in most parts of the cell area. Especially regions of low bulk lifetime, which appear red in Fig. 6.8(c), do not show an increased ideality factor. This is the proof that the corresponding structures, which are weakly visible already in the shunt image measured at +0.5 V in Fig. 6.8(b), are indeed due to an inhomogeneous diffusion current and not to a recombination current. However, all other structures visible in the shunt image are due to local recombination currents, since they all show an increased ideality factor in Fig. 6.11(a). Most of the edge region of the cell shows an ideality factor close to 2 (red). The non-linear shunt at the top of this cell even shows a local

ideality factor above 4. Note that also the ohmic shunts (especially shunt ‘B’ and the edge region around) show a high ideality factor in Fig. 6.11(a). This is an artifact of the evaluation since for these shunts the exponential assumption (6.4) does not hold. Since the saturation current density evaluated by (6.4) spans over many orders of magnitude, in Fig. 6.11(b) the logarithm of this value is displayed. This image not only displays the inhomogeneity of the recombination current but also that of the diffusion current. Indeed, while the high-lifetime (low-lifetime) regions appear blue (red) in Fig. 6.8(c), in Fig. 6.11(b) they appear black (blue). This example demonstrates how ideality factor mapping and saturation current mapping can help to identify the nature of different current contributions in solar cells.

6.2.1.5 Local I-V curves measured Thermally (LIVT)

DLIT not only allows one to image local current densities but also to measure the individual I-V characteristics of single shunts in an extended bias range without cutting a cell into small pieces. This technique has been named “Local I-V curves measured Thermally” (LIVT) [152]. It was developed originally for the technique of Dynamic Precision Contact Thermography (DPCT, [67, 68]). Here a temperature sensor was placed in shunt position on top of the cell, a pulsed bias of different height was applied, and the bias-dependent local temperature modulation was detected by lock-in techniques. Since the amplitude of this temperature modulation (i.e. the lock-in thermography signal $S(V)$) is proportional to the locally dissipated power and the applied bias V is known, the locally flowing current $I(V)$ is given by:

$$I(V) = c\frac{S(V)}{V}. \tag{6.5}$$

In DPCT the sensor was permanently placed in shunt position and the signal was successively measured for all required biases. Of course, LIVT can also be performed with IR camera-based lock-in thermography by taking images for all required biases and evaluating only the data in shunt position. The proportionality factor c in (6.5) is generally unknown. If the shunt is really point-like and the IR emissivity is known, it can be estimated according to Table 4.1 in Sect. 4.5. For a point source at the surface the 0° signal should dominate; a realistic value for the contributing pixel width is $D = 300\,\mu\text{m}$ (156 mm field of view, distributed over 512 pixels). If only the shunt region is imaged, the pixel size can be as small as $30\,\mu\text{m}$. Unfortunately, for a cell thickness of $200\,\mu\text{m}$, this geometry can neither be called clearly thermally thin nor thermally thick, see the discussion at the beginning of Sect. 4.1. It is not clearly thermally thin, since the pixel size is small compared to the sample thickness, hence 3-dimensional heat diffusion has to be considered. Purely 2-dimensional heat diffusion would hold only if the shunt were not a point shunt at the surface but a heated line vertically crossing the cell. On the other hand the geometry is also not clearly thermally thick since, for a typical lock-in frequency of 10 Hz, the thermal diffusion length is $\Lambda \approx 1.7$ mm, which is large compared to

the sample thickness of typically 200 μm. By realistically simulating a point shunt at the surface using the software "DECONV" (see Sect. 4.5.2) regarding a finite sample thickness of 200 μm, a value of $c = 12.5\,\mu$W/mK was estimated assuming an emissivity of 1 and that $S(V)$ is given in units of mK. This value is much closer to the value from Table 4.1 for thermally thick samples (12.7 μW/mK) than that for thermally thin samples (59.9 μW/mK), which were also both confirmed by DECONV. Alternatively, if the shunt is lying well-separated from others, the scaling factor c in (6.5) can also be measured for any emissivity making a scaling measurement at one bias V by using the image integration method described in Sect. 4.5.1. For this scaling measurement the highest applied bias and the strongest shunt should be chosen, since there the thermal signal is largest. From this procedure (which uses the −90° signal!) the current $I(V)$ flowing through this shunt at this voltage V can be measured, which allows to calculate c according to (6.5) also for the 0° or the amplitude signal, where the signal in shunt position is much higher than for the −90° signal [121]. This value of c then also holds for lower biases. In most cases it is sufficient to present the local I-V characteristics in arbitrary units (a.u.; which is usually mK/V), e.g. for measuring the ideality factor of a non-linear shunt. Figure 6.12 shows results of LIVT measurements of the two shunts 'A' and 'B' indicated in Fig. 6.8 in linear and that of shunt 'A' in logarithmic scaling, respectively. The exponential and the linear curve shape of shunt 'A' and shunt 'B' are clearly revealed. At a forward bias above 0.5 V, for shunt 'B' the diffusion current of the surrounding area starts to dominate, therefore this characteristic becomes super-linear. Here for the signal height $S(V)$ in (6.5) the amplitude signal was used. Note that this signal always contains a certain additive noise contribution. This is the reason why, for low voltages, the LIVT data systematically tend to increase in magnitude, which is a clear artifact of the measurement. The expected real shape of the characteristics is indicated in (a) as dotted lines. For the non-linear shunt A the reverse current is expected to be zero in this scaling. If the 0° signal would be

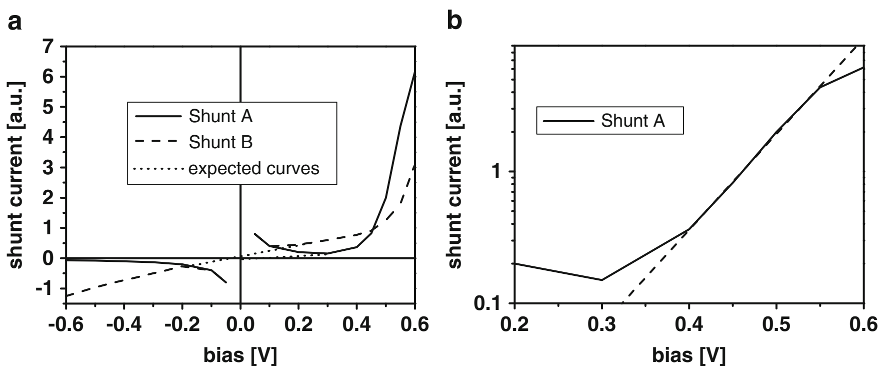

Fig. 6.12 Local I-V curves of shunts A and B of Fig. 6.8 (**b**) measured thermally (LIVT) (**a**) in linear drawing, and (**b**) of shunt A in half-logarithmic drawing. The expected "real" characteristics are indicated in (**a**) as dotted lines, the dashed line in (**b**) shows a curve with an ideality factor of 2.3

used, there would be no systematic outrunning, but the values for low voltages nevertheless would become increasingly inaccurate due to the inevitable noise. Hence, due to this noise limitation, LIVT is only able to measure I-V characteristics above a certain bias limit, which depends on the strength of the shunt. The dashed line in the logarithmic drawing (b) of the characteristic of shunt 'A' shows that the ideality factor of this characteristic is 2.3. This result nicely confirms the ideality factor mapping in Fig. 6.4 in Position 'A'. At low voltages the measured curve deviates from this line due to the noise and at high voltage due to the series resistance.

6.2.1.6 Reverse-bias DLIT

In the last years also reverse-bias DLIT has gained increasing attention for the following reason: In a solar module, usually 20 to 24 solar cells are connected in series to yield one "string" of cells. The current through all these cells is all identical, but the individual cell biases are floating, with only the sum of all biases being defined. Only if all these cells should have identical I-V characteristics, they behave like one cell generating 24 times the voltage of one individual cell. However, if e.g. one of these cells should be shadowed, it generates less current, thereby limiting the total string current. In this case the equilibrium of cell biases is disturbed and all the other cells may bias the shadowed cell into reverse direction. If then this cell "breaks down", i.e. if a large reverse current flows, excessive heat may be dissipated at the breakdown sites, leading in the worst case to the destruction of the module. According to conventional diode theory, a silicon solar cell should break down at a reverse bias above -50 V by avalanche breakdown [45]. Up to this bias, the reverse current density should be below 10^{-7} A/cm^2, which is uncritical. However, as the measured reverse bias I-V characteristics in Fig. 6.7(b) show, typical multicrystalline cells show a strong reverse current (breakdown) already at -10 V reverse bias and below. Interestingly, here, as in many other cases, the reverse I-V characteristics measured at two temperatures are crossing, hence under high reverse bias another breakdown mechanism seems to be active than under low reverse bias. For all these reasons breakdown in crystalline Si solar cells is an important reliability issue which has to be studied in detail.

The dissipated power under a reverse bias of several volts is usually orders of magnitude larger than under forward bias, where only 0.5–0.6 V are applied. For an ohmic shunt, for example, the dissipated power increases with the square of the applied bias. Thus, from the sensitivity point of view, lock-in thermography is not necessary for investigating shunts under reverse bias. Reverse-bias shunt imaging also works by using standard thermography and is often used. However, besides the fact that shunts under reverse bias may differ from those at the working point of the cell, the spatial resolution of lock-in thermography is decisively better than that of steady-state thermography. This is demonstrated in Fig. 6.13 comparing two reverse-bias lock-in thermograms (a, b) of the cell used for Fig. 6.8, measured at -10 and -17 V reverse bias, with the steady-state thermogram (c) of this cell also measured at -17 V. The -10 V image looks very similar to the -0.5 V image in Fig. 6.8(a) as it

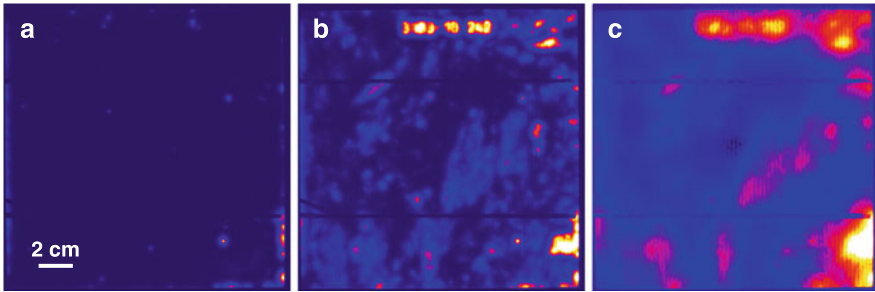

Fig. 6.13 Reverse bias DLIT images of the cell of Fig. 6.8 (**a**) measured at −10 V (scaled to 300 mK) and (**b**) at −17 V (scaled to 500 mK), (**c**): steady-state thermogram measured at −17 V (scaled to 10 K temperature increase)

essentially shows the linear (ohmic) shunts with only some weak additional features. Indeed, up to −10 V the reverse characteristic of this cell is essentially linear. In the −17 V image (b), however, many new features appear, which are strongly correlated with the low lifetime regions visible in Fig. 6.8(c). These are defect-induced breakdown sites, showing a highly super-linear ("hard") breakdown characteristic. At the top of the cell a laser marking of the wafer becomes visible which was already visible in the high-current forward-bias 0° image Fig. 6.8(d). Note that the scratch in the bottom left region, which was dominating the forward-bias thermograms, is not visible under reverse bias. In the steady-state thermogram Fig. 6.13(c) the strongest breakdown regions can also be localized, but single shunt positions are only hardly visible. Steady-state thermography is equivalent to a lock-in frequency close to zero. The scaling limit in (b) is 500 mK and in (c) it is 10 K, demonstrating that the signal height reduces with increasing lock-in frequency, see Sect. 5.2. Nevertheless, due to the high reverse bias the signal is strong enough that the whole measurement for (b) could be performed within only 1 s. Hence, lock-in thermography under reverse bias is able to be used as an in-line test measurement in an industrial fabrication line. It was shown that the time for shunt measurements can even be reduced to 10 ms by using only four images of an IR camera running at 400 Hz in one lock-in cycle with 0° correlation [153].

6.2.1.7 Temperature Coefficient and Slope Imaging

To distinguish different breakdown mechanisms, which may appear in different breakdown positions and in different bias ranges, their physical parameters have to be measured locally. Important parameters, which can be measured by evaluating bias- and temperature-dependent DLIT investigations, are e.g. the temperature coefficient and the slope of a local breakdown current. Since any breakdown mechanism may work at different magnitudes, the values of these coefficients have to be normalized to the local current values, hence we need the images of the relative temperature coefficient and of the relative slope of the reverse current density. It was shown in

Sect. 4.5.1 that −90° images can be converted into current density images by using (4.32). If DLIT images are measured at a number of different temperatures T_j and, for each temperature, at a number of different reverse biases V_i, these images are first converted into a set of current density images $J(x, y)_{i,j}$. Then images of the relative temperature coefficient (TC) and of the relative slope are calculated by the following relations [154]:

$$\mathrm{TC}(x, y) = \frac{2(J(x, y)_{i,j} - J(x, y)_{i,j-1})}{(T_j - T_{j-1})(J(x, y)_{i,j} + J(x, y)_{i,j-1})}, \qquad (6.6)$$
$$\mathrm{Slope}(x, y) = \frac{2(J(x, y)_{i,j} - J(x, y)_{i-1,j})}{(V_i - V_{i-1})(J(x, y)_{i,j} + J(x, y)_{i-1,j})}.$$

These techniques have been named "TC-DLIT" and "Slope-DLIT" [154]. Note that the reverse biases V_i are assumed to be positive values in (6.6). The data appear in units of K^{-1} and V^{-1} and may also be given in "percent change per K (or V)" by multiplying the values by 100. Since these are "central-difference derivatives" (due to the normalization to the average current density), the parameters T_j and T_{j-1} and V_i and V_{i-1}, respectively, have to be chosen sufficiently close together, and the results refer to the midpoint values between T_j and T_{j-1} respectively, V_i and V_{i-1}. If for slope measurements V_i and V_{i-1} are chosen too distant so that $J(V_{i-1}) \ll J(V_i)$ holds, (6) always leads to a slope of $2/(V_i - V_{i-1})$, independent of the real slope. If this slope should be measured, V_{i-1} has to be chosen closer to V_i [154]. Figure 6.14(a) shows a TC-DLIT image and (b) a slope-DLIT image of the cell used

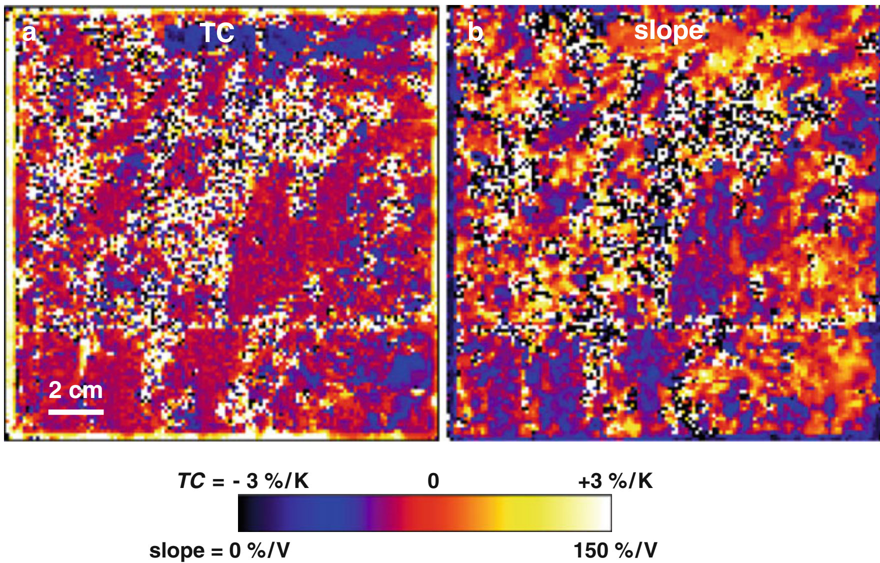

Fig. 6.14 (**a**) TC-DLIT image of the cell of Fig. 6.8, measured between 25 and 50°C at −16.5 V, (**b**) slope-DLIT image of this cell, measured between −16 and −17 V at 25°C

already in Figs. 6.8 and 6.11 to 6.13. The measurement parameters are given in the caption and the scaling ranges below the figure. Note that, due to their normalization to the average signal values, signals (a) and (b) of Fig. 6.14 show excessive noise in regions of low signal height in the regions between the breakdown sites, where the DLIT signals are low. This noise does not disturb very much in the Slope-DLIT image (b) since this signal is always positive. The TC-DLIT image (b), however, may be both positive (yellow to white) and negative (blue to black). Therefore the TC-DLIT signal may be artificially blanked to zero in regions where the signal is noisy [154]. We have refrained from this here since the predominantly positive TC between the breakdown sites in (a) is real. In fact, the dominant breakdown sites may have negative TC (blue) or nearly zero TC (red), but the homogeneous current contribution between the breakdown sites is responsible for the positive TC of the whole cell for reverse biases smaller than 13 V, which is visible also in Fig. 6.7(b) [155]. The normalization is also the reason why (a) and (b) appear blurred compared to the DLIT images. In fact, the whole area influenced by one breakdown site shows the same signal value, and weak breakdown sites appear with the same signal value as strong ones. The comparison of (a) and (b) with Fig. 6.13 shows that there are at least two different types of breakdown present, one showing a clearly negative TC and high slope, and one showing a TC close to zero and lower slope. The dominant breakdown sites in Fig. 6.13b belong to the first type.

All examples in this section have been made on wafer-based silicon solar cells. However, DLIT is applicable very successfully also on thin film solar cells. In fact, the sensitivity and also the spatial resolution of lock-in thermography on thin film cells on glass substrates is even better than for wafer-based silicon cells since glass is a poor heat conductor. It should be noted that, since usual glass substrates are thicker than the thermal diffusion length in this material, and the thickness of the active layers is usually small compared to the pixel size, thin film cells are often considered as thermally thick samples. However, recent calculations and experiments on thin film crystalline silicon on glass (CSG [143]) modules have shown that even the 1.5 μm thin silicon layer on the glass considerably affects the lateral heat diffusion [156]. In fact, the effective spatial resolution of CSG is between that of pure glass and that of pure silicon. Shunt imaging, LIVT, and the technique of ideality factor mapping have also been applied to CIS (copper indium sulfide) based solar cells and modules [157, 158]. Some examples of lock-in thermography on thin film modules will be presented in Sect. 6.3.

6.2.2 Illuminated Lock-in Thermography (ILIT)

Typical current–voltage (I-V) characteristics of silicon solar cells without illumination were shown in Fig. 6.7 in the previous section. The dark forward characteristics are, in the absence of ohmic shunts, essentially exponential; hence, the current steeply increases for increasing forward bias. Figure 6.15 shows a typical illuminated characteristic (a) together with a characteristic of the generated electric

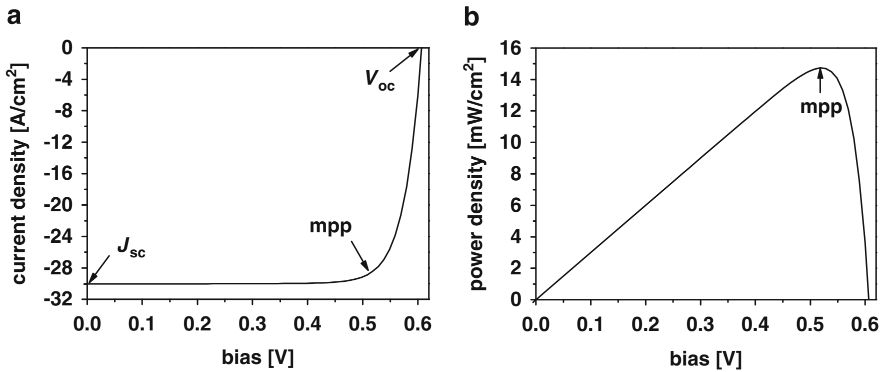

Fig. 6.15 (**a**) Illuminated current-voltage characteristic and (**b**) generated power characteristic of a typical solar cell, both referred to the area. The scaling ranges are indicated below

power (b). In order to be independent on the cell size, also these magnitudes are referred to the cell area, instead of the currents I, the current densities J are presented. These characteristics can be obtained by varying an electric load connected to the cell under illumination between zero resistance (short circuit) and infinite resistance (open circuit). By definition, the dark current is counted positively, and the photo-induced current being a reverse current is counted negatively. A negative current at a positive (forward) voltage means that the dissipated electric power is negative, hence the solar cell produces electric energy.

The three most important points in the illuminated I-V characteristic are the short circuit point where the current is the short circuit current I_{sc} (resp. J_{sc}) and the bias V is zero, the open circuit point where the bias is the open circuit voltage V_{oc}, and the current I is zero (here the bias-independent photocurrent is completely balanced within the cell by the dark forward current), and the maximum power point (mpp) where the generated power is maximal and the I-V characteristic shows I_{mpp} and V_{mpp}. All these magnitudes depend on the illumination intensity, the currents essentially linearly and the voltages logarithmically. If series resistances can be neglected, the illuminated I-V characteristic equals the dark characteristic shifted by the short circuit current, which is called the "superposition principle". In reality and under standard solar illumination intensity (which is called "1 sun", corresponding to an irradiated power density of $100\,\mathrm{mW/cm^2}$), the series resistances of the cell (typically $0.5\,\Omega\,\mathrm{cm}^2$) lead to an internal voltage drop of up to approximately 10 mV, depending on the magnitude of the current. The voltage drop is positive for dark currents (terminal voltage larger than internal bias) and negative under illumination (terminal voltage lower than internal bias). Due to this voltage drop, a forward bias somewhat larger than the open circuit voltage has to be applied in the dark to generate a dark current with the same amount as the short circuit current.

For several years, lock-in thermography had been performed on solar cells only in the dark. Indeed, shunts in solar cells can most easily be investigated in the dark, since then they are the only existing heat sources, see previous section. In 2004 two

groups, one at Fraunhofer Institute of Solar Energy Systems (ISE) and the other at Konstanz University, had proposed independently to perform lock-in thermography on solar cells by pulsed illumination [14, 15]. These techniques had been named independently "ILT" (Illuminated Lock-in Thermography) and "LimoLIT" (Light-modulated Lock-In Thermography) by the first and second groups, respectively. Later on, the name "ILIT" (Illuminated Lock-In Thermography) was generally accepted for all kinds of lock-in thermography on solar cells performed under illumination, whereby different short prefixes are used to characterize the type of the investigation [16]. In this section, we introduce and demonstrate several different ILIT techniques, which have been developed for imaging different kinds of inhomogeneities in solar cells.

6.2.2.1 V_{oc}-ILIT

The simplest and most popular ILIT technique is called V_{oc}-ILIT. Here, the cell is not contacted at all and is illuminated homogeneously by pulsed light. Because no current is drained here, the cell is under open circuit conditions (which is at forward bias) under illumination, so the bias modulation is, in principle, the same as for DLIT; therefore, all results visible in DLIT (especially shunts) can also be observed in V_{oc}-ILIT. This is demonstrated in Fig. 6.16(a)–(c), which has to be compared with Fig. 6.8(b)– (d) of Sect. 6.2.1. By varying the light intensity, the value of the V_{oc} modulation can be adjusted, e.g., to match V_{mpp} at standard illumination (typically about +0.5 V, Fig. 6.16(a)) and V_{oc} (about +0.6 V, b). The basic advantage of V_{oc}-ILIT compared to DLIT is that it does not need any electric contacts at the cell. Therefore, it can be applied, e.g., for shunt imaging already in an early technological state of a solar cell, where no contacts are made yet. This was the basic motivation for the development of V_{oc}-ILIT. This advantage has to be paid by the disadvantage that in V_{oc}-ILIT always a homogeneous heating contribution is present. This is due to the two "local" heating power contributions P_{th} and P_{pn+}, which are both dissipated in the position of light absorption and have been discussed in Sect. 2.8 in

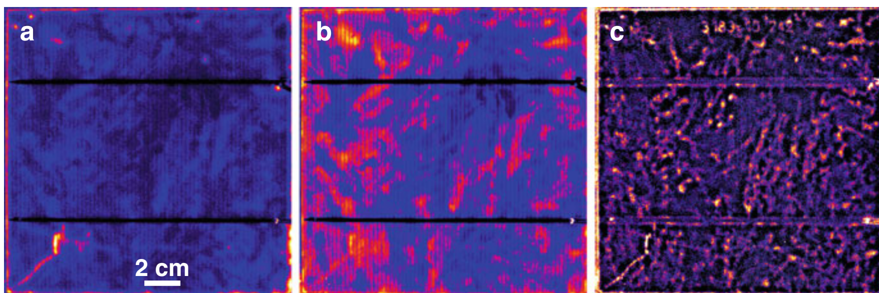

Fig. 6.16 V_{oc}-ILIT images of the cell taken for Figs. 6.8, 6.13, and 6.14, measured at (**a**) mpp (0.5 V, reduced light intensity, scaled from 0.2 to 2.5 mK) and (**b**) at V_{oc} (0.6 V, full light intensity, scaled from 5 to 20 mK). (**c**): 0° component of the 0.6 V image (scaled to 2 mK)

(2.37) and (2.38). This additional homogeneous heating disturbs in most ILIT techniques, only in some differential techniques it is compensated. It can be minimized by working at a wavelength in the near-IR range where the thermalization heat is minimal. The optimum wavelengths for ILIT on crystalline silicon cells are typically between 850 and 950 nm. In Fig. 6.16, this homogeneous heating was compensated by scaling the figures not between zero and a certain maximum signal value, but between two signal values. Another way to cope with the homogeneous heating is to display the 0° signal, which for thermally thin samples is insensitive to homogeneous heating, see Sects. 4.4 and 5.1. This signal also has the advantage that it displays local heat sources with the best possible spatial resolution, see the grain boundaries visible in Figs. 6.8(d) and 6.16(c).

Another advantage of V_{oc}-ILIT compared to DLIT is that the cell can easily be investigated even under standard open circuit condition without the necessity to feed in a high current. Note that for performing DLIT at V_{oc}, a current as high as the short circuit current had to be fed in, which is above 7 A for actual solar cells. In ILIT, just as in DLIT, any differences in the local heating are governed by differences of the local dark forward current, which may be due to local shunts, local recombination currents, or the local diffusion current, which depends on the minority carrier lifetime in the bulk material. In a homogeneous solar cell, under open circuit condition, the photocurrent is balanced by the dark forward current in any position. In this case, no lateral currents are flowing in the cell and the heating is homogeneous. If there are local low-lifetime regions in the cell showing an increased diffusion current, or if there are any local shunts, these regions are effective current sinks in the cell, whereas high-lifetime regions are effective current sources. Between these regions, lateral balancing currents are flowing in the emitter and in the bulk of the cell (or in the two contact metals, respectively) from high-lifetime regions to low-lifetime regions or to local shunts, but the external net current is zero. The thermal contrast in Fig. 6.16 is basically due to these lateral balancing currents. If there are strong ohmic shunts in a solar cell, they can be detected through V_{oc}-ILIT within less than 1 s without the need to contact the cell electrically. It has been shown that the best way for doing this is to illuminate the cell with IR light equivalent to about 1 sun, pulsed at a relatively low frequency of 3 Hz, and to display the 0° signal [159]. As mentioned above, this signal shows the highest spatial resolution and is not affected by the homogeneous heating contribution, which is inherent to ILIT. However, because the cell is not in thermal equilibrium after short acquisition times, it is necessary to apply the temperature drift correction as described in Sect. 4.2. If a highly sensitive and fast IR camera is used for this investigation, sufficient strong shunts can be detected reliably after an acquisition time of 1 s [159].

Another difference between V_{oc}-ILIT and DLIT is that nonlinear shunts, which are due to local recombination sites crossing the p–n junction, appear for the same forward bias somewhat stronger in V_{oc}-ILIT than in DLIT. This may be partly due to the inevitable series resistance of the cell, which leads to the fact that under V_{oc} in the dark usually only $I_{sc}/2$ flows (see discussion of Fig. 6.8(c) of the Sect. 6.2.1). However, it had been mentioned already in [14] and had been discussed in more detail in Sect. 5.4 that for optical excitation (under V_{oc}-conditions), if the carriers

are flowing to local recombination sites not through the back contact but in the bulk material, at least some part of the additional Peltier heat from the contacts and from the p–n junction may be dissipated at local recombination sites. How much of this additional heat is dissipated there depends on the fraction of majority and minority carriers directly flowing to the recombination sites compared to the fraction flowing across the contacts, if there are any. At least it is clear that this effect is not small. Note that Fig. 6.8(b) of Sect. 6.2.1 is scaled to 1 mK, whereas Fig. 6.16(a) is scaled from 0.2 to 2.5 mK, under otherwise identical conditions. Because the illumination intensity was weak, the homogeneous heating contribution alone was not responsible for this effect, and also the influence of the series resistance should be negligible here. So the lock-in thermography signal values may be higher in V_{oc}-ILIT than in DLIT due to local recombination and a higher contribution of Peltier heat. It had been discussed in [15] and [160] that another difference between DLIT and V_{oc}-ILIT is that the sign of internal voltage drops in the cell is different in both cases. For DLIT, the regions between grid fingers always show a lower local bias than that directly below grid fingers, whereas for ILIT, this region shows the same or even a somewhat higher bias, depending on the load condition. However, these internal bias differences are only in the order of some mV. It can be suspected that the influence of the additional Peltier heat is larger than the influence of these internal bias differences.

6.2.2.2 J_{sc}-ILIT

Another kind of illuminated lock-in thermography is J_{sc}-ILIT, which is performed by irradiating pulsed light to a cell being electrically short-circuited. Under this condition, the maximum possible amount of current I_{sc} is flowing, hence (just as for high forward current DLIT) the current has to be fed out very low-ohmically. According to Sect. 2.8, the two dominant heat dissipation mechanisms in this case are Joule heat in the emitter and Peltier heating at the p–n junction. In Fig. 6.17(a), a J_{sc}-ILIT image of an enlarged region of another cell is shown [15, 160]). For displaying only local heat sources, the 0° image is presented here. Moreover we also have Peltier heating at the contacts. Originally, this signal had been interpreted to be due to Joule heating in the emitter. However, recent simulations have shown that this signal is predominantly caused by the Peltier effect at the emitter grid lines, as for Fig. 5.7(b). Near the tips of the emitter grid lines, an increased amount of Peltier heat is generated since these tips have to collect the current generated in the whole edge region.

J_{sc}-ILIT is also appropriate to detect poorly contacted regions of high series resistance R_s [160,161]. This can be understood by considering Fig. 2.14 in Sect. 2.8. Here, we see that the maximum amount of dissipated heat under illumination occurs under short and open circuit conditions. If the well-contacted regions of a cell are under short circuit condition, any high-R_s regions are not, since the photocurrent increases the forward bias. Then in these regions, the amount of dissipated heat is lower because the Peltier heat (“thermalization heat”) at the p–n junction is lower.

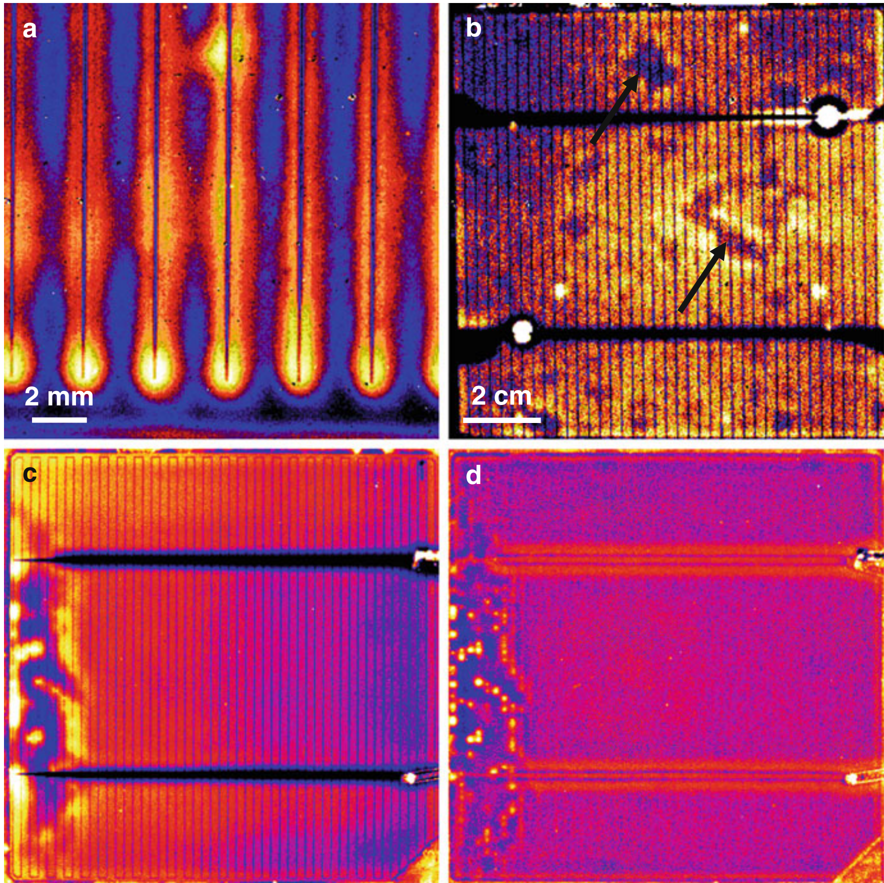

Fig. 6.17 (**a**) J_{sc}-ILIT (0° image) image of a region of a cell showing Peltier heat at the emitter contacts, (**b**) J_{sc}-ILIT image (amplitude) of a cell showing high-R_s regions (arrows), (**c**) J_{sc}-ILIT amplitude-image of the cell used already for Fig. 6.9, (**d**) 0°-image of (**c**). (**a**) and (**b**) by courtesy of J. Isenberg, now Centrotherm, Konstanz [160]. All images arbitrarily scaled

At the edge of this region, however, an increased signal is observed, because the photocurrent generated in the noncontacted region flows horizontally through the emitter out of this region by generating Joule heat. In fact, the average heat generated in a faulty device is the same as in a good device because no electric energy is fed away; hence, high-R_s regions have to generate a dark–bright contrast. This can be seen in Fig. 6.17(b) showing the J_{sc}-ILIT amplitude image of a cell containing high-R_s regions (see arrows). In (c), the same type of image is shown for the cell that had been used already for Fig. 6.9. Here, we also see a lower J_{sc}-ILIT signal in the high-R_s region at the left. However, in this case, the high ILIT-signal around this region is especially strong and highly localized. As the 0° signal of this measurement (d) shows, there are some point-like positions in this region dissipating

a large amount of heat. The arrangement of these positions in vertical lines shows that they are lying below emitter grid lines. It turns out that these positions are local Schottky contacts between the emitter and the emitter contact lines [162]. Due to insufficient firing conditions in this region, instead of a continuous ohmic contact, some local Schottky contacts have been formed here. If the cell is under short circuit, the p–n junction and these Schottky diodes are electrically switched in parallel with the emitter potential floating. Under illumination, the Schottky diodes become forward-biased by the p–n junction, leading to the observed hot spots because the p–n junction shows a larger barrier height than the Schottky diodes. If a certain forward bias is applied to the cell under illumination, these hot spots vanish since then the Schottky diodes are not sufficiently forward biased anymore.

6.2.2.3 R_s-ILIT

The basic limitation of J_{sc}-ILIT for series resistance imaging is that it may be hard to interpret the images correctly due to the inherent dark–bright contrast of high-R_s regions. If these regions are spatially extended, they come into open circuit condition in the middle, even if the terminals are short-circuited. Hence, these regions show the same thermal signal as well-contacted regions (see Fig. 2.14). To overcome these limitations, the technique of R_s-ILIT was developed [42, 149]. In this technique, the illumination is applied continuously and the bias is pulsed between short circuit and mpp (typically $+0.5$ V). In this case, however, since for zero and positive bias a negative current occurs, the power supply must be able to work as a current sink (2-quadrant operation). An ordinary power supply may also be used if an electronic load is switched parallel to the power supply for draining the generated photocurrent to ground. In R_s-ILIT not the amplitude signal but the $-90°$ signal is displayed because positive and negative signals may occur. According to Fig. 2.14 in a well-contacted cell, the dissipated heat is minimum at mpp. Hence, if the cell is at mpp in the "+" phase of the lock-in cycle and at short circuit in the "−" phase, the resulting R_s-ILIT signal of such a region is negative. In a high-R_s region under constant illumination, all biases are shifted towards V_{oc}. Thereby, the R_s-ILIT signal becomes less negative or even positive. Even in a spatially extended high-R_s region, the R_s-ILIT signal is zero (because this region remains permanently under open circuit); hence, it can easily be distinguished from a well-contacted region showing negative signal. The optimum excitation wavelength for R_s-ILIT is about 850 nm, because even in low-lifetime regions nearly all absorbed photons are leading to a photocurrent. One advantage of R_s-ILIT is that it is not disturbed by the homogeneous heating caused by the illumination because this illumination is acting both in the "+" and in the "−" phase of the lock-in cycle. Also, the heating influence of the current flowing laterally in the emitter, which generates the bright contrast in J_{sc}-ILIT, is considerably reduced in R_s-ILIT, because this current flows essentially in both lock-in periods. One limitation of R_s-ILIT is that it cannot be interpreted quantitatively yet, because the signal height depends nonlinearly and even nonmonotonically on R_s. For quantitatively imaging the dark R_s, the RESI

method described in Sect. 6.2.2 should be used. Alternatively, techniques based on luminescence imaging only are available. For an overview and practical comparison, see [163, 164]. Another limitation of R_s-ILIT is that it also shows shunts as bright regions, because the bias is pulsing. However, this can be corrected by subtracting a DLIT shunt-image from the R_s-ILIT signal. It has turned out that if the R_s-ILIT image was measured between 0 and 0.5 V the optimum bias for this DLIT shunt-image is 0.55 V. This voltage shift may be a series resistance effect, but probably under illumination the shunts also show an increased signal due to a certain contribution of Peltier heating, see Sect. 5.4. Alternatively, the shunt contribution can be avoided by forming the R_s-ILIT signal as the difference of two ILIT signals measured with pulsed illumination at constant biases, one measured under short circuit and the other at the maximum power point [149]. Figure 6.18 shows a standard R_s-ILIT image of a cell containing grid line disruptions, which appear bright. In addition, some shunts are visible. (b) shows the shunt image measured at 0.55 V, and (c) shows the difference between (a) and (b), which is the shunt-corrected R_s-ILIT image. The image obtained by subtracting two pulsed-irradiation ILIT images at constant biases of 0 and 0.5 V looked like (c).

The third variant of electric loading for ILIT performed by pulsed light illumination is to keep it during the light pulses at the maximum power point (mpp) of a solar cell. This variant is called mpp-ILIT and can image any kind of power loss at the real operation point of a solar cell. It is performed simply by connecting a load resistance to the cell which is adjusted so that during the light pulse V_{mpp} is measured. Alternatively, the bias can also actively be pulsed parallel to the light pulsing. Also, just as for R_s-ILIT, the power supply must be able to work as a current sink. If in mpp-ILIT the $-90°$ signal is displayed, within the spatial resolution limit of about one thermal diffusion length, the local signal is a quantitative measure of the locally dissipated power density in the cell. Assuming homogeneous in-coupling of the light, according to Sect. 2.8 this power density should have a minimum value in all regions producing electric power. Any deviations from homogeneity (local heat sources) can be attributed to specific power losses. The only problem for a quantitative evaluation of such images is the high amount of homogeneous heating, which is inherent to any ILIT measurement. It has been proposed by Ramspeck et al. that

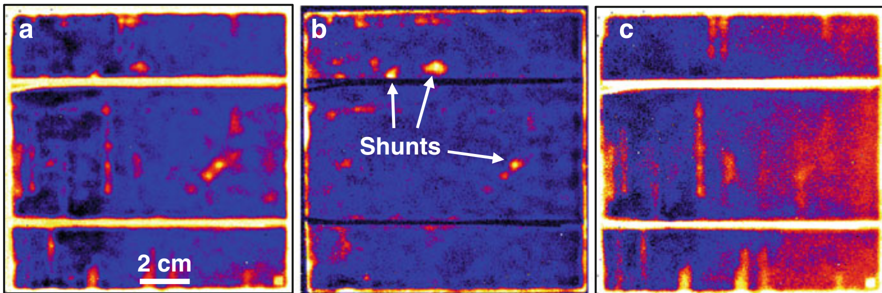

Fig. 6.18 (**a**) R_s-ILIT image of a cell containing disrupted grid lines, (**b**) DLIT shunt image (measured at +0.55 V), (**c**) shunt-corrected R_s-ILIT image

the amount can be compensated by subtracting the mpp-ILIT image from the J_{sc}-ILIT image [165]. Note that according to Fig. 2.14 in Sect. 2.8 under short circuit condition, the complete amount of absorbed power $P_{absorbed}$ is dissipated as heat. Thus, the difference between J_{sc}-ILIT and mpp-ILIT just should be proportional to the local amount of generated electric energy P_{out}. Then the local efficiency is given by the ratio:

$$\eta_{int}(x, y) = \frac{P_{out}(x, y)}{P_{absorbed}(x, y)} = \frac{S_{sc}^{-90^\circ}(x, y) - S_{mpp}^{-90^\circ}(x, y)}{S_{sc}^{-90^\circ}(x, y)} \tag{6.7}$$

As for any quantitative evaluation, the $-90°$ components of the short circuit and the mpp signal should be used. This efficiency automatically corrects for the IR emissivity of the cell and even for weak inhomogeneities of the irradiation intensity, which affect both signals in the same way. It holds for the selected kind of irradiation, which may be monochromatic or realistic solar light. Note that (6.7) is an internal efficiency, which relates the output power to the absorbed optical power. Thus, it is independent on the local reflectivity, which affects the external efficiency. An external energy conversion efficiency could also be imaged by dividing through the local incident light intensity [165]. Then $(S_{sc}^{-90^\circ} - S_{mpp}^{-90^\circ})$ has to be scaled separately in units of W/cm^2, which can easily be done using the proportionality method described in Sect. 4.5.1. The relevant total power is just the electric power generated by the cell at mpp.

Note that this efficiency imaging procedure works only if the considered region is really at short circuit and/or if the terminals of the cell are short-circuited. If the investigated cell does have any series resistance problems or if there are, e.g., non-contacted regions in the cell, this procedure does not work correctly any more in these regions. This is because, as described for the J_{sc}- and R_s-ILIT technique above, in high-R_s regions the local bias under illumination is always higher than in well-contacted regions. Thus, in high-R_s regions the dissipated power under illumination at short circuit is less than the absorbed power, and the measured power loss due to high-R_s regions is somewhat overestimated. Note also that the nominator (6.7) is just the inverse of the R_s-ILIT signal without shunt correction. Remember that the R_s-ILIT signal is negative in well-contacted regions. Yielding the difference between the J_{sc}-ILIT and the mpp-ILIT signal, both measured with pulsed irradiation, is just equivalent to pulsing the bias between short circuit and mpp at constant illumination. Thus, the negative R_s-ILIT signal is quantitatively proportional to the local external efficiency, provided that the illumination is homogeneous. This holds exactly in well-contacted regions, whereas R_s-losses may appear somewhat overestimated. For imaging high-R_s regions by R_s-ILIT, an illumination wavelength of 850 nm is optimum, whereas for efficiency imaging, a longer wavelength of 950 nm or even light with a realistic solar spectrum should be used. Then also lifetime-induced variations of the internal quantum efficiency can be imaged. Note that the R_s-ILIT procedure has the advantage that the light needs not to be pulsed.

6.2.2.4 Avalanche Multiplication Factor Imaging (MF-ILIT)

Finally, a special ILIT variant is introduced which works under reverse bias. It has been mentioned already in the previous section that the physical investigation of breakdown sites in silicon solar cells has attracted a good deal of interest in recent times. The two well-known breakdown mechanisms in semiconductors are internal field emission (Zener effect) and impact ionization (avalanche effect) [45] and between these two, only impact ionization has the property to multiply photo-induced minority carriers flowing through the depletion region. This effect is used in Avalanche photodetectors. For checking the breakdown type of different breakdown sites in a solar cell, it is useful to image its local avalanche multiplication factor MF at different biases, which can be performed using MF-ILIT [154]. This technique relies on the evaluation of two ILIT images taken under special conditions. Here, two ILIT images measured with pulsed irradiation but under constant reverse bias of different heights are used. The illumination intensity may be as weak as 0.1 sun (corresponding to a photocurrent of about 3 mA/cm^2) or below, because the appearing signals are high. Again, because these images are evaluated quantitatively for silicon solar cells, the $-90°$ signal has to be used. Under these conditions, all steady-state breakdown currents, which are not affected by the pulsed photocurrent, do not contribute to the measured signal. In fact, according to Sect. 2.8, the complete modulated heat generated under these conditions is due to thermalization of photo-generated carriers. This is the thermalization of absorbed photons in the bulk (giving a contribution of $eV_{\text{th}} = h\nu - E_{\text{g}}$ per electron) and, to the biggest part, heat dissipation of the photocurrent at the p–n junction, which is related to Peltier heat at the p–n junction, see Sect. 5.4. The contributing barrier potential is the sum of the applied reverse bias V (assumed to be a positive number here) and the diffusion voltage V_{D} of the junction, which can be measured, e.g., by capacitance–voltage techniques and is about 0.95 V for silicon solar cells. If we neglect the small kinetic energies of the carriers, for a generated photocurrent J_{ph} without avalanche multiplication the dissipated power per unit area is:

$$p(V) = J_{\text{ph}}(V + V_{\text{D}} + V_{\text{th}}). \tag{6.8}$$

Note that the reverse biases are taken here as positive numbers. If one of these photo-generated carriers gets multiplied on its way through the depletion layer, it loses some of its kinetic energy and the newly generated electron-hole pair dissipates the energy $e(V + V_{\text{D}})$. Thus, neglecting the small influence of V_{th} which does not apply for multiplied carriers, (6.8) also holds for an "effective avalanche current" density J_{aval} flowing in addition to J_{ph}. By definition, the avalanche multiplication factor MF is the ratio of the total current flowing under multiplication condition at a reverse bias V to its constant value at small reverse bias V_{low}. Because (6.8) is proportional to the corresponding ILIT signals $S^{-90°}$, the multiplication factor becomes [154]:

$$\text{MF}(V) = \frac{J_{\text{ph}} + J_{\text{aval}}}{J_{\text{ph}}} = \frac{(V_{\text{low}} + V_{\text{D}} + V_{\text{th}})S^{-90°}(V)}{(V + V_{\text{D}} + V_{\text{th}})S^{-90°}(V_{\text{low}})}. \tag{6.9}$$

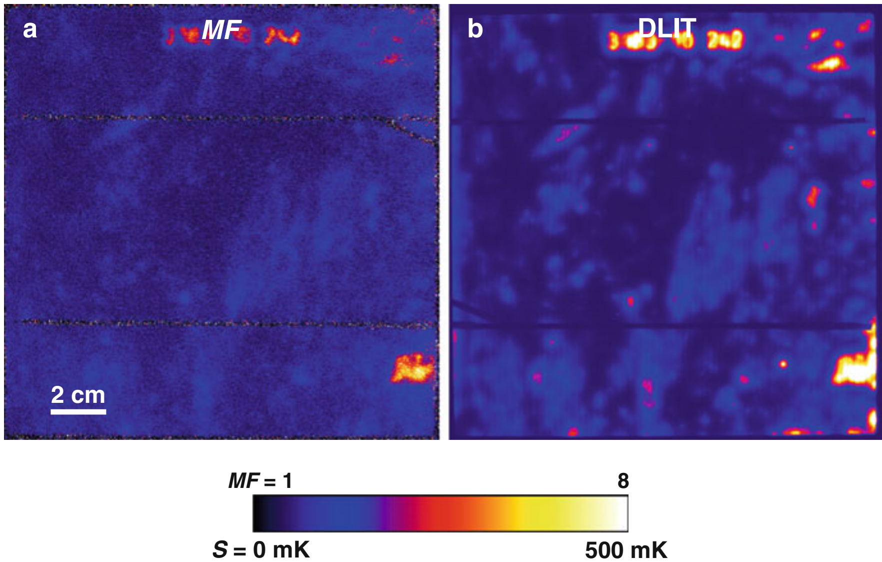

Fig. 6.19 (**a**) MF-ILIT image of the cell of Fig. 6.16, measured at $V_{low} = 10$ and $V = 15$ V at 25°C, (**c**) reverse-bias DLIT image at −17 V of (see also Fig. 6.13 (**b**) in Sect. 6.2.1). The scaling ranges are indicated below

If both V and V_{low} are chosen so low that no avalanche multiplication takes place, or if in a certain position no avalanche multiplication takes place, the measured MF should be unity, because the photocurrent is independent of V and the ILIT signal increases proportional to $(V + V_D + V_{th})$. An example of such a measurement, taken with the cell of Fig. 6.16 and before at $V_{low} = 10$ V and $V = 15$ V by irradiating light with $\lambda = 850$ nm ($V_{th} = 0.35$ V), is shown in Fig. 6.19(a). For comparison, (b) shows the −17 V reverse-bias DLIT image of this cell, which was shown already in Fig. 6.13(b) of Sect. 6.2.1. The comparison of Fig. 6.4 with the TC-DLIT and the slope-DLIT images in Fig. 6.14 of Sect. 6.2.1 shows that the regions of dominant breakdown at −17 V reverse bias, which show a negative TC and a high slope, are indeed regions of considerable avalanche multiplication of up to a factor of 8. Because in this material avalanche multiplication actually should occur only above 50 V reverse bias [45], this may be an effect of sharp surface structures [166]. Also, the other defect regions show a weak avalanche multiplication effect, which is not completely understood yet. According to recent investigations [167] these breakdown sites are caused by metal-containing precipitates lying in grain boundaries.

Note that for all techniques described here homogeneous generation of minority carriers was assumed, which not necessarily holds. If there are any technically induced inhomogeneities of the irradiation field, they can be measured and the images can be corrected for this inhomogeneity, as it was done for CDI/ILM [53], see Sect. 3.5. If a locally varying reflectivity leads to an inhomogeneity of the

radiation intensity coupled into the material, this inhomogeneity can be corrected by imaging the local reflectivity, just as it was done for measuring the internal quantum efficiency of solar cells [168]. The examples presented also in this section were exclusively given for crystalline silicon solar cells, because the authors are specialized in this field. However, these techniques should work as well for thin-film solar cells and modules. One specific problem in thin-film cells (maybe except for silicon-based ones) is that their contacts may be not purely ohmic but may imply certain energy barriers. This is one reason why in thin-film cells the superposition principle usually only poorly holds. In operation these contact barriers do not disturb so much because their barrier height is reduced during illumination. Thus, especially in such cells the comparison between DLIT and ILIT results should be a valuable tool for studying, e.g., such "photoconductive contacts". Moreover, any lateral inhomogeneity of the barrier height of thin-film cells can easily be observed by imaging local current densities by lock-in thermography.

6.2.3 Summary of Solar Cell Applications

Since the large number of different lock-in thermography techniques to be applied to solar cells may be a little confusing, a summary about these possible applications is given here. Lock-in thermography is certainly most useful as DLIT under forward bias close to the maximum power point (about +0.5 V for silicon cells) for imaging all kinds of shunts ("shunt imaging," Sect. 6.2.1.1). This investigation always should be complemented by measuring an image under –0.5 V and displaying it in the same scaling as the +0.5 V one, see Fig. 6.8. This comparison allows one to check which of the shunts has a linear (ohmic) and which one has a nonlinear (diode-like) characteristic, since the DLIT image under –0.5 V displays only ohmic shunts. Note that all these results may be interpreted quantitatively, see Sect. 4.5. DLIT imaging at higher reverse bias than –0.5 V (see Sect. 6.2.1.6) usually shows new "hot spots" in addition to the ohmic shunts visible under –0.5 V, which are local junction breakdown sites. If DLIT investigations are done at many different biases, the evaluation of the bias-dependent local signals allows one to measure local I-V characteristics thermally (LIVT, see Sect. 6.2.1.5). While the nonlinear shunts measured at +0.5 V are responsible for the depletion region recombination current (described by J_{02}, see Sect. 2.8), inhomogeneities of the diffusion current (described by J_{01}, see Sect. 2.8) may be imaged by performing DLIT at a forward bias corresponding to the open circuit voltage (about +0.6 V for silicon cells, see Sect. 6.2.1.2). This "high current DLIT" image also allows an easy identification of non-contacted regions showing a high local series resistance R_s, see Fig. 6.9. However, in multicrystalline cells it may be hard to distinguish non-contacted regions from "good" regions showing a low forward current density. Note that DLIT at +0.5 V may also show J_{01} contributions weakly, and DLIT at +0.6 V will still show contributions of the nonlinear shunts (J_{02}). A separate imaging of these two contributions may be reached by evaluating images belonging to more than two biases which, according to the knowledge of

the authors, has not been done yet. If DLIT is combined with electroluminescence (EL) imaging, it allows to image the local series resistance quantitatively (RESI, see Sect. 6.2.1.3). The imaging of the local ideality factor and the saturation current (Sect. 6.2.1.4), as well as the imaging of the temperature coefficient and the slope of breakdown sites (Sect. 6.2.1.7), all rely on the quantitative interpretation of the $-90°$ signal as a measure of the locally flowing current, see Sect. 4.5.1.

The most interesting application of illuminated lock-in thermography (ILIT) is certainly V_{oc}-ILIT, see Sect. 6.2.2.1. Note that the only advantages of V_{oc}-ILIT compared to high-current DLIT are the facts that V_{oc}-ILIT may be applied without contacting the cell, and that here series resistances play only a minor role, since the current is locally generated. Earlier speculations that V_{oc}-ILIT could display anything that high-current DLIT does not display could not be confirmed. A clear disadvantage of V_{oc}-ILIT is that it displays a homogeneous background signal, which is due to carrier thermalization immediately after photon absorption and if the photocurrent passes the p–n junction (Peltier heat, see Sect. 2.8). J_{sc}-ILIT performed under short circuit of the cell (Sect. 6.2.2.2) may image Joule heat due to lateral current flow, Peltier effects, or (qualitatively) high resistance regions. However, all these things can also be imaged by high-current DLIT. Only the detection of local Schottky contacts of the grid really needs to perform J_{sc}-ILIT. The R_s-ILIT technique introduced in Sect. 6.2.2.3 allows to detect regions of high series resistance reliably also in multicrystalline cells, but it also cannot image the series resistance quantitatively. For this purpose, besides using RESI, pure luminescence methods should be considered [163, 164]. If the cell under consideration does not show any significant series resistance problems, its local efficiency can be mapped by the efficiency imaging procedure also described in Sect. 6.2.2.3, which is physically related to R_s-ILIT. Finally, the avalanche multiplication factor of a solar cell under reverse bias can be imaged quantitatively using the MF-ILIT technique introduced in Sect. 6.2.2.4. Table 6.1 summarizes the different lock-in thermography techniques.

6.3 Failure Analysis of Solar Modules

The nondestructive investigation of complete solar modules is experimentally very similar to the investigation of single solar cells, but, due to the interconnection of solar cells, the interpretation of the results differs. It had been mentioned that in a solar module, a larger number of solar cells are connected in series in “strings”, which are connected in parallel and encapsulated behind a glass plate. To achieve a module efficiency close to the efficiency of the cells interconnected in the module, the single cells have to be carefully selected. All cells switched in series have to carry the same current, and all strings of cells switched in parallel have to build up the same voltage under illumination at the maximum power point. If the cells in a solar module are mismatched, the cells are not simultaneously working at their maximum power point, leading to a considerable loss in efficiency of the whole

Table 6.1 Overview of different lock-in thermography techniques applied to solar cells

Technique	Variables	Results
DLIT ±0.5 V (shunt imaging)	Polarity	Linear and nonlinear shunts, J_{02}, quantitative evaluation possible
DLIT +0.6 V (high current DLIT)	V	J_{01}, R_s (qualitatively)
DLIT at different biases, LIVT	V	Local I-V characteristics
Reverse bias DLIT	V (reverse bias)	Breakdown sites
Ideality factor/saturation current mapping	V	Local ideality factor/saturation current
Slope-DLIT, TC-DLIT	V, T	Temperature coefficient and slope of breakdown current
V_{oc}-ILIT	Light intensity	Linear and nonlinear shunts, J_{01}, J_{02} (less accurate due to thermalization)
J_{sc}-ILIT	Light intensity	Joule heat, Peltier sites, R_s (qualitatively)
R_s-ILIT	V, light intensity	R_s (qualitatively)
Efficiency imaging	V, light intensity	Local efficiency, if no R_s problems
MF-ILIT	V, light intensity	Local avalanche multiplication factor (quantitatively)

module. The same happens if any kind of failure damages some of the cells as, e.g., soldering. Once the module is encapsulated, the electrical testing of single cells is no longer possible.

Applying LBIC-related techniques [169, 170], and also steady-state thermography [171, 172], attempts have been made to characterize the single solar cells in a complete solar module. Both these methods may detect shunted cells as well as disruptions of the current leads. However, in both techniques only the whole shunted cells can be recognized by a different brightness in the image, leading to a “patchwork” appearance of the images of modules. These images do not allow one to fix the exact position of a shunt in the cell, which would allow to yield conclusions about the shunt origin. A much better spatial resolution can be obtained by using electroluminescence (EL) imaging of whole solar modules [173, 174]. Also lock-in thermography is able to investigate solar modules, thereby making use of its improved sensitivity and spatial resolution compared to steady-state thermography. A problem here is the glass encapsulation itself, since glass is nearly opaque in the mid-IR wavelength range. Besides, it is a rather poor heat conductor. Hence, in order to image the frontside of glass-encapsulated solar panels, a very low lock-in frequency has to be used to ensure that the thermal waves from the cells are reaching the glass front. This inherently would strongly reduce the effective spatial resolution. A way out is to image solar modules from their rear, since the rear cover of the module is often a considerably thinner plastic film, which may be penetrated more easily by the thermal waves. This option has been used in the following investigation. It might also be interesting to image the whole solar cell array immediately after assembling, as long as it is not encapsulated yet. This would still allow one to perform repairs, if faults should be detected.

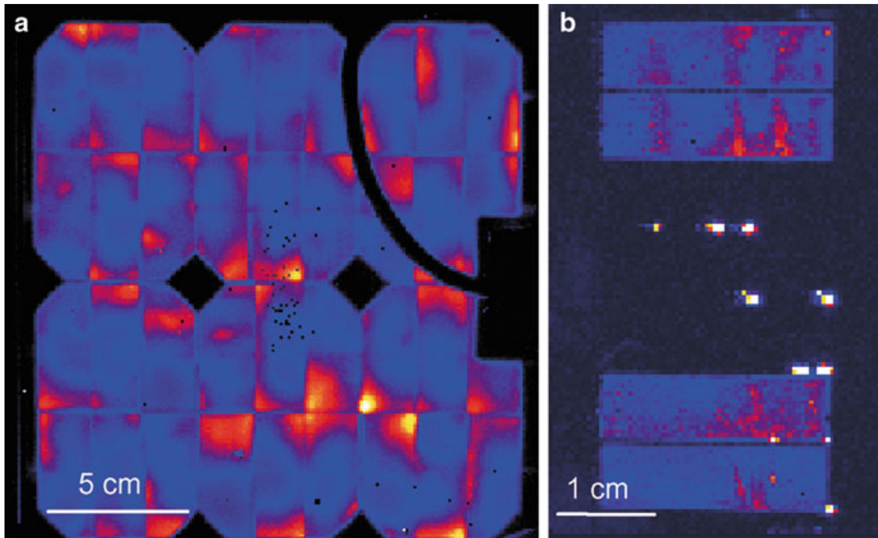

Fig. 6.20 (**a**) Amplitude image of a module 20 × 20 cm^2 in size, consisting of 36 single cells, measured at 0.1 Hz and a forward bias of 18 V at the rear. (**b**) Thin-film CuInS solar module on glass consisting of 7 cells, measured at 13 Hz and a forward bias of 4.1 V

Figure 6.20(a) shows a small solar module consisting of 36 silicon solar cells, which are cut from standard monocrystalline silicon cells. The module is imaged from behind, the shadows of the connecting cable and of the box for the electrical interconnection appear as dark regions. Most of the single solar cells show local shunts, which are located mainly at the edges of the cells. They are strongest in some corners of some cells, which had been observed also in other cases (see Fig. 5.6 of Sect. 5.3). Note that there is no indication of a shunt caused by the soldering procedure, which would be located in the middle of the cells. All cells are showing a comparable heat production in their interior (indicated by blue colour), which proves that the biases across each individual cell are comparable in this series connection. Hence, the observed shunts seems to be too weak to disturb the uniform distribution of the biases across the different cells.

This is not the case in the next example of a small $CuInS_2$ thin-film module shown in Fig. 6.20(b) [158]. It is a non-encapsulated laboratory module on a glass substrate imaged at 13 Hz. Note that glass is a much weaker heat conductor than silicon (see Appendix A). Therefore, for a given power source at the surface, the temperature modulation of a thin-film device on glass is much larger than of a silicon device, and the degradation of the spatial resolution due to the lateral heat conduction is much weaker. For this reason, unlike silicon solar cells, thin film devices can be investigated also successfully by steady-state thermography [9]. Nevertheless, also here lock-in thermography improves the sensitivity and ensures a quasi-adiabatic measurement, which is the presupposition for a straightforward quantitative interpretation of the results. The measurement as to Fig. 6.20(b) took

less than 1 min. Only 4 of the 7 cells in this module show a thermal signal in their interior, but the 3 in the middle do not. Instead, there are a number of bright spots surrounding these cells, indicating the positions of the local shunts, which here are actually short-circuiting these 3 cells. All shunts are located at the interconnecting lines, which are the most critical positions in these integrated interconnected modules [9, 157, 158]. Hence, here the shunts are so strong that they seriously disturb the distribution of the forward biases across the single cells connected in series. In the 3 cells in the middle the resulting forward bias was so low that current injection in the area of these cells was negligible.

This example shows that the interpretation of lock-in thermograms of solar modules interconnected in series differs from that of single solar cells: Single cells are driven under constant voltage conditions. Hence, for a given applied voltage bright regions correspond to a large local current density, which degrades V_{oc} and FF, and dark regions are the good parts of the cell. Solar cells interconnected in series, on the other hand, are driven under constant current conditions. Here, too, single bright spots correspond to local shunts. However, since the biases of the single cells are floating, the bias across each cell is influenced by its individual shunts. The stronger the shunting action, the lower is the bias across the corresponding cell. This is revealed by observing the amount of the homogeneous heat generation in the interior of the cells. The brighter this region, the weaker is the corresponding cell shunted. Hence, in a solar panel investigation a homogeneously bright signal indicates a good cell, contrary to the single cell investigation, where bright regions always indicate poor cell properties. Nevertheless, local differences in the brightness within one cell are occurring also in Fig. 6.20(b), here, too, indicating local inhomogeneities of the I-V characteristic. Within one cell, also incorporated in a module, bright regions of the corresponding cells correspond to the poor parts and dark regions to the good parts.

It has to be emphasized that one advantage of lock-in thermography is that it can easily be interpreted quantitatively. Hence, from an image like Fig. 6.20(a) the total heat dissipated by each single cell can be measured by evaluating the $-90°$ signal averaged over each cell according to the image integration method described in Sect. 4.5.1. Since the current across all cells in one string is constant, this value is proportional to the floating bias under this unilluminated condition, which thus can be measured non-contacting. In the same way, by steady-state illuminating the module and pulsing the electrical load of the module between open circuit and maximum power point, the electrical power generated by each cell can be measured, which has already been proposed for single solar cells by Rappich et al. [90]. If this technique is applied to solar modules, the scattering between the efficiencies of the cells within a module owing to their floating bias, which is a main cause for the reduced fill factor of modules compared to that of the single cells, can be investigated quantitatively under realistic conditions.

Finally, the investigation of a "Crystalline Silicon on Glass" (CSG) thin film module will be presented. In this technology the light enters the 1.5 μm thick silicon cell stack through the glass substrate (superstrate technology). The electrical interconnection is made at the surface by a dense arrangement of interdigitated Al-lines,

each 12 mm long and 0.5 mm wide, which through special contact holes are connecting the n-side of one 6 mm wide cell stripe with the p-side of a neighboring cell in one position [143]. This interconnection scheme provides a low resistance in the direction of the current flow but a high one in perpendicular direction along the elongated cell stripes. This makes this technology especially tolerant to local shunting [175]. Nevertheless, due to some irregularities in this metallization pattern, local shunts or even conductive or non-contacted channels across the whole module may appear, which can easily be made visible by DLIT under forward bias. However, due to the fact that in this technology the current is flowing horizontally within the semiconductor layers (from and to the small contact holes), Peltier effects are much more pronounced here than in other technologies. Figure 6.21 shows DLIT images of a small experimental CSG module, (a) under a relatively weak forward bias (400 mV/cell, about 1 mA/cm^2), and (b) under high forward bias (650 mV/cell, about 40 mA/cm^2). The current is flowing vertically, this module contains eight horizontally extended single cells. For these investigations the IR emissivity of the surface was increased and homogenized by sucking on a thin black IR emitter foil to the surface of the module, as described in Sect. 6.2. As for crystalline solar cells (see

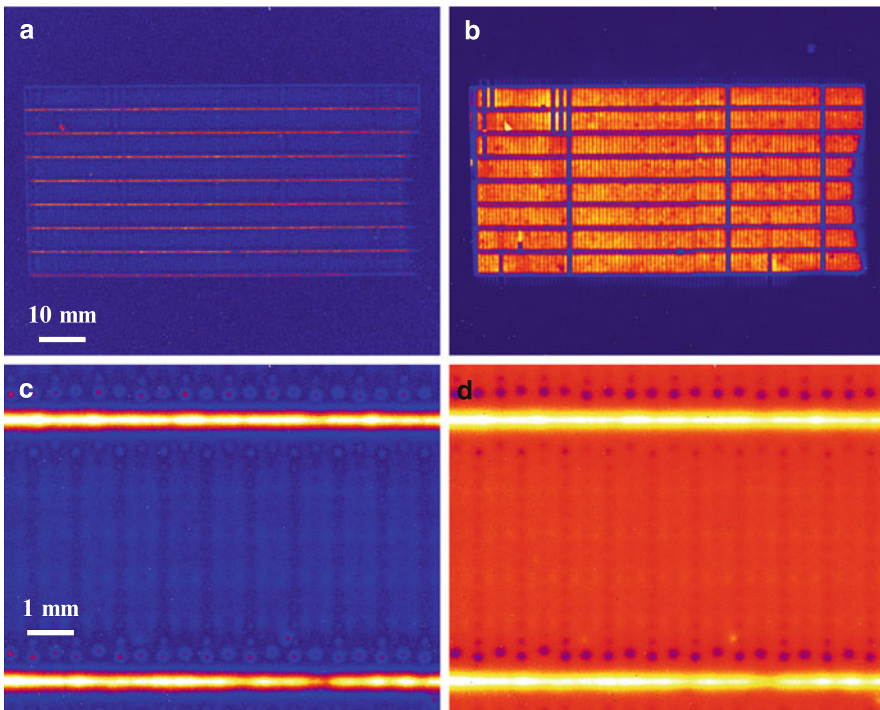

Fig. 6.21 (**a**) DLIT amplitude image of an experimental CSG module, measured at 1 mA/cm^2, scaled to 3 mK, (**b**) DLIT image of the same module measured at 40 mA/cm^2, scaled to 20 mK, (**c**) detail (one cell) measured at 1 mA/cm^2, amplitude image scaled to 3 mK, (**d**) same measurement, −45° image scaled from −3 to 3 mK

Sect. 6.2.1), depending on the magnitude of the forward bias, different effects can be observed. At low forward bias (Fig. 6.21(a)) the homogeneously flowing current is weak, and the dominating heat sources are due to local recombination currents in the depletion region (recombination-type shunts/leakage current). These current contributions are located mostly at the grooves between two cells where the p–n junction comes to the surface (compare to Fig. 6.8(b) in Sect. 6.2.1). The high-bias/current image (b) looks very different. Here, according to the physics described at the beginning of Sect. 6.2.1, the areal diffusion (injection) current and series resistance effects are dominating the thermal signal. In (b) the edges of the cells appear dark because they are more distant to the contact holes than the cell interior. Due to the higher forward bias the edge recombination current is not dominating anymore. There are three dark vertical stripes visible in (b). These stripes are due to technological problems, here the contact holes are completely missing (note that these are experimental modules). Due to the locally increased series resistance in these stripes the injection current is lower, just as in the regions of the cell edges. In addition, there are some smaller sites where also contact holes are locally missing. Also these sites appear dark, and they are mostly surrounded by a bright edge. This edge is due to a locally increased current density in the semiconductor material around, where the current in the non-contacted regions has to flow through, since it cannot flow through the missing contact holes. In the high magnification low-bias amplitude image (c), the contact holes, especially those close to the cell edge which feed the edge recombination current, also appear bright. One might argue that this is due to the contact resistance of these holes. However, as the -45° single-phase image (d) shows, in these contact regions the thermal signal is negative, hence here Peltier cooling is dominant. In this image colour red means zero signal, yellow/white means local heating, and blue/black means local cooling, just as in Fig. 5.7 of Sect. 5.4. The cooling action is also easily visible in the phase image (not shown here), since in the contact hole positions the phase signal is 180° shifted to the expected value. Quantitative lock-in thermography measurements of the Peltier coefficient, similar to that shown for a wafer-based cell in Fig. 5.7 of Sect. 5.4, have revealed that here the Peltier coefficient of the p-material is about 90 mV and that of the n-material is about -90 mV.

In the high-current image (b) the Peltier cooling signal is much lower compared to the heat dissipation signal as discussed already in Sect. 5.4. Here it just diminishes the amount of local heating at the positions of the contact holes. Also this example shows how lock-in thermography may help to identify different physical mechanisms in dependence on the operation conditions of solar modules. Especially, it shows that the knowledge about possible Peltier signals and the correct way to identify them (by displaying the phase image or a single-phase signal instead of the amplitude signal; if possible by reversing the polarity) is necessary for avoiding misinterpretation of lock-in thermography results.

6.4 CDI/ILM on Solar Materials

6.4.1 Analysis of Material Evolution During Processing

Images of the excess carrier lifetime of multicrystalline wafers are the most important application of CDI/ILM. The properties of solar material undergo an evolution between the as-grown state after crystallisation and the state in the final processed solar cell. For the investigation and understanding of how final material properties can be optimised, imaging of excess carrier lifetime has evolved as a very useful tool. Decisive improvements compared to the previously available microwave photoconductivity decay (MW-PCD) point-by-point mapping equipment are not only given by the speed (seconds to minutes versus hours for comparable high resolution), but also by principal advantages: Although CDI/ILM measures in the steady state, MW-PCD evaluates a transient, which always reflects the differential lifetime, if recombination processes are dependent on excess carrier density [176]. Time constants are extracted from the transients in MW-PCD measurements in a fixed time window, which is determined beforehand as best compromise for high- and low-lifetime regions. Adaptation of the window during a measurement would lead to unacceptable long measurement times. This restriction always limits the dynamics in lifetime maps for MW-PCD, it does not occur for a CDI/ILM measurement.

Another advantage is the possibility to zoom into an image thereby increasing spatial resolution. From a study aiming to extent the usable part of an ingot [177] enlarged images performed with a spatial resolution of 50 μm are compared in Fig. 6.22. In this example, a transition region in a multicrystalline block is analysed: At the lower height (2.2 cm above the block bottom), only narrow regions around grain boundaries are depleted from recombination active impurities by segregation into precipitates at the grain boundaries. Somewhat higher in the block (3.5 cm) overall impurity concentrations are reduced, the gettering effect of a phosphorus diffusion (e.g. in a solar cell process) is now sufficient to raise carrier lifetimes in large grains to values around 100 μs (upper left image).

6.4.2 Temperature-dependent measurements

With CDI/ILM in emission mode, the temperature dependence of the local carrier lifetime above room temperature is easily accessible. An example of a measurement on an aluminium-doped Cz-wafer, where an Al-complex is known to limit the lifetime, was reported at the EU-PVSEC in Paris 2004 by Pohl et al. (Fig. 6.23, [56]). For the Al-related defect, a defect level of 0.44 eV above the valence band had been reported [178]. With this deep energy level, the results from an ILM/CDI measurement and the calculations shown in Fig. 6.24 are well consistent.

Schubert et al. [179] reported temperature-dependent carrier lifetime images at the same conference in parallel to the results given in Fig. 6.23. To achieve a precise

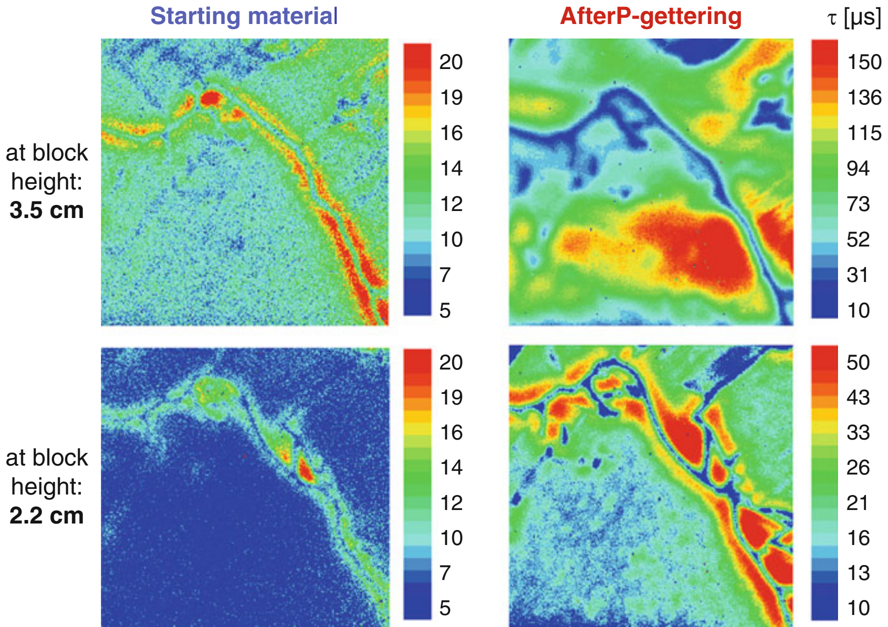

Fig. 6.22 CDI/ILM lifetime images ($13 \times 13\,\mathrm{mm}^2$ segments, scale in μs) with high resolution taken on samples from different height in a multicrystalline block, as grown and after phosphorus diffusion (courtesy of S. Riepe, private communication)

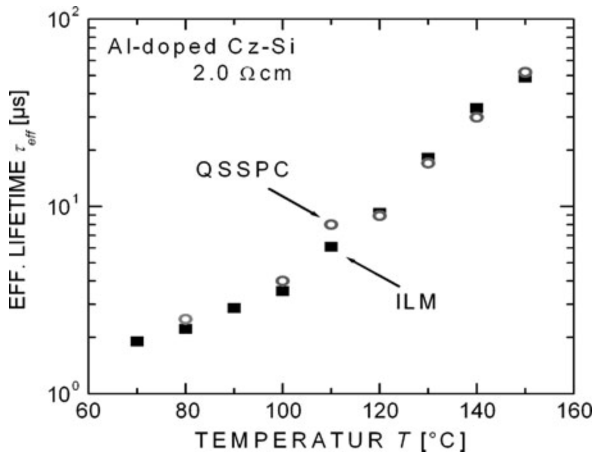

Fig. 6.23 Temperature dependent carrier lifetime measurement in emission mode (labelled ILM), compared to a measurement with the temperature dependent Quasi-Steady State Photoconductance technique (QSSPC) (from [56], courtesy of P. Pohl)

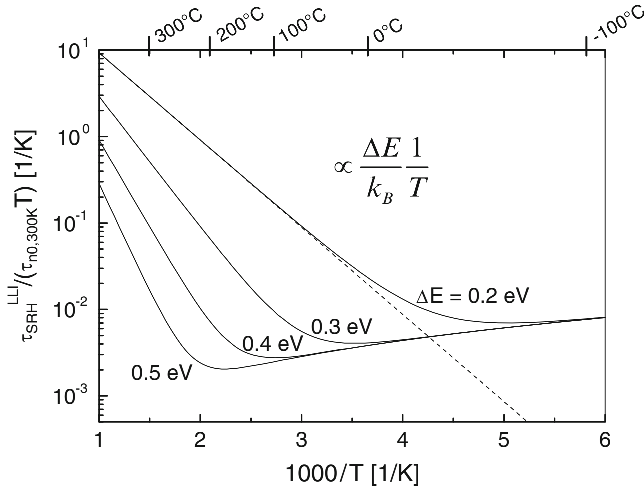

Fig. 6.24 Temperature dependent carrier lifetime calculated according to the SRH recombination mechanism for different defects with energy level distance ΔE from the conduction band edge (Fig. 6.24 to Fig. 6.28 from [179], courtesy of M. Schubert)

control of the wafer temperature, a setup had been developed, where samples can be heated to temperatures between 25 °C and 270 °C. The possibility of temperature control up to high temperature enables lifetime spectroscopy in a way similar to Temperature Dependent Lifetime Spectroscopy (TDLS) [180], but contrary to this technique with high spatial resolution. In PV-grade silicon Shockley-Read-Hall (SRH) recombination is mostly the dominating recombination process and determines the lifetime in the bulk material. If recombination over one defect level is assumed, the measurement of the lifetime dependence on temperature allows the determination of the energy difference between defect level and band edge (valence or conduction band). This is the basic idea of TDLS, where the MW-PCD technique is used to measure lifetimes. Disadvantages of that method are a lack of spatial resolution and the restricted sample size.

We assume that the carrier lifetime is dominated by defect recombination following the Shockley-Read-Hall description of recombination statistics. If the logarithmic quotient of measured lifetime in low injection (LLI) $\tau_{\mathrm{SRH}}^{\mathrm{LLI}}$ and $\tau_{\mathrm{n0,300K}}$ (the low injection lifetime of electrons at 300 K) times temperature is plotted against the inverse of temperature, a linear dependence for high temperatures is expected (see Fig. 6.24). The gradient in this temperature region depends directly on the energy level of the defect.

In [179], the application of CDI/ILM to determine an image of the distribution of the energy level of the defect dominating the recombination was introduced and named Thermal Defect Imaging TDI. TDI overcomes the restriction in sample size of TDLS and allows a spatially resolved determination of defect levels. The technique combines the TDLS technique and Emission CDI/ILM at different temperatures.

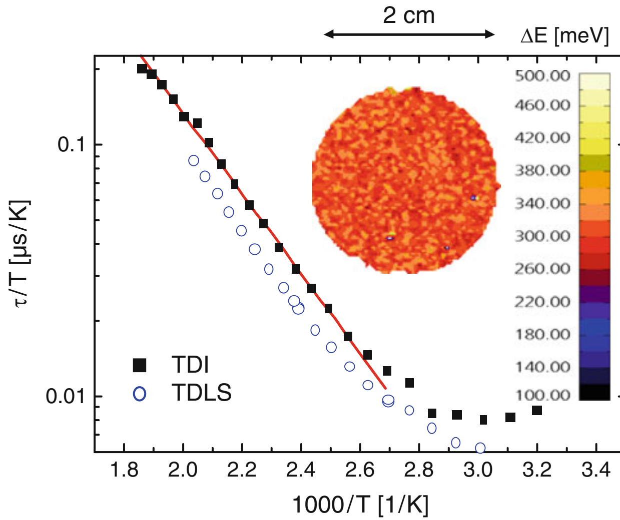

Fig. 6.25 TDI measurement on a Mo-contaminated sample (black squares) and TDLS measurement (open circles)

A TDI measurement on an FZ-silicon sample intentionally contaminated with Molybdenum was performed in [179] to compare the results with TDLS measurements and to prove the functionality of TDI. Figure 6.25 shows Emission CDI/ILM measurements for a temperature range from 30 °C to 270 °C. For a comparison with TDLS measurements, the mean value of carrier density over the sample is displayed. From the gradient of the linear region of the TDI measurement, the difference ΔE between band edge and defect level can be calculated to $\Delta E_{\mathrm{TDI}} = 316\,\mathrm{meV}$, which corresponds well with $\Delta E_{\mathrm{TDLS}} = 330\,\mathrm{meV}$ for the TDLS measurement. This calculation has been performed for each camera pixel, resulting in a calculated defect level for each wafer position (insert in Fig. 6.25). High homogeneity over the wafer for this example provides a good comparability between both measurement techniques.

Also, in [179], the application to multicrystalline silicon was demonstrated. Figure 6.26 shows an Emission-CDI/ILM measurement of a $100 \times 100\,\mathrm{mm}^2$ multicrystalline silicon wafer. The wafer had been vertically cut from a block-cast silicon ingot. The top region of the ingot (top of the image) shows very low lifetimes, whereas in the lower part high lifetime grains can be seen. On the right-hand side, the influence of the crucible reduces lifetime. Three different regions have been selected for closer examination (arrows in Fig. 6.26): A region with high crystal lattice distortion (1), a region with fair lifetime (2), and a low-lifetime region at the right side (3). The respective temperature dependence of lifetime is shown in Fig. 6.27. A linear region between 59 °C and 139 °C can be determined for all areas whereby the gradient differs for the three positions. The temperature dependence for high lifetimes deviates from the SRH theory for a single defect level.

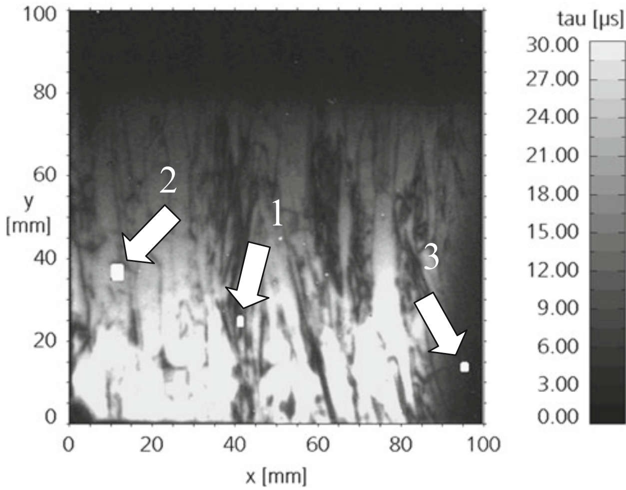

Fig. 6.26 Lifetime measurement of an industrial mc-sample

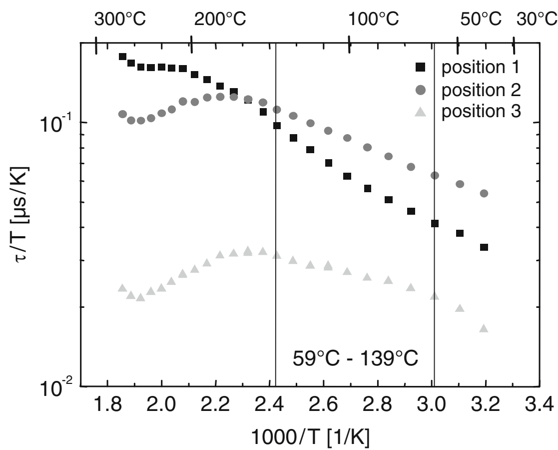

Fig. 6.27 Temperature dependence of lifetime for three selected positions on the wafer of Fig. 6.26

The observed linear region was used to determine a gradient for each camera pixel. For the case of a single and discrete dominating defect level, the gradient should result in the energy difference ΔE between band edge and defect level. Figure 6.28 shows the calculated spatially resolved gradients that are a measure for an "effective" energy level, which may represent a more complex distribution of defect levels. The defect levels detected at grain boundaries are shallower than within the grains. Although the lifetime gradient from the bottom to the top of the image is significant, the defect level distribution does not show a clear correlation with lifetime level. At $y > 80\,\text{mm}$ in Fig. 6.28, the detection limit had been reached

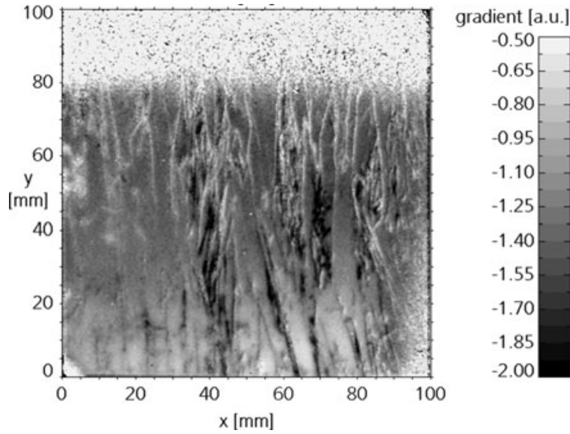

Fig. 6.28 Image of the gradient of TDI analysis of the sample of Fig. 6.26

resulting in a vanishing gradient. How to extract more defect-specific information from TDI measurements is still an open question.

6.4.3 Trap density images from CDI/ILM

Free excess minority carriers can be trapped in shallow trap levels or levels with asymmetric capture cross-sections for holes and electrons [181, 182]. Charge neutrality requires that the trapped minority carriers are compensated by additional majority carriers in steady-state condition. Lifetime measurements, such as CDI/ILM, are based on the assumption that the excess majority carrier density equals the excess minority carrier density. This assumption does not hold anymore for low injection if trapping occurs. Because CDI/ILM detects the absorption and emission of both, majority and minority carriers, the carriers trapped in a fixed amount of trapping states dominate the signal more and more with decreasing free excess minority carrier density. CDI/ILM then measures a higher apparent lifetime than the actual recombination lifetime in low level injection. This effect appears for all methods which determine the excess conductivity to extract the excess carrier density. An anomalous increase in the apparent excess carrier lifetime under low injection conditions has thus been reported in many publications and generally assumed to be caused by trapping of minority carriers [183, 184], a concept which is supported by both injection- and temperature-dependent measurements [185, 186]. In 1953, Fan [181] and in 1955 Hornbeck and Haynes [182] independently developed a theoretical model to describe this trapping of minority carriers. The injection dependence of the apparent lifetime τ_{app} following the Hornbeck-Haynes model for p-type silicon is [187]:

$$\tau_{\text{app}}(\Delta n) = \frac{1}{\alpha_{\text{n}} + \alpha_{\text{p}}} \tau_{\text{rec}} \left[\alpha_{\text{n}} + \alpha_{\text{p}} \left(1 + \frac{n_{\text{T}}(\Delta n)}{\Delta n} \right) \right] \tag{6.10}$$

with α_n and α_p being the free carrier absorption coefficients for electrons, respectively, holes. The recombination lifetime is denoted here as τ_{rec} to distinguish it from the apparent lifetime $\tau_{app} \cdot \tau_{rec}$ is assumed to be injection independent in low injection. n_T is the density of trapped minority carriers, which depends on the trap density N_T and the trap escape ratio r_{esc} [183]:

$$n_{\text{T}} = \frac{N_{\text{T}} \Delta n}{\Delta n + N_{\text{T}} r_{\text{esc}}} \tag{6.11}$$

Although trap images are mostly seen as an artefact in a lifetime measurement, these can be used as a valuable source for additional information on the material properties. By fitting the above model to a low injection CDI-measurement at each point of a wafer, a trap density image can be deduced [187,188]. A qualitative image of the trap density can be obtained readily by a single CDI/ILM measurement at very low injection [189].

Trap densities had been reported to correlate with dislocation densities [187]. A more detailed study revealed that the correlation between trap and dislocation density varies over the height of a multicrystalline block [190]. Figure 6.29 gives an example from a wafer close to the bottom of an ingot. The trap density image (Fig. 6.29(a)) is compared with the reflection image of a neighbouring polished and Secco-etched wafer, where structural defects as dislocations are visible as clouds

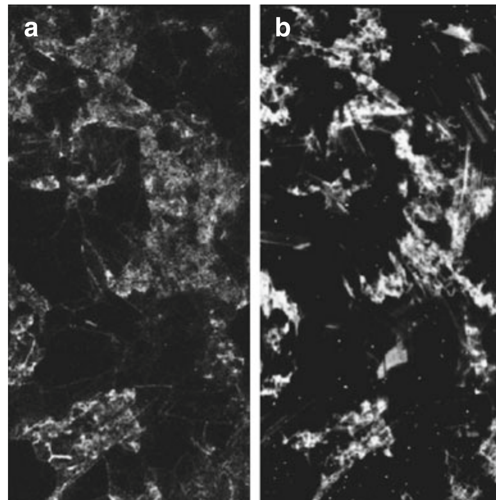

Fig. 6.29 (**a**) Qualitative trap density of a wafer from the bottom of an ingot. High trap densities are bright. (**b**) Qualitative structural crystal defect density of the same area that is depicted in (**a**). High structural crystal defect densities are bright. The image shows a high positive correlation with the trap density

of etch pits (Fig. 6.29(b)). The structural crystal defect density and the trap density show a high positive correlation, which is in good agreement with [183, 186, 187]. In contrast, in a wafer of the top region (Fig. 6.30), there is a positive correlation in some areas, but there are also regions with high structural crystal defect densities and simultaneously low trap densities. Please note that because the trap density of the wafer from the bottom is about one order of magnitude higher than the trap density of the wafer from the top, Figs. 6.29 and 6.30 have different grey scales.

The understanding of trapping effects was put forward by experiments on different material types with variable oxygen concentration, which revealed a clear relation between trap density and oxygen concentration [190]. It was concluded that the origin of increased trap densities in multicrystalline silicon could be structural crystal defects, which are highly decorated with oxygen precipitates. It was further inferred from the experiments on intentionally metal contaminated wafers that the segregation of metallic impurities towards the top of the ingot and the accumulation at structural crystal defects suppresses trapping and explains, e.g., the existence of areas with high structural crystal defect densities and low trap densities in the sample of Fig. 6.30.

Highly dislocated areas are often the critical zones in a multicrystalline material, which do not respond to getting in the solar cell process and form low lifetime areas in the final cell. It is thus an interesting option to use the easily accessible trap images as indication for such problematic areas in a starting wafer. In a study of the trap density across a multicrystalline ingot, it was found that the trap density itself and its correlation to the diffusion length is decreasing from the bottom to the

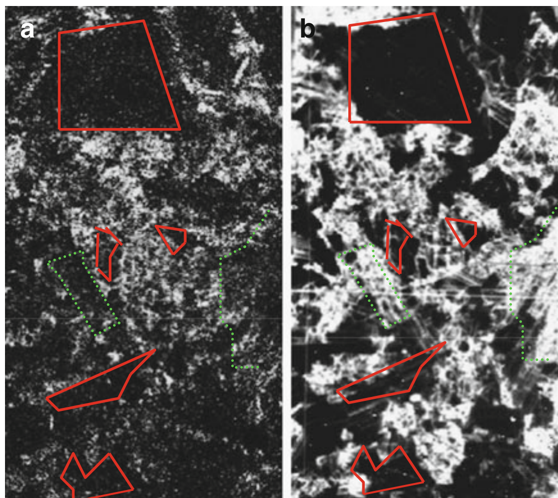

Fig. 6.30 (**a**) Qualitative trap density of a wafer from the top of an ingot. High trap densities are bright. (**b**) Qualitative structural crystal defect density of the same area that is depicted in (**a**). High structural crystal defect densities are bright. In some areas (i.e. the solid marked areas) there is a positive correlation between trap density and structural crystal defect density, but there are also areas with high structural crystal defects densities and low trap densities (i.e. dashed marked areas)

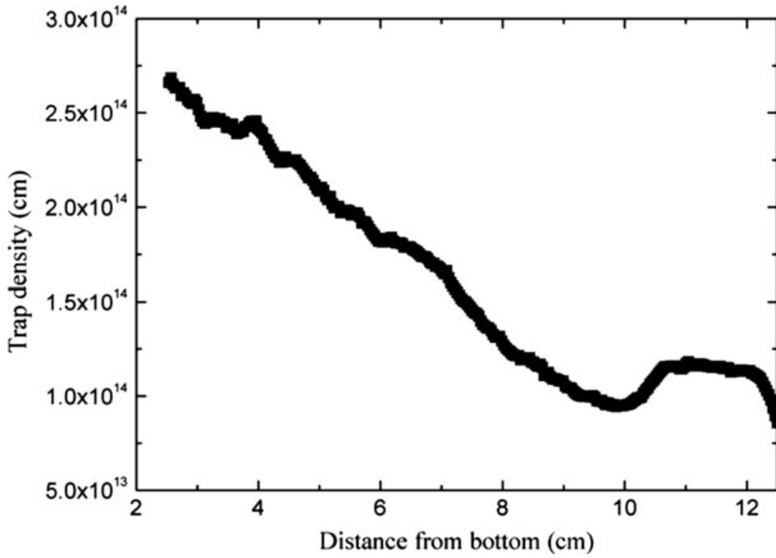

Fig. 6.31 Trap density against height. The trap density is decreasing with increasing distance from the bottom except for the topmost region

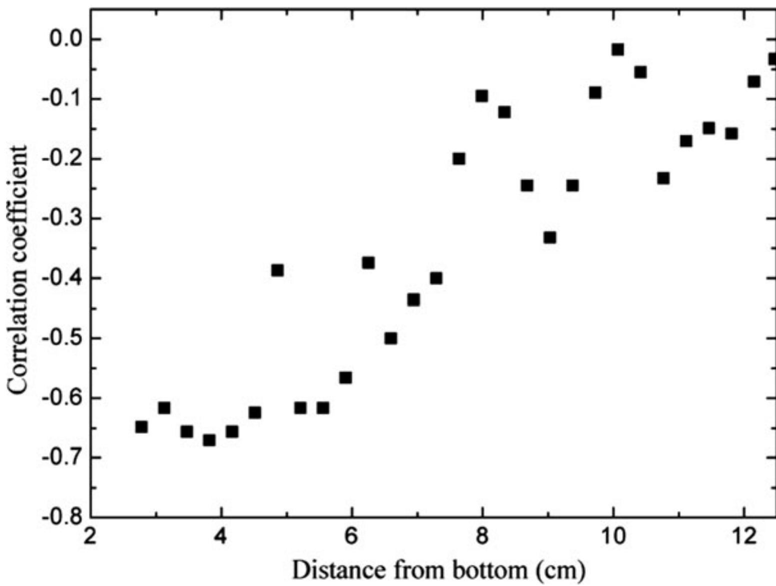

Fig. 6.32 Correlation coefficient between trap density in the as-cut wafer and diffusion length in the processed solar cell. The correlation is quite high in the bottom region and decreases with height

top of the ingot [190]. The trap density measured on a vertically cut wafer from the bottom region of a directionally solidified multicrystalline ingot was compared with the image of the reciprocal lifetime of the solar cell processed on a neighbouring wafer calculated from an SR-LBIC [191] measurement on the finished solar cell. Figure 6.31 reveals a clear decrease in average trap density with height above the bottom. In parallel, the spatial correlation between trap density in the as-cut wafer and diffusion length in the processed solar cell becomes less pronounced (Fig. 6.32). Thus, concentrations of traps on a high level of trap density observed in starting material can be taken as an indication that in these areas high dislocation densities exist, which are in turn likely to lead to low diffusion length areas in the final solar cell.

Chapter 7
Summary and Outlook

In this book, the technique of lock-in thermography is being reviewed with special emphasis on its application to the characterization and functional testing of electronic components. The investigation of shunting phenomena in solar cells, which our lock-in thermography originally was developed for, among a lot of other applications is presented to demonstrate and discuss all the different possibilities of this rather new technique. We hope to have shown that the use of lock-in thermography instead of conventional (steady-state) thermography is a qualitatively new thermographic approach to electronic device testing and failure analysis. It not only improves the sensitivity tremendously by up to 3 orders of magnitude, but it also considerably improves the effective spatial resolution of the investigations by suppressing lateral heat conduction. Besides, it opens new ways of correcting the IR emissivity of the investigated surface and it enables new efficient methods for wafer analysis. Since the objects investigated usually are in a quasi-adiabatic state, the results of lock-in thermography are not influenced by heat conduction to the surrounding and therefore can more easily be evaluated quantitatively. With these properties and with the further development of reasonably priced thermocameras, lock-in thermography is continuing to become a widely used technique in electronic device testing in future. This book was intended to contribute to this development and to generally encourage a wider application of lock-in thermography. The considerably extended second edition presented here already implements many new applications of lock-in thermography which have been developed also under the influence of the first edition of this book.

Within this book, we describe the basic principles of IR thermography itself and briefly discuss different lock-in thermography realizations. Different variants of the digital signal correlation are introduced and discussed. A noise analysis of lock-in thermography is performed, connecting the noise properties of the IR camera to the resulting amplitude noise of the lock-in image. A simple test structure for performing scaling measurements is proposed. With the "pixel-related noise density" we propose a universal figure of merit, which allows one to compare the noise properties of different lock-in thermography systems with each other, including serially scanning ones. The heat dissipation and transport mechanisms in solar cells are described in some detail, since they are the base of several newly introduced lock-in thermography techniques. Also the physical basis of new IR camera-based lifetime imaging

techniques is introduced, which rely on non-thermal effects. Practical aspects of realizing lock-in thermography systems are being discussed with special emphasis on reaching the highest possible detection sensitivity. After comparing the most important thermography and lock-in thermography approaches from the literature, an overview is given about the presently available commercial lock-in thermography systems. Different possibilities for providing a homogeneous illumination of the sample are reviewed, which are necessary for realizing the newly developed techniques of illuminated lock-in thermography of solar cells and lifetime imaging of solar materials. Also the application of solid immersion lenses is described, which allow to overcome the diffraction limit of the spatial resolution by up to a factor of 4. This is especially important for failure analysis of integrated circuits, where the limited spatial resolution of IR microscopy always has been an obstacle for its application. In the theory chapter, first, some general questions as to the influence of the heat conduction to the surrounding are discussed, leading to the definition of quasi-adiabatic measurement conditions as a presupposition for a straightforward quantitative interpretation of lock-in thermography results. Then, a novel simple technique of compensating the influence of a temperature drift on lock-in thermography results is introduced, which should be interesting also in the field of non-destructive testing. The theory of the propagation of thermal waves is reviewed for different heat source geometries, showing that the spatial resolution attained also depends on the heat source geometry and on the mode of presenting the results. Different approaches of the quantitative interpretation of lock-in thermograms are described, including new techniques of solving the inverse problem by the two-dimensional numerical deconvolution of lock-in thermograms. A comprehensive discussion of the optimum measurement strategies should be helpful for the operator to find the optimum measurement conditions, parameters, and display options for different demands. Especially for microscopic investigations, the newly proposed display of the results as the "emissivity-corrected 0° image" ($0°/-90°$ image) is most advantageous. This display option provides inherent emissivity correction but, contrary to the well-known phase image, it at least approximately preserves the additivity of signals of different heat sources. Therefore, these images may even numerically be deconvoluted to correct the image for the lateral heat spreading. Moreover, techniques of measuring local I-V characteristics thermally (LIVT) and distinguishing Peltier heating from Joule type heating are described. The potentialities of lock-in thermography for solving analytical problems in semiconductor technology are demonstrated by introducing several typical applications selected from different technical and scientific fields.

There are a number of recent developments in lock-in thermography, which have not been considered in this book. Thus, the technique of "pulsed phase thermography" was developed for non-destructive testing [192], which is a combination of pulse thermography [3] and lock-in thermography. In this technique, a number of short heat generation pulses are applied periodically, and each pixel signal is evaluated by performing a Fourier transform. The result is a number of amplitude and phase images taken at different frequencies, which, physically, are equivalent to the results of a number of lock-in measurements at different frequencies. For

each of these frequencies, the signal-to-noise ratio is below that of ordinary lock-in thermography, therefore this technique has not been considered here. If instead of a Fourier transform a wavelet transform is used to evaluate a pulsed thermography experiment, this technique is called wavelet pulsed phase thermography [193]. Here, contrary to the Fourier evaluation, the time delay information of the thermal relaxation is explicitly preserved, which is especially useful for retrieving any depth information. Nonetheless, contrary to pure pulse thermography, the phase information is still present, which makes the results independent from the IR emissivity of the surface. Since in electronic device testing, the heat sources are usually near the surface, and since also wavelet pulsed phase thermography is less sensitive than lock-in thermography, this technique has also not been considered here.

Fortunately, the further technical development of thermocameras towards a higher sensitivity and frame rate, and lower prices is going on. It was already mentioned in Sect. 2.1 that the omission of the wavelength range of 5–8 μm, which is common for standard thermocameras in order to get rid of the atmospheric absorption in this wavelength range, is not necessary for low-distance lock-in thermography investigations. Maybe, in future also this wavelength range can be used by IR cameras, providing an improved signal-to-noise ratio in lock-in thermography. The influence of the frame rate on the sensitivity had been discussed in Sect. 2.6, allowing the conclusion to be drawn that further increasing the frame rate might further significantly improve the sensitivity. When the second edition of this book was written (2009), the pixel transfer rate of 40 MHz of the TDL 640 SM 'Lock-in' system was regarded to be standard. Todays "high speed" cameras have a transfer rate of about 80 MHz [11], but can be hoped that future IR cameras will have even higher rates. CCD cameras in the visible range are already offered with pixel transfer rates above 126 MHz [194]. Since the trend to further increase the processing speed of PCs can be expected to continue, it should be no problem to process also these data rates in low-cost PCs on-line. The big challenge is to make these high-speed IR cameras attainable at a reasonable price. However, in many cases, it is not necessary to have the ultimate detection sensitivity, for instance, if hot spots in solar cells have to be imaged under reverse bias in an in-line process monitoring in an industrial environment. Then also low-priced thermocameras with a standard frame rate of 50–60 Hz can be used in a lock-in thermography set-up. It can be expected that also such low-priced lock-in thermography systems will become popular in future, since they also allow one to utilize most of the advantages of lock-in thermography. While already in the last few years a number of completely new applications of lock-in thermography like CDI/ILM and ILIT have appeared, it can be hoped that this technique will find even new applications in future. For example, lock-in thermography has also been used for imaging the net doping concentration in solar cells [195].

In recent years, a new technology for imaging defects in solar cells has been established, which is electroluminescence (EL) imaging of solar cells [196] and photoluminescence (PL) imaging of solar cells and wafers [197]. Both EL and PL imaging are based on the exponential dependence of the luminescence intensity on the local "internal voltage," i.e., the local separation of the quasi Fermi levels of

electrons and holes under excitation. These methods allow to image recombination-active crystal defects and sufficiently strong shunts, as well as cracks, breakage, and other faults in solar cells and modules [173, 174]. Also luminescence techniques for imaging the local series resistance and the local saturation current density have been developed [163, 164]. EL imaging has been found to be also very advantageous for investigating junction breakdown phenomena in solar cells, which also lead to light emission [153, 167]. The advantages of luminescence methods, compared to lock-in thermography, are their lower necessary acquisition time (except for reverse-bias EL, which needs more time than reverse-bias DLIT) and their better spatial resolution, since they do not suffer from the inevitable lateral heat spreading of all thermal methods. The advantage of lock-in thermography (especially DLIT) compared to luminescence methods is that only DLIT allows to measure any leakage current really quantitatively, see Sect. 4.5. Moreover, leakage currents based on depletion region recombination (nonlinear shunts, being responsible for J_{02}, see Sect. 2.8) are generally not observable by luminescence methods, since they do not significantly influence the internal voltage in the bulk. The reason is that this current flows as a majority carrier current through the base. However, nonlinear shunts may strongly influence the low light level performance of solar cells, especially their fill factor. EL imaging under reverse bias only may image junction breakdown sites but not ohmic shunts, which are actually the most dangerous ones. Therefore, we are convinced that even if the popularity of luminescence imaging methods still will increase, thermal methods will never become obsolete. Already now the most successful solar cell research groups have both methods at choice.

Finally, the authors want to express their gratitude to all colleagues and friends who helped to accomplish the work with all the results presented here. This work was supported by the SolarFocus project (BMU project No. 0327650 D) and its foregoing projects, and by the department of U. Gösele at the Max Planck Institute of Microstructure Physics. The authors want to express their thanks to the members of these projects for fruitful discussions and providing samples for respective investigations. The cooperation with our former and present coworkers I. Konovalov, St. Huth, J.P. Rakotoniaina, M.H. Al Rifai, S. Neve, J. Bauer, and H. Straube, who has significantly contributed to the work on Peltier effects, all at MPI (Halle), and J. Isenberg, M. Schubert, S. Riepe, M. Kasemann and P. Gundel at Fraunhofer ISE (Freiburg) is gratefully acknowledged. Most of the IC failure analysis work was performed by F. Altmann, T. Riedinger, Ch. Große, and Ch. Schmidt of Fraunhofer Institute of Mechanics of Materials (IWMH, Halle). Many thanks to J.-M. Wagner (MPI Halle) and K. Ramspeck (ISFH Hameln) for carefully reading parts of the manuscript and to G. Busse (IKP Stuttgart) for pointing to older references. Samples for the investigations presented here have been kindly provided by S. Seren (Univ. Konstanz), L. Carnel (REC ScanWafer AS, Porsgrunn), Photowatt (Bourgoin-Jallieu), F. Altmann (Fraunhofer Institute of Material Mechanics, Halle), I. Gavilanes Pèrez (Hahn Meitner Institute, Berlin), and by CSG Solar (Thalheim). Many thanks to W. Eberhardt (MPI Halle) and the electronic workshop of MPI Halle for designing and manufacturing electronic equipment, and to K. Iwig from MSC Technik GmbH (Halle) [198] for writing the DECONV software. The fruitful

and ongoing cooperation with Thermosensorik GmbH (Erlangen) in constructing and further developing the TDL ‘Lock-in’ thermography systems is gratefully acknowledged. Many thanks also to InfraTec (Dresden) for their permission to use construction details of their sample holder. This work would not have been possible without the constructive and cooperative atmosphere in the department of U. Gösele (†2009) at the Max Planck Institute of Microstructure Physics (Halle) as well as at the Fraunhofer Institute for Solar Energy Systems (Freiburg).

References

1. J.L. Miller: *Principles of Infrared Technology: A Practical Guide to the State of the Art.* (John Wiley Sons, New York NY 2001)
2. X.P.V. Maldague: *Theory and Practice of Infrared Technology for Nondestructive Testing.* (Wiley, New York 2001)
3. J.M. Milne, W.N. Reynolds: 'The Non-Destructive Evaluation of Composites and Other Materials by Thermal Pulse Video Thermography'. SPIE **520**, 119 (1984)
4. P.K. Kuo, T. Ahmed, Huijia Jin, R.L. Thomas: 'Phase-Locked Image Acquisition in Thermography'. SPIE **1004**, 41, (1988)
5. S.K. Lau, D.P. Almond, J.M. Milne: 'A Quantitative Analysis of Pulsed Video Thermography'. NDT&E International, **24** (4), 195, (1991)
6. www.thermalwave.com
7. N. Harwood, W.M. Cummings: *Thermoelastic Stress Analysis*, (Adam Hilger, Bristol, Philadelphia and New York) IOP, Bristol 1991
8. M. Danner, K. Bücher: 'Reverse Characteristics of Commercial Silicon Solar Cells – Impact on Hot Spot Temperatures and Module Integrity'. In: *26th IEEE Photovoltaic Specialists' Conference*, Anaheim, CA, USA, September 29–October 04, 1997, (IEEE 1997) pp. 1137–1140
9. W. Gross, H. Scheuerpflug, T. Hierl, M. Schulz, F. Karg: 'Defect Localization in $CuInSe_2$ Thin Film Solar Modules by Thermal Infrared Microscopy'. In: *2nd World Conference on Photovoltaic Solar Energy Conversion*, Vienna, Austria, July 6–July 10, 1998, ed. by J. Schmidt, H. A. Ossenbrink, P. Helm, H. Ehmann, E. D. Dunlop (Arte Stampa, Daverio (VA) 1998) pp. 522–524
10. C. Canali, F. Chiussi, G. Donzelli, F. Magistrali, E. Zanoni: 'Correlation Between Thermal Resistance, Channel Temperature, Infrared Thermal Maps and Failure Mechanisms in Low Power MESFET Devices'. Microelectron. Reliab., **29** (2), 117, (1989)
11. www.aim-ir.de
12. M. Bail, J. Kentsch, R. Brendel, M. Schulz: 'Lifetime Mapping of Si Wafers by an Infrared Camera'. In: *28th IEEE Photovoltaic Specialists Conference*, Anchorage (2000), p. 99
13. S. Riepe, J. Isenberg, C. Ballif, S.W. Glunz, W. Warta, 'Carrier Density and Lifetime Imaging of Silicon Wafers by Infrared Lock-in Thermography'. In *17th Eur. Photovoltaic Solar Energy Conference*, Munich, Germany, October 22–October 26, 2001, ed. by B. McNelis, W. Palz, H. A. Ossenbrink, P. Helm, (ETA Florence 2002) pp. 1597–1599
14. M. Kaes, S. Seren, T. Pernau, G. Hahn: 'Light-Modulated Lock-in Thermography for Photosensitive pn-Structures and Solar Cells'. Prog. Photovolt: Res. Appl. **12**, 355 (2004)
15. J. Isenberg, W. Warta: 'Realistic Evaluation of Power Losses in Solar Cells by Using Thermographic Methods'. Journal of Applied Physics **95**, 5200 (2004)
16. O. Breitenstein, J.P. Rakotoniaina, G. Hahn, M. Kaes, T. Pernau, S. Seren, W. Warta, J. Isenberg: 'Lock-in Thermography–A Universal Tool for Local Analysis of Solar Cells'. In: *20th European Photovoltaic Solar Energy Conference and Exhibition*, Barcelona (2005), 590–593
17. www.cedip-infrared.com

18. www.stressphotonics.com
19. www.thermosensorik.com
20. sales.hamamatsu.com
21. www.flir.com
22. www.AutomationTechnology.de
23. www.edevis.de
24. www.aescusoft.de
25. www.infratec.de
26. www.fainstruments.com
27. www.ircam.de
28. www.movitherm.com
29. J.C. Krapez: 'Compared Performance Algorithms Used for Modulation Thermography'. In: *Quantitative Infrared Thermography 4 (QIRT'98)*, Lodz, Poland, September 7–September 10, 1998, ed. by D. Balageas, G. Busse, C. M. Carlomagno, (Lodart S.A. Lodz 1999) pp. 148–153
30. A. Kaminski, J. Jouglar, M. Mergui, Y. Jourlin, A. Bouille, P.L. Vuillermoz, A. Laugier: 'Infrared Characterization of Hot Spots in Solar Cells with High Precision Due to Signal Treatment Processing'. Solar Energy Mat. & Solar Cells **51**, 233 (1998)
31. W.H. Press, S.A. Teukolsky, W.T. Vetterling, B.P. Flannery: *Numerical Recipes in C*, 2nd edn. (Cambridge University Press 1992)
32. I.N. Bronshtein, K.A. Semendyayev: *Handbook of Mathematics*, 3rd edn. (Springer, Berlin 1998)
33. J.C. Krapez, D. Pacou, G. Gardette: 'Lock-in Thermography and Fatigue Limit of Metals'. In: *Quantitative Infrared Thermography 5 (QIRT 2000)*, July 2000, Reims, France, pp. 277–282
34. S. Grauby, B.C. Forget: 'High Resolution Photothermal Imaging of High Frequency Phenomena Using a Visible Charge Coupled Device Camera Associated with a Multichannel Lock-in Scheme'. Rev. Sci. Instrum. **70**, 3603 (1999)
35. A. Altes, K. Mutamba, R. Heiderhoff, H.L. Hartnagel, L.J. Balk: 'Scanning Near Field Thermal Microscopy on a Micromachined Thin Membrane'. Superlattices and Microstructures **35**, 465 (2004)
36. M. Kasemann, W. Kwapil, B. Walter, J. Giesecke, B. Michl, M. The, J.-M. Wagner, J. Bauer, A. Schütt, J. Carstensen, H. Kampwerth, P. Gundel, M.C. Schubert, R.A. Bardos, H. Föll, H. Nage, P. Würfe, T. Trupke, O. Breitenstein, W. Warta, S.W. Glunz: 'Progress in Silicon Solar Cell Characterization with Infrared Imaging Methods'. In: *23rd European Photovoltaic Solar Energy Conference*, Valencia, Spain, 2008, p. 965
37. C.S. Welch, M.J. Zickel: 'Thermal Coating Characterization Using Thermoelasticity', Review of Progress in Quantitative Nondestructive Evaluation **12**, ed. by D.O. Thompson, D.E. Chimenti, (Plenum, NY 1993) pp. 1923–1930
38. M.J. Zickel, C.S. Welch: 'Thermal Coating Characterization Using Thermoelasticity, II', Review of Progress in Quantitative Nondestructive Evaluation **13**, ed. by D.O. Thompson, D.E. Chimenti (Plenum, NY 1994) pp. 1849–1855
39. O. Breitenstein, J.P. Rakotoniaina, M.H. Al Rifai, M. Gradhand, F. Altmann, T. Riediger: 'New Developments in IR Lock-in IR Thermography'. In: *30th Int. Symposium for Testing and Failure Analysis (ISTFA 2004)*, Worchester (MA) November 14–November 18, pp. 595–599
40. K. Ramspeck, S. Reissenweber, J. Schmidt, K. Bothe, R. Brendel: 'Dynamic Carrier Lifetime Imaging of Silicon Wafers Using an Infrared-Camera-Based Approach'. Appl. Phys. Lett. **93**, 102104 (2008); DOI: 10.1063/1.2972122
41. P. Kolodner, J.A. Tyson: 'Microscopic Fluorescent Imaging of Surface Temperature Profiles with 0.01 °C Resolution'. Appl. Phys. Lett. **40**, 782 (1982)
42. O. Breitenstein, J.P. Rakotoniaina: 'Electrothermal Simulation of a Defect in a Solar Cell'. J. Appl. Phys. **97**, 074905 (2005)
43. C.-T. Sah: *Fundamentals of Solid-State Electronics* (World Scientific, Singapore, 1991)
44. G.S. Nolas, J. Sharp, H.J. Goldsmid: *Thermoelectrics – Basic Principles and New Materials Developments*. (Springer, Berlin/Heidelberg/New York 2001)

45. S.M. Sze: *Physics of Semiconductor Devices*, 2nd Edition (Wiley, New York 1981)
46. D.K. Schroder, R.N. Thomas, J.C. Swartz: 'Free Carrier Absorption in Silicon'. IEEE Trans. Electron Dev. **ED-25**, 254–261 (1978)
47. J. Waldmeyer: 'A Contactless Method for Determination of Carrier Lifetime, Surface Recombination Velocity and Diffusion Constant in Semiconductors'. J. Appl. Phys. **63**, 1977 (1988)
48. J. Linnros: 'Carrier Lifetime Measurements Using Free Carrier Absorption Transients. I. Principle and Injection Dependence'. J. Appl. Phys. **84**, 275 (1998)
49. J. Linnros: 'Carrier Lifetime Measurements Using Free Carrier Absorption Transients. II. Lifetime Mapping and Effects of Surface Recombination'. J. Appl. Phys. **84**, 284 (1998)
50. F. Sanii, R.J. Schwartz, R.F. Pierret, W.M. Au: 'The Measurement of Bulk and Surface Recombination by Means of Modulated Free Carrier Absorption'. In: *20th IEEE Photovoltaic Specialists Conference*, Las Vegas (1988), p. 575
51. S.W. Glunz, W. Warta: 'High-Resolution Lifetime Mapping Using Modulated Free-Carrier Absorption'. J. Appl. Phys. **77**, 3243 (1995)
52. R.A. Smith: *Semiconductors*. (Cambridge University Press, New York 1961)
53. J. Isenberg, S. Riepe, S.W. Glunz, W. Warta: 'Imaging Method for Laterally Resolved Measurement of Minority Carrier Densities and Lifetimes: Measurement Principle and First Results'. Journal of Applied Physics **93**, 4268 (2003)
54. J.C. White, T.F. Unter, J.G.Smith: 'Observation of Carrier Densities in Silicon Devices by Infrared Emission'. Solid-State Electron Devices **1**, 139 (1977)
55. M.C. Schubert, J. Isenberg, W. Warta: 'Spatially Resolved Lifetime Imaging of Silicon Wafers by Measurement of Infrared Emission', J. Appl. Phys. **94**, 4139 (2003)
56. P. Pohl, R. Brendel: 'Temperature Dependent Infrared Camera Lifetime Mapping (ILM)', In: *19th European Photovoltaic Solar Energy Conference and Exhibition*, Paris (2004), p. 46
57. M.C. Schubert, J. Isenberg, S. Riepe, W. Warta: 'Thermographic Imaging of Free Carrier Density in Silicon'. QUIRT Journal **1**, 89 (2004)
58. C.C. Williams, H.K. Wickramasinghe: 'Scanning Thermal Profiler'. Appl. Phys. Lett. **49**, 1587 (1986)
59. A. Majumdar, J.P. Carrejo, J. Lai: 'Thermal Imaging Using the Atomic Force Microscope'. Appl. Phys. Lett. **62**, 2501 (1993)
60. R. Forster, E. Gmelin: 'Thermal Conductivity and Diffusivity Measurements in the sub-μm and sub-μs Scale on Centimeter Area Samples Using a Microthermocouple'. Rev. Sci. Instrum. **67**, 4246 (1996)
61. A. Hammiche, D.J. Hourston, H.M. Pollock, M. Reading, M. Song: 'Scanning Thermal Microscopy: Subsurface Imaging, Thermal Mapping of Polymer Blends, and Localized Calorimetry'. J. Vac. Sci. Technol. B **14**, 1486 (1996)
62. www.veeco.com
63. M. Palaniappan, G.B.M. Fliege, V. Ng, R. Heidenhoff, J.C.H. Phang, L.J. Balk: 'Correlation of electronic and Thermal Properties of Short Channel 'MOSFETs', Proc. of the 25th International Symposium for Testing and Failure Analysis (ISTFA), Santa Clara, CA (1999) pp. 465–470
64. E. Hendarto, A. Altes, R. Heiderhoff, J.C.H. Phang, L.J. Balk: 'Investigation on the Thermal Distribution of nMOSFETs Under different Operation Modes by Scanning Thermal Microscopy'. In: *43rd International Reliability Physics Symposium (IRPS)*, Piscataway NJ 2005, pp. 294–299. ISBN 0-7803-8803-8
65. www.anasysinstruments.com
66. I.W. Rangelow, T. Gotszalk, N. Abedinov, P. Gabriec, K. Edinger: 'Thermal Nano-Probe'. Microelectronic Engineering **57–58**, 737 (2001)
67. O. Breitenstein, W. Eberhardt, K. Iwig: 'Imaging the Local Forward Current Density of Solar Cells by Dynamical Precision Contact Thermography'. In: 1st World Conf. on Photovoltaic Energy Conversion, Waikaloa, Hawaii, December 5–December 9, 1994, ed. by D.J. Flood (IEEE 1995), pp. 1633–1636

68. O. Breitenstein, M. Langenkamp: 'Lock-in Contact Thermography Investigation of Lateral Electronic Inhomogeneities in Semiconductor Devices'. Sensors and Actuators A **71**, 46 (1998)
69. Y.S. Ju, O.W. Käding, Y.K. Leung, S.S. Wong, K.E. Goodson: 'Short-Timescale Thermal Mapping of Semiconductor Devices'. IEEE Electron Device Lett. **18**, 169 (1997)
70. P. Voigt, J. Hartmann, M. Reichling: 'Thermal Wave Imaging of Electrically Heated Microstructures'. J. Appl. Phys. **80**, 2013 (1996)
71. K.E. Goodson, M. Ashegi: 'Near-Field Optical Thermometry'. Microscale Thermophysical Engineering **1**, 225 (1997)
72. J. Opsal, A. Rosencwaig, D.L. Willerborg: 'Thermal-Wave Detection and Thin-Film Thickness Measurements with Laser Beam Deflection'. Applied Optics **22**, 3169 (1983)
73. J.C. Murphy, L.C. Aamodt: 'Optically Detected Photothermal Imaging'. Appl. Phys. Lett. **38**, 196 (1981)
74. I. Suemune, H. Yamamoto, M. Yamanishi: 'Noncontact Photoacoustic Measurements of Semiconductors with Michelson Interferometry'. J. Appl. Phys. **58**, 615 (1985)
75. www.acceleratedanalysis.com
76. C. Ballif, S. Peters, J. Isenberg, S. Riepe, D. Borchert: 'Shunt Imaging in Solar Cells using Low Cost Commercial Liquid Crystal Sheets'. Proc. of the 29th IEEE PVSEC, New Orleans 2002, p. 446
77. www.pasan.ch
78. O. Breitenstein, J.P. Rakotoniaina, F. Altmann, J. Schulz, G. Linse: 'Fault Localization and Functional Testing of ICs by Lock-in Thermography'. In: *28th International Symposium for Testing and Failure Analysis (ISTFA 2002)*, Phoenix 2002, pp. 29–36
79. J.B. Colvin: 'Moiré Stabilized Thermal Imaging'. In: *12th International Symposium on the Physical and Failure Analysis of Integrated Circuits (IPFA)*, Singapore 2005, pp. 163–166
80. www.optomet.com
81. K. Nikawa, S. Tozaki, Proc of the International Symposium for Testing and Failure Analysis (ISTFA), 1993, pp. 303–310
82. E.I. Cole, P. Tangyunyong, D.L. Barton: 'Backside Localization of Open and Shorted IC Interconnections'. Proc. of the International Reliability Physics Symposium (IRPS), Reno (1998), pp. 129–126
83. M. de la Bardonnie, R. Ross, K. Ly, F. Lorut, M. Lamy, C. Wyon, L.F.Tz. Kwakman, Y. Hiruma, J. Roux: 'The Effectiveness of OBIRCH Based Fault Isolation for Sub-90nm CMOS Technologies'. In: *31st Int. Sympos. for Testing and Failure Analysis (ISTFA)*, November 6–November 10, 2005, San Jose, CA, USA, p. 49
84. A.C.T. Quah, C.M. Chua, S.H. Tan, L.S. Koh, J.C.H. Phang, T.L. Tan, C.L. Gan: 'Laser-Induced Detection Sensitivity Enhancement with Laser Pulsing'. Electronic Device Failure Analysis **10**, 18 (2008)
85. O. Breitenstein, K. Iwig, I. Konovalov, D. Wu: 'Lock-in Contact Thermography on Solar Cells – Comparison with IR-Measurements'. In: *Quantitative Infrared Thermography 3 (QIRT'96)*, Stuttgart, Germany, September 2–September 5, 1996, ed. by D. Balageas, G. Busse, C.M. Carlomagno, (Edizioni ETS, Pisa 1997) pp. 383–388
86. D.A. Fletcher, K.B. Crozier, C.F. Quate, G.S. Kino, K.E. Goodson, D. Simanovskii, D.V. Palanker: 'Near-Field Infrared Imaging with a Microfabricated Solid Immersion Lens'. Appl. Phys. Lett. **77**, 2109 (2000)
87. D.A. Fletcher, N.U. Webb, G.S. Kino, C.F. Quate, K.E. Goodson: 'Thermal Microscopy with a Microfabricated Solid Immersion Lens'. In: *Extended Abstracts of IEEE/LEOS Int. Conference on Optical MEMS*, Okinawa, Japan, 2001, pp. 88–89
88. G. De Mey, B. Wiecek: 'Application of Thermography for Microelectronic Design and Modelling'. In: *Quantitative Infrared Thermography 4 (QIRT'98)*, Lodz, Poland, September 7–September 10, 1998, ed. by D. Balageas, G. Busse, C.M. Carlomagno, (Lodart S.A. Lodz 1999) pp. 23–27
89. A. Simo, S. Martinuzzi: 'Hot Spots and Heavily Dislocated Regions in Multicrystalline Silicon Cells'. In: *21rst IEEE Photovoltaic Specialists' Conference*, Kissimee, May 21–May 25, 1990, (IEEE 1990) pp. 800–805

90. J. Rappich, M. Mueller, F. Schneider, H. Tributsch: 'Thermographic sampling technique applied to microelectronics and photovoltaic devices'. Solar Energy Materials and Solar Cells **53**, 205 (1998)
91. www.quantumfocus.com
92. G.M. Carlomagno, P.G. Bernardi: 'Unsteady thermotopography in non-destructive testing'. In: *3rd Biannual Infrared Information Exchange*, Aug. 24–26, St. Louis, USA (1976), pp. 33–39
93. J.L. Beaudoin, E. Merienne, R. Danjoux, M. Egee: 'Numerical system for infrared scanners and application to the subsurface control of materials by photothermal radiometry'. *Infrared Technology and Applications*, SPIE, Vol. **590**, 287 (1985)
94. G. Busse, D. Wu, W. Karpen: 'Thermal Wave Imaging with Phase Sensitive Modulated Thermography'. J. Appl. Phys. **71**, 3962 (1992)
95. W. Karpen, D. Wu, R. Stegmüller, G. Busse: 'Depth Profiling in Laminates with Local Lock-in Thermography'. In: *Quantitative Infrared Thermography (QUIRT 94)*, ed. by D. Balageas, Elsevier 1997, pp. 281–285
96. D. Wu, J. Rantala, W. Karpen, G. Zenzinger, B. Schönbach, W. Rippel, R. Stegmüller, L. Diener, G. Busse: 'Application of Lock-in Thermography Methods'. In: *Review of Progress in Quantitative Nondestructive Evaluation* **15**, ed. by D.O. Thompson, D.E. Chimenti (Plenum, New York 1996), pp. 511–519
97. O. Breitenstein, M. Langenkamp, F. Altmann, D. Katzer, A. Lindner, H. Eggers: 'Microscopic Lock-in Thermography Investigation of Leakage Sites in Integrated Circuits'. Rev. Sci. Instrum. **71**, 4155 (2000)
98. R. Gupta, O. Breitenstein, J. Zettner, D. Karg: 'In-Line Shunt Detection in Solar Cells by Fast Lock-in Infrared Thermography'. In: *22nd European Photovoltaic Solar Energy Conference and Exhibition*, Milan 2007, pp. 1975–1978
99. www.csgsolar.com
100. http://catalog.osram-os.com
101. E. Hecht: '*Optics*'. (Addison-Wesley, San Francisco, CA 2002)
102. H. Suzuki, K. Koshikawa, T. Kuroda, T. Ishizuka, F.P. Gyue, F.P. Yuan, W.J. Ji. Improvement of Performance for Higher Magnification Thermal Imaging. Proceedings of the 16th IEEE International Symposium on the Physical and Failure Analysis of Integrated Circuits (IPFA), pp. 489–492 (2009)
103. S.M. Mansfield, G.S. Kino: 'Solid Immersion Microscope'. Appl. Phys. Lett. **57**, 2615 (1990)
104. S.B. Ippolito, A.K. Swan, B.B. Goldberg, M.S. Ünlü: 'High Resolution Subsurface Microscopy Technique'. In: *IEEE Lasers and Electro-Optics Society 2000 Annual Meeting*, November 2000 **2**, pp. 430–431
105. O. Breitenstein, F. Altmann, T. Riediger, D. Karg, V. Gottschalk: 'Use of a solid immersion lens for thermal IR imaging'. In: *32nd International Symposium for Testing and Failure Analysis (ISTFA/2006)*, Austin, TX, 12.-16.11.2006, pp. 382–388
106. A.C.T. Quah, S.H. Goh, V.K. Ravikumar, S.L. Pjoa, J.C.H. Phang, V. Narang, C.M. Chua, J.M. Chin: 'Combining Refractive Solid Immersion Lens and Pulsed Laser Induced Techniques for Effective Defect Localization on Microprocessors'. In: *Int. Symposium for Testing and Failure Analysis (ISTFA 2008)*, Portland (OR) 2008, pp. 402–406
107. T. Koyama, E. Yoshida, J. Komori, Y. Mashiko, T. Nakasuji, H. Katoh: 'High Resolution Fault Isolation Technique Using Directly Forming Si Substrates into Solid Immersion Lens'. In: *International Reliability Physics Symposium (IEEE IRPS)*, Dallas TX (2003), pp. 529–535
108. P. Scholz, U. Kerst, C. Boit, C.-C. Tsao, T. Lundquist: 'Creation of a Solid Immersion Lens in Bulk Silicon Using Focused Ion Beam Backside Editing Techniques'. In: *Int. Symposium for Testing and Failure Analysis (ISTFA 2008)*, Portland (OR) 2008, pp. 157–162
109. F. Zachariasse, M. Goossens: 'Diffractive Lenses for High Resolution Laser Based Failure Analysis'. In: *31st International Symposium for Testing and Failure Analysis (ISTFA/2005)*, San Jose, CA, 06.-10.11.2005, pp. 1–7
110. www.limo.de
111. M.C. Schubert, S. Pingel, M. The, W. Warta: 'Quantitative carrier lifetime images optically measured on rough silicon wafers'. J. Appl. Phys. **101**, 124907 (2007)

112. K. Ramspeck, K. Bothe, J. Schmidt, R. Brendel: ‘Combined dynamic and steady-state infrared camera based carrier lifetime imaging of silicon wafers’. J. Appl. Phys. **106**, 114506 (2009)
113. H.S. Carslaw, J.C. Jaeger: *Conduction of Heat in Solids*, (Clarendon, Oxford, 1959)
114. D. Wu: Lockin Thermographie für die zerstörungsfreie Werkstoffprüfung und Werkstoffcharakterisierung (in German), Ph.D. Thesis, Stuttgart University (1996)
115. T. Mangold: Dynamische Thermographie mit einer schnellen IR-Array-Kamera (in German), Ph.D. Thesis, Universität des Saarlandes, Saarbrücken (2000)
116. M. Abramowitz, I.A. Stegun: *Handbook of Mathematical Functions*, (National Bureau of Standards: Applied Mathematics Series **55**, Washington DC 1994)
117. C. Donolato: ‘On the Theory of SEM Charge-Collection Imaging of Localized Defects in Semiconductors’. Optik **52**, 18 (1978)
118. C. Groth, G. Müller: *FEM für Praktiker - Temperaturfelder* (in German), (Expert Verlag, Renningen-Malmsheim 1998)
119. www.comsol.de
120. I. Konovalov, O. Breitenstein: ‘Evaluation of Thermographic Investigations of Solar Cells by Spatial Deconvolution’. In: *2nd World Conference on Photovoltaic Solar Energy Conversion*, Vienna, Austria, July 6–July10, 1998, ed. by J. Schmidt, H.A. Ossenbrink, P. Helm, H. Ehmann, E.D. Dunlop (Arte Stampa, Daverio (VA) 1998), pp. 148–150
121. I. Konovalov: ‘Zusammenhang zwischen elektrischen Verlustmechanismen und der Struktur von Solarzellen’ (in German), Ph.D. Thesis, Martin Luther University, Halle (2000) (Der Andere Verlag, Osnabrück 2000)
122. O. Breitenstein, M. Langenkamp: ‘Quantitative Local Analysis of Solar Cells by Thermal Methods’. In: *2nd World Conference on Photovoltaic Solar Energy Conversion*, Vienna, Austria, July 6–July10, 1998, ed. by J. Schmidt, H.A. Ossenbrink, P. Helm, H. Ehmann, E.D. Dunlop (Arte Stampa, Daverio (VA) 1998), pp. 1382–1385
123. O. Breitenstein, J.P. Rakotoniaina, M.H. Al Rifai: ‘Quantitative Evaluation of Shunts in Solar Cells by Lock-in Thermography’. Prog. Photovolt: Res. Appl. **11**, 515 (2003)
124. O. Breitenstein, M. Langenkamp, K.R. McIntosh, C.B. Honsberg, M. Rinio: ‘Localization of Shunts Across the Floating Junction of DSBC Solar Cells by Lock-in Thermography’. In: *28th IEEE Photovoltaic Specialists’ Conference*, Anchorage, Alaska, September 15–September 22, 2000, (IEEE 2000) pp. 124–127
125. G. Demoment: ‘Image Reconstruction and Restauration: Overview of Common Estimation Structures and Problems’. IEEE Transactions on Acoustics, Speech, and Signal Processing **37**, 2024 (1989)
126. U. Seidel, K. Haupt, H.G. Walther, J.A. Burt, M. Munidasa: ‘An Attempt Towards Quantitative Photothermal Microscopy’. J. Appl. Phys. **78**, 2050 (1995)
127. D.J. Crowther, L.D. Favro, P.K. Kuo, R.L. Thomas: ‘Inverse Scattering Algorithm Applied to Infrared Thermal Wave Images’. J. Appl. Phys. **74**, 5828 (1993)
128. www.VayTek.com
129. O. Breitenstein, I. Konovalov, M. Langenkamp: ‘Highly Sensitive Lock-in Thermography of Local Heat Sources Using 2-Dimensional Spatial Deconvolution’. In: *Quantitative Infrared Thermography 5 (QIRT’2000)*, Reims, France, July 18–July 21, 2000, ed. by D. Balageas, L.-J. Beaudoin, G. Busse, C.M. Carlomogno (Lodart S. A. Lodz 2001), pp. 218–223
130. O. Breitenstein, J.P. Rakotoniaina, M.H. Al Rifai, M. Gradhand, F. Altmann, T. Riediger: ‘New Developments in IR Lock-in IR Thermography’. In: *Int. Symposium for Testing and Failure Analysis (ISTFA 2004)*, Worchester (MA) 2004, pp. 595–599
131. O. Breitenstein, F. Altmann: ‘Inversion of Microscopic Lock-in Thermograms in the Presence of Emissivity Contrast’. NDT&E International **39**, 636 (2006)
132. S. Riegel, University of Konstanz, Germany, Personal Communication
133. www.x20.org/library/thermal/emissivity.htm
134. M. Gradhand, O. Breitenstein: ‘Preparation of Nonconducting Infrared-Absorbing Thin Films’. Rev. Sci. Instr. **76**, 053702 (2005)

135. M. Kasemann, B. Walter, C. Meinhardt, J. Ebser, W. Kwapil, W. Warta: 'Emissivity-Corrected Power Loss Calibration for Lock-in Thermography Measurements on Silicon Cells'. J. Appl. Phys. **103**, 113503 (2008)
136. M. Lundstrom. *Fundamentals of Carrier Transport*, 2nd edn. Cambridge University Press, Cambridge (2000)
137. T.H. Geballe, G.W. Hull: 'Seebeck Effect in Silicon'. Phys. Rev. **98**, 940 (1955)
138. H. Straube, J.-M. Wagner, O. Breitenstein. Measurement of the Peltier coefficient of semiconductors by lock-in thermography. Appl. Phys. Lett. **95**, 052107 (2009)
139. E.H. Rhoderick, R.H. Williams: 'Metal–Semiconductor Contacts', 2nd edn., (Clarendon, Oxford 1988)
140. K.P. Pipe, R.J. Ram, A. Shakouri: 'Bias-Dependent Peltier Coefficient and Internal Cooling in Bipolar Devices'. Phys. Rev. B **66**, 125316 (2002)
141. G.C. Dousmanis, C.W. Mueller, H. Nelson, K.G. Petzinger: 'Evidence of Refrigeration Action by Means of Photon Emission in Semiconductor Diodes'. Phys. Rev. **133**, A316 (1964)
142. W. Shockley, H.J. Queisser: 'Detailed Balance Limit of Efficiency of p–n Junction Solar Cells'. J. Appl. Phys. **32**, 510 (1961)
143. M.A. Green, P.A. Basore, N. Chang, D. Clugston, R. Egan, R. Evans, D. Hogg, S. Jarnason, M. Keevers, P. Lasswell, J. O'Sullivan, U. Schubert, A. Turner, S.R. Wenham, T. Young: 'Crystalline Silicon on Glass (CSG) Thin-Film Solar Cell Modules'. Solar Energy **77**, 857 (2004)
144. D. Wu, H. Hamann, A. Salerno, G. Busse: 'Lock-in Thermography for Imaging of Modulated Flow in Blood Vessels'. In: *Quantitative Infrared Thermography 3 (QIRT'96)*, Stuttgart, Germany, September 2–September 5, 1996, ed. by D. Balageas, G. Busse, C.M. Carlomagno, (Edizioni ETS, Pisa 1997) pp. 343–347
145. Microelectronic Failure Analysis, Desk Reference Fifth Edition, ed. by the EDFAS Desk Reference Committee (ASM International, Ohio 2004), ISBN: 0-87170-804-3
146. F. Altmann, IWMH (Halle), Personal Communication
147. P. Jacob, J. Reimer: 'Assembly Process – A Surface Electrostatic Discharge Killer for Devices and a FA Challenge'. Electronic Device Failure Analysis **7**, 6 (2005)
148. O. Breitenstein, J.P. Rakotoniaina, M.H. Al Rifai, M. Werner: 'Shunt Types in Crystalline Silicon Solar Cells'. Prog. Photovolt: Res. Appl. **12**, 529 (2004)
149. O. Breitenstein, J.P. Rakotoniaina, A.S.H. van der Heide, J. Carstensen: 'Series Resistance Imaging in Solar Cells by Lock-in Thermography'. Prog. Photovolt: Res. Appl. **13**, 645 (2005)
150. K. Ramspeck, K. Bothe, D. Hinken, B. Fischer, J. Schmidt, R. Brendel: 'Recombination Current and Series Resistance Imaging of Solar Cells by Combined Luminescence and Lock-in Thermography'. Appl. Phys. Lett. **90**, 153502 (2007)
151. K. Bothe, P. Pohl, J. Schmidt, T. Weber, P. Altermatt, B. Fischer, R. Brendel: 'Electroluminescence Imaging as an In-Line Characterisation Tool for Solar Cell Production'. In: *21st Eur. Photovolt. Solar Energy Conf.*, September 4–September 8, 2006, Dresden, Germany, pp. 5200–5209
152. I.E. Konovalov, O. Breitenstein, K. Iwig: 'Local Current–Voltage Curves Measured Thermally (LIVT): A New Technique for Characterizing PV Cells'. Solar Energy Materials and Solar Cells **48**, 53 (1997)
153. M. Kasemann, W. Kwapil, M.C. Schubert, H. Habenicht, B. Walter, M. The, S. Kontermann, S. Rein, O. Breitenstein, J. Bauer, A. Lotnyk, B. Michl, H. Nagel, A. Schütt, J. Carstensen, H. Föll, T. Trupke, Y. Augarten, H. Kampwerth, R.A. Bardos, S. Pingel, J. Berghold, W. Warta, S.W. Glunz: 'Spatially Resolved Silicon Solar Cell Characterization Using Infrared Imaging Methods'. In: *33rd IEEE Photovoltaic Specialists Conference*, May 11–May 16, 2008, San Diego, CA, USA, pp. 148–154
154. O. Breitenstein, J. Bauer, J.-M. Wagner, A. Lotnyk: 'Imaging Physical Parameters of Pre-Breakdown Sites by Lock-in Thermography Techniques'. Prog. Photovolt: Res. Appl. **16**, 679 (2008)

155. J.-M. Wagner, J. Bauer, O. Breitenstein: 'Classification of pre-breakdown phenomena in multicrystalline silicon solar cells'. In: *24th Eur. Photovoltaic Solar Energy Conference and Exhibition*. Hamburg, Germany, September 21–September 25, pp. 925–929 (2009)
156. H. Straube, O. Breitenstein, J.-M. Wagner: 'Lock-in thermography on crystalline silicon on glass (CSG) thin film modules: influence of Peltier contributions'. In: *24th Eur. Photovoltaic Solar Energy Conference and Exhibition*. Hamburg, Germany, September 21–September 25, pp. 2500–2505 (2009)
157. J. Klaer, I. Luck, A. Boden, R. Klenk, I. Gavilanes Perez, R. Scheer: 'Mini-modules From a $CuInS_2$ Baseline Process'. Thin Solid Films **431–432**, 534 (2003)
158. I. Gavilanes Pérez: 'Non Destructive Electrical and Morphological Characterisation of Chalcopyrite Solar Cells by Infrared Thermographical Analysis'. Ph.D. Thesis, University of Salamanca, Spain (2003)
159. R. Gupta, O. Breitenstein, J. Zettner, D. Karg: 'In-Line Shunt Detection in Solar Cells by Fast Lock-in Infrared Thermography'. In: *22nd European Photovoltaic Solar Energy Conference*, September 3–September 7, 2007, Milan, Italy, pp. 1975–1978
160. J. Isenberg: 'Neue Infrarotmeßtechniken für die Photovoltaik' (in German). Ph.D. Thesis, University Konstanz (2003)
161. J. Isenberg, A.S.H. van der Heide, W. Warta: 'Investigation of Series Resistance Losses by Illuminated Lock-in Thermography'. Prog. Photovolt: Res. Appl. **13**, 697 (2005)
162. O. Breitenstein, J.P. Rakotoniaina: 'Unusual Lock-in Thermography Signals: Schottky-Type Grid Contacts, Peltier Effects, and Thermal Wave Interference'. In: *IV. World Conference on Photovoltaic Energy Conversion*, May 7–May 12, 2006, Waikaloa, Hawaii, pp. 912–915
163. B. Michl, M. Kasemann, J. Giesecke, M. Glatthaar, A. Schütt, J. Carstensen, H. Föll, S. Rein, W. Warta, H. Nagel: 'Application of Luminescence Imaging Based Series Resistance Measurement Methods in an Industrial Environment'. In: *23rd European Photovoltaic Solar Energy Conference*, September 1–September 5, 2008, Valencia, Spain, pp. 1176–1181
164. M. Glatthaar, J. Haunschild, M. Kasemann J. Giesecke, W. Warta, S. Rein: 'Spatially resolved determination of dark saturation current and series resistance of silicon solar cells'. Phys. Stat. Sol. RRL **4**, 13 (2010)
165. K. Ramspeck. K. Bothe, J. Schmidt, R. Brendel: 'Correlation Between Spatially Resolved Solar Cell Efficiency and Carrier Lifetime of Multicrystalline Silicon'. J. Mater. Sci: Mater. Electron. **19**, S4 (2008)
166. J. Bauer, J.-M. Wagner, A. Lotnyk, H. Blumtritt, B. Lim, J. Schmidt, O. Breitenstein: 'Hot Spots in Multicrystalline Solar Cells: Avalanche Breakdown Due to Etch Pits'. Phys. Stat. Sol. RRL **3**, 40 (2009), DOI 10.1002/pssr.200802250
167. W. Kwapil, P. Gundel, M.C. Schubert, F.D. Heinz, W. Warta, E.R. Weber, A. Goetzberger, G.M. Martinez-Criado: 'Observation of metal particles at breakdown sites in multicrystalline silicon solar cells'. Appl. Phys. Lett. **95**, 232113 (2009)
168. M. Rinio, H.J. Möller, M. Werner: 'LBIC Investigations of the Lifetime Degradation by Extended Defects in Multicrystalline Solar Silicon'. Solid State Phenomena **63–64**, 115 (1998)
169. S.V. Litvinenko, L.M. Ilchenko, S.O. Kolenov, A. Kaminski, A. Laugier, E.M. Smirnov, V.A. Skryshevsky: 'Remote Control of the I-V Characteristic of Solar Cells in the Encapsulated Modules'. In: *16th Eur. Photovoltaic Solar Energy Conference*, Glasgow, UK, May 1–May 5 2000, ed. by W. Freiesleben, W. Palz, H.A. Ossenbrink, P. Helm (Stephens & Associates, Bedford 2000) pp. 2410–2413
170. G. Agostinelli, G. Friesen, F. Merli, E.D. Dunlop, M. Acciarri, A. Racz, J. Hylton, R. Einhaus, T. Lauinger: 'Large Area Fast LBIC as a Tool for Inline PV Module and String Characterization'. In: *17th Eur. Photovoltaic Solar Energy Conference*, Munich, Germany, October 22–October 26, 2001, Proceedings, ed. by B. McNelis, W. Palz, H.A. Ossenbrink, P. Helm (ETA Florence 2002), pp. 410–413
171. D.L. King, J.A. Kratochvil, M.A. Quintana: 'Application for Infrared Imaging Equipment in Photovoltaic Cell, Module, and System Testing'. In: *28th IEEE Photovoltaic Specialists' Conference*, Anchorage, Alaska, September 15–September 22, 2000 (IEEE 2000) pp. 1487–1490

172. C. Vodermayer, M. Mayer, M. Mayer, T. Müller, M. Niess, G. Wotruba, G. Becker, M. Zehner, J. Schumacher: 'First Results: Correlation Between IT Images and Electrical Behavior and Energy Yield of PV Modules'. In: *23rd European Photovoltaic Solar Energy Conference*, September 1–September 5, 2008, Valencia, Spain, pp. 3134–3137
173. U. Hoyer, C. Buerhop, U. Jahn: 'Electroluminescence and Infrared Imaging for Quality Improvements of PV Modules'. In: *23rd European Photovoltaic Solar Energy Conference*, September 1–September 5, 2008, Valencia, Spain, pp. 2913–2916
174. T. Potthoff, K. Bothe, U. Eitner, D. Hinken, M. Köntges: 'Detection of the voltage distribution in photovoltaic modules by electroluminescence imaging'. Prog. Photovolt Res. Appl. **18**, 100 (2010)
175. R. Gupta, O. Breitenstein, J. Schneider: 'Characterization of Crystalline Silicon on Glass (CSG) Modules by Surface Potential Mapping'. In: *22nd European Photovoltaic Solar Energy Conference and Exhibition*, September 3–September 7, 2007, Milan, Italy, pp. 1434–1437
176. A.G. Aberle, J. Schmidt, R. Brendel: 'On the Data Analysis of Light-Biased Photoconductance Decay Measurements'. J. Appl. Phys. **79**, 1491 (1996)
177. S. Riepe, H. Lautenschlager, J. Isenberg, W. Warta, R. Schindler, M. Ghosh, A. Müller: 'Increased Wafer Yield for Solar Cells in Top and Bottom Regions of Cast Multicrystalline Silicon'. In: *19th European Photovoltaic Solar Energy Conference*, Paris, France, 2004, p. 986
178. P. Rosenits, T. Roth, S.W. Glunz, S. Beljakowa: 'Determining the Defect Parameters of the Deep Aluminum-Related Defect'. Appl. Phys. Lett. **91**, 122109 (2007)
179. M.C. Schubert, J. Isenberg, M. Rinio, W. Warta: 'Temperature Dependent Carrier Lifetime Images'. In: *19th European Photovoltaic Solar Energy Conference*, Paris, France, 2004, p. 500
180. S. Rein, T. Rehrl, W. Warta, S.W. Glunz: 'Temperature-Dependent Lifetime Spectroscopy (TDLS) in Silicon'. In: *17th European Photovoltaic Solar Energy Conference*, Munich, Germany, 2004, p. 1561
181. H.Y. Fan: 'Effect of Traps on Carrier Injection in Semiconductors'. Physical Review **92**, 1424 (1953)
182. J.R. Haynes, J.A. Hornbeck: 'Temporary Traps in Silicon and Germanium'. Physical Review **100**, 606 (1955)
183. D. Macdonald, A. Cuevas: 'Trapping of Minority Carriers in Multicrystalline Silicon'. Applied Physics Letters **74**, 1710 (1999)
184. D. Macdonald, A. Cuevas: 'On the Use of a Bias-Light Correction for Trapping Effects in Photoconductance-Based Lifetime Measurements of Silicon'. Solar Energy Materials and Solar Cells **65**, 509 (2001)
185. P. Pohl, J. Schmidt, C. Schmiga, R. Brendel: 'Defect Imaging in Multicrystalline Silicon Using a Lock-in Infrared Camera Technique'. Journal of Applied Physics **101**, 1 (2007)
186. P. Gundel, M.C. Schubert, W. Warta: 'Systematic Analysis of Trapping as a Tool to Predict Diffusion Length in Multicrystalline Silicon Cells'. In: *22nd European Photovoltaic Solar Energy Conference*, Milan, Italy, 2007, p. 1608
187. M.C. Schubert, S. Riepe, S. Bermejo, W. Warta: 'Determination of Spatially Resolved Trapping Parameters in Silicon with Injection Dependent Carrier Density Imaging'. Journal of Applied Physics **99**, 114908 (2006)
188. P. Pohl, J. Schmidt, K. Bothe, R. Brendel: 'Mapping of Trap Densities and Energy Levels in Semiconductors Using a Lock-in Infrared Camera Technique'. Applied Physics Letters **87**, 142104 (2005)
189. M.C. Schubert, S. Riepe, W. Warta: 'Spatially Resolved Trapping Detection and Correlation with Material Quality in Multicrystalline Silicon'. In: *21st European Photovoltaic Solar Energy Conference*, Dresden, Germany, 2006, p. 629
190. P. Gundel, M.C. Schubert, W. Warta: 'Origin of Trapping in Multicrystalline Silicon'. J. Appl. Phys. **104**, 073716 (2008)

191. W. Warta, J. Sutter, B.F. Wagner, R. Schindler: 'Impact of Diffusion Length Distributions on the Performance of mc-Silicon Solar Cells'. In: *2nd World Photovoltaic Solar Energy Conference*, Vienna, Austria, 1998, p. 1650
192. X. Maldague, J.P. Couturier, S. Marinetti, A. Salerno, D. Wu: 'Advances in Pulsed Phase Thermography'. In: *Quantitative Infrared Thermography 3 (QIRT'96)*, Stuttgart, Germany, September 2–September 5, 1996, ed. by D. Balageas, G. Busse, C.M. Carlomagno, (Edizioni ETS, Pisa 1997) pp. 377–382
193. F. Galmiche, X. Maldague: 'Depth Defect Retrieval Using the Wavelet Pulsed Phase Thermography'. In: *Quantitative Infrared Thermography 5 (QIRT'2000)*, Reims, France, July 18–July 21, 2000, ed. by D. Balageas, L.-J. Beaudoin, G. Busse, C.M. Carlomogno (Lodart S. A. Lodz 2001), pp. 194–199
194. http://www.baslerweb.com
195. P. Pohl, R. Brendel: 'Mapping of Solar Cell Base Doping Concentration Using Lock-in Thermography'. In: *20th European Photovoltaic Solar Energy Conference and Exhibition*, Barcelona (2005), p. 140
196. T. Fuyuki, H. Kondo, T. Yamazaki, Y. Takahashi, Y. Uraoka: 'Photographic surveying of minority carrier diffusion length in polycrystalline silicon solar cells by electroluminescence'. Appl. Phys. Lett. **86**, 262108 (2005)
197. T. Trupke, R.A. Bardos, M.C. Schubert, W. Warta: 'Photoluminescence imaging of silicon wafers'. Appl. Phys. Lett. **89**, 044107 (2006)
198. www.msc-technik.de
199. http://en.wikipedia.org/wiki/Silicon
200. http://www.harvel.com/tech-support-downloads.asp download "PVC Duct Brochure"
201. http://www.kayelaby.npl.co.uk/general_physics/2_3/2_3_6.html
202. http://boehmtec.com/index.php?opt=products&sopt=6

Appendix A
Thermal and IR Properties of Selected Materials

Table A.1 Thermal properties of selected materials

Material	Density ϱ [kg/m^3]	Specific Heat c_p [kJ/kg°C]	Heat Conduct. λ [W/m°C]	th. Diffusion Length Λ at 1 Hz [mm]	Reference
aluminium	2,707	0.896	204	5.17	[2]
copper	8,954	0.3831	386	5.98	[2]
nickel	8,906	0.4459	90	2.68	[2]
silver	10,525	0.234	407	7.25	[2]
nickel silver[a]	8,618	0.394	24.9	1.53	[2]
glass (window)	2,700	0.84	0.78	0.33	[2]
silicon	2,330	0.70	149	5.37	[199]
PVC	1,400	0.88	0.16	0.187	[200–202]

[a] (62%Cu,15%Ni,22%Zn)

Table A.2 IR properties of selected materials

Material	IR Emissivity ε	Reference
paper	0.93	[133]
white Al_2O_3	0.90	[133]
black laquer	0.96	[133]
oil on Ni, thick	0.82	[133]
oil on Ni, 2.5 μm	0.27	[133]
Ni, polished	0.05	[133]
Al, unoxidized	0.03	[133]
stainless steel	0.22	[133]

List of Symbols

A	area
A	amplitude of the detected lock-in signal, amplitude factor
A_{noise}	noise component of measured signal
A_{shunt}	area in which the shunt signal is measured
A_{test}	temperature modulation amplitude of test device
A_{whole}	area of the whole sample
c	scaling factor of the camera (in mK/digit)
c	velocity of light
c_{p}	specific heat
d	sample thickness
d	SIL thickness
D	pixel distance
e	electronic charge
f	focal length of optics, spatial frequency
f_{fr}; f_{frame}	frame rate
$f_{\mathrm{lock\text{-}in}}$	lock-in frequency
f_s	sampling rate
F; $F(t)$; F_k	detected signal; time dependent; digitized
$\bar{F}$	mean value of the detected signal
F_i^N	noise signal in digits of the i th measured value
$F^{\mathrm{topo}}(x, y)$	topography correlated signal contribution
Fd	d.c.-component of the digitized temperature signal
Fo	oscillating component of the digitized temperature signal
Fl	linear slope component of the digitized temperature signal
FF	fill factor of a solar cell
$\Delta F_j(x, y)$	phase correlated signal contribution
h	Planck constant
i; j; k	summation indices
$I(R)$	areal integral of measured signal up to radius R
I	current

Symbol	Meaning
J	current density
J_0	saturation current density
J_{aval}	avalanche current
J_{dr}	depletion region current
J_{ph}	photocurrent
J_{sc}	short circuit current density of a solar cell
k	number of measured frames
k	Boltzmann constant
K	adjustment parameter of Wiener filter
$K_j^{0°}; K_j^{-90°}$	correlation factors
$K(t); K_k$	correlation function; digitized
$\text{kei}(x)$	imaginary part of the Kelvin function
$\text{ker}(x)$	real part of the Kelvin function
l	line index of a thermogram
L	number of lines in a thermogram
m	mass, magnification factor
m	parameter of synchronous undersampling
m	parameter for the "loop gain" in iteration procedure
M	total number of measured (digitized) frames
M	dimension of the PSF matrix
$M1$	first moment of the correlation vector
$M_\lambda(T)$	spectral specific irradiation
n	number of measurement points within a lock-in period
n	number of frames per lock-in period
n	ideality factor of a diode
n	refractive index
$n_{\max}$	number of iterations
N	number of measured lock-in periods
$N(x, y)$	noise contribution to measured signal
N_{sys}	pixel-related system noise density
NA	numeric aperture
NETD_{cam}	noise equivalent temperature difference of a camera
p; p_0	density of dissipated power; amplitude
p^l; p_0^l	power per unit length; amplitude
$p(u, v)$	Fourier transform of the power distribution
P, P_0	dissipated (electrical) power; amplitude
$P_1, P_2, \ldots$	mirror sources
$P_1(x, y) \ldots P_n(x, y)$	iterations of the power distribution (for deconvolution)
$P_{\max}$	maximum power point of a solar cell
P_{shunt}	power dissipated at the shunt
P_{whole}	power dissipated in the whole sample
P_{loc}	locally dissipated power
p_{th}	thermalization heat

p_{pn}^{+}	positive Peltier heat at p–n junction
p_{pn}^{-}	negative Peltier heat at p–n junction
r	radius in cylindrical coordinates
r	row index in a thermogram
R	number of rows in a thermogram
R	radial integration boundary
R	SIL radius
R_{h}	heat resistance
R_c	contact resistance
R_{s}	series resistance
R_{if}	resistance of a bonded interface
R_p	path resistance
S	camera output signal
S	correlated output signal
$S^{\mathrm{amb}}(x, y)$	signal at ambient temperature
S_{em}	signal contribution from emitted photons
S_{eq}	correlated signal measured in quasi-equilibrium
S_{shunt}	averaged signal measured in the shunt region
S^{topo}	topography contribution to the signal
$S_{\mathrm{black}}^{\mathrm{topo}}$	topography signal of a black body
S_{meas}	measured signal with T-drift
S_{whole}	averaged signal measured for the whole sample
$S^{\Delta T}(x, y)$	signal due to temperature difference ΔT
t	time
$t(u, v)$	fourier transform of the temperature distribution
t_{int}	integration time of a lock-in measurement
t_{acq}	total acquisition time
$t_{\mathrm{acq}}^{\mathrm{min}}$	minimum possible acquisition time
$tp(u, v)$	Fourier transform of the point spread function
$tp^{*}(u, v)$	complex conjugate of the Fourier transformed PSF
T	temperature (in Kelvin)
$\bar{T}$	mean value of temperature
$T_1(x, y) \ldots T_n(x, y)$	iterations of the temperature distribution (for deconvolution)
T^{after}	temperature at the end of the measurement
T^{amb}	ambient temperature
T^{before}	temperature at the beginning of the measurement
T_0	starting temperature
T_{eq}	equilibrium temperature
$T_{\mathrm{corr}}(x, y)$	measured temperature, emissivity corrected
$T_{\mathrm{meas}}(x, y)$	measured temperature, not emissivity corrected
ΔT	temperature difference
ΔT_{e}	temperature modulation in equilibrium
$Tp(x, y)$	point spread function
u, v	coordinates in the Fourier space

V	voltage
V_{loc}	local voltage
V_{oc}	open circuit voltage of a solar cell
$x; y$	summation indices
$x; y; z$	coordinates
X, Y	image size in pixels
X	line distance
α	absorption coefficient
$\alpha(\lambda)$	absorbance
$\varepsilon(\lambda); \varepsilon(x, y)$	emissivity (spectral; local)
Λ	thermal diffusion length
λ	wavelength
λ	heat conductivity
ρ	reflectance
ϱ	density of mass
σ_{cam}	standard deviation of the camera noise
σ_{sys}	system standard deviation
τ	transmittance
τ	thermal relaxation time constant
τ_i	integration time of a single frame
Π	Peltier coefficient
ϕ	angle of cylindrical coordinates
φ	phase shift of detected signal
Φ	phase of the detected signal
ω	$2\pi f_{lock\text{-}in}$

Abbreviations

a.c.	alternating current
ADC	analog digital converter
AFM	atomic force microscopy
ASCII	American standard code information interchange
CCD	charge coupled device
CDI	carrier density imaging
CL	cathodoluminescence
D	pixel width
d.c.	direct current
DLIT	dark lock-in thermography
DPCT	dynamic precision contact thermography
DSP	digital signal processor
EBIC	electron beam induced current
EL	electroluminescence
ESD	electrostatic discharge
FFT	fast Fourier transformation
FMI	fluorescent microthermal imaging
FPA	focal plane array
GOI	gate oxid integrity (defects)
IC	integrated circuit
ILIT	illuminated lock-in thermography
ILM	infrared lifetime mapping
InSb	indium antimonide (IR-detector material)
IR	infrared
I-V	current-voltage (characteristic)
LBIC	light beam induced current
LIVT	local I-V characteristic measured thermally
LSB	least significant bit
MCT	mercury cadmium telluride (HgCdTe, IR-detector material)
MESFET	metal Schottky field effect transistor
MOS	metal oxide semiconductor
MW-PCD	microwave photoconductivity decay

NDT	non destructive testing
NETD	noise equivalent temperature difference
NTC	negative temperature coefficient thermistor
OBIRCH	optical beam induced resistance change
PC	personal computer
PL	photoluminescence
PSF	point spread function
PtSi	platinum-silicide (IR-detector material)
QWIP	quantum well infrared photodetector
ROM	read only memory
SNOM	scanning near-field optical microscopy
SIL	solid immersion lens
SOI	silicon on insulator
TIVA	thermally induced voltage analysis
UV	ultraviolet

Index

$-45°$ signal, 19, 134, 155
$-90°$ signal, 19, 125, 127, 153, 155
0° signal, 18, 125, 127, 153, 155

absorbance, 8, 159
acquisition time, 23
  total, 40
amplitude error, 37, 112
analog digital converter, 16
aquarelle paint, 161
atomic force microscope, 61
Avalanche multiplication factor, 210

calibration, 42
cathodoluminescence, 118
charge coupled device, 11
colour table, 150, 152, 153
correlation
  4-bucket, 34, 37, 70
  4-point, 20, 37
  asynchronous, 17, 70
  digital lock-in, 16
  function, 16
  lock-in, 16, 24, 69
  on-line, 16, 69
  synchronous, 38
  two-channel, 18

dark lock-in thermography, 187
deconvolution, 137, 180
  iterative, 140, 142
detected signal, 14, 16
detection limit, vii, 3, 128
digital signal processor, 13
dissipated power, 3, 150
  at shunt, 133
  density, 102, 128

drift compensation, 107
dynamic precision contact thermography, 71

effective spatial resolution, 156
electroluminescence, 231
electron beam-induced current, 118
electrostatic discharge, 67
emissivity, 8, 159
  contrast, 147, 154, 162, 180
equilibrium temperature, 105

failure analysis, 71, 178
  of solar modules, 213
finite elements, 121
first moment
  of the correlation vector, 110
fluorescent microthermal imaging, 65, 71, 178
focal plane array camera, 11
Fourier transform, 16, 21, 98, 139
frame rate, 24, 40

harmonic frequency, 34
heat conduction, 102, 104
heat resistance, 106, 108
heat sink, 43, 106
heat source
  extended, 118, 126
  line, 119, 126
  local, 151, 158
  point, 114, 126, 131

illuminated lock-in thermography (ILIT), 187, 203
image
  amplitude, 23, 149, 153, 155
  in-phase, 22, 137, 149

integration technique, 129, 136
phase, 23, 149, 153, 155
quadrature, 22, 137, 149
through the chip, 183
image integration technique, 129
in-phase signal, 18
indium-antimonide detector, 11
information depth, 2
inhomogeneity, 2, 164, 186, 216
initial heating phase, 107
integrated circuit, 154, 178
integration time, 16, 41
IR
emitter film, 153, 161
long-range, 9
microthermography, 178
mid-range, 9

J_{sc}-ILIT, 205
Joule signal, 174

Kelvin function, 116, 117
Kirchhoff's law, 8, 51, 54, 159

liquid crystal technique, 65, 178
lock-in frequency, 14, 20, 41, 156
lock-in thermography, 2, 22, 69, 71

mercury-cadmium-telluride detector, 11
MESFET, 62
MF-ILIT, 210
microscopic image, 62, 71, 154
mirror scanner, 10, 67, 69
mirror source, 115, 123, 141, 143
missing pixels, 13

Narcissus effect, 13
noise, 38
amplitude, 41
noise equivalent temperature difference, 38, 54, 93
non-harmonic heating, 33
nondestructive testing, vii, 1, 4, 20, 30, 33, 72, 107, 137, 150
NTC thermistor, 62

OBIRCH, 67, 80, 184
overshoot, 117, 125, 131

Peltier coefficient, 168
Peltier effect, 47, 168, 205
Peltier signal, 174
phase error, 37, 112
photoluminescence, 231
photon emission microscopy, 67
photoreflectance, 65
pixel distance, 121, 155
pixel-related system noise density, 41, 71
Planck's law, 8
point spread function, 121, 138
positivity constraint, 140, 144
proportionality technique, 129
pulse thermography, 1

quadrature signal, 18
quantitative interpretation, 216
quasi adiabatic, 105, 215
quasi equilibrium, 105

reflectance, 8
resistive thermometer, 62, 63
reverse-bias DLIT, 198

sample thickness, 103, 115, 118
sampling rate, 20
scaling factor, 38
Schlieren imaging, 67, 178
Series resistance imaging, 193
shunt, 132, 186
edge shunt, 124, 215
local shunt, 133, 215
signal
d.c. component, 109
in-phase, 18
linear slope component, 109
noise contribution, 39
oscillating component, 109
phase, 38, 156
phase correlated, 39
phase-coupled, 109
quadrature, 18
topography, 154, 166
topography correlated, 39
Slope-DLIT, 200
SNOM, 65
solar cell, 68, 70, 153, 186
efficiency, 186
monocrystalline silicon, 186
multicrystalline silicon, 152, 186

solar module, 213
  $CuInS_2$ thin-film, 215
  silicon, 215
spatial resolution
  effective, 68, 103
specific heat, 43
spectral specific irradiation, 8
steady-state thermography, 1, 68
system standard deviation, 39

TC-DLIT, 200
test device, 42
thermal diffusion length, 36, 102, 114, 116, 131, 156
thermal relaxation time, 104, 106, 107
thermal wave, 2, 102, 114
  cylindric, 117
  damping, 103
  spherical, 117
thermally thick, 103, 126, 134, 150, 154
thermally thin, 103, 126, 131, 150, 153
Thermo-AFM, 62
thermocouple, 62, 63
thermoreflectance, 64
topography contrast, 68, 159
transmittance, 8
two-point calibration, 13, 74, 77, 164

undersampling, 17, 26, 70, 113, 184

V_{oc}-ILIT, 203

Wiener filter, 98, 139